FLUIDELASTIC INSTABILITY IN HEAT EXCHANGER TUBE ARRAYS

FLUIDELASTIC INSTABILITY IN HEAT EXCHANGER TUBE ARRAYS

BY

AHMED KHALIFA, M.Sc., B.Eng. (Honors)

A Thesis

Submitted to the School of Graduate Studies

in Partial Fulfilment of the Requirements

for the Degree

Doctor of Philosophy

McMaster University

©Copyright by Ahmed Khalifa, September 2011

Doctor of Philosophy (2011) — McMaster University

(Mechanical Engineering) — Hamilton, Ontario, Canada

TITLE: Fluidelastic Instability in Heat Exchanger Tube Arrays

AUTHOR: Ahmed Khalifa

M.Sc., B.Eng. (Honors), Mechanical Engineering

Cairo University, Cairo, Egypt

SUPERVISOR: Dr. David Weaver

Dr. Samir Ziada

NUMBER OF PAGES: xxxiv; 256

"In the name of Allah , the Entirely Merciful, the Especially Merciful"

To the Good Memory of My Father

Abstract

Of the various excitation mechanisms causing excessive tube vibrations in tube and shell heat exchangers, fluidelastic instability is the most dangerous, and therefore has received the most attention. The objective of this research is to advance the current understanding of the fluidelastic instability in tube arrays through a fundamental investigation of the phenomenon experimentally, numerically and analytically.

The concept of using a single flexible tube in a rigid array to investigate fluidelastic instability has been critically reviewed. It was found that the fluidelastic instability threshold in tube arrays is significantly affected by array geometry, pitch ratio, mass ratio and tube row location in the array. The results showed that, in general, fluidelastic instability in tube arrays is caused by a combination of the damping and the stiffness mechanisms. It was concluded that while the use of a single flexible tube in a rigid array provided a useful model for fundamental research and physical insights, it must be cautioned that it is not generally adequate for determining the experimental stability limits of tube arrays. The outcomes of this critical review helped in the design of a new experiment which facilitated precise control of the system parameters, and provided more comprehensive measurements.

Experimental investigation of the interaction between tube vibrations and fluid forces was conducted using surface pressure measurements at the tube surface. The results showed that, there is a finite time delay between tube vibration and the associated fluid forces acting on the tube. The resulting phase lag was found to increase as the mean gap velocity increased, and ultimately the fluid forces became in phase with the tube velocity during the onset of instability. Velocity measurements of the interstitial flow perturbations associated with tube vibrations were carried out along the flow path in the array. It was found that the flow perturbation amplitude is most pronounced at the flow separation point from the vibrating tube, and that the flow perturbation amplitude decays continuously to a negligible amplitude at about one and a half rows upstream. This suggests that the flow perturbations are caused by the flow separation from the tube and the associated vorticity shedding and convection. The phase lag measurements between tube vibrations and flow perturbations support this conclusion, and show that the flow perturbations propagate upstream and downstream at different rates.

Computational Fluid Dynamics modeling of the tube array was developed to assist in understanding the experimental results. The CFD models were validated using experimental data from both the literature and from the present research. It was found that there are two propagation mechanisms for the flow perturbations associated with tube vibrations. The first mechanism is caused by the pressure pulsation due to tube vibrations. This mechanism is dominant at lower reduced velocities, and propagates at the speed of sound. The second mechanism is caused by the flow separation and the associated vorticity shedding, and this mechanism is dominant at higher reduced velocities. The transition between the two mechanisms occurs at a reduced velocity of about ($U_r \approx 2$).

Mathematical models of the flow perturbation phase lag and amplitude decay

were developed. The new models were coupled with the semi-analytical model after modifying its geometrical parameters according to the flow visualizations in the literature. The resulting stability maps show a significant improvement to the current prediction of the fluidelastic instability data in the literature. The outcomes of the present work can contribute to improve the future design guidelines for tube and shell heat exchangers to achieve extended service time with higher efficiency.

Acknowledgements

I would like to express sincere gratitude to my supervisor Dr. Weaver whom I'm greatly indebted to. I thank him for his insights, patience, and encouragements throughout the course of this work. I would like also to express my deep appreciation to my supervisor Dr. Ziada for his constant support and guidance, not only during this work but throughout the whole graduate degree experience. It was a great honor workinf with both Dr. Weaver and Dr. Ziada. I would like also to extend my thanks to the supervisory committee members for their valuable guidance.

I would like to thank the technical staff at the Department of Mechanical Engineering, Joe, Ron, Jim, Mark and Jean Paul, and special thanks to the department administrative staff Vania, Florence, and Lily for their constant help. I would like to extend my gratitude to my fellows at the FIV group for the interesting discussions, and to all my friends at McMaster University for the nice times I had there.

Last, but not the least, I would like to thank my family for their belief in me and for helping me to become who I am. I especially thank my beloved wife Mona for her patience and support. I would like also to thank the apples of my eye Solomon, and Farida for sacrificing many sunny days for me.

Table of Contents

Abstract **vii**

Acknowledgements **xi**

Table of Contents **xiii**

List of Tables **xix**

List of Figures **xxi**

Nomenclature **xxxi**

1 Introduction **1**

1.1 Flow-Induced Vibrations in Steam Generators 2

1.2 Research Objectives 6

1.3 Thesis Outline 9

2 Background **11**

2.1 Physical Modeling 12

2.2 Excitation Mechanisms 17

2.3 Fluidelastic Instability in Tube Bundles 20
2.4 Models for Fluidelastic Instability 23
2.4.1 Jet-Switching Model 23
2.4.2 Quasi-Static Model 25
2.4.3 Unsteady Models 28
2.4.4 Semi-Analytical Model 30
2.4.5 Quasi-Steady Model 34
2.4.6 Quasi-Unsteady Model 36
2.4.7 Computational Fluid Dynamics Models 38
2.5 Discussion 41

3 Stability Behavior of a Single Flexible Tube in a Rigid Array 43
3.1 Parallel Triangular Tube Array ($\alpha = 30°$) 44
3.2 Rotated Square Tube Array ($\alpha = 45°$) 51
3.3 Normal Triangular Tube Array ($\alpha = 60°$) 56
3.4 Square Tube Array ($\alpha = 90°$) 59
3.5 Discussion 63

4 Experimental Facility and Methodology 75
4.1 Wind Tunnel Facility 75
4.2 Model Design 78
4.2.1 Tube Array Geometry 78
4.2.2 Tube Dynamic Control 80
4.2.3 Test Section 83
4.3 Instrumentation 85
4.3.1 Flow Velocity Instrumentation 86
4.3.2 Tube Instrumentation 88

4.4 Signal Processing Techniques 90
4.4.1 Amplitude and Frequency 90
4.4.2 Damping 92
4.4.3 Coherence and Phase 95
4.5 Tube Array Tuning 100

5 Experimental and Numerical Results 103

5.1 Tube Array Stability Analysis 104
5.1.1 Fully Flexible Tube Array 104
5.1.2 A Single Flexible Tube in a Rigid Array 110
5.1.3 Effect of Restraining the Third row tube in flexible array . . . 116
5.1.4 Discussion 120
5.2 Tube Surface Pressure Measurements 121
5.2.1 Fully Flexible Array 121
5.2.2 Single Flexible Tube in a Rigid Array 122
5.2.3 Discussion 126
5.3 Flow Perturbation Amplitude 128
5.3.1 Tube Vibrations Amplitude Effect 131
5.3.2 Scaling and Data Analysis 133
5.4 Phase Lag Between Tube Motion and Induced Flow Perturbation . . 135
5.4.1 Effect of Turbulence Level 136
5.4.2 Effect of Tube Vibration Frequency 138
5.4.3 Tube Tuning 141
5.4.4 Phase Measurements Along Flow Channel 143
5.4.5 Discussion 147
5.5 Computational Fluid Dynamics Modeling 149

5.5.1 Model Details 149
5.5.2 Model Validation 153
5.5.3 Parallel Triangular Array Results 156
5.5.4 Discussion 164

6 Theoretical Modeling **165**

6.1 Theoretical model development 165
6.1.1 Theoretical Model Fundamentals 168
6.1.2 Conservation of Mass 170
6.1.3 Conservation of Linear Momentum 172
6.1.4 Equations of Motion 173
6.2 System Parameters 175
6.2.1 Geometrical Aspects 175
6.2.2 Area Perturbation Phase Function 176
6.2.3 Flow Perturbation Decay Function 183
6.3 Solution Procedure 185
6.4 Stability of a Parallel Triangular Array 191
6.4.1 Semi-Analytical Model (Lever and Weaver, 1986a) 191
6.4.2 Present Model 193
6.5 Sensitivity Analysis 196
6.5.1 Perturbation Propagation Rate U_p 197
6.5.2 Mechanisms of Perturbation Propagation 197
6.5.3 Flow Perturbation Decay Rate 202
6.6 Stability of Other Tube Array Patterns 203
6.6.1 In-line Square Array 203
6.6.2 Normal Triangular Array 205

6.6.3 Rotated Square Array 205
6.7 Discussion 207

7 Conclusions and Recommendations **211**
7.1 Conclusions 211
7.2 Research Contributions 216
7.3 Recommendations for Future Work 217

References **219**

A Test Section **229**
A.1 Tube Assembly 229
A.2 Supporting Frame 231

B Instrument Calibration **235**
B.1 Pitot Tube 235
B.2 Accelerometer 235
B.3 Pressure Transducer 235
B.4 Hot-wire Anemometry 236

C Uncertainty Analysis **241**
C.1 Flow Velocity 241
C.2 Frequency Spectrum 243
C.3 Phase Measurements 244

D Experimental Results **245**
D.1 Tube Response 245
D.2 Tube Surface Pressure Measurements 245
D.3 Phase Lag Between Tube Motion and Induced Flow Perturbation . . 247

E Computational Fluid Dynamics Modeling **249**

E.1 Meshing 249

E.2 Boundary Conditions 250

E.3 Domain size Independence Study 250

E.4 Grid Independence Study 251

E.5 Turbulence Modeling 252

E.6 Surface Pressure Distribution for a Parallel Triangular Array 253

List of Tables

2.1 The physical variables involved in fluidelastic instability. 13

3.1 Parallel Triangular Array ($\alpha = 30°$) 64

3.2 Rotated Square Array ($\alpha = 45°$) 65

3.3 Normal Triangular Array ($\alpha = 60°$) 66

3.4 Square Array ($\alpha = 90°$) 67

4.1 Sensors locations and functions 90

4.2 Logarithmic decrement of the array tubes before and after tuning . . 101

5.1 Fitting data and propagation velocities upstream of point (K). 147

5.2 Fitting data and propagation velocities downstream of point (K). . . 147

5.3 CFD Simulations data for low range of reduced velocity. 158

6.1 Geometrical parameters adopted in Lever and Weaver (1986a) theoretical model 177

6.2 Geometrical parameters adopted in the present study 178

A1 Natural frequencies and mode shapes of the steel frame 233

D1 Natural frequencies of array tubes. 246

D2 Tube (1) frequencies in the longitudinal and transverse directions . . 246

E1 Details of grid refinement study 252

List of Figures

1.1 Diagram of a CANDU power plant. (Source: www.canteach.candu.org) 4

1.2 Diagram showing the main components of a CANDU steam generator. (Source: www.canteach.candu.org) 5

1.3 Samples of steam generator tube failures due to flow-induced vibrations. (a), (b), and (c) show the effect of fretting wear at the support (AECL). (d) Left tube shows both fretting wear at support and tube-to-tube clashing, and right tube shows damage caused by a broken piece of a tube that hit other tubes in its path (UKAEA Harwell) . . 7

2.1 Common tube array geometrical configurations. 15

2.2 Critical flow velocities for fluidelastic instability according to array geometry; (a) Square array, (b) Rotated square array, (c) Normal triangular array, (d) Parallel triangular array. (Weaver and Fitzpatrick, 1988) 16

2.3 Typical tube response pattern in a tube array subjected to cross flow. 18

2.4 Fluid coupling between adjacent tubes vibrations. 21

2.5 Fluidelastic stability map adopted by ASME heat exchanger design guidelines. (Weaver and Fitzpatrick, 1988) 24

2.6 Theoretical Stability boundaries for fluidelastic instability compared to the experiments; ∘, multiple flexible tubes in liquid flow; •, multiple flexible tubes in gaseous flow; □, single flexible tube in gaseous flow; (—), Roberts (1966) solution; (- - -), Connors (1970) solution; (...), Blevins (1974) solution. (Price, 1995) 25

2.7 System total damping for a fully flexible parallel triangular array $P_r = 1.375$ subjected to air flow. (Little, 2003) 29

2.8 Stability boundaries for fluidelastic instability developed by Chen (1983a,b) compared to the experiments; ∘, multiple flexible tubes in liquid flow; •, multiple flexible tubes in gaseous flow; □, single flexible tube in gaseous flow; (—), practical stability boundaries; (- - -), theoretical stability boundaries. (Price, 1995) 30

2.9 Typical flow pattern through a staggard tube array 31

2.10 Stability boundaries developed by Lever and Weaver (1982) theoretical model for parallel triangular tube array $P_r = 1.375$; (—), practical stability boundaries; (- - -), theoretical stability boundaries. 33

2.11 Stability boundaries developed by Price and Paidoussis (1986b); $\delta = 0.05$; $\mu = 1.0$; parallel triangular tube array $P_r = 1.375$. 35

2.12 Transient variation of fluid force coefficient induced by a step tube displacement. (Granger and Paidoussis, 1996) 36

2.13 Stability boundaries for a single flexible tube in a rigid normal triangular array; (- - -), Quasi-Steady model; (—), Quasi-Unsteady model (first order); (-.-), Quasi-Unsteady model (second order). (Granger and Paidoussis, 1996) 37

3.1 Critical velocity ratio vs. frequency difference. Weaver and Lever (1977). 45

3.2 Stability behavior for a single flexible tube and a fully flexible parallel triangular array $P/D = 1.375$ tested in air by Lever and Weaver (1986a) 46

3.3 Third row tube RMS response amplitude in a parallel triangular array subjected to air cross flow, $P_r = 1.375$. (Little, 2003) 47

3.4 Third row tube RMS response amplitude in a parallel triangular array subjected to water cross flow, $P_r = 1.375$. (Scott, 1987) 49

3.5 Third row tube response in a parallel triangular array subjected to water cross flow, $P_r = 1.75$. (Scott, 1987) 50

3.6 Response of a single flexible tube located in the fifth row of a rigid rotated square array subjected to water cross flow, $P_r = 2.12$. (Price et al., 1987) 52

3.7 Third row tube response in a rotated square array subjected to water cross flow, $P_r = 1.7$. (Scott, 1987) 54

3.8 Response of the fifth row tube in a rotated square array subjected to water cross flow, $P_r = 1.5$. (Weaver and Yeung, 1983) 55

3.9 Third row tube response in a normal triangular array subjected to water cross flow, $P_r = 1.5$. (Scott, 1987) 57

3.10 Stability threshold for a single flexible tube located in a rigid normal triangular array subjected to air cross flow, $P_r = 1.375$. (Austermann and Popp, 1995) 59

3.11 Response of the fifth row tube in a square array subjected to water cross flow, $P_r = 1.5$. (Weaver and Yeung, 1983) 60

3.12 Third row tube response in a nsquare array subjected to water cross flow, $P_r = 1.33$. (Scott, 1987) 62

3.13 Flow path in the main array geometries, flow visualizations by Scott (1987) 69

3.14 Region of fluidelastic instability mechanisms for a parallel triangular array (P/D=1.375), Paidoussis and Price (1988). 70

3.15 Instability boundaries developed based on different mechanisms for a parallel triangular array (P/D=1.5), Yetisir and Weaver (1993a,b). . . 70

4.1 Diagram of the Wind tunnel used in the present research, adapted from Grover (1977). 77

4.2 Array geometrical configuration. 80

4.3 General vibrations of a rigid tube suspended on a piano wire. 81

4.4 Sketch of the tube support arrangement. 82

4.5 Exploded view of the test section. 84

4.6 90° Hot-wire probe. (TSI Measurement Tools) 87

4.7 Diagram of the hot-wire rigs installed in the wavy channel of the test section top. 88

4.8 Sectional view of an instrumented tube. 89

4.9 Photograph of the experimental facility. 91

4.10 Sample of the cross-stream response of tube (1) in time and frequency domains. 93

4.11 General free response of a damped system. 94

4.12 Exponential decay method for evaluating the logarithmic decrement of tube (1) free response. 96

4.13 Evaluation of damping ratio using the half-power bandwidth method. 97

4.14 General sign convention adopted in the present study. 100

5.1 The response of tube 1 in a fully flexible parallel triangular array $P_r = 1.54$. 106

5.2 The response of tube 2 in a fully flexible parallel triangular array $P_r = 1.54$. 108

5.3 The response of tube B as located in the third row of a fully flexible array. 109

5.4 The response of tube 1 as a single flexible tube in a rigid parallel triangular array $P_r = 1.54$. 111

5.5 Response pattern of tube 1 as a single flexible tube in a rigid parallel triangular array $P_r = 1.54$ at different mean gap velocities. 112

5.6 The response of tube B as a single flexible tube in a rigid parallel triangular array $P_r = 1.54$. 114

5.7 The vibration response of a single flexible tube located at different positions in a rigid parallel triangular array $P_r = 1.54$. 115

5.8 The effect of holding the third row tube rigid during instability onset of a fully flexible parallel triangular array $P_r = 1.54$ array at $U_g = 7m/s$.117

5.9 The effect of releasing the third row tube during instability onset of a fully flexible parallel triangular array $P_r = 1.54$ array at $U_g = 7m/s$. . 118

5.10 The stability behavior of tube 1 located in the third row of both single flexible tube and fully flexible cases for parallel triangular array $P_r = 1.54$. 119

5.11 The phase lag between tube motion and fluid forces acting on tube (1) when located in the second row of a fully flexible array. 123

5.12 The phase lag between tube motion and fluid forces acting on tube (1) when located in the third row of a fully flexible array. 124

5.13 The phase lag between tube motion and fluid forces acting on tube (1) when located in the second row of a rigid array. 125
5.14 The phase lag between tube motion and fluid forces acting on tube (1) when located in the third row of a rigid array. 127
5.15 The scaled time between tube motion and induced fluid forces on tube (1). 128
5.16 Locations of hot-wire measurements along an assumed flow channel . 129
5.17 Hot-wire measurements signal at point (H), tube vibration amplitude 1%D. 130
5.18 Flow velocity perturbation amplitude along flow channel. 132
5.19 Flow velocity perturbation amplitude along flow channel and near the tubes. 134
5.20 Scaled flow velocity perturbation amplitude along the middle of a flow channel. 135
5.21 Decay function of the velocity perturbation amplitude. 136
5.22 Effect of turbulence level on the coherence between tube vibrations and flow perturbations signal. 137
5.23 Variation of mean gap velocity with tube natural frequency to obtain constant vibration amplitude. 139
5.24 Phase lag between tube vibration and flow perturbation at point (D), tube vibration amplitude 0.8%D. 140
5.25 Time delay between tube vibration and flow response at point (D), tube vibration amplitude 0.8%D. 140
5.26 Effect of tube frequency on normalized time $\tau U_g/D$ at point (D), tube vibration amplitude 0.8%D. 141
5.27 Tube (1) response as a single flexible tube in a rigid array. 143

5.28 Relative phase along flow path at tube frequency $25Hz$ and response amplitude $1\%D$. 144

5.29 Effect of mean gap velocity on phase lag value at tube frequency $25Hz$. 146

5.30 Geometrical configurations of the present CFD models. 151

5.31 Meshing details for a parallel triangular array, $P_r = 1.54$. 152

5.32 Surface pressure distribution on a flexible tube located in the third row of a rigid normal triangular array, $P_r = 1.32$ and $R_e = 57000$. 154

5.33 Surface pressure distribution on a flexible tube located in the third row of a rigid parallel triangular array, $P_r = 1.54$ and $R_e = 39000$. 155

5.34 Comparison of present model Strouhal number prediction to the data reported in literature by Polak and Weaver (1995). 156

5.35 Comparison between numerical and experimental phase between tube vibrations and flow perturbation along the flow channel for a parallel triangular array, $P_r = 1.54$, $R_e = 30500$, and $U_r = 6.2$. 157

5.36 Development of the phase lag trends with reduced velocity over the range of $U_r = 1 - 6$. 160

5.37 Comparison between numerical and experimental phase between tube vibrations and flow perturbation along the flow channel for a parallel triangular array, $P_r = 1.54$. Experimental ($U_r = 6.2$,$R_e = 30500$, and $U_r = 7.0$,$R_e = 33200$), numerical ($U_r = 6.0$,$R_e = 12000$, and $U_r = 7.0$,$R_e = 14000$). 161

5.38 Pressure field variation over one cycle of tube vibration, $P_r = 1.54$, $U_r = 2$, and $R_e = 4000$. 162

5.39 Pressure field variation over once cycle of tube vibration, $P_r = 1.54$, $U_r = 3$, and $R_e = 6000$. 163

6.1 Geometrical parameters of the flow in the four main array geometries, flow visualizations by Scott (1987) 167
6.2 Idealized flow in a parallel triangular array. 168
6.3 The element control volume. 170
6.4 Comparison between Lever and Weaver (1986a) theoretical phase prediction and the present experimental results for a parallel triangular array, $P_r = 1.54$. 179
6.5 Comparison between present phase prediction and the experimental results for a parallel triangular array, $P_r = 1.54$. 181
6.6 Comparison between present phase prediction and the numerical results for a parallel triangular array, $P_r = 1.54$, and $U_r = 1$. 182
6.7 Comparison between present phase prediction and the numerical and experimental results for a parallel triangular array, $P_r = 1.54$. 184
6.8 Vibration patterns associated with different combination of complex frequencies. 190
6.9 Stability maps for the common tube array configurations developed using the geometrical parameters adopted by Lever and Weaver (1986a). 192
6.10 Stability map and response frequency for a parallel triangular tube array with $P_r = 1.375$. 195
6.11 Effect of varying flow perturbation propagation rate on the stability boundaries for a parallel triangular array $P_r = 1.375$. 198
6.12 Effect of varying slightly the relative importance of phase lag mechanism on the stability boundaries for a parallel triangular array $P_r = 1.375$. 200
6.13 Effect of varying significantly the relative importance of phase lag mechanism on the stability boundaries for a parallel triangular array $P_r = 1.375$. 201

6.14 Effect of flow perturbation decay rate on the stability map for a parallel triangular tube array $P_r = 1.375$. 202
6.15 Stability map and response frequency for an in-line square tube array with $P_r = 1.33$. 204
6.16 Stability map and response frequency for a norma triangular tube array with $P_r = 1.4$. 206
6.17 Stability map and response frequency for a rotated square tube array with $P_r = 1.4$. 208

A1 A picture of the test section assembly mounted on the wind tunnel. . 230
A2 A picture of the tensioning mechanism. 230
A3 Theoretical and experimental prediction of the tube natural frequency variation with piano wire tension. 231
A4 A picture of the damping devices. 232
A5 The effect of damping cup liquid level and viscosity on the tube total damping. 232

B1 Calibration curve for the differential pressure transducer. 236
B2 Accelerometer specifications. 237
B3 Pressure transducer specifications. 238
B4 Hot-wire anemometer calibration curve. 239

C1 Effect of number of averages on the results RMS amplitude. 243

D1 Phase lag between the fluid forces and tube (1) vibrations when located in the third row of a rigid array. 247
D2 Phase lag between tube vibrations and flow perturbations along the stream channel. 248

D3 Effect of hot-wire probe location across the stream channel on the phase lag measurements. 248

E1 Typical behavior of scaled velocity $U+$ in the inner region of the boundary layer. Source(www.wikipedia.com) 250

E2 Predictions of surface pressure distribution using several domain sizes, NT array, $P_r = 1.32$, $R_e = 57000$. 251

E3 Predictions of surface pressure distribution using several grid sizes, NT array, $P_r = 1.32$, $R_e = 57000$. 252

E4 Tube surface pressure distribution using (SST) and $(k-\epsilon)$ turbulence models, NT array, $P_r = 1.32$, $R_e = 57000$. 253

E5 Surface pressure distribution on a tube located in the third row of a parallel triangular array, $P_r = 1.54$ and $R_e = 39000$. 254

E6 Flow field images showing the downstream wake instability. 255

Nomenclature

A	RMS Response amplitude.
A	Stream channel area for a unit spanwise length (m).
A_o	Mean stream channel area for a unit spanwise length (m).
C	Slope of the phase lag trend.
C_p	Pressure coefficient.
C_r	Courant number.
C_s	System damping matrix.
c	Equivalent total damping coefficient (Nm/s).
D	Tube diameter (m).
E	Hot-wire anemometer output (V).
F	Force per unit length (N/m).
F_L	Longitudinal force per unit length (N/m).
F_T	Transverse force per unit length (N/m).
f	Tube response frequency (Hz).
f_n	Tube natural frequency (Hz).
f_s	Sampling frequency (Hz).
f_v	Vortex shedding frequency (Hz).

H	Tube length (m).
h	Pressure loss coefficient.
I	Turbulence intensity.
i	Complex number $= \sqrt{-1}$.
K	Connors constant.
K_s	System stiffness matrix.
k	Equivalent total stiffness (N/m).
L	Piano wire free length (m).
L_o	Stream channel length (m).
M_s	System mass matrix.
m	Tube mass per unit length including fluid added mass (Kg/m).
$\bar{n}$	Directional unit vector.
P	Array pitch (m).
P	Pressure (Pa).
P_h	Pressure drop per row in the array (Pa).
P_o	Mean pressure (Pa).
P_r	Array pitch ratio.
p	Pressure perturbation component (Pa).
R_e	Reynolds number.
R^2	Goodness of the fitting curve.
S_t	Strouhal number.
s	Curvilinear coordinate (m).
s_a	Coordinate of flow attachment on the tube (m).
s_s	Coordinate of flow separation from the tube (m).
s_i	Coordinate of flow entrance to the stream channel (m).

T	Piano wire tension force (N).
T	Signal period (s).
t	Time (s).
t	Tube thickness (m).
U	Flow velocity (m/s).
U_c	Critical flow velocity (m/s).
U_{cf}	Critical flow velocity for a fully flexible array (m/s).
U_{cs}	Critical flow velocity for a single flexible tube (m/s).
U_g	Mean gap flow velocity (m/s).
U_o	Upstream flow velocity (m/s).
U_o	Mean flow velocity (m/s).
U_p	Flow perturbation propagation velocity (m/s).
U_r	Reduced flow velocity.
u	Flow velocity perturbation component (m/s).
W	Test section width (m).
x	Displacement in the longitudinal direction (m).
y	Displacement in the transverse direction (m).

Greek

α	Array pitch angle (rad).
β_a	Flow attachment angle on the tube (rad).
β_s	Flow separation angle from the tube (rad).
γ	Transition weight factor.
δ	Logarithmic decrement of damping.
ζ	Damping ratio.
θ	Position angle on the tube surface (deg).

μ	Fluid dynamic viscosity (Kg/ms).
ρ	Fluid density (Kg/m^3).
τ	Delay time (s).
ϕ	Phase lag function (rad).
Φ	Modified phase lag function (rad).
ψ	Flow perturbation decay function.
ω	Response frequency (rad/s).
ω_n	Natural frequency (rad/s).
η	Coherence function.

Chapter 1

Introduction

On a windy day, if you stop by a traffic light, you will likely notice the light pole shaking without any visible forces affecting it. In fact, it is the interaction between the blowing wind and the traffic light structure that causes this vibrations in a phenomenon called flow-induced vibrations. Flow-induced vibrations materialize around us in numerous forms ranging from musical instruments to skyscrapers. The mechanical vibrations associated with fluid flow can be useful in some cases such as energy harvesting. However, in other cases it can be extremely destructive such as in aircraft wings, offshore platforms, and tube and shell heat exchangers. Thus, flow-induced vibrations have become an important design criterion in a broad range of engineering applications.

Flow-induced vibrations are treated by several disciplines depending on the application and the source of excitation. As such, several scientific terms have been developed to describe different forms of the phenomenon. The flow-induced vibrations of ice-coated transmission lines is referred to as "galloping", while the excessive vibration of aircraft wings is called "flutter", and the dramatic increase in heat ex-

changer tube array vibrations is known as "fluidelastic instability". Each example of the aforementioned is defined based on the nature of the fluid flow and structure involved. Each is associated with the coupling of the fluid flow and structure motion in such a way that energy from the flow is transferred to the structure.

Tube and shell heat exchangers are commonly used in a wide range of applications such as food industry, chemical, and power plants. When the fluid forces cause excessive vibrations of the heat exchanger tubes, tube-to-tube clashing may occur and premature tube failure may arise due to fatigue or fretting wear. As such, flow-induced vibration is an important design concern, especially in the nuclear power industry due to the strict safety regulations and the extremely high cost of unplanned plant shutdown and repair. In order to provide reliable heat exchangers design guidelines, the nuclear power industry has led the way in tube bundle flow-induced vibration research for the past 40 years.

1.1 Flow-Induced Vibrations in Steam Generators

As the global demand for energy is constantly increasing and the fossil fuel supply is limited, more interest is being dedicated to renewable energy sources such as solar, wind, and nuclear energy. In 2005, nuclear power provided 6.3% of the world's energy and about 15% of the world's electricity. According to the International Atomic Energy Agency IAEA there are 436 nuclear power reactors in 31 countries worldwide as of December 2009. There are currently 22 nuclear power reactors in Canada producing 15% of the total electricity production which is equivalent to 85 Billion kW/h.

There are a few types of nuclear power reactors such as pressurized water reactors, and boiling water reactors. In the late 1950s and 1960s Atomic Energy Canada

Limited (AECL) invented a new pressurized heavy water reactor called "Canada Deuterium Uranium" (CANDU) which uses heavy water or Deuterium Oxide (D_2O) as the moderator. Today there are 34 CANDU reactors in use around the world. CANDU reactors use tube and shell heat exchangers in their steam generators due to their thermal capabilities. Like most nuclear steam generators, those used in CANDU power plants are sensitive to flow-induced vibrations.

The CANDU reactor has two main cycles as shown in Figure 1.1. Fission reactions in the reactor core heat Deuterium Oxide (D_2O) known as heavy water in the primary cooling cycle. During this cycle, heavy water becomes contaminated with radiation due to the direct contact with the radioactive fuel, and thus it has to be contained in a closed system. The secondary cooling cycle takes place inside a steam generator as seen in Figure 1.2. The heated heavy water circulates through several thousand tubes to lose the heat it acquired from the reactor core. Light water flows into the steam generator from the feed-water inlet nozzle, and moves from the steam generator bottom upwards as it transforms into steam. The water-steam mixture flows outside the tubes which convey heavy water in the axial direction until it reaches the U-bend region. The steam mixture then flows through a set of moisture separators and steam dryer to ensure that only steam phase exits the steam generator. The pressurized hot steam is used to power steam turbines connected to set of generators to produce electricity. The steam flowing out from the turbine is cooled down in a condenser using external cooling water from sources like lakes or oceans, and circulated back to the steam generator as light water. Some CANDU reactors use a set of diffusers on the condenser outlet to spread the effect of warm water over a large area, which limits the plant environmental effects.

While the steam mixture flows along the tubes and across the U-bend region inside the steam generator, it has the potential to produce tube vibrations. Tube

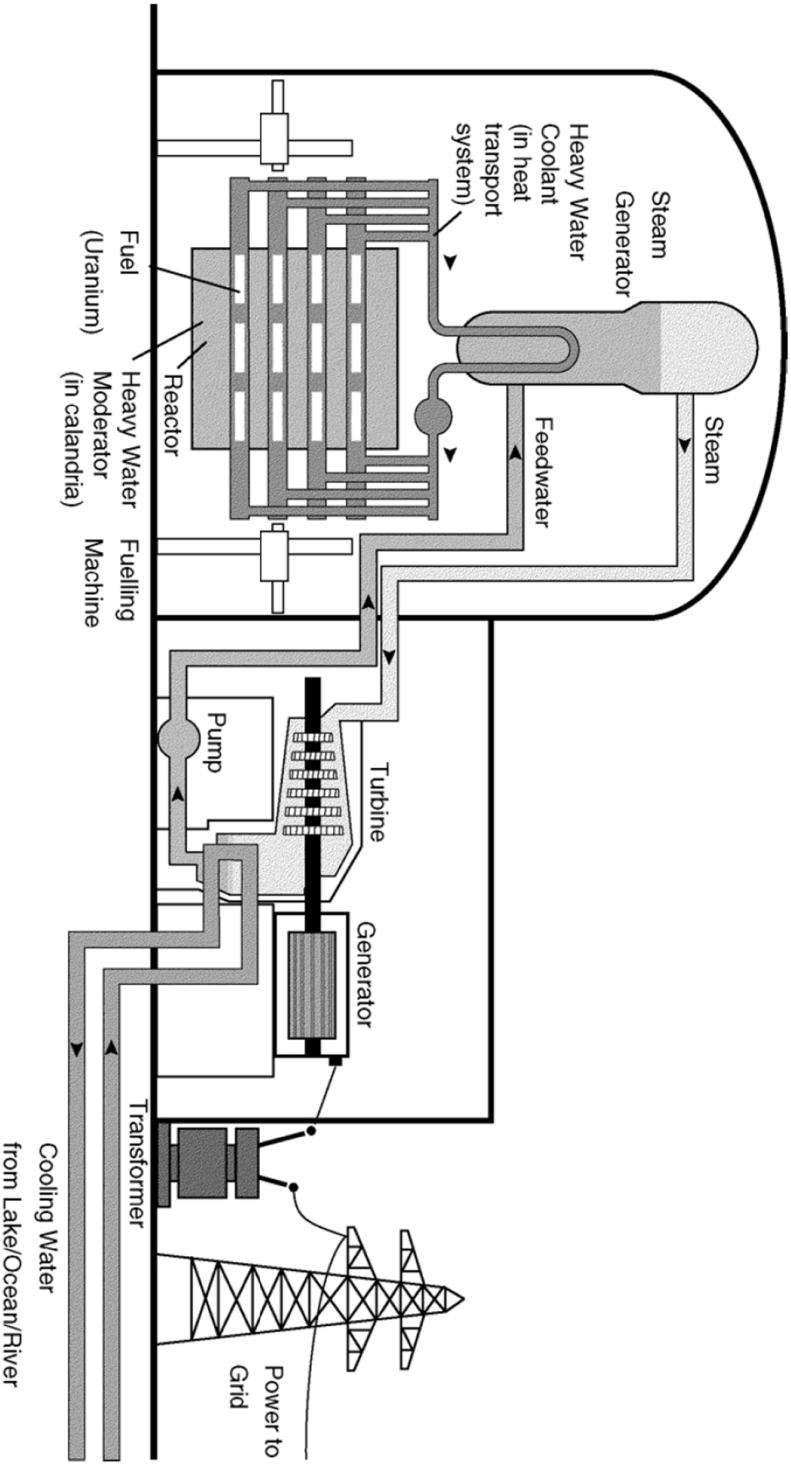

Figure 1.1: Diagram of a CANDU power plant. (Source: www.canteach.candu.org)

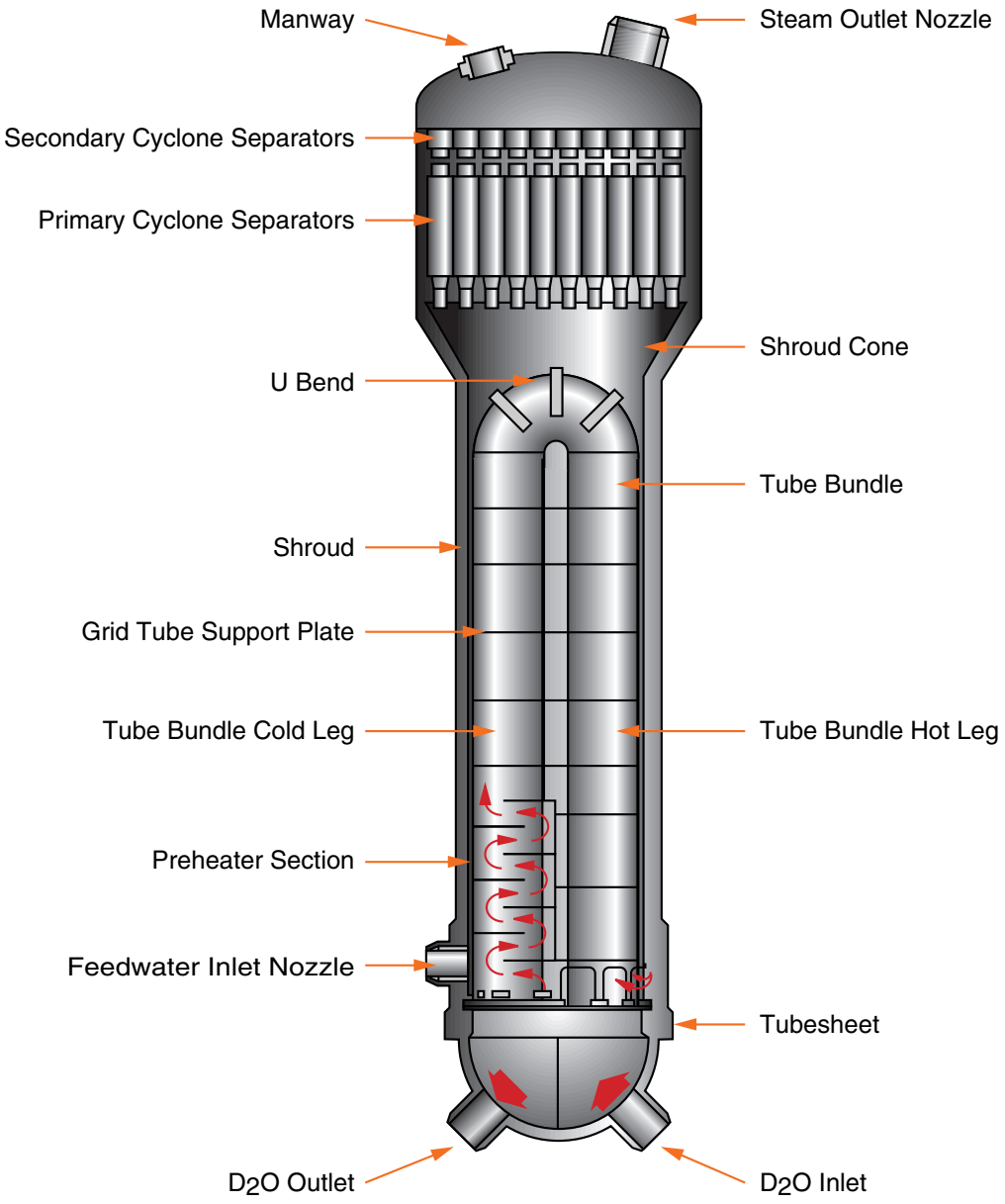

Figure 1.2: Diagram showing the main components of a CANDU steam generator. (Source: www.canteach.candu.org)

support plates are installed to limit these vibrations, however due to functionality constraints, finite gaps are left between the tubes and the tube supports. Due to these gaps and particularly in the outer U-bend region where the array stiffness is minimum, large amplitude tube vibrations may occur and lead to early failure by impact and fretting wear at the supports as in Figures 1.3(a), 1.3(b), and 1.3(c), thinning due to mid-span collision as in Figure 1.3(d), or fatigue caused by high bending stress. Flow-induced vibration is identified to be a major cause for premature failures of steam generator tubes, and thus it has gained special attention in the last few decades.

Since the late 1960s, significant research effort has been dedicated to predict, mitigate and understand the excitation mechanisms causing flow-induced vibrations in steam generators. Four main excitation mechanisms are defined in most flow-induced vibrations books like Blevins (1994) and Naudascher and Rockwell (2005) as well as heat exchanger design handbooks like Annaratone (2010). These mechanisms are (a)Turbulent Buffeting, (b)Vortex Shedding, (c)Acoustic Resonance, and (d)Fluidelastic instability. Fluidelastic instability is particularly crucial, as the damage caused by the first three mechanisms over years of service can be produced by fluidelastic instability in a matter of hours. Such short term failures can cause unplanned facility shutdown or leakage of contaminated substances which is extremely expensive and potentially dangerous.

1.2 Research Objectives

Fluidelastic instability is known to be the most critical flow-induced vibration mechanism in tube and shell heat exchangers, but still inadequately understood. A number of attempts have been made to model this phenomenon as noted by Price (1995), which advanced our understanding. While the developed theoretical models

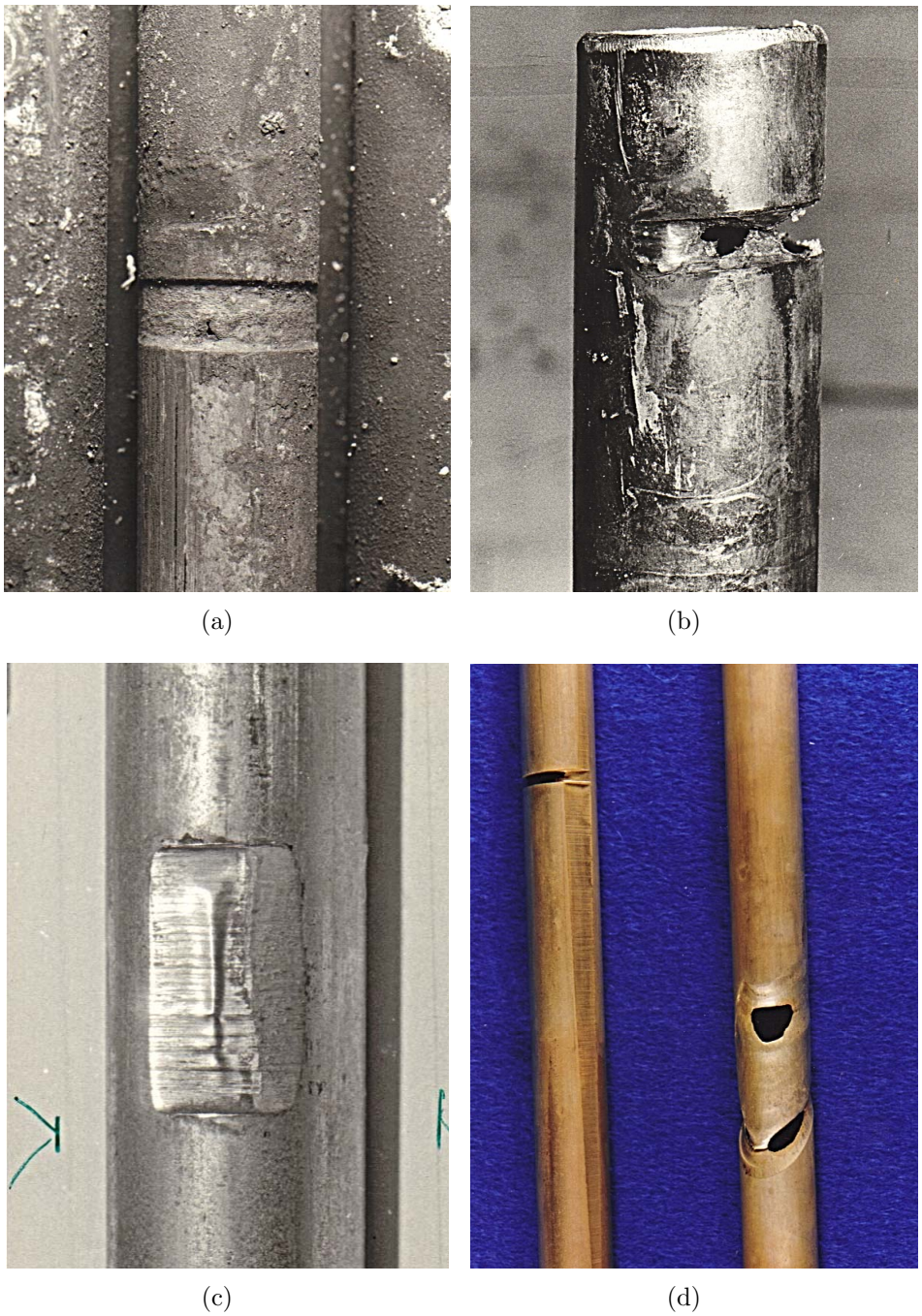

(a) (b)

(c) (d)

Figure 1.3: Samples of steam generator tube failures due to flow-induced vibrations. (a), (b), and (c) show the effect of fretting wear at the support (AECL). (d) Left tube shows both fretting wear at support and tube-to-tube clashing, and right tube shows damage caused by a broken piece of a tube that hit other tubes in its path (UKAEA Harwell)

may in some cases capture the physical trend of the phenomenon, it seems that there are some missing details required to achieve reliable predictions. One of these missing details is the time elapsed between tube motions and fluid response. While this time delay factor must be incorporated in all theoretical models to predict fluidelastic instability, the exact physical nature of this phenomenon remains unknown. As such, the present American Society of Mechanical Engineers (ASME) heat exchangers design guidelines provide an empirical stability map to predict this phenomenon. While this design guidelines may seem conservative, they don't provide any physical insights to the problem, and thus limit the room for future improvements in steam generators design. Moreover, the nuclear power industry has been facing failures due to fluidelastic instability in steam generators which are designed according to the present ASME design guidelines as noted by Paidoussis (2005) and Weaver (2008).

The purpose of the research reported in this thesis is to develop a better understanding of the fluidelastic instability phenomenon in tube bundle heat exchangers through investigating some of the missing details in the theoretical models including the time delay between tube vibrations and fluid response. In order to provide these new insights, both numerical and experimental studies were undertaken introducing a number of changes from the traditional approaches in measurements and data analysis. A wind tunnel tube bundle model was designed and constructed to facilitate precise control of the problem parameters. A novel measurement technique involving the interaction between tube vibrations and fluid response using hot-wire anemometer and pressure transducers was introduced. In a parallel investigation, numerical models of tube bundles subjected to single phase flows were developed using ANSYS-CFX commercial package to conduct parametric studies. The numerical simulations were used to provide flow visualizations to assist in understanding the phenomenon. It is anticipated that developing an improved understanding of the physics under-

lying fluidelastic instability will lead to improved design criteria for predicting this phenomenon.

1.3 Thesis Outline

This thesis is divided into 7 chapters. Chapter 2 presents a background review of the fluidelastic instability phenomenon. A survey of the instability mechanisms as well as the theoretical models reported in literature are provided. Chapter 3 presents a critical review of the use of a single flexible tube in a rigid array to study the stability behavior of a fully flexible array, including a comprehensive review of the related published data. The chapter consists of 5 sections, each section is concerned with a particular array geometry and the last section provides the resulting guidelines for the present study. Chapter 4 presents a detailed description of the experimental setup employed in the present research. Details of the wind tunnel facility, tube suspension mechanisms, and array geometry are discussed. The instrumentations and signal processing techniques adopted in data analysis are introduced.

Chapter 5 presents the experimental and the numerical simulations results. The stability behavior of a fully flexible array and a single flexible tube in a rigid array are discussed. Measurements of the tube surface pressures are presented, and amplitude and phase of flow perturbations associated with tube vibrations are discussed. Numerical simulation results are discussed in the last section and compared to the experimental results. In Chapter 6, theoretical modeling of the interaction between tube vibrations and fluid flow based on the observations of the present study is introduced. The new fluidelastic stability maps developed using the proposed model are presented. Chapter 7 summarizes the important novel contributions of this research and the recommendations for future work.

Chapter 2

Background

The new generation of steam generators is designed to last $50 - 60$ years and to operate more efficiently by accommodating higher flow velocities with lighter structures. However, lighter structures are more susceptible to flow-induced vibration at higher flow velocities which can cause extremely expensive plant outage due to short term tube failures. Of the several mechanisms causing flow-induced vibrations in tube arrays, fluidelastic instability is known to be the most common cause for short term tube failures (Weaver et al., 2000a). Thus, significant research effort has been dedicated to understand and reliably predict this phenomenon over the last four decades. Blevins (1994) has written a book on flow-induced vibrations which includes a chapter on fluidelastic instability in tube bundle heat exchangers, and later another book on flow induced vibrations was written by Naudascher and Rockwell (2005). The flow around circular cylinders was discussed in the book of Zdravkovich (1997) in terms of fundamentals and applications which included fluidelastic instability in tube bundles. A number of papers have summarized the current state of knowledge and presented design guidelines such as the work of Chen (1982), Paidoussis (1983), Weaver and

Fitzpatrick (1988), Gelbe et al. (1995), Goyder (2002), and Pettigrew and Taylor (2003a,b). This chapter presents a literature survey of the excitation mechanisms and theoretical models for fluidelastic instability in heat exchanger tube bundle.

2.1 Physical Modeling

Tube bundle heat exchangers are used in many applications, and as such are subjected to various operating conditions. It follows that scaling the problem parameters is essential to develop a physical model that can be used at all operating conditions. There are two ways in which the dimensionless parameters required for modeling a system can be determined; non-dimensionalizing the governing equations, and the application of the Buckingham Pi theory. In this section the Buckingham theory is adopted to determine the scaling parameters for studying fluidelastic instability considering the following assumptions:

1. The phenomenon can be modeled as two dimensional problem.

2. The tubes walls are considered rigid.

3. The tube vibration mode is considered to be translational.

4. The logarithmic decrement presents the system total damping.

5. The fluid flow is incompressible.

The phenomenon of fluidelastic instability in tube bundle heat exchangers has three main elements; array geometry, tube dynamics, and fluid flow. The physical variables involved in each element and the fundamental dimensions have to be carefully defined in order to develop a reliable physical model of the phenomenon.

Table 2.1: The physical variables involved in fluidelastic instability.

Variable	*Symbol*	*Dimensions*
Array geometry		
Tube diameter.	D	L
Array pitch.	P	L
Tube dynamics		
Mass per unit length including fluid added mass.	m	M
Tube natural frequency.	f_n	T^{-1}
Logarithmic decrement.	δ	—
Fluid flow		
Flow velocity.	U	LT^{-1}
Fluid density.	ρ	ML^{-3}
Fluid viscosity.	μ	$ML^{-1}T^{-1}$
Turbulence magnitude.	u'	LT^{-1}

According to the Buckingham theory (White, 2008), the number of dimensionless groups or *"Π Groups"* is equal to the total number of physical parameters minus the number of fundamental dimensions. The physical variables involved in the fluidelastic instability problem and their dimensions are detailed by Blevins (1994) and are shown in Table 2.1. The dimensionless parameters that most affect tube bundle instability are shown in Relation 2.1 where n_0, n_1, n_2, n_3 and n_4 are constant exponents.

$$\frac{U}{fD} \propto \left(\frac{m}{\rho D^2}\right)^{n_0} \delta^{n_1} \left(\frac{P}{D}\right)^{n_2} \left(\frac{\rho U D}{\mu}\right)^{n_3} \left(\frac{u'}{U}\right)^{n_4} \tag{2.1}$$

The left hand side of Relation 2.1 refers to the reduced velocity term (U/fD), which presents physically the relative magnitude of flow velocity to the tube vibrations velocity. This term is used as an indicator of the stability threshold for fluidelastic instability. The mean gap velocity U_g is often used to present the flow velocity in the array instead of the upstream flow velocity U_o. Equation 2.2 can be used to obtain the mean gap velocity based on the upstream flow velocity which is often

more convenient to measure. This equation is based on continuity and represents the mean flow velocity in the minimum gap between the tubes only for normal triangular and rotated square arrays. However, it is generally used as the mean interstitial flow velocity for all tube arrays.

$$U_g = \frac{P}{P-D} U_o \tag{2.2}$$

The right hand side of Relation 2.1 presents the contributing factors to determine the reduced velocity threshold. The first term on the right hand side refers to the mass ratio $m/\rho D^2$, which presents physically the ratio between the dynamic tube mass per unit length including the fluid added mass to the displaced mass of the surrounding fluid. This term indicates the momentum exchange as it represents the tube inertia relative to the fluid inertia. Heat exchangers operate over a wide range of mass ratios associated with various working fluids such as air, steam, water, liquid sodium, etc. It follows that a logarithmic scale is used to present the mass ratio term which spans typically over six orders of magnitudes $(10^{-2} - 10^4)$.

The second right hand side term of Relation 2.1 refers to the logarithmic decrement δ, which is a measure of the amount of energy lost per oscillation cycle. Several approaches can be used to determine the logarithmic decrement according to the working fluid such as damping in air, damping in stationary fluid, or damping in moving fluid. This factor is important since it represents the capacity for energy dissipation in the array.

The third term refers to the array pitch ratio P/D or P_r, which is the ratio between tube spacing and tube diameter. This term is a measure of the array spacing and represents the compactness of the array tubes. Typical pitch ratios in nuclear steam generators are about $P_r = [1.25 - 1.75]$, and it can vary up to $P_r = 3.0$ in other

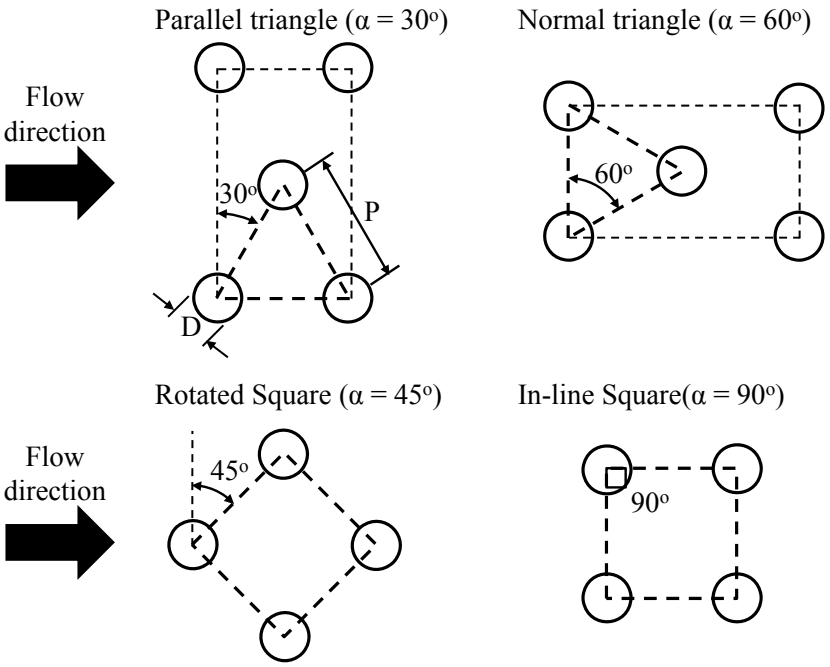

Figure 2.1: Common tube array geometrical configurations.

applications. Another geometrical parameter which is not included in Relation 2.1 is the array pitch angle α as seen in Figure 2.1. While the array pitch angle α is neither included in the dimensional analysis presented by Blevins (1994) nor considered as an affecting parameter by the ASME design guidelines, it was shown by Weaver and Fitzpatrick (1988) that classifying the literature experimental data according to the array pitch angle reduced significantly the amount of data scatter as shown in Figure 2.2.

The fourth term refers to Reynolds number $R_e = \rho U_g D/\mu$ which physically represents the ratio between fluid inertia forces to fluid viscous forces. The Reynolds numbers at fluidelastic instability in practical tube arrays are high, typically ($R_e > 10^4$), and little evidence of Reynolds number dependence has been observed. Therefore, most analyses ignore Reynolds number.

The last term is the turbulence intensity u'/U, which is the ratio between the statistical variance of flow velocity to the mean velocity. It represents the level

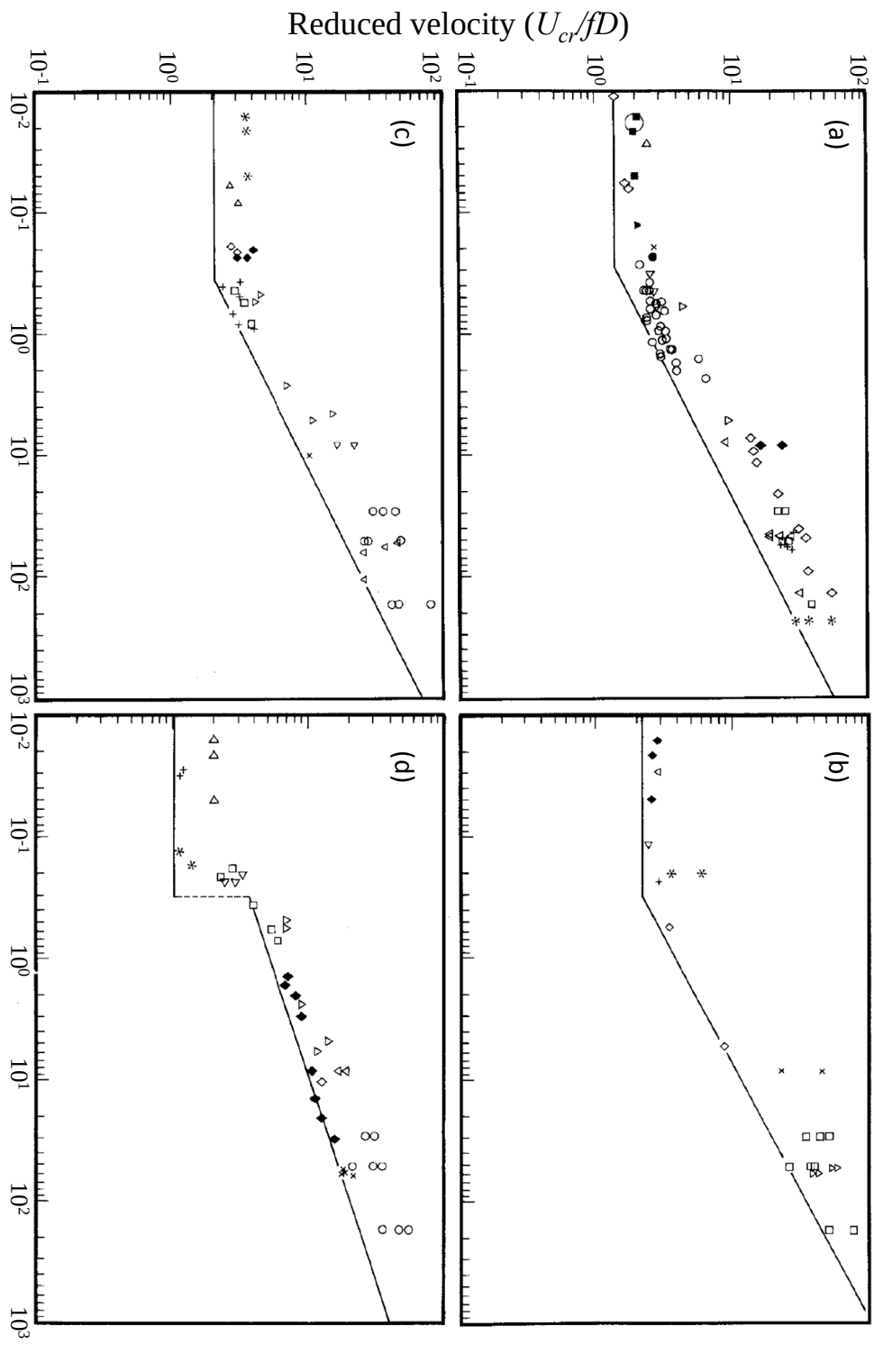

Figure 2.2: Critical flow velocities for fluidelastic instability according to array geometry; (a) Square array, (b) Rotated square array, (c) Normal triangular array, (d) Parallel triangular array. (Weaver and Fitzpatrick, 1988)

of broad band random excitations in the flow, these random fluid forces cause random small vibration of the tubes typically known as turbulent buffeting. Polak and Weaver (1995) found that the turbulence level increases as the flow proceeds deeper in the array to the fourth or fifth row and asymptote, which implies that the turbulence generated by the tube bundle itself overwhelms the upstream turbulence. While some researchers such as Rzentkowski and Lever (1998) have found the fluidelastic instability virtually unaffected by turbulence level, other researchers such as Rottmann and Popp (2003) have found that increasing turbulence level reduces the fluidelastic instability threshold. However, the exact effect of turbulence level on fluidelastic instability is not fully understood yet.

Discrete vortex shedding is another phenomenon affecting the general tube response to cross flow but not included in the fluidelastic instability dimensional analysis. The Strouhal number S_t, as expressed in Equation 2.3, acts as a non-dimensional frequency parameter for scaling vortex shedding. It represents the frequency of vortex shedding from the tube for a given flow velocity where f_v is the vortex shedding frequency. Vortex shedding can affect the fluidelastic stability threshold in liquid flows for certain array geometries if there is coincidence between vortex shedding resonance and fluidelastic instability.

$$S_t = \frac{f_v D}{U} \tag{2.3}$$

2.2 Excitation Mechanisms

Flow-induced vibrations can be classified generally into three main categories as noted by Naudascher and Rockwell (2005); forced vibration, self controlled-vibrations, and self-excited vibrations which corresponds to steady state response, resonance,

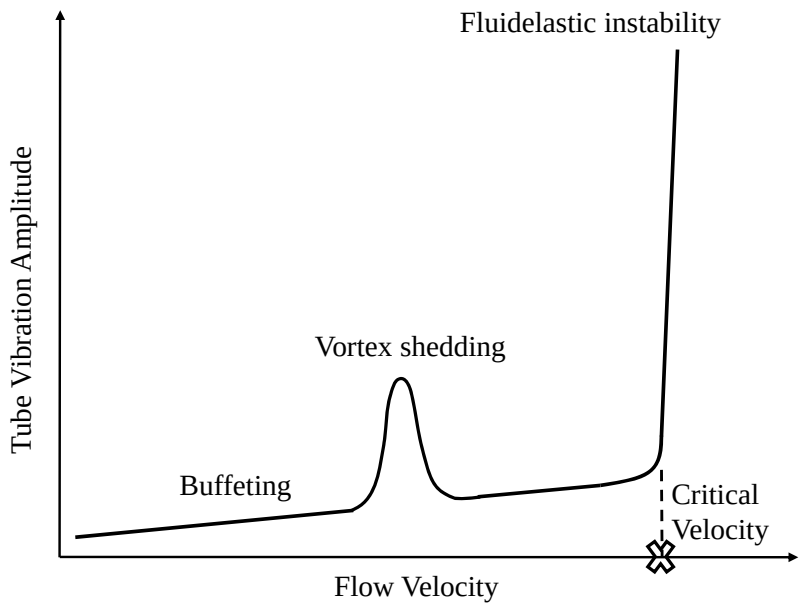

Figure 2.3: Typical tube response pattern in a tube array subjected to cross flow.

and instability respectively. Tube bundle heat exchangers subjected to cross flow are subjected to four excitation mechanisms known as: turbulent buffeting which is a forced vibration mechanism, vortex shedding and acoustic resonance which are self-controlled mechanisms, and fluidelastic instability which is a self-excited mechanism. A typical response of a tube in a bundle subjected to cross flow is shown in Figure 2.3. The gradual increase in tube vibration amplitude with increase in flow velocity is due to turbulent buffeting. When the vortex shedding frequency coincides with the tube natural frequency, tube resonance may take place in a phenomenon called *"lock-in"* where the tubes may experience relatively larger vibration amplitudes. As the flow velocity increases, the tube comes out from the lock-in zone and the response amplitude decreases following the vibration trend due to turbulent buffeting. When the flow velocity reaches the critical velocity threshold for fluidelastic instability, a dramatic increase of the vibration amplitude takes place.

Turbulence in tube bundles subjected to cross flow increases as the fluid flows

across the array geometry (Polak and Weaver, 1995), and as such, the tubes are subjected to turbulent buffeting at all practical Reynolds numbers. Turbulence buffeting acts as random excitation force on the array tubes which produces random displacements. While the turbulence in heat exchangers is beneficial for heat transfer, the small vibration amplitudes caused by turbulent buffeting have to be estimated to determine the effective life of the equipment (Hassan et al., 2003). Axisa et al. (1990) have conducted a detailed investigation of the turbulent buffeting in heat exchanger tube bundles both in single and two-phase flows. They developed a theoretical framework relating the vibration amplitude to the flow dimensionless force spectrum. An excellent review of the turbulent buffeting modeling techniques was introduced by Weaver et al. (2000b).

Vortex shedding and acoustic resonance are self-controlled excitation mechanisms in tube bundle heat exchangers. Vortex structures are shed from the tubes at a frequency which is linearly related to the flow velocity as seen in Equation 2.3 where S_t is the Strouhal number, f_v is the vortex shedding frequency, D is the tube diameter, and U is the flow velocity (Bearman, 1984). These vortex structures are convected downstream causing pressure and velocity fluctuations which appear as discrete frequencies in the spectral analysis (Weaver et al., 2000b). It is known that vortex shedding and acoustic resonance in heat exchanger tube bundles are geometrical dependent phenomena, and as such, the phenomenon is investigated for each array geometrical pattern separately. Weaver (1993) introduced an interesting review of vortex shedding and acoustic resonance in tube bundle heat exchangers, and later another review was written by Ziada (2006).

Ziada et al. (1989a,b) investigated experimentally the acoustic resonance in in-line and staggered tube bundles subjected to air and water cross flows. The authors found that there are multiple Strouhal numbers for each array which are not

necessarily harmonic of one another. Detailed investigation of the vortex shedding in an in-line array was introduced by Ziada and Oengoren (1992), the authors found that the flow lanes jet instability is the source of vortex shedding excitation. They concluded that this jet instability distinguishes the vortex shedding phenomenon in in-line tube arrays from that in staggered tube arrays. Ziada and Oengoren (2000) studied the vortex shedding and acoustic resonance in staggard parallel triangular tube arrays. The authors found multiple Strouhal numbers for the vortex shedding excitation in this array pattern. Lately, greater attention has been dedicated to the numerical simulations of vortex shedding in tube bundle for more details, the reader is referred to the work of Sweeney and Meskell (2003), Liang and Papadakis (2007), and Liang et al. (2009).

2.3 Fluidelastic Instability in Tube Bundles

The fourth excitation mechanism in tube bundles is fluidelastic instability. The phenomenon can be described as a self-excited feedback mechanism between tube motion and fluid forces. When a tube bundle is subjected to cross flow, the tubes vibrate with an amplitude proportional to the upstream flow velocity until the flow velocity reaches a threshold limit called the critical velocity where the tube's response amplitude increases dramatically, potentially causing catastrophic failure. In order to describe what happens when the upstream flow velocity reaches the critical threshold, consider a tube bundle subjected to cross flow as shown in Figure 2.4. The general equation of motion for the system can be written as

$$[M_s]\{\ddot{y}\} + [C_s]\{\dot{y}\} + [K_s]\{y\} = \sum F_{ext.} \tag{2.4}$$

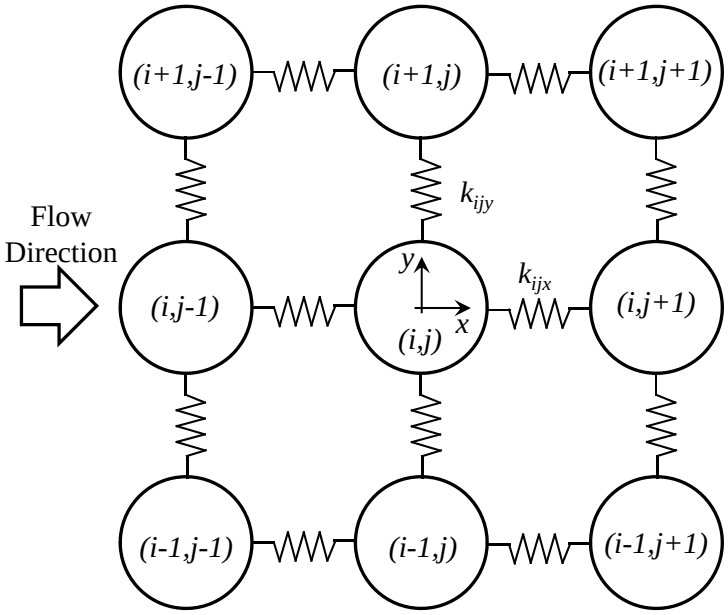

Figure 2.4: Fluid coupling between adjacent tubes vibrations.

where $[M_s]$ is the mass matrix, $[C_s]$ is the damping matrix, $[K_s]$ is the stiffness matrix, and $\sum F_{ext.}$ is the sum of all external forces acting on the system. In the case of a tube array subjected to cross flow, the external forces include fluid added mass, fluid damping forces, and fluid stiffness forces. These forces are a function of tubes dynamics, i.e the tubes acceleration vector $\{\ddot{y}\}$, the tubes velocity vector $\{\dot{y}\}$, and the tube displacement vector $\{y\}$, and hence the system equation of motion can be written as

$$[M_s + m_f]\{\ddot{y}\} + [C_s + c_f]\{\dot{y}\} + [K_s + k_f]\{y\} = \sum F \tag{2.5}$$

where m_f represents the fluid added mass, c_f represents the fluid damping, and k_f represents the fluid stiffness. The system is considered to be stable if the response motion decays with time, while the system is considered to be unstable if energy is fed to the system through self excitation and the response motion increase with time (Rao, 2004). In order to satisfy the condition of system stability, both total damping

and total stiffness terms in Equation 2.5 have to be positive. A positive total damping means physically that there is a net energy loss per oscillation cycle, while a positive total stiffness means physically that external forces proportional to displacements are acting to stabilize the system.

Static instability or divergence is precipitated by a negative fluid stiffness exceeding the structural stiffness which leads to a negative total stiffness term. As the total stiffness goes to zero the system natural frequency, as shown in Equation 2.6, goes to zero. Thus, the static instability is characterized physically by a frequency of oscillation going to zero at stability threshold. This instability is rarely materialized in heat exchanger tube arrays as dynamic instability is materialized first.

$$\omega_n = \sqrt{\frac{K}{M}} \tag{2.6}$$

Dynamic instability can be caused by one or a combinations of three main mechanisms. The first mechanism requires at least two degrees of freedom, where fluid stiffness produces off-diagonal stiffness matrix terms which can cause instability. The second mechanism is due to the nonlinear hysteretic fluid forces which depend on the tube vibration mode. The most significant dynamic instability mechanism is caused by a negative fluid damping exceeding the positive damping in the system which leads to a negative total damping in the system. As the total damping goes to zero, the net energy loss per cycle is zero, and energy starts to feed into the system causing a dramatic increase in response amplitude as seen in Figure 2.3. This phenomenon is materialized physically by a fluid force component in-phase with tube velocity. It follows that, fluidelastic instability in heat exchanger tube arrays takes place when either or both the total damping and total stiffness terms go to zero switching from positive to negative. Details of the theoretical models of fluidelastic

instability phenomenon in tube arrays subjected to cross flow are discussed in the following section.

2.4 Models for Fluidelastic Instability

The ASME design guidelines for tube bundle heat exchangers adopt the stability map, shown in Figure 2.5, where experimental data for fluidelastic instability in tube bundles of various geometrical configurations are plotted and a lower bound for the data is considered to be the stability threshold. While this design guideline may seem conservative, it doesn't provide any physical insights to the problem and thus limits the room for future improvements in steam generator design (Weaver, 2008). In order to provide a reliable prediction tool and to improve our understanding of the phenomenon, several theoretical models have been developed over the last few decades. Following is a description of these models in chronological order.

2.4.1 Jet-Switching Model

The jet-switching model was developed by Roberts (1966) and it was a purely analytical model with no need for any experimental inputs. Roberts investigated single and two rows of tubes subjected to cross flow and noticed that instability occurs predominantly in the stream-wise direction. By solving Laplace's equation, Roberts obtained the pressure distribution around the cylinders and integrated the pressures to obtain the drag force on the tubes. Roberts derived a form for the critical velocity based on the energy balance calculations. The equation related the reduced velocity term U_{cr}/fD where U_{cr} is the critical velocity, to the mass damping parameter $m\delta/\rho D^2$.

Roberts developed his model based on a few assumptions as follows. First,

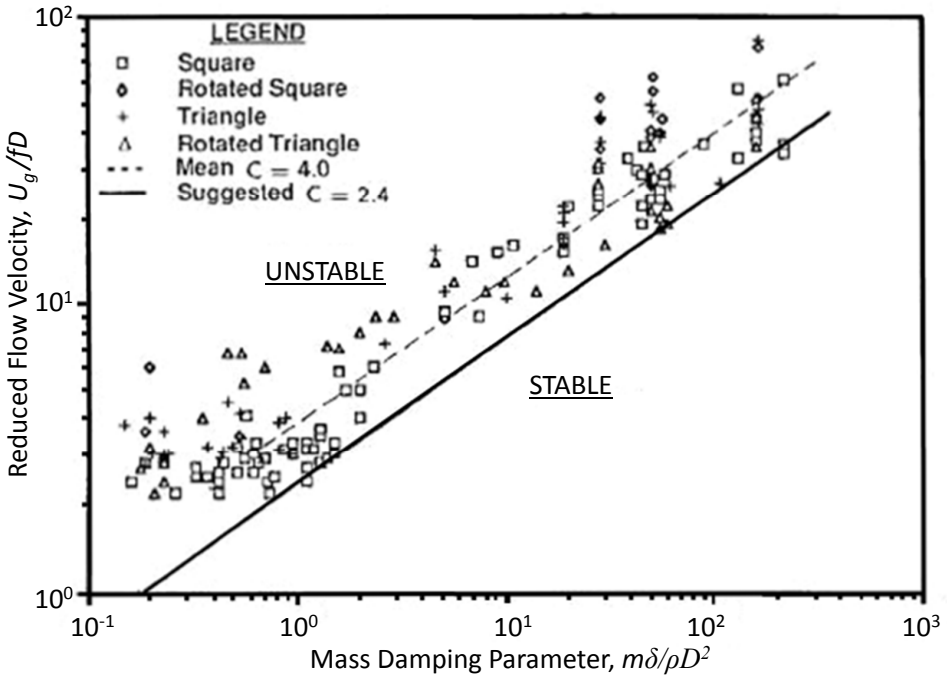

Figure 2.5: Fluidelastic stability map adopted by ASME heat exchanger design guidelines. (Weaver and Fitzpatrick, 1988)

a single or two rows of tubes can be used to model the fluidelastic instability phenomenon in a tube array. Second, the fluid flow separates at the minimum gap between cylinders. Third, the pressure in the wake region behind the tubes is constant giving a constant pressure difference across the jet, and fourth, the flow is inviscid upstream of the separation point and in the wake region. The stability boundaries developed by Roberts were in good agreement with experimental results for higher values of mass damping parameter using a single row of tubes subjected to cross flow. However, when the stability boundaries from Roberts theory are compared to the data from later experiments at lower mass damping parameter as seen in Figure 2.6, it becomes clear that the jet-switching model is not describing the phenomenon accurately as noted by Price (1995).

Later Seitanis et al. (2005) carefully designed an experiment to replicate the

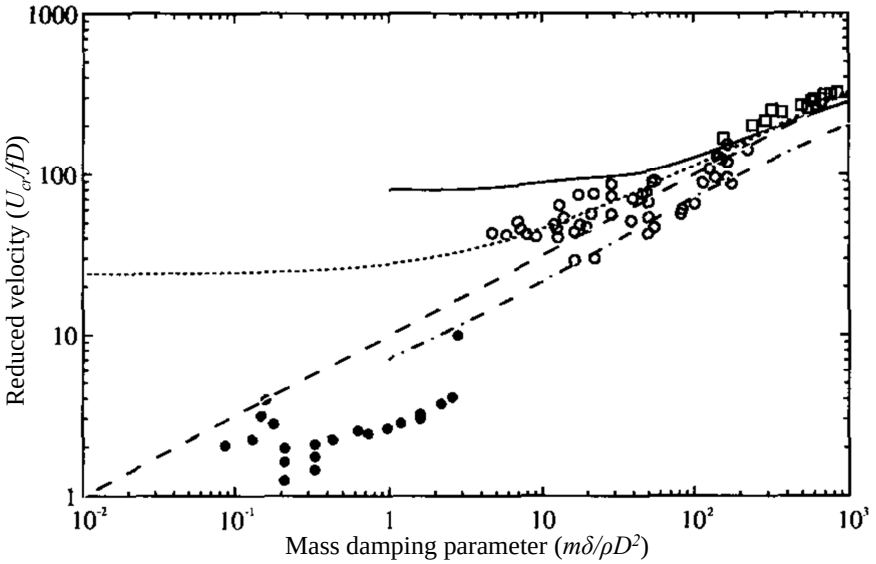

Figure 2.6: Theoretical Stability boundaries for fluidelastic instability compared to the experiments; ∘, multiple flexible tubes in liquid flow; •, multiple flexible tubes in gaseous flow; □, single flexible tube in gaseous flow; (—), Roberts (1966) solution; (**- - -**), Connors (1970) solution; (**...**), Blevins (1974) solution. (Price, 1995)

results reported by Roberts (1966). The authors were able to change the mean stream-wise location of the flexible tubes, and they showed that the excitation mechanism, in this particular case, is not Jet-switching, rather it is negative fluid stiffness. Roberts (1966) presented a break through work as he addressed, for the first time, the self excited vibrations to be a source of failure in heat exchanger tube bundles. Roberts also presented the reduced velocity and mass damping terms based on the dimensional analysis, and these terms are used in defining the stability boundaries until now.

2.4.2 Quasi-Static Model

The quasi-static model developed by Connors (1970) considered the instability of a tube row subjected to cross flow. Connors observed that the tubes were oscillating in elliptical orbits predominantly either stream-wise or cross-stream. He simulated this pattern by moving the two adjacent tubes for a cylinder in elliptical

orbits symmetrically and asymmetrically, and measured the fluid forces coefficients. By performing an energy balance for stream-wise and cross-stream directions, Connors derived Equation 2.7 which is the most commonly used expression for predicting fluidelastic instability. U_{cr} is the critical flow velocity, f is the tube natural frequency, D is the tube diameter, m is the tube mass per unit length including the fluid added mass, δ is the tube logarithmic decrement, ρ is the fluid density, and K and n are constants. Connors (1970) found the constants K and n equal to 9.9 and 0.5 respectively, while Blevins (1974) found these constants to depend on array geometry and fluid characteristics. Albeit, the values of these constants have been a topic of discussion for the last four decades to the extent that some have called them the variable constants (Weaver, 2008).

$$\frac{U_{cr}}{fD} = K\left(\frac{m\delta}{\rho D^2}\right)^n \tag{2.7}$$

Connors equation was developed based on a single row of tubes and on the assumption that oscillation of neighboring tubes at the same frequency is essential for fluidelastic instability. Nevertheless, Connors model was used to design tube bundles of various geometrical patterns which motivated further investigation of the problem. Weaver and Lever (1977) attempted to mitigate the instability by detuning adjacent tubes in the array. The authors found that detuning the adjacent tubes in the array had a stabilizing effect but it did not eliminate the fluidelastic instability. Weaver and Elkashlan (1981a) investigated the effect of damping and mass ratio on the stability of a tube array. They found that the tube damping term δ is not linearly related to the mass ratio term $m/\rho D^2$ in Equation 2.7, and as such Connors equation can be presented in the form of Equation 2.8 where n_1 and n_2 are constants.

$$\frac{U}{fD} = K\left(\frac{m}{\rho D^2}\right)^{n_1}\delta^{n_2} \tag{2.8}$$

Weaver and Elkashlan (1981b) found that a single row of tubes behaves differently from a tube array. Moreover, the authors found that the array fluidelastic stability threshold is affected by the number of rows, and a minimum of six tube rows was recommended to obtain a typical stability behavior of a tube array. Weaver and Koroyannakis (1982) carried out an experimental study on tube array response in air and water flows. The authors observed significant variations of tube response frequency in water flows which is not pronounced in air flows. The authors attributed this phenomenon to the effect of surrounding tube vibration mode on the added mass term which is more significant in water flows than air flows. These findings indicate that neither Roberts not Connors models explain completely the phenomenon of fluidelastic instability.

Price (1995) compared the stability boundaries obtained using the quasi-static model of Connors to the experimental results for fluidelastic instability, shown in Figure 2.6, and showed that the model is not capable of predicting the phenomenon correctly. According to Paidoussis (2006), designers adopted during the 1970's Connors equation with $K = 9.9$ for multiple row tube arrays which resulted in a large number of badly designed heat exchangers, and the cumulative damage worldwide was estimated at 1000 million USD. Blevins (1974, 1977, 1979) carried out a series of studies in which he re-derived Equation 2.7 using a different approach. He considered the fluid forces to be a function of the relative tube displacement. However, this assumption was questioned by Price and Paidoussis (1986a).

2.4.3 Unsteady Models

Tanaka and Takahara (1980, 1981) measured the unsteady fluid forces directly instead of the theoretical prediction. The authors carried out an experimental study in which a centered tube in an in-line tube array was excited harmonically and the fluid forces acting on the surrounding tubes were measured. They assumed that the fluid forces affecting a tube in the array are a function of the tube motion as well as the motions of the four adjacent tubes only. Amplitude and phase measurements of the lift and drag forces were carried out over a range of Reynolds number and reduced velocity. Tanaka and Takahara (1981) reported a discontinuity in the stability boundary in the range of mass damping parameter ($m\delta/\rho D^2 = 50 - 500$). They concluded that the instability mechanism below this range is different from the instability mechanism above this range. However, later Tanaka et al. (1982) published an experimental study on a single flexible tube in a rigid array, in which they showed that this discontinuity is not due to a fundamental change in the instability mechanisms. Tanaka and Takahara's model provided a good agreement with the experimental results. However, the number of force coefficients and measurements effort required for this model is unpractical for heat exchanger design.

Chen (1983a,b) found that there are two basic mechanisms causing fluidelastic instability; the first is controlled by fluid damping while the second is controlled by fluidelastic forces. The damping controlled instability is the dynamic instability caused by fluid damping forces and known as the *"damping mechanism"*. The fluid damping forces are a function of flow velocity such that the fluid damping decreases as the flow velocity increases. When the flow velocity exceeds a certain value, the total damping becomes negative and the system becomes unstable.

The second mechanism is controlled by fluidelastic forces and known as the

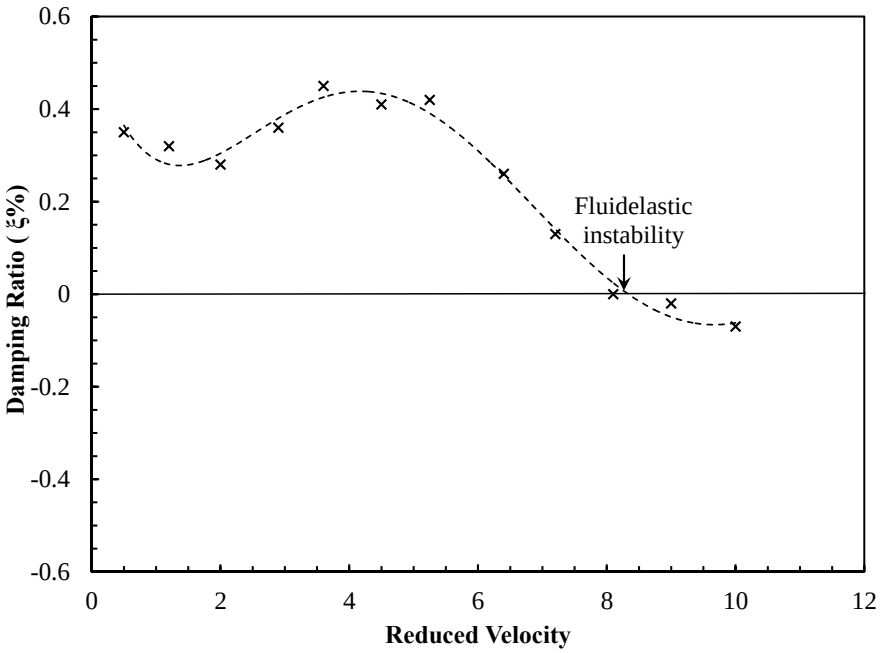

Figure 2.7: System total damping for a fully flexible parallel triangular array $P_r = 1.375$ subjected to air flow. (Little, 2003)

"stiffness mechanism". The coupling between array tube vibrations and fluid flow produces fluidelastic forces which contribute to the total system stiffness. As the flow velocity increases the fluidelastic forces increases, and ultimately at a certain velocity threshold the system becomes fluidelastically unstable. Later, Paidoussis and Price (1988) introduced another study on the mechanisms of fluidelastic instability which supports the existence of the aforementioned mechanisms. Similar results were found by Yetisir and Weaver (1993a,b) in their theoretical model. Measurements of the system total damping in a tube bundle subjected to cross flow were conducted by Weaver and Elkashlan (1981a) and later by Little (2003) which showed the switch of total damping sign from positive to negative at instability as seen in Figure 2.7

Chen (1983a,b) used the force measurements obtained by Tanaka and Takahara as an empirical input to a mathematical model which couples the fluid forces with the tube equations of motion. The stability boundaries obtained using Chen's

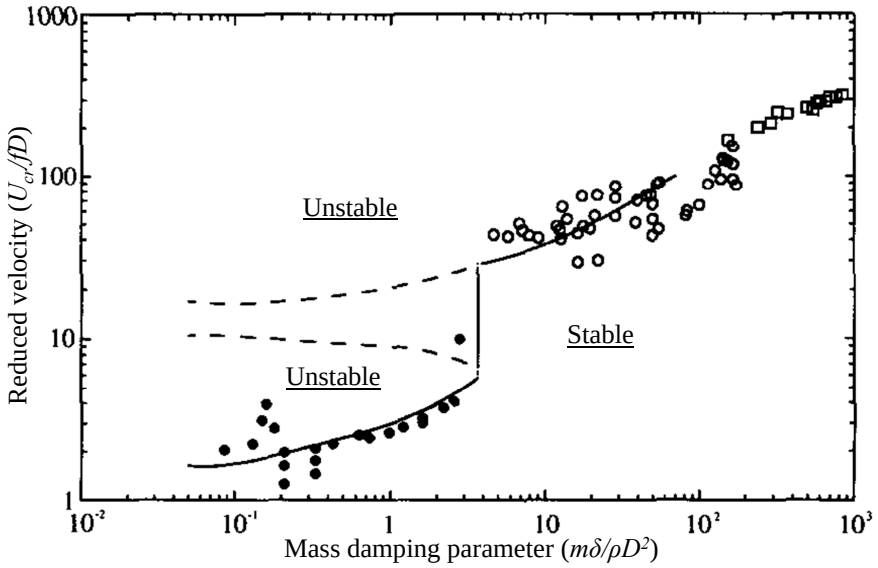

Figure 2.8: Stability boundaries for fluidelastic instability developed by Chen (1983a,b) compared to the experiments; ∘, multiple flexible tubes in liquid flow; •, multiple flexible tubes in gaseous flow; □, single flexible tube in gaseous flow; (—), practical stability boundaries; (- - -), theoretical stability boundaries. (Price, 1995)

model were in good agreement with the experimental data of Tanaka and Takahara (1981) as shown in Figure 2.8. Chen attributed the discontinuity of the experimental results reported by Tanaka and Takahara (1981) to the existence of multiple stability boundaries as predicted by his model. Chen (1983a) was the first to introduce the existence of multiple stability boundaries. These multiple stability boundaries were generated by most of the later theoretical models, however, the physical existence of these multiple stability boundaries remains questionable (Paidoussis et al., 1996). The practical application of Chen's model was quite limited, (Weaver, 2008), as the model depends mainly on the fluid forces empirical values which are function of the array geometry, and thus it cannot be generalized.

2.4.4 Semi-Analytical Model

Lever and Weaver (1982) found experimentally that a single flexible tube in a

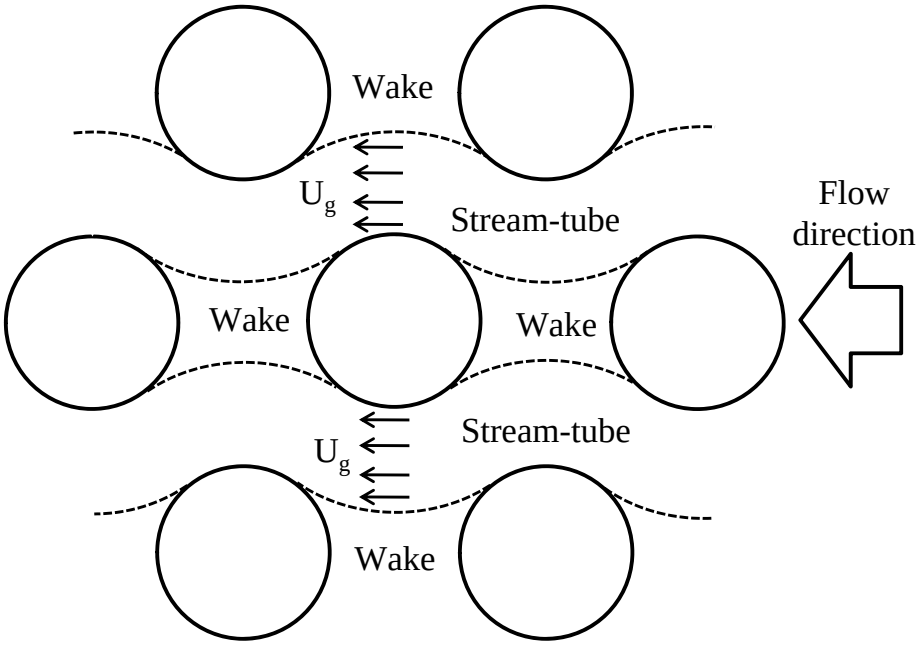

Figure 2.9: Typical flow pattern through a staggard tube array

rigid array could have essentially the same stability threshold as for the fully flexible array. Thus, they carried out an analysis based on a single flexible tube in a cell of rigid tubes subjected to cross flow. Lever and Weaver (1982) divided the flow through an array into wake regions and flow channels which were called stream tubes as seen in Figure 2.9. The stream tube cross-sectional area was assumed to fluctuate about a constant value which is equal to the entrance sectional area. The flow in these stream tubes was assumed to be inviscid, one dimensional, and the friction losses were presented using a pressure drop term.

Lever and Weaver (1982) assumed that the tube motion will disturb the stream tube area relative to its magnitude. The stream tube disturbance over the flow attachment length is in phase with tube motion, while a finite delay time is required for the disturbance caused by tube vibration to propagate upstream. The physical nature of this delay time was unknown to the authors, and as such they assumed this

delay to be a result of the fluid inertia and equal to the time required by the flow to reorganize its pattern when the tube moves. Lever and Weaver (1982) considered the delay time to be in the form of a phase lag function $\phi(s^*)$ in Equation 2.9, where (ϕ) is a phase angle that represents the delay time, U_g is the mean gap flow velocity, (ω) is the tube vibration frequency in (rad/s), and (s^*) is the distance from the vibrating tube.

$$\phi\left(s\right) = \frac{2\omega_n s}{U_g} \tag{2.9}$$

Knowing the stream tube cross-sectional area in terms of time and space, Lever and Weaver (1982) used the one dimensional unsteady Bernoulli's equation to solve the flow field in the stream tubes. By integrating the pressures over the flow attachment length on both sides of the tube, they obtained the fluid forces which are coupled with the tube equation of motion to predict the tube response. The stability boundaries are obtained by setting the damping term in the tube equation of motion to zero, which corresponds physically to the point in Figure 2.7 where the system total damping switches from a positive to a negative value. The stability boundaries obtained using Lever and Weaver (1982) are array geometrical dependent which is more practical.

Despite the relative simplicity of this model, the stability boundaries obtained by Lever and Weaver (1982) followed remarkably the experimental data trend as shown in Figure 2.10. This implies that this model captures to some extent the physical nature of fluidelastic instability, however fine tuning of the model parameters is required to achieve better quantitative agreement with the experimental results. It is important to note here that the theoretical model of Lever and Weaver predicted multiple stability loops in the lower mass damping parameter regions similar to what

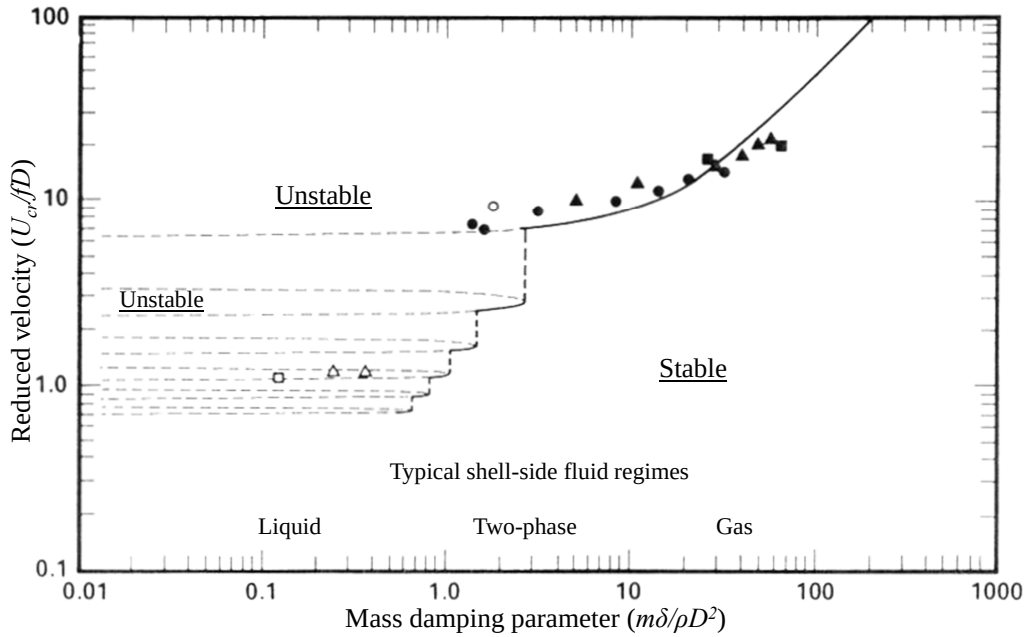

Figure 2.10: Stability boundaries developed by Lever and Weaver (1982) theoretical model for parallel triangular tube array $P_r = 1.375$; (—), practical stability boundaries; (**- - -**), theoretical stability boundaries.

Chen (1983a) found.

Price (1995) questioned the flow delay model shown in Equation 2.9 and pointed out that this semi-analytical model needed some empirical terms to be employed such as the pressure drop term used to present the friction losses in the array, the attachment and separation points in the stream tube, and the length of the stream tubes. Lever and Weaver (1986a,b) investigated the effect of these parameters and showed that they have minor effects on the stability boundaries. However, changing the delay time value in Lever and Weaver model affects the stability boundary significantly, which was considered a deficiency in the model by Weaver (2008).

Yetisir and Weaver (1993a,b) introduced some refinements to the theoretical model of Lever and Weaver. They accounted for the stream-wise tube motion, considered all flexible tubes in the array, introduced a generic function to model the decay

of perturbations caused by tube vibrations upstream, and unconstrained the tube response frequency which was constrained by Lever and Weaver (1982) to be equal to the tube natural frequency. The modifications introduced by Yetisir and Weaver showed that at low mass damping parameters, the fluidelastic instability is attributed mainly to the damping mechanism while at high mass damping parameters the instability is attributed to the stiffness mechanism. The stability boundaries reported by Yetisir and Weaver (1993a) showed minor differences as compared to the stability boundaries of Lever and Weaver (1982).

2.4.5 Quasi-Steady Model

Price and Paidoussis (1984) developed a mathematical model for fluidelastic instability based on the quasi-steady approach where the fluid forces coefficients are measured in a rigid tube array and used to represent the fluid forces on the flexible array. The authors considered an array of flexible tubes, and assumed that the motion of a tube is affected by the motion of the two adjacent tubes. Price and Paidoussis (1984) incorporated a time delay between tube motion and fluid response based on the time required for the mean flow to travel one tube row downstream. They presented a first order time delay expression in the form of Equation 2.10 where τ is the delay time between tube motion and fluid response, μ is a constant, D is the tube diameter, and U_g is the mean gap velocity.

$$\tau = \mu \frac{D}{U_g} \tag{2.10}$$

The tube displacements and fluid forces were coupled through the system equation of motion to determine the tube response. Fluidelastic instability was obtained by setting the damping term to zero as discussed previously. The model was improved

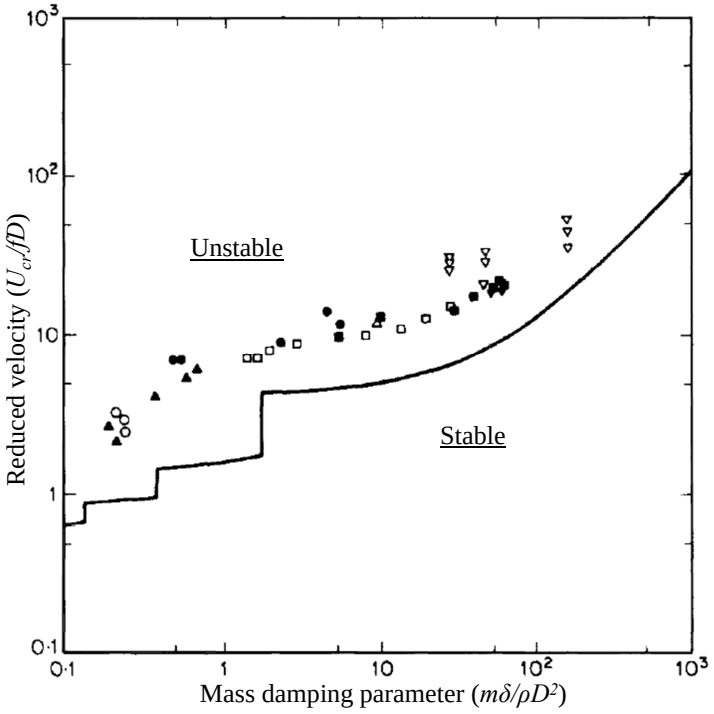

Figure 2.11: Stability boundaries developed by Price and Paidoussis (1986b); $\delta = 0.05$; $\mu = 1.0$; parallel triangular tube array $P_r = 1.375$.

later by Price and Paidoussis (1986a,b) to predict the instability of a single flexible tube in a rigid array. Paidoussis and Price (1988) showed the effect of the damping mechanism and stiffness mechanism by comparing the stability boundaries for a fully flexible array to those for a single flexible tube in a rigid array. The authors concluded that instability for mass damping parameters less than 300 is predominantly due to damping mechanism, while for mass damping parameters more than 300 the instability is predominantly due to the stiffness mechanism, and around the mass damping parameter of 300 both mechanisms are active.

The stability boundaries obtained from Price and Paidoussis (1984, 1986a,b) theoretical model showed multiple stability regions which were considered impractical and a practical stability threshold was considered as in Figure 2.11. The delay time constant μ adopted in this model was shown to significantly affect the stability

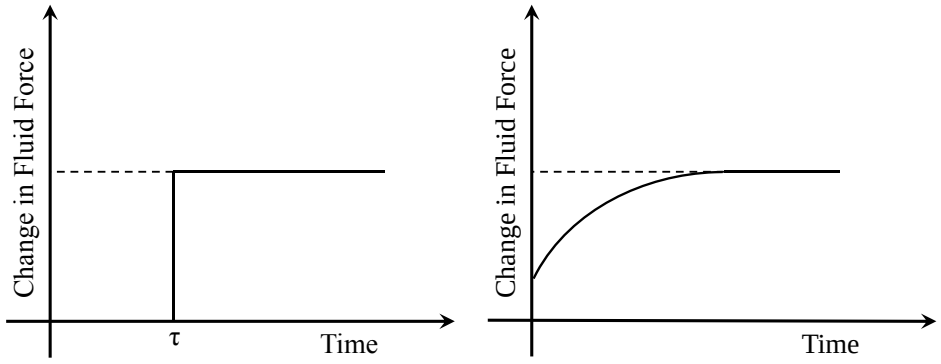

(a) Constant delay time. (b) Continuous delay time.

Figure 2.12: Transient variation of fluid force coefficient induced by a step tube displacement. (Granger and Paidoussis, 1996)

boundaries, albeit no physical justification for that model was introduced. While the quasi-steady model is more complex than the the semi-analytical model of Lever and Weaver, the stability boundaries predicted by Price and Paidoussis (1986b) underestimated the stability threshold as shown in Figure 2.11.

2.4.6 Quasi-Unsteady Model

Granger and Paidoussis (1996) included the unsteady effects which were neglected in Price and Paidoussis (1984) theoretical model and introduced the quasi-unsteady model. The authors considered the model of a single flexible tube in a rigid array, which implies that the instability is attributed to the damping mechanism only. They solved the continuity and Navier-Stokes equations to predict the fluid response to an impulse motion of the tube. They concluded that due to the impulse motion of the tube, a finite layer of small vortices is generated at the tube surface, and these vortices transform the disturbance from the tube to the flow around them. They attributed the delay time between tube vibration and fluid response to the time required to form these layers of vortices.

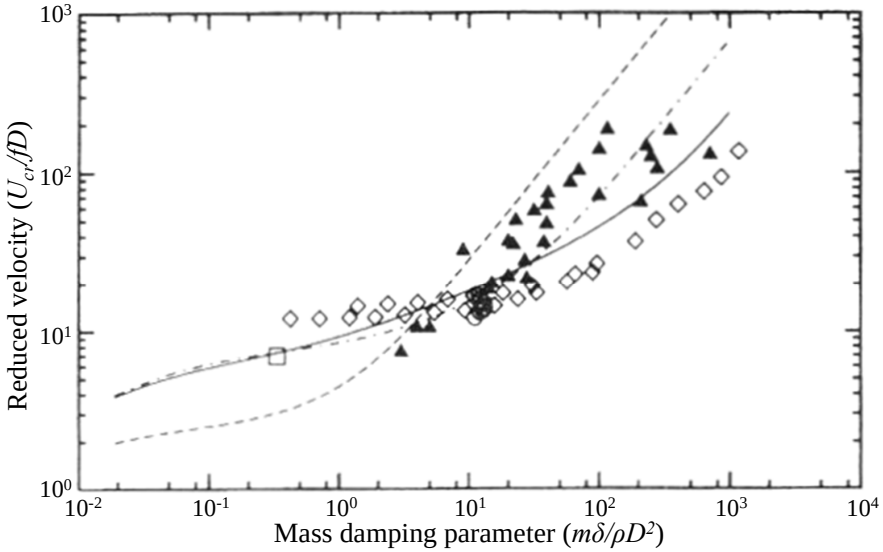

Figure 2.13: Stability boundaries for a single flexible tube in a rigid normal triangular array; (- - -), Quasi-Steady model; (—), Quasi-Unsteady model (first order); (-.-), Quasi-Unsteady model (second order). (Granger and Paidoussis, 1996)

The nature of the delay time between tube vibration and fluid forces was assumed by Price and Paidoussis (1984) to be a constant time shift as seen in Figure 2.12(a), however Granger and Paidoussis (1996) proposed a memory effect as shown in Figure 2.12(b) to model the delay time resulted from the generation and convection of vorticity on the tube surface. This memory effect can be modeled using either a first or second order empirical equations in which a set of factors, depending on the equation order, is obtained from experimental measurements of the tube array.

The quasi-unsteady model developed by Granger and Paidoussis (1996) provided better prediction of fluidelastic instability than the quasi-steady model. The agreement between the quasi-unsteady stability boundaries and the experimental data was improved by increasing the memory effect function order as seen in Figure 2.13. While the quasi-unsteady model was based on physical analysis of the problem, the improvement in stability prediction came at the expense of a more complex model and the need for experimentally evaluated delay time parameters which vary based

on array geometry.

2.4.7 Computational Fluid Dynamics Models

Computational fluid dynamics (CFD) is a very powerful research tool which can be used to solve many fluid mechanics as well as fluid-structure interaction problems. The interstitial flow through a tube array at all the practical Reynolds numbers is typically viscous and turbulent, hence the solver has to consider the full Navier-Stokes equations using moving boundary conditions to present the tube motions. The numerical solution procedure consists of two main phases; the fluid flow is solved first to obtain the added mass and damping as well as the fluid forces that act on the tubes, and then the added mass and damping terms are coupled with the tubes equation of motions while the fluid forces are used as the excitation source. Solving the tube equations of motion results in new set of tubes displacements which are compared to the initial tube displacement in an iterative solver until convergence is achieved. The research effort spent on fluid-structure interaction problems using numerical simulations can be classified into two categories; one is concerned with the development of numerical techniques, while the second is concerned with explaining the problem physics.

Due to the relatively large computational resources required to handle the fluid-structure interaction problems, investigating the phenomenon of fluidelastic instability in tube bundles using (CFD) simulations started to gain potential by the early 1990's. Marn and Catton (1990) developed a relatively simple code based on the one dimensional unsteady integral approach to investigate the flow induced vibrations in tube bundles. Later, Marn and Catton (1991) considered two dimensional analysis to solve the problem, however these early attempts to predict the tube bun-

dle response did not provide good agreement with the experimental data. Eisinger et al. (1995) presented a finite element model of an in-line tube array using the commercial finite element package ABAQUS, while the fluid forces were obtained from the Unsteady model developed by Chen (1983a,b). The results obtained using this simulations were in good agreement with the results provided by Chen (1983a,b).

Kassera and Strohmeier (1997) developed a two dimensional model for flow-induced vibrations in tube bundles subjected to cross flow. The model solves the unsteady Navier-Stokes equations including turbulence modeling using $k-\omega$ model and tube motion. The simulations provided a relatively good prediction of velocity and pressure fields at low Reynolds numbers, however the model was unable to predict the fluidelastic instability correctly. Barsamian and Hassan (1997) investigated the fluid forces fluctuations due to turbulent buffeting in an in-line tube array using a Large Eddy Simulation (LES) technique. The power spectral data obtained using the (LES) simulations were in good qualitative agreement with the experimental results for the same array geometry, however the quantitative agreement was not as good. Schroder and Gelbe (1999) developed two and three dimensional models for a row of flexible tubes in an attempt to improve the design guidelines for fluidelastic instability. They compared the performance of several turbulence models and found that the $k-\omega$ model provides the most satisfactory results. Their simulation results for pressure coefficients agreed well with the experimental results, however the same agreement was not achieved for fluidelastic instability patterns.

Longatte et al. (2003) introduced a study of the numerical methods used to predict tube bundle vibrations in cross flow. They used the Arbitrary Lagrange Euler technique to couple the fluid forces coefficients obtained from the fluid dynamics solution to the finite element code used to solve the structure motion. While this work was a first step in developing a (CFD) code capable of predicting fluidelastic instability,

a relatively good agreement of tube response frequency was reported. Sweeney and Meskell (2003) carried out a numerical investigation of the vortex shedding excitations in tube bundles subjected to cross flow using the discrete vortex method for a relatively low Reynolds number ($R_e = 2200$). Comparing the predicted Strouhal number from the simulations to the experimental results in literature showed an agreement within 6%. Schneider and Farge (2005) investigated numerically the flow patterns in both staggard and in-line arrays of different tube shapes. The simulations provided reasonable agreement for Reynolds numbers $R_e < 1000$.

Liang and Papadakis (2007) used a Large Eddy Simulation (LES) technique to model the vortex shedding in staggered tube arrays subjected to cross flow for Reynolds numbers $R_e < 8600$. The Strouhal number obtained from the simulations was in good agreement with the experimental results. Hassan et al. (2010) introduced a numerical estimation of the fluidelastic instability threshold in tube arrays. The authors solved the flow using Reynolds averaged Navier-Stokes equations to obtain the fluid forces coefficients, and used the unsteady-model developed by Chen (1983a) to predict fluidelastic instability. The stability boundaries predicted by Hassan et al. (2010) numerical solution were in a relatively good agreement with the experimental results in the literature.

The computational fluid dynamics research has improved significantly in the last few years and provided relatively good results due to the rapid improvements in the computational abilities. However, the present computational techniques are either restricted to low Reynolds numbers or depend on one of the aforementioned theoretical models to predict fluid elastic instability. Computational Fluid Dynamics has not shown, at least to the present time, the ability to solve the fully coupled Navier-Stokes equations with the tubes equations of motions for practical Reynolds numbers. It is anticipated that in the near future, numerical codes will be able to

provide reliable prediction of the tube array response at practical Reynolds numbers without the need to model neither the fluid forces nor the tube motion parts.

2.5 Discussion

The theoretical models reviewed in this chapter have advanced our understanding of fluidelastic instability in heat exchanger tube bundles significantly. However, a reliable prediction of the phenomenon is not achieved yet, and several issues still need more clarifications such as:

1. The concept of using a single flexible tube in a rigid array has reduced the problem complexity and provided significant physical insights over the last 30 years. However, the experimental data available in the literature using this concept are quite scattered. While in some cases a single flexible tube in a rigid array has the same stability threshold as for the fully flexible array, in other cases a single flexible tube in a rigid array is completely stable. What is the feasibility of using a single flexible tube in a rigid array to investigate fluidelastic instability?

2. In order for all the theoretical models to predict the damping instability mechanism, a time delay factor between tube motion and fluid forces has to be introduced. This time delay factor affects the stability boundaries predicted by all models significantly. Lever and Weaver (1982) modeled this time delay as the finite time required for flow reorganization, while Price and Paidoussis (1984) modeled this time delay as the time required for the flow to move one row downstream, and Granger and Paidoussis (1996) modeled this time delay as the time required for the generation and convection of a finite layer of vortices

on the tube surface. However, the exact physical nature of this phenomenon and the value of the time delay remain unknown, especially with the lack of the delay time experimental measurements.

3. It is accepted that there are two mechanisms causing fluidelastic instability, namely the *"damping mechanism"* and the *"stiffness mechanism"*. While both the quasi-steady model of Price and Paidoussis (1984) and the semi-analytical model of Yetisir and Weaver (1993a) predict that the damping mechanism is dominant at lower mass damping parameters and the stiffness mechanism is dominant at higher mass damping parameters, it seems that the experimental data at lower mass damping parameters are independent of the damping term, while significant dependence on the damping is observed at higher mass damping parameters. What is the relative importance of the two instability mechanisms over the mass damping parameter ranges?

4. Most of the theoretical models predict multiple stability loops at the lower range of mass damping parameters. While some believe that these multiple stability loops are result of the mathematical modeling (Paidoussis et al., 1996), others claim that they have measured these loops physically (Andjelic et al., 1992). What is the exact physical nature of these multiple stability loops?

These are some of the aspects that must be investigated to improve our understanding of the fluidelastic instability phenomenon. This thesis presents an attempt to answer these questions which can help developing a reliable design tool for the future tube and shell heat exchangers.

Chapter 3

Stability Behavior of a Single Flexible Tube in a Rigid Array

The problem of fluidelastic instability is affected by many parameters such as array geometry, tube pitch ratio, turbulence level, type of working fluid, relative motion of neighboring tubes, etc. As seen in the work of Chen (1983a,b), a full model is very complex, requiring a large number of empirical coefficients measured for every array geometry and pitch ratio. Therefore, for a fundamental study to gain insights into the physics of the phenomenon, there is considerable interest in reducing the problem complexity and the amount of empirical inputs required.

One such simplification involves using a single flexible tube in a rigid array to study the phenomenon. This concept was based on the experimental observations of Weaver and Lever (1977), and Lever and Weaver (1986a,b) which showed that a single flexible tube placed in a rigid array of tubes underwent fluidelastic instability at essentially the same stability threshold as the same array with all the tubes flexible. The use of this idea greatly simplifies experimental and theoretical studies

of fluidelastic instability in tube arrays, but needs to be applied with caution since it also eliminates the effect of the fluid dynamic coupling of neighboring tubes and, therefore, the so-called *stiffness mechanism*.

Since this simplification was first introduced, a number of studies have been conducted on this basis, including Price et al. (1986, 1987) and Austermann and Popp (1995). However, a single flexible tube in a rigid array has not shown consistent behavior in all cases, even for the same array pattern. This apparent contradiction in experimental observations is investigated in this Chapter. A critical review of the experimental data reported in literature for a single flexible cylinder in a rigid array is presented.

The behavior of a single flexible tube in a rigid array is discussed in this chapter in relation to each of the common array geometries shown in Figure 2.1. The single flexible tube, as referred to in this chapter, is generally free to vibrate in both lift and drag directions unless otherwise specified. The results reported in the open literature are critically reviewed, and an attempt is made to identify the common threads and differences observed.

3.1 Parallel Triangular Tube Array ($\alpha = 30°$)

The parallel triangular array pattern has the configuration shown in Figure 2.1, where P is the array pitch, and D is the tube diameter. The pitch ratio P_r is defined as $P_r = P/D$. It is important to note here that some authors use the upstream flow velocity U_o as a reference, while others use the mean gap velocity U_g as a reference. The relation between upstream flow velocity and mean gap velocity most commonly used is given by Equation 2.2. This equation is based on continuity and represents the mean velocity in the minimum gap between the tubes only for normal triangular

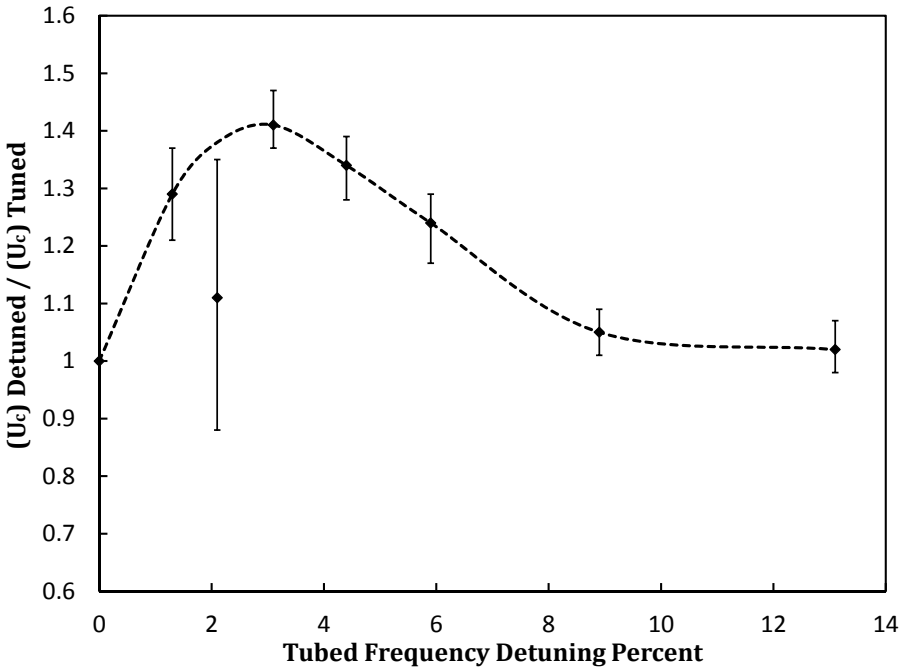

Figure 3.1: Critical velocity ratio vs. frequency difference. Weaver and Lever (1977).

and square arrays. However, it is generally used as the mean interstitial flow velocity for all tube array geometries.

Weaver and Lever (1977) investigated the effect of detuning the array tubes on the fluidelastic stability threshold. Experiments were conducted on a parallel triangular array with a pitch ratio of 1.375 in air flow. The tubes were suspended on piano wires that facilitated precise control of their frequencies. It was found that detuning the adjacent tubes as little as 3% of the targeted frequency could lead to a delay in the stability threshold of about 40% as seen in Figure 3.1. The vertical axis is the ratio of the critical velocity for the detuned tube bundle to that of the carefully tuned tube bundle while the horizontal axis is the detuning percent. It is also seen that detuning the adjacent tubes more than about 10% has no effect on the stability threshold. These observations demonstrate that a single flexible tube in a rigid array

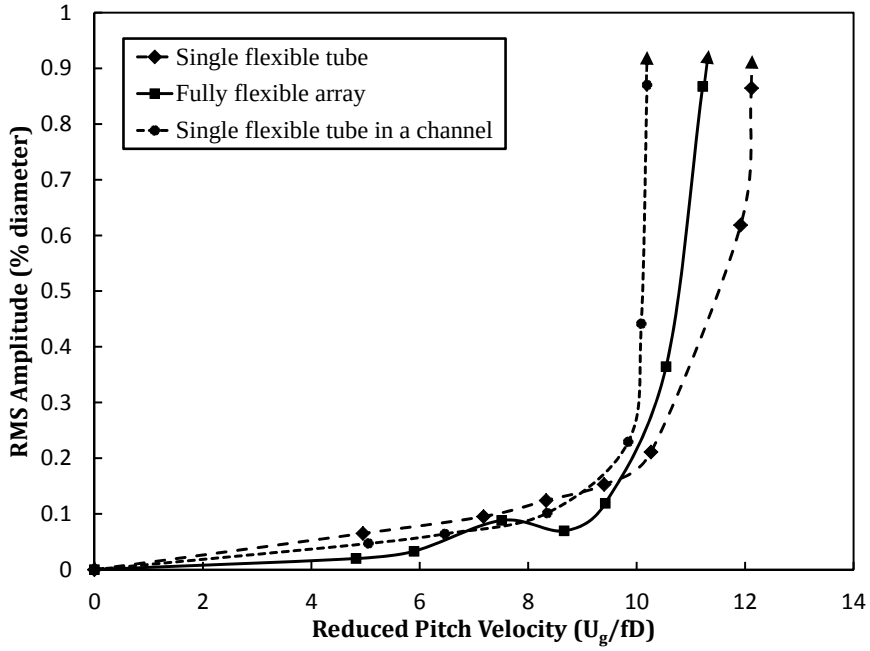

Figure 3.2: Stability behavior for a single flexible tube and a fully flexible parallel triangular array $P/D = 1.375$ tested in air by Lever and Weaver (1986a)

can become fluidelastically unstable.

In order to study this issue further, Lever and Weaver (1982, 1986a,b) carried out a theoretical and experimental study of a parallel triangular tube array. The experimental array consisted of 12 rows and 11 columns of aluminum tubes with a pitch ratio of 1.375, and the flexible tube was located in the eighth row. The experiments showed that the single flexible tube in a rigid parallel triangular array became unstable essentially at the same stability threshold for the array with all the tubes flexible as shown in Figure 3.2.

Little (2003) conducted experiments on a parallel triangular array with a pitch ratio of 1.39 in air. The array consisted of 7 rows and 5 columns of cantilevered acrylic tubes, $D = 64mm$, with the flexible tube located in the third row. This particular location was suggested by Weaver and Elkashlan (1981b) to be the least stable location in the array. The array with all tubes flexible showed distinct fluidelastic instability

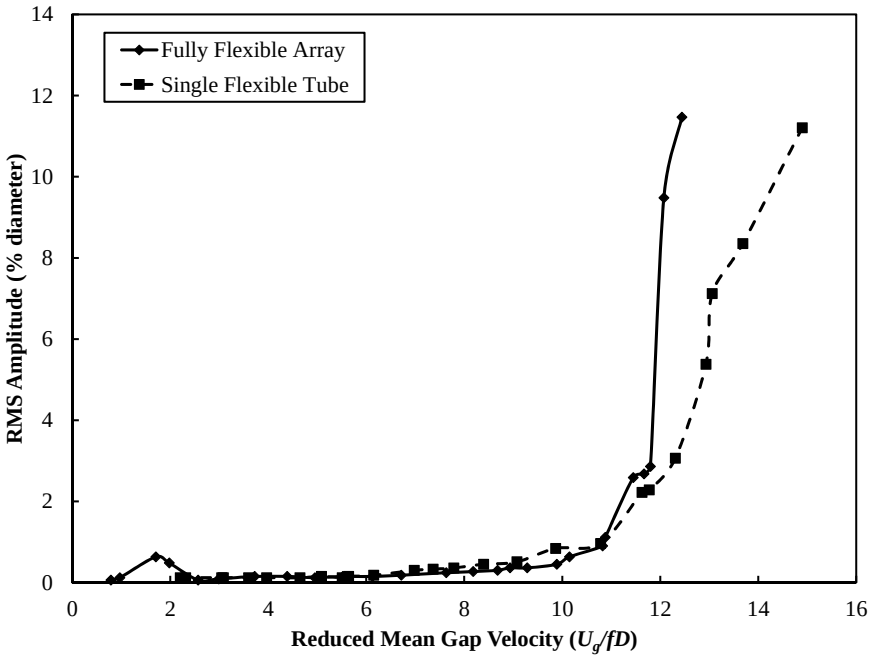

Figure 3.3: Third row tube RMS response amplitude in a parallel triangular array subjected to air cross flow, $P_r = 1.375$. (Little, 2003)

behavior well separated from any Strouhal excitation. The case of a single flexible tube showed fluidelastic instability as shown in Figure 3.3; however the post stability behavior was different due to the effect of fluid coupling in the case of all flexible tubes. The post stable behavior for a single flexible tube showed a less rapid increase in RMS amplitude with increasing flow, and the motion was primarily in the cross-stream direction. Thus, for this pitch ratio, fluid coupling appears to have a little influence on the stability threshold but a significant effect in the post stability region.

Scott (1987) conducted experiments using two parallel triangular tube arrays with pitch ratios of 1.375 and 1.73 in water flow. The first array with $P_r = 1.375$ consisted of 6 rows and 11 columns of acrylic tubes, $D = 25.4mm$, and the flexible tube was located in the third row. In the case of a single flexible tube, fluidelastic instability was predominantly in the cross-stream direction, and essentially at the same stability threshold for the array with all tubes flexible as shown in Figure 3.4.

The response patterns showed small frequency shift and rather irregular amplitude increase with flow velocity because of significant fluid added mass effects in liquid flow, and the resulting changes in tube natural frequency depending on relative tube motion. The post stability patterns were different as shown in Figure 3.4(b) due to the strong liquid flow coupling of adjacent tube vibrations.

The second array investigated by Scott (1987) had a pitch ratio of 1.73 and consisted of 6 rows and 9 columns of acrylic tubes, $D = 25.4mm$, and the flexible tube was located in the third row. The stability threshold for a single flexible tube was less clearly defined and delayed about 30% from the stability threshold for a fully flexible array as in Figure 3.5. It seems that pitch ratio is also a factor in determining the significance of fluid coupling of tubes, i.e. the *stiffness mechanism* in comparison to the *damping mechanism*. This study also showed the effect of relative tube motions on fluid added mass and the associated change in tube frequency. In the fully flexible array, the variability of tube relative mode is reflected in significant changes in tube frequency with flow velocity as shown in Figure 3.5(a). In comparison, the constrained relative mode behavior of the single flexible tube produces a more regular pattern of frequency shifting as shown in Figure 3.5(b).

Austermann and Popp (1995) conducted experiments in air flow using parallel triangular tube arrays with pitch ratios of 1.25, and 1.375. The first array $P_r = 1.25$ consisted of 6 rows and 7 columns of aluminum tubes with $D = 80mm$, and a flexible tube was studied in each one of the first four rows. The results obtained in these experiments showed that a single flexible tube only became unstable in the first row, while a tube in the second, third, or fourth row did not show instability. It was also shown that a shift in the tube static equilibrium position by more than 10% of the gap in the stream-wise direction resulted in instability for the third row tube. The second array with $P_r = 1.375$ consisted of 6 rows and 7 columns of aluminum tubes

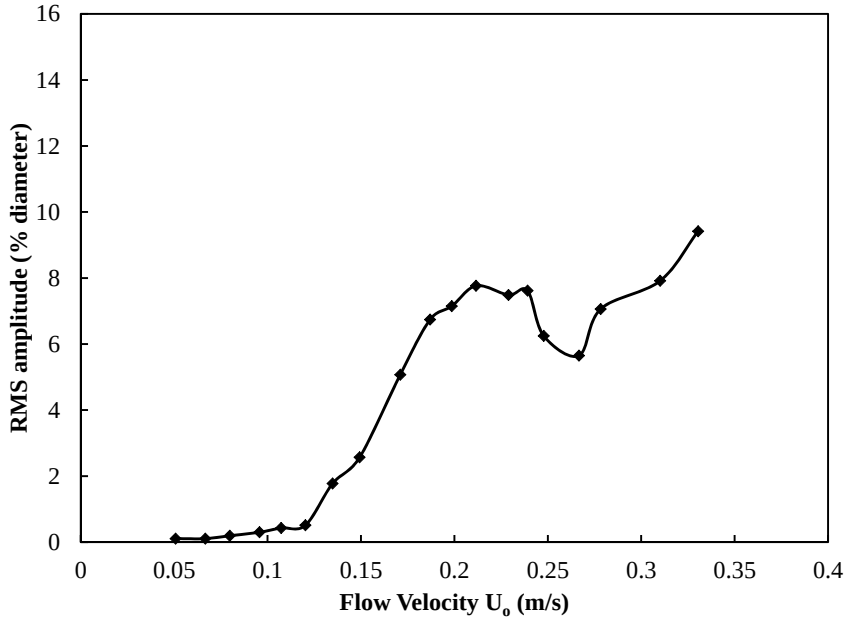

(a) Fully flexible array.

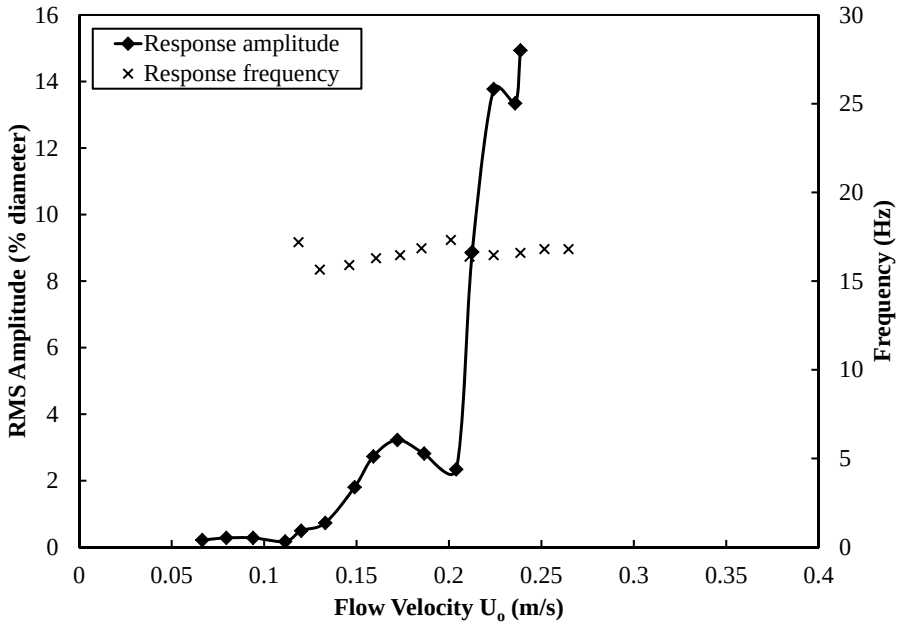

(b) Single flexible tube in a rigid array.

Figure 3.4: Third row tube RMS response amplitude in a parallel triangular array subjected to water cross flow, $P_r = 1.375$. (Scott, 1987)

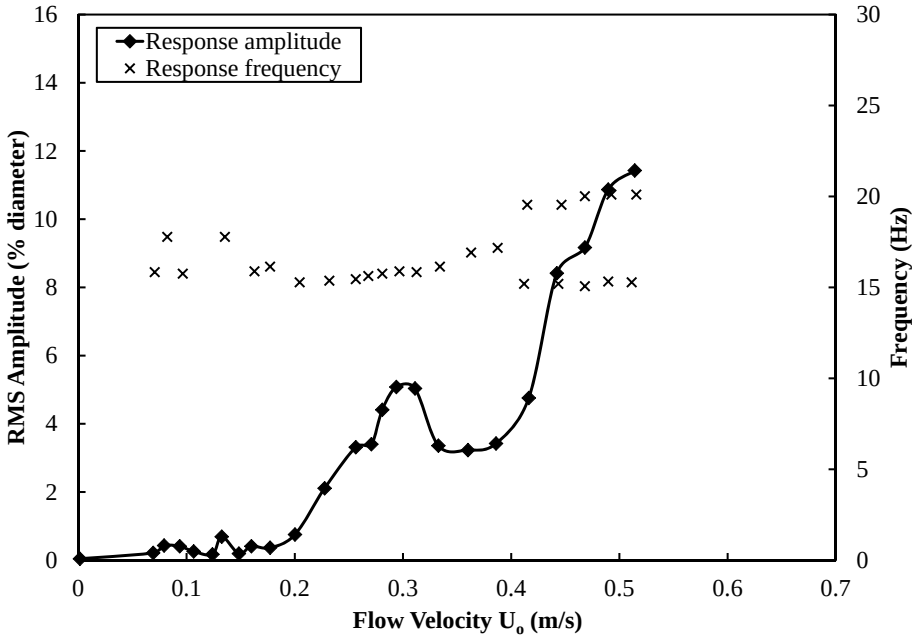

(a) Fully flexible array.

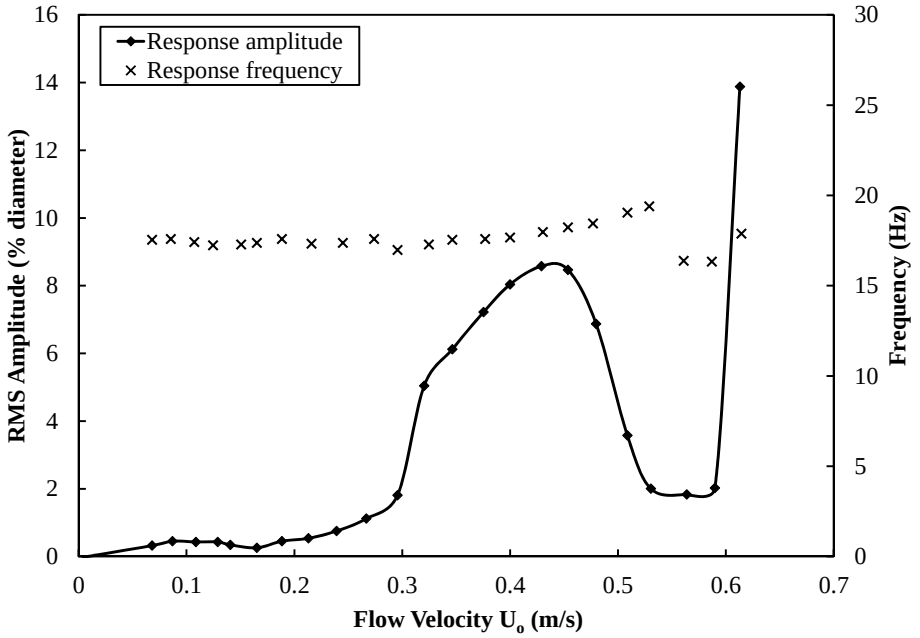

(b) Single flexible tube in a rigid array.

Figure 3.5: Third row tube response in a parallel triangular array subjected to water cross flow, $P_r = 1.75$. (Scott, 1987)

and showed different stability behavior. In all first four rows, a single flexible tube became unstable. The least critical flow velocity and the largest vibration amplitude were reported at the third row of tubes. It was reported that small shifts in the tube equilibrium position resulted in a slight increase in critical velocity, which suggests that the ideal array geometry was the least stable one.

In summary, whether in air or water flows, a single flexible tube in a rigid parallel triangular array has generally been found to become fluidelastically unstable. The mass ratio and strong fluid coupling are seen to have an important effect on the post stability behavior especially in water flows. The pitch ratio seems to be an important parameter in this array geometry, as the small pitch ratio 1.25 showed somewhat inconsistent results, the medium pitch ratio 1.375 showed agreement between single flexible tube behavior and a fully flexible array behavior, and the large pitch ratio 1.7 showed instability but with different behavior prior to critical velocity. The geometrical precision of the array pattern was proven to have an effect on the stability behavior as well.

3.2 Rotated Square Tube Array ($\alpha = 45°$)

Price et al. (1987) conducted experiments to investigate the response of a single flexible tube in a rigid array versus a completely flexible array in both water and air flows for a rotated square array pattern. The experiments were conducted for an array of 7 rows and 13 columns of aluminum tubes with a pitch ratio of 2.12. The mass damping parameter ($m\delta/\rho D^2$) for the air experiments was 7 and for the water experiments was 0.065. The instrumented tube was located in the first, second, and fifth rows of the array to investigate the effect of tube location. The mass damping parameter as well as the flexible tube location seemed to have a little effect on the

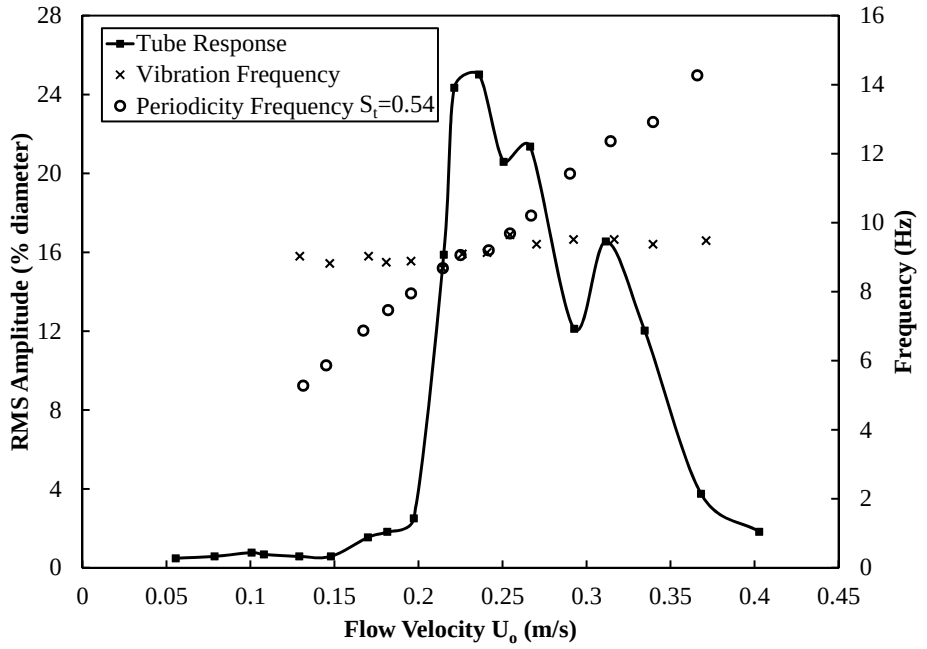

Figure 3.6: Response of a single flexible tube located in the fifth row of a rigid rotated square array subjected to water cross flow, $P_r = 2.12$. (Price et al., 1987)

stability behavior for an array subjected to air cross flow. The results obtained using a single flexible tube located in the fifth row did not show any instability behavior, and it was concluded that a single flexible tube in a rotated square array did not become fluidelastically unstable.

The experiments conducted in water flow showed a different behavior. A dramatic increase in the tube RMS response was detected at a certain flow velocity. The fifth row tube showed a similar response to an isolated tube in a cross flow, where a maximum response amplitude occurs when the vortex shedding frequency coincides with the tube natural frequency, thereby producing a resonance response as shown in Figure 3.6. It was therefore concluded that the observed sudden increase in tube RMS response was associated with flow periodicity excitation not fluidelastic instability.

Paidoussis et al. (1989) conducted similar experiments but for arrays with a

pitch ratio of 1.5 in both air and water flows. The tube arrays used in these experiments consisted of 7 rows and 13 columns of tubes. In these experiments the authors monitored a single flexible tube located in the first, second, third, fourth and sixth row while the other tubes in the array were held rigid. The wind-tunnel experiments showed fluidelastic instability behavior in the stream-wise direction for a single flexible tube located in the second row. This unexpected behavior was suspected to be due to a "blow back effect". Experiments conducted with a flexible tube located deeper in the array did not show fluidelastic instability behavior. The authors concluded that a single flexible tube in a rigid rotated square array pattern subjected to air flow did not experience fluidelastic instability. However a static divergence might occur depending on the tube location in the array. The experiments conducted in water with the flexible tube located in the first, second, third, and sixth rows showed a similar general behavior. The authors reported no fluidelastic instability. However a local peak in the tube response was detected and attributed to Strouhal periodicity, not fluidelastic instability.

Scott (1987) conducted experiments in water flow on a rotated square array with a pitch ratio of 1.7 and consisted of 5 rows and 9 columns of acrylic tubes with $D = 25.4mm$. The fully flexible array showed a gradual increase in the tube response which nearly coincides with the vortex shedding resonance as shown in Figure 3.7(a). It is not clear whether the response observed represents resonance, a coincidence of vortex shedding resonance and fluidelastic instability, or instability promoted by vortex shedding resonance. The response of a single flexible tube is very similar to that for the fully flexible array, but the gradual increase in tube response occurs before vortex shedding resonance as shown in Figure 3.7(b). This implies that the observed phenomenon is fluidelastic instability followed closely by a coincidence of vortex shedding frequency with the tube natural frequency, but this resonance is not

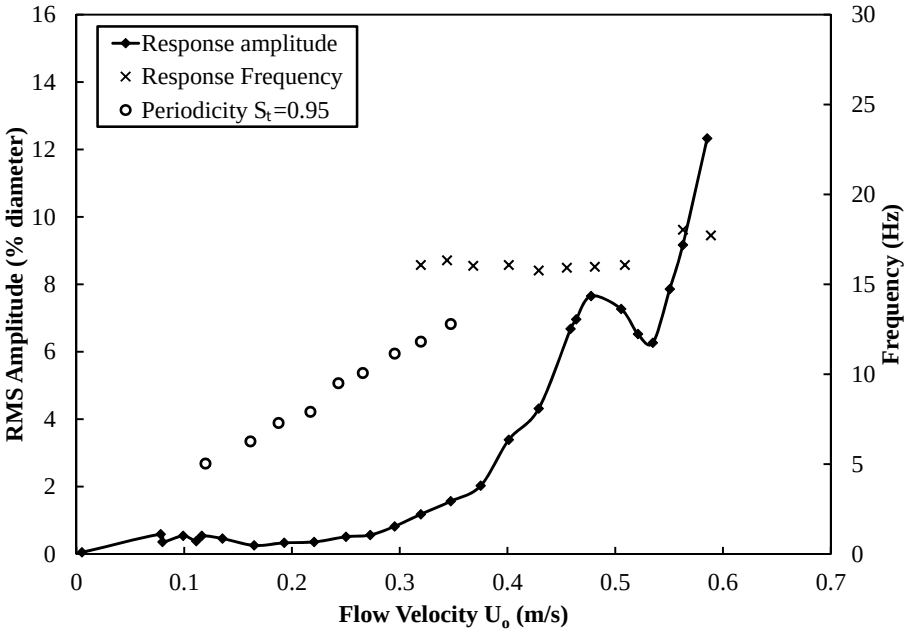

(a) Fully flexible array.

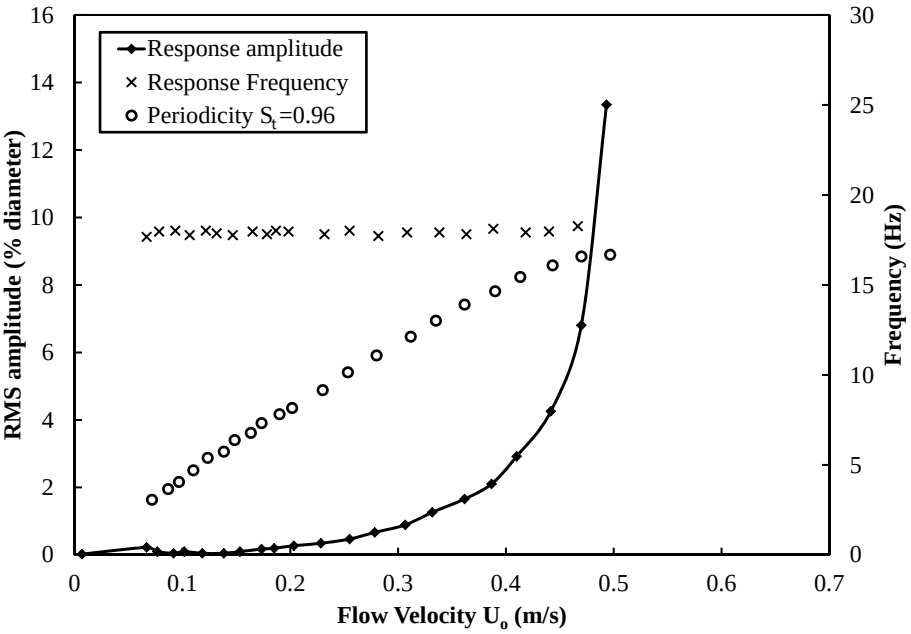

(b) Single flexible tube in a rigid array.

Figure 3.7: Third row tube response in a rotated square array subjected to water cross flow, $P_r = 1.7$. (Scott, 1987)

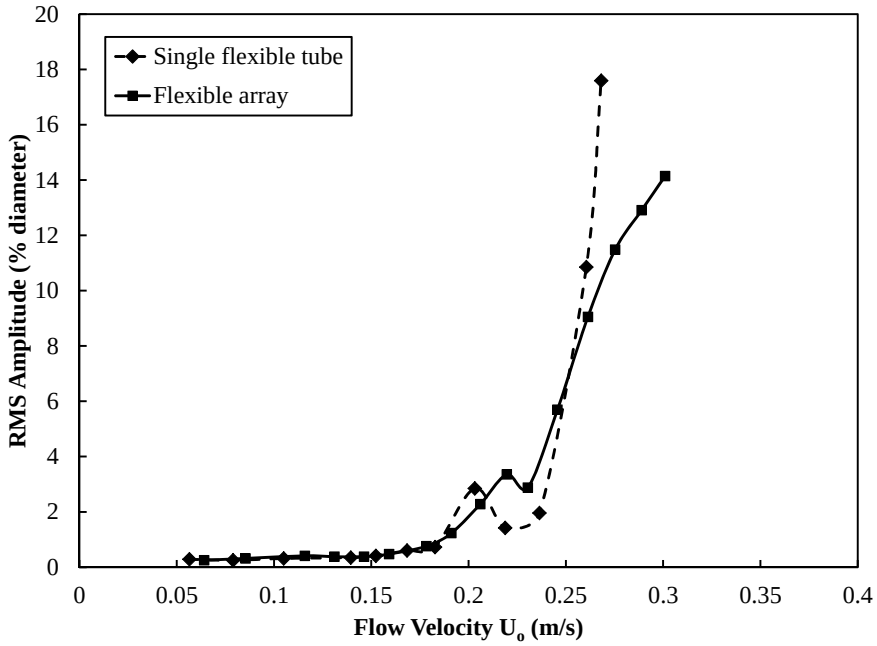

Figure 3.8: Response of the fifth row tube in a rotated square array subjected to water cross flow, $P_r = 1.5$. (Weaver and Yeung, 1983)

the driving force. It was concluded that the single flexible tube became unstable at essentially the same velocity as the fully flexible array.

Price et al. (1986) conducted experiments on a single flexible tube in a rigid rotated square array in air flow with a pitch ratio of 2.12 but with 2 rows and 7 columns of tubes. A single flexible tube was found to become unstable essentially at the same stability threshold as for the fully flexible array. However when a third row was added to the array, no instability was observed.

Weaver and Yeung (1983) conducted experiments on a rotated square array of $P/D = 1.5$ in water. The array consisted of 11 rows and 11 columns of aluminum tubes, $D = 12.7mm$, mounted as cantilevers on a rotating table. The results showed that a single flexible cylinder in this array became fluidelastically unstable essentially at the same stability threshold as for the fully flexible array as shown in Figure 3.8. Austermann and Popp (1995) conducted experiments in air with a rotated square

tube array with a pitch ratio of 1.25. The array consisted of 7 rows and 8 columns of aluminum tubes, and the flexible tube was tested in each one of the first four rows. In all these cases, no fluidelastic instability behavior was observed.

In summary, the experiments reported for rotated square arrays seem to be contradictory. Price et al. (1987) concluded that, for their 2.12 pitch ratio array, the dramatic increase in tube response was due to the "lock-in" with flow periodicity. Comparison of these findings with the results of Scott (1987) and Weaver and Yeung (1983, 1984) are very revealing. It becomes clear that vortex shedding is a significant excitation mechanism in rotated square arrays in water flow and nearly coincides with the fluidelastic stability threshold. As the pitch ratio becomes smaller, it appears that the vortex shedding resonance tends to occur after the stability threshold. In air flow, no fluidelastic instability was observed for a single flexible tube in a rigid array. Thus, mass ratio and pitch ratio are critical parameters in the fluidelastic stability of a single flexible tube in a rigid rotated square array.

3.3 Normal Triangular Tube Array ($\alpha = 60°$)

Scott (1987) conducted experiments in water flow on normal triangular arrays with pitch ratios 1.33 and 1.5. The arrays consisted of 5 rows and 17 columns of cantilevered acrylic tubes with $D = 25.4mm$. The experiments for both pitch ratios showed very similar results. The response pattern in the case of a fully flexible array showed local peaks as shown in Figure 3.9(a) which were attributed to switching in relative tube vibration modes. However, the case of a single flexible tube showed only small vibration amplitude due to turbulence buffeting, and no instability behavior was observed as shown in Figure 3.9(b). Generally, a single flexible tube in a normal triangular tube array with small pitch ratios did not become fluidelastically unstable.

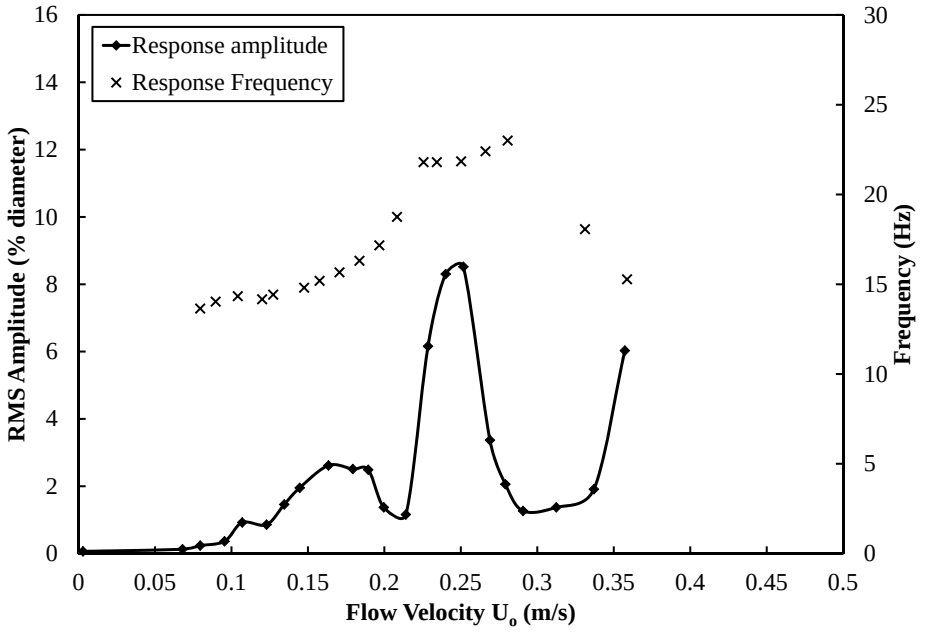

(a) Fully flexible array.

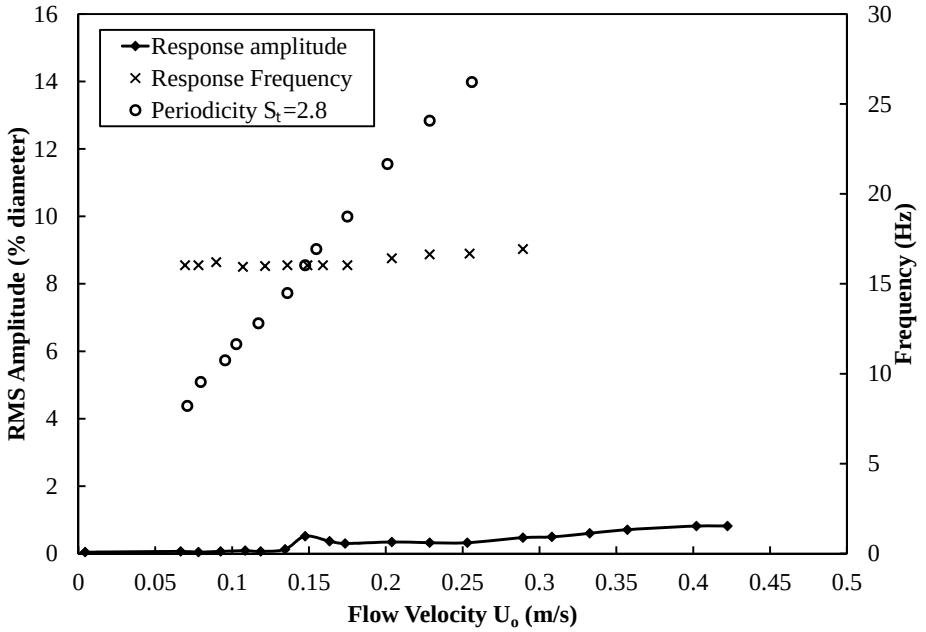

(b) Single flexible tube in a rigid array.

Figure 3.9: Third row tube response in a normal triangular array subjected to water cross flow, $P_r = 1.5$. (Scott, 1987)

Austermann and Popp (1995) conducted experiments in air flow with normal triangular tube arrays with pitch ratios of 1.25 and 1.375. The 1.25 array consisted of 4 rows and 13 columns of aluminum tubes $D = 80mm$, and the flexible tube was located in each of the first three rows. The second row tube did not become unstable even by shifting its static equilibrium position by 15% of the gap. The authors reported that a single flexible tube in the first or third row became unstable with the lowest threshold for a tube in the third row. It was also found that small geometrical imperfections had an effect on the stability threshold for the first row, while it did not seem to have much effect on the stability in the third row. The second array had a pitch ratio of 1.375 and consisted of 5 rows and 11 columns of aluminum tubes. The tube array behavior was somewhat different. The first row tube was stable for the investigated range of reduced velocity, while the second, third, and fourth row tubes became fluidelastically unstable. The third row tube was the least stable tube up to a mass damping parameter $m\delta/\rho D^2 = 30$, and beyond this the least stable row was the second row as shown in Figure 3.10.

Meskell and Fitzpatrick (2003) conducted experiments in air flow on normal triangular tube arrays with pitch ratios of 1.3 and 1.58. The arrays consisted of 5 rows and 13 columns of aluminum tubes, $D = 38mm$, with only one flexible tube located in the third row. The authors reported that a single flexible tube in a rigid array showed fluidelastic instability behavior. The authors also noted that there could be coupling between vortex shedding and the excitation of the first acoustic mode of the test section.

In summary, a single flexible cylinder in a rigid normal triangular array can become unstable when tested in air, but apparently not in water. The range of pitch ratios for the different experiments was relatively small and similar. Thus, for this series of experiments, the differences cannot be explained by the pitch ratio parameter.

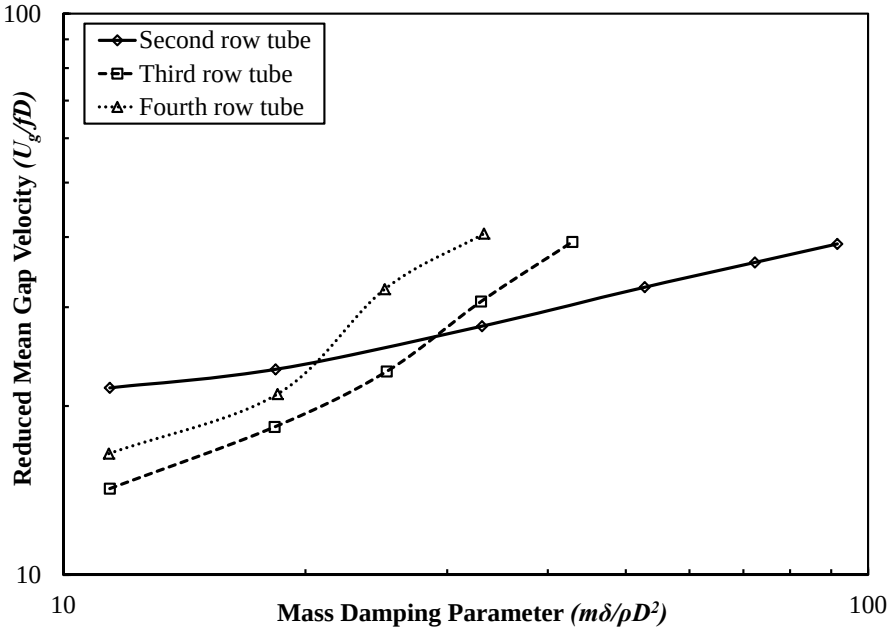

Figure 3.10: Stability threshold for a single flexible tube located in a rigid normal triangular array subjected to air cross flow, $P_r = 1.375$. (Austermann and Popp, 1995)

It seems that the most obvious difference is mass ratio, smaller mass ratios apparently being stable.

3.4 Square Tube Array ($\alpha = 90°$)

Price and Paidoussis (1989) conducted experiments on a 5 rows and 6 columns in-line tube array with a pitch ratio of 1.5 in both air and water flows. Aluminum tubes with $D = 25.4mm$ and suspended on piano wires were used in air, while in water, tubes with $D = 12.7mm$ were mounted as cantilevers. For a single flexible tube located in any of the first five rows of the array in air, fluidelastic instability was observed at values higher than the typical critical flow velocity for fully flexible array. The experiments in water flow showed similar behavior to the experiments in air flow. The authors concluded from this work that a single flexible cylinder in

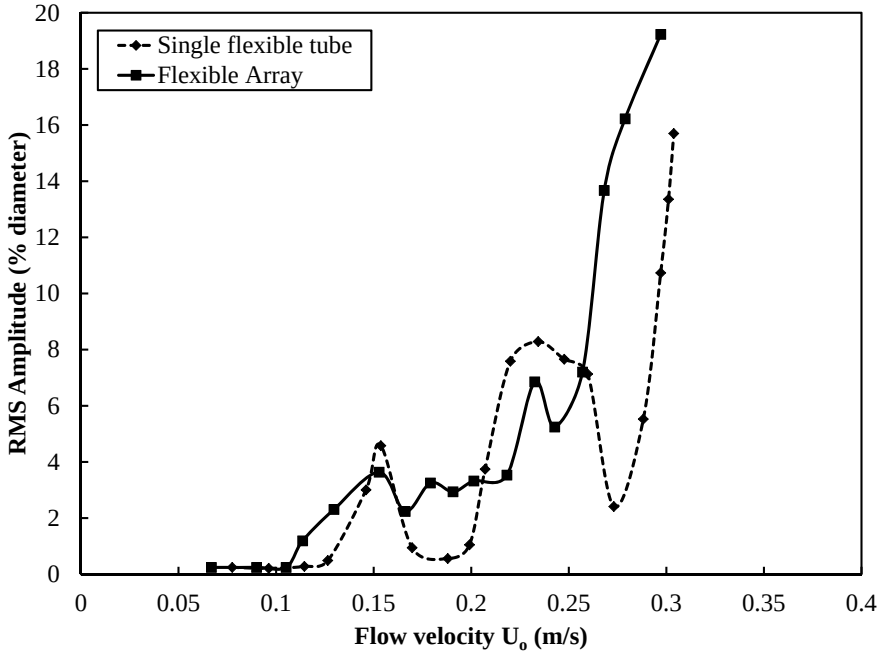

Figure 3.11: Response of the fifth row tube in a square array subjected to water cross flow, $P_r = 1.5$. (Weaver and Yeung, 1983)

a square in-line array could become unstable at a higher critical velocity than the threshold for a fully flexible array.

Weaver and Yeung (1983) conducted experiments on an in-line tube array with a pitch ratio of 1.5 in water flow. The array consisted of 8 rows and 8 columns of aluminum tubes $D = 12.7mm$ mounted as cantilevers on a rotating base. The authors reported that a single flexible tube could become fluidelastically unstable at a threshold within about 20% of the threshold for the same array with all flexible tubes as shown in Figure 3.11.

Scott (1987) conducted experiments on a square in-line array $P/D = 1.33$ in water. Four rows and 10 columns of acrylic tubes $D = 25.4mm$ were used, and the tubes in the second and third row were monitored. In the case of fully flexible array, fluidelastic instability occurred at a point very close to a local peak in tube response as shown in Figure 3.12(a), making it difficult to determine the stability threshold

precisely. The tube response frequency shifted upwards with increasing flow velocity, but there was no indication of a constant Strouhal number excitation frequency in the tube response. The undulations in the vibration response above a velocity of $0.1m/s$ are associated with relative mode frequency shifting due to change in fluid added mass and obscure fluidelastic stability threshold. However, there seems little doubt that the tube array has become unstable. This behavior is discussed in more details for a parallel triangular array of tubes in water by Weaver and Koroyannakis (1982).

The response of a third row tube as a single flexible tube in a rigid array showed no fluidelastic instability behavior as shown in Figure 3.12(b). The absence of fluidelastic instability in this case was attributed to the lack of precise alignment of the tubes and to the small pitch ratio. However, Austermann and Popp (1995) also did not observe fluidelastic instability in their wind tunnel study of an in-line array with a pitch ratio of 1.25. Note that the response frequency did not shift around or drift substantially with increasing flow velocity because of the lack of fluid coupling between adjacent tubes. Therefore, a strongly varying fluid added mass was observed when all the tubes were free to vibrate because of the switching in tube vibration relative modes.

In summary, local peaks are observed in the tube response curves for in-line square arrays which are attributed to coherent vorticity in the tube lanes. As noted by Ziada and Oengoren (1993), this excitation mechanism is different from that in staggered arrays, being associated with jet instability down the tube lane. A single flexible tube in a rigid array becomes unstable in large pitch ratio arrays but the stability threshold may be difficult to determine precisely because of the nearly coincident vorticity phenomena. The results in both air and water for pitch ratios 1.33 or smaller suggest that a single flexible tube in a rigid array does not become unstable.

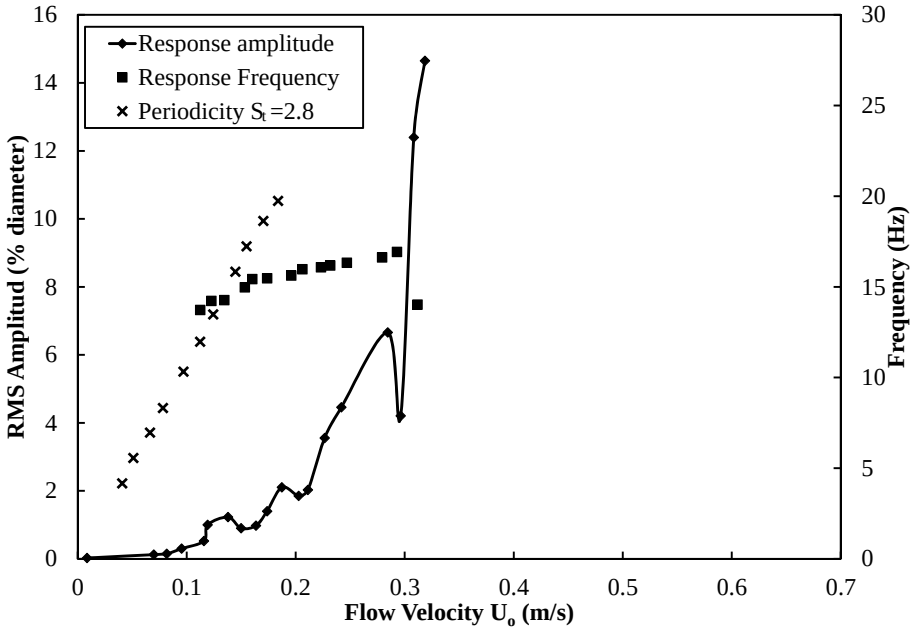

(a) Fully flexible array.

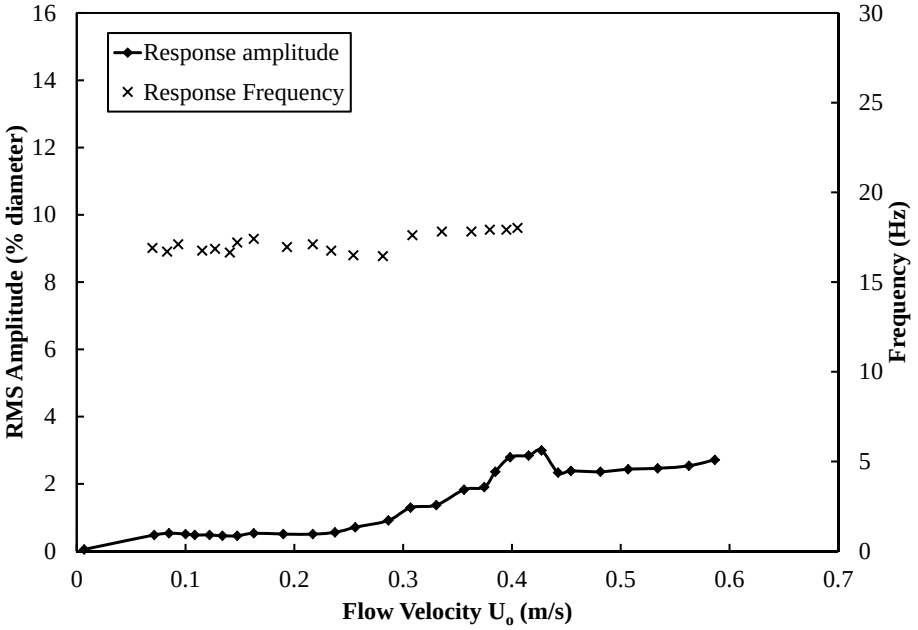

(b) Single flexible tube in a rigid array.

Figure 3.12: Third row tube response in a nsquare array subjected to water cross flow, $P_r = 1.33$. (Scott, 1987)

3.5 Discussion

In an attempt to better understand the results presented above, Tables 3.1, 3.2, 3.3, and 3.4 summarize these observations for parallel triangular, rotated square, normal triangular, and in-line square array patterns respectively. Six parameters are compared in each table: the array pitch ratio P_r, the type of working fluid used in the experiment, the single flexible tube location in the array, the mass damping parameter $m\delta/\rho D^2$, the reduced velocity for instability of a single flexible tube in a rigid array $U_{cs} = U_g/fD$, and the ratio of the stability threshold for a single flexible tube to the stability threshold for a fully flexible array U_{cs}/U_{cf}.

While the individual data appear rather confusing and contradictory, a careful overall examination produces some interesting trends. All researchers have observed fluidelastic instability for a single flexible tube in a rigid parallel triangular ($\alpha = 30°$) array regardless of working fluid, albeit with some sensitivity to tube frequency tuning and precision of array geometry. For rotated square ($\alpha = 45°$) arrays, a single flexible tube in a rigid array is observed to become fluidelastically unstable in water flows but not in air flows. This implies that tube-to-tube coupling is necessary for fluidelastic instability in air flows but not for the higher density fluid. Moreover, in water flows, strong vortex shedding excitation is nearly coincident with fluidelastic instability such that it becomes difficult to distinguish between them and to define the stability threshold with precision. In contrast, the behavior of a single flexible tube in a rigid normal triangular ($\alpha = 60°$) array defies expectations with clear instability in air flows and no instability in water flows.

As the staggered tube array progresses from 30°, through 45° to 60°, for the same pitch ratio, the wavy path of the flow through the array tends to become more torturous as seen in Figure 3.13. This appears to reduce the potential for a single

Table 3.1: Parallel Triangular Array ($\alpha = 30°$)

Reference	P_r	*Fluid*	*Location*	$m\delta/\rho D^2$	U_{cs}	U_{cs}/U_{cf}
Lever and Weaver (1986b)	1.375	Air	Row 15	1.8	9.8	9.8/9.5=1.03
Weaver and Grover (1978)	1.375	Air	Row 15	1.8	9.3	9.3/8.75=1.06
Little (2003)	1.39	Air	Row 3	2.4	11.6	11.6/11.2=1.02
Scott (1987)	1.375	Water	Row 3	0.18	1.15	1.1/1.1=1.0
	1.73			0.28	1.55	1.5/1.2=1.25
Austermann and Popp (1995)	1.25	Air	Row 1	11.7	30	No Data
	1.375		Rows 1,2,3, 4	11.7	28,19,10, 14	No Data

Table 3.2: Rotated Square Array ($\alpha = 45°$)

Reference	P_r	*Fluid*	*Location*	$m\delta/\rho D^2$	U_{cs}	U_{cs}/U_{cf}
Price et al. (1987)	2.12	Water	—	0.065 - 0.117	Stable	—
		Air	—	4.2 - 40	Stable	—
Paidoussis et al. (1989)	1.5	Water	—	0.065	Stable	—
		Air	—	10.36	Stable	—
Scott (1987)	1.7	Water	Row 3	0.24	2.42	2.4/2.2=1.08
Austermann and Popp (1995)	1.25	Air	—	11.7	Stable	—
Weaver and Yeung (1983)	1.5	Water	Row 6	0.21	3	3.0/2.66=1.13

Table 3.3: Normal Triangular Array ($\alpha = 60°$)

Reference	P_r	*Fluid*	*Location*	$m\delta/\rho D^2$	U_{cs}	U_{cs}/U_{cf}
Meskell and Fitzpatrick (2003)	1.32	Air	Row 3	180	56	No Data
	1.58	Air	Row 3	19	32	No Data
Scott (1987)	1.33	Water	—	0.24	Stable	—
	1.5		—	0.24	Stable	—
Austermann and Popp (1995)	1.25	Air	Row 3	11.7	14	No Data
	1.375	Air	Row 3	11.7	15	No Data

Table 3.4: Square Array ($\alpha = 90°$)

Reference	P_r	*Fluid*	*Location*	$m\delta/\rho D^2$	U_{cs}	U_{cs}/U_{cf}
Price and Paidoussis (1989)	1.5	Water	Row 3	0.0379	1.41	No Data
		Air	Rows 1, and 2	7	67	No Data
Weaver and Yeung (1983)	1.5	Water	Row 5	0.21	2.52	2.52/2.38=1.06
Scott (1987)	1.33	Water	—	0.24	Stable	—
Austermann and Popp (1995)	1.25	Air	—	11.7	Stable	—

flexible tube in a rigid array to become fluidelastically unstable, suggesting that the nature of the excitation mechanism is affected by length of the flow attachment on a tube as well as the stream-wise distance between tube rows.

For square in-line arrays, where the flow path down the tube lanes is straight, the instability of a single flexible tube in air or water flows seems to occur only for pitch ratios of 1.5 or greater. However, jet instability down these tube lanes for in-line arrays is known to produce strong tube coupling, especially of stream-wise modes, which distinguish this geometry from staggered array geometries when it comes to vorticity phenomena as outlined by Ziada and Oengoren (1993). This behavior can also obscure the fluidelastic excitation response in water flows. It follows that array geometry, pitch ratio, and fluid density are all significant parameters in determining the fluidelastic stability threshold of a single flexible tube in a rigid array, i.e., the relative importance of the *"damping"* and *"stiffness"* excitation mechanisms.

The stability plot from the theoretical model of Paidoussis and Price (1988) for a parallel triangular tube array with a pitch ratio of 1.375 is shown in Figure 3.14. Mechanism I is the negative damping while Mechanism II is the so-called stiffness mechanism or tube-to-tube coupling. It is seen that negative damping is the dominant mechanism for mass damping parameters less than about 200 while fluid stiffness is dominant at much higher values of this parameter. Similar results from the theoretical model by Yetisir and Weaver (1993a,b) are shown in Figure 3.15 along with experimental data from the review by Weaver and Fitzpatrick (1988).

Despite the different approach, both theoretical models provide qualitatively similar predictions, although the transition between excitation mechanisms occurs at somewhat lower values of mass damping parameter in the Yetisir and Weaver model. Considering either of the two theoretical models means that nearly all the data in Tables 3.1, 3.2, 3.3, and 3.4 should be damping mechanism dominant, i.e.,

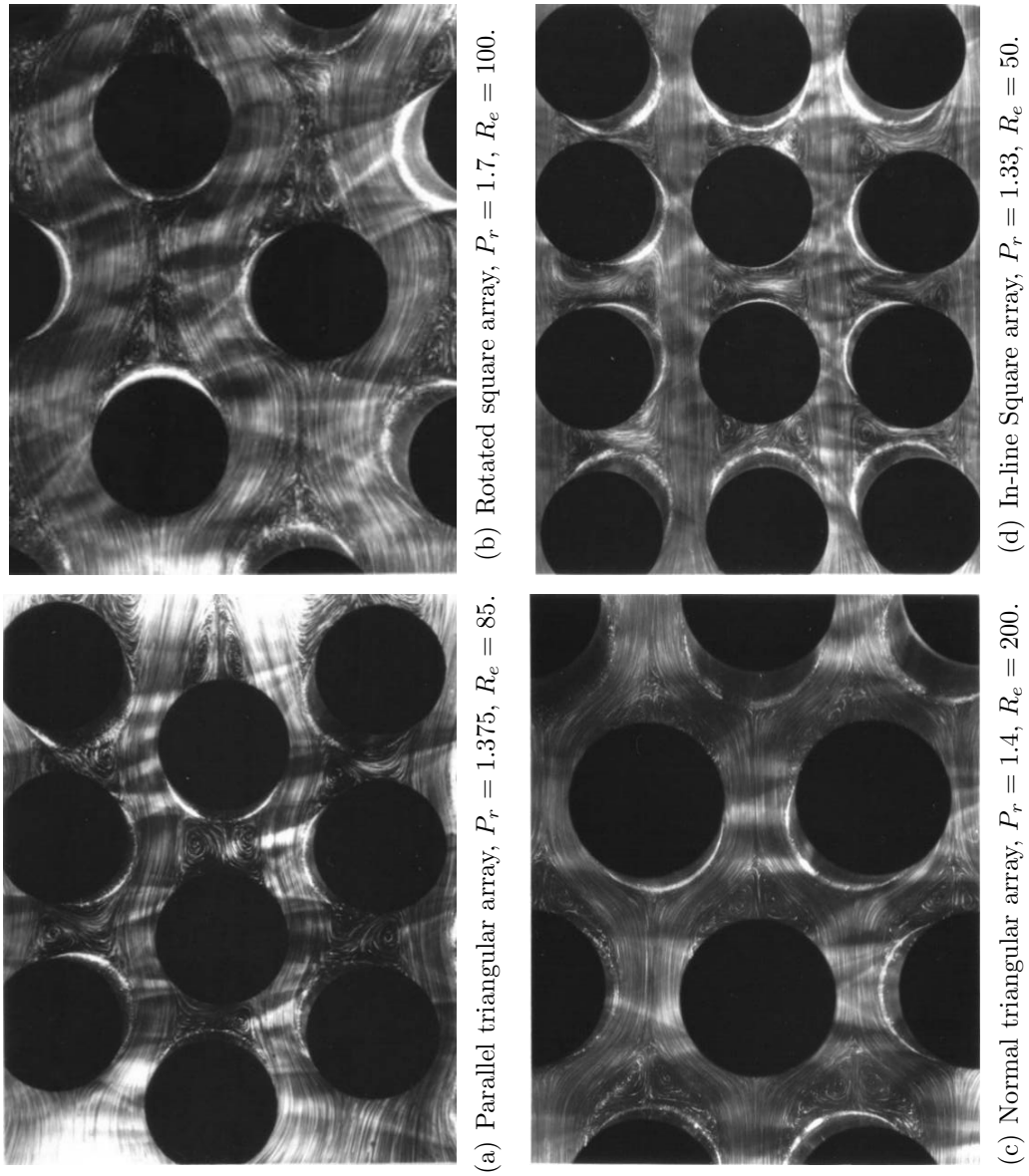

(a) Parallel triangular array, $P_r = 1.375$, $R_e = 85$.

(b) Rotated square array, $P_r = 1.7$, $R_e = 100$.

(c) Normal triangular array, $P_r = 1.4$, $R_e = 200$.

(d) In-line Square array, $P_r = 1.33$, $R_e = 50$.

Figure 3.13: Flow path in the main array geometries, flow visualizations by Scott (1987)

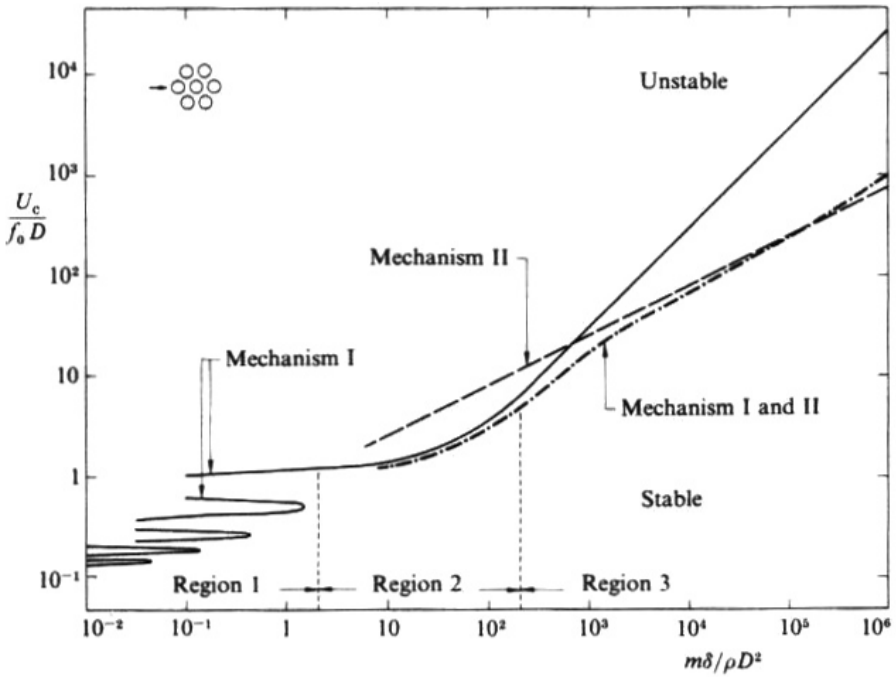

Figure 3.14: Region of fluidelastic instability mechanisms for a parallel triangular array (P/D=1.375), Paidoussis and Price (1988).

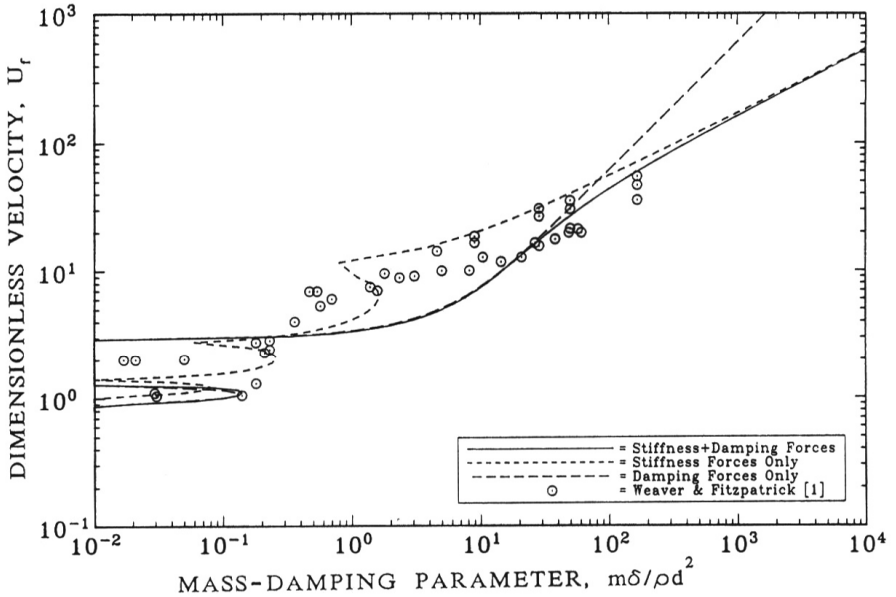

Figure 3.15: Instability boundaries developed based on different mechanisms for a parallel triangular array (P/D=1.5), Yetisir and Weaver (1993a,b).

a single flexible tube in a rigid array is expected to become unstable. Clearly these expectations are not met, at least for some of the arrays. Thus, while the essence of fluidelastic instability in tube arrays seems to be captured by the theoretical models, additional details are needed to achieve better quantitative agreement.

The experimental observation that a single flexible tube in a rigid array could become fluidelastically unstable at essentially the same flow velocity as the fully flexible array offered the possibility of greatly simplifying the physical and mathematical modeling of the phenomenon. Such modeling considers only the "fluid damping" mechanism of fluidelastic instability and assumes that fluid coupling between the tubes, "fluid stiffness", is not an essential component of the overall excitation mechanism. This is demonstrably true for those cases where the stability threshold for a single flexible tube in a rigid array is the same as that for the fully flexible array. While this has often been observed, there are many cases where it has not. Indeed, there are a number of cases for which a single flexible tube in a rigid array appears never to become unstable, i.e., where fluid coupling between tubes is essential for instability. While the available data are not exhaustive, some general threads can be drawn as follow:

1. The relative importance of the *"fluid damping"* and *"fluid stiffness"* mechanisms of fluidelastic instability in tube arrays is strongly dependent on array geometry and pitch ratio, as well as the theoretically predicted mass ratio.

2. The most consistent results for fluidelastic instability of a single flexible tube in a rigid array in both air and water flows are for parallel triangular (30°) arrays.

3. As the staggered array geometry moves from 30° through 45° to 60°, the behavior of a single flexible tube in a rigid array becomes less consistent. In water flows, vortex shedding resonance in rotated square (45°) arrays nearly coincides

with fluidelastic instability and the stability behavior becomes obscured. For normal triangular (60°) arrays, the stability behavior of a single flexible tube in a rigid array is opposite to that expected, being stable at low mass ratios ($waterflows$), and unstable at high mass ratios ($airflows$). This suggests that the instability is fluid stiffness ($coupling$) dominant at low mass ratios, and fluid damping dominant at high mass ratios, contrary to the prediction of any of the existing theoretical models.

4. As found for the case of vorticity phenomenon in square in-line arrays, the straight open tube lane flows tend to create distinctive fluidelastic instability behavior for this array geometry. Of particular significance is the large amplitude coupled tube response associated with vorticity phenomenon in water flows which tend to obscure the stability behavior, especially at small pitch ratios.

5. For repeatable and reliable fluidelastic stability data from tube arrays, great care needs to be taken to tune all the tubes to the same frequency (within 1% is recommended) and to maintain the array geometry precisely. Experiments have shown that small detuning of adjacent tubes in an array has a stabilizing effect, and that relatively small distortion of array geometry (dislocation of tube from its perfect array geometry) can affect the stability of a single flexible tube in a rigid array.

6. The concept of "negative fluid damping" and "fluid stiffness" mechanisms driving fluidelastic instability is a useful mathematical construct to assist in explaining the phenomenon. In reality, however, both mechanisms are active simultaneously and cannot be separated.

It follows that, the concept of using a single flexible tube in a rigid array is

useful for fundamental studies of fluidelastic instability in heat exchangers. However, it is not generally suitable for establishing the stability threshold for tube arrays.

Chapter 4

Experimental Facility and Methodology

A new experimental program was designed and carried out in an attempt to shed some light on the missing details in the theoretical fluidelastic instability models and to gain better understanding of the phenomenon. The experimental setup was carefully designed to facilitate precise control of the array parameters which is anticipated to provide more comprehensive measurements of the interaction between tubes vibrations and fluid flow. In addition, the experimental setup enabled examining a fully flexible array, as well as a single flexible tube at any row location in the rigid array. This chapter provides a detailed description of the wind tunnel facility, the tube array model, the instrumentation, and the signal processing techniques.

4.1 Wind Tunnel Facility

The suction-type, open circuit wind tunnel facility used in the present research was first designed and constructed by Grover (1977). It draws air through a polished

birch plywood contraction section, through the test section, and expands gradually through a square-to-round diffuser until it reaches the vane-axial fan to exhaust as shown in Figure 4.1. The contraction section upstream smoothly changes the $1450mm$ square inlet section to a $306mm$ square working section over a length of $1157mm$. The large contraction ratio, $(16:1)$, accelerates the inlet air flow to a uniform velocity and reduces the turbulence intensity. The inlet flow velocity profile was reported by Grover (1977) to be flat within 1% over the middle 80% of the test section area with a boundary layer thickness of $12.7mm$ at a flow velocity of $U_o = 2.8m/s$. The turbulence intensity upstream of the test section is below 1%. These data were verified for the present research.

The test section is $825mm$ long with an internal $306mm$ square cross section. The section is constructed of polished Acrylic sheets with a thickness of $19mm$ to provide sufficient stiffness and to allow unobstructed visualization of the tube array. The test section assembly is separated from the contraction and diffuser section of the wind tunnel by $6.4mm$ foam rubber gaskets. These gaskets act to seal the test section and to isolate the test section from ambient vibrations.

After the test section is a $2590mm$ long square-to-round diffuser. The diffuser is formed from 12 gauge steel, and the transition from square to round section takes place over the first $420mm$ of this section. The main diffuser body expands 6° in the flow direction, and splitters permit 10° expansion in the latter part. The diffuser acts to transform the kinetic energy in the flow to pressure energy.

The air flow is derived by a four-bladed vane-axial fan located following the diffuser section. The fan housing is $630mm$ diameter and has a stationary directional vanes to direct the exhaust flow. Flexible coupling is used to isolate the fan unit from the diffuser, which is $170mm$ wide and made of vapor-proof plastic.

The wind tunnel is powered by a $10Hp$ D.C. variable speed motor which drives

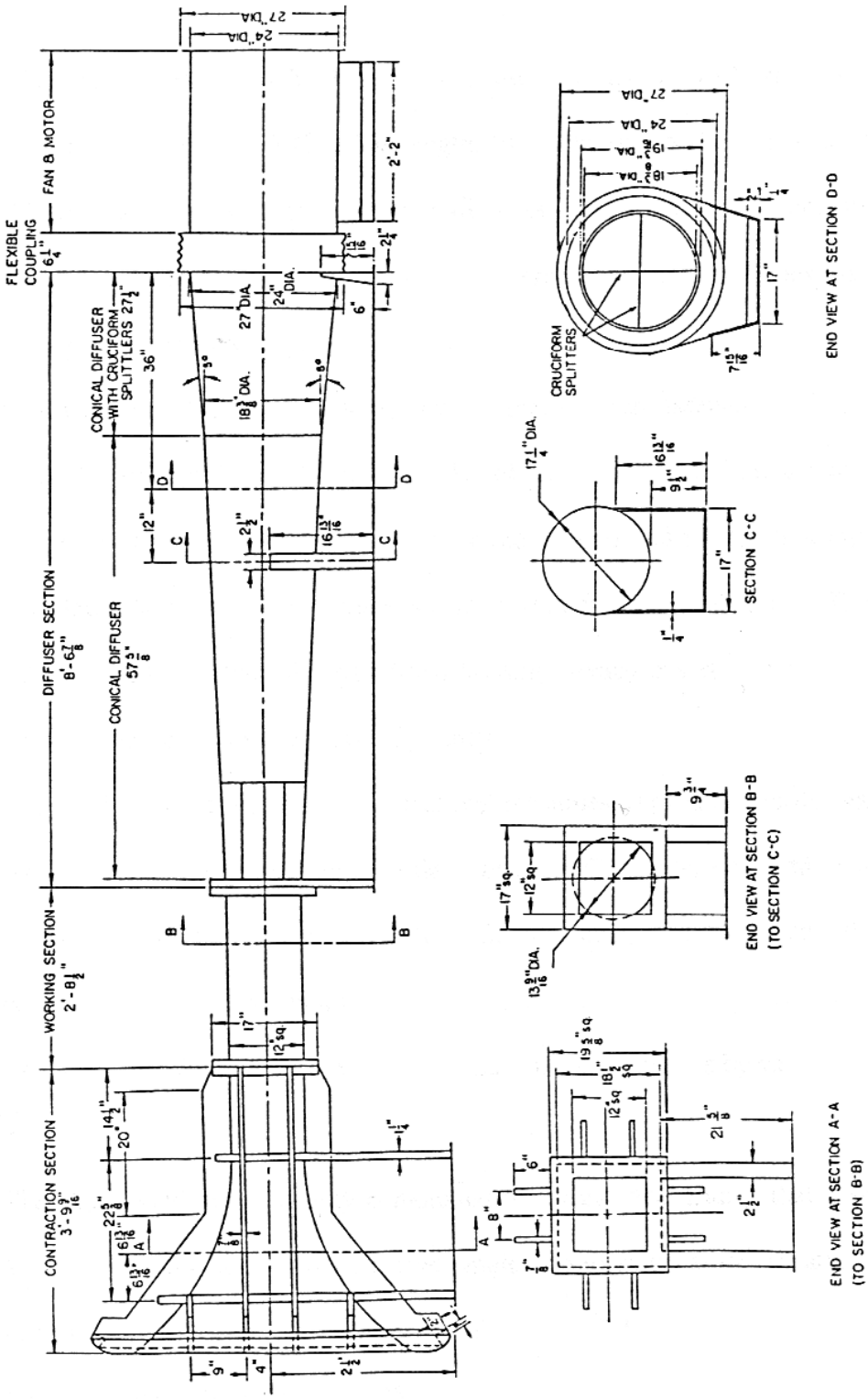

Figure 4.1: Diagram of the Wind tunnel used in the present research, adapted from Grover (1977).

the vane-axial fan. Line voltage feeds a three-phase A.C. motor which drives a D.C. generator at $3500rpm$ to power the D.C. driving motor. The fan speed is regulated by varying an external resistor for steady operation within $\pm 1rpm$. The fan and motor combination provides $3.8m^3/s$ of air at $0.038mm(H_2O)$ static pressure.

The three sections of the wind tunnel facility are mounted on a rigid steel frame secured to the laboratory floor. The wind tunnel centerline is elevated from the laboratory floor by $1680mm$, and the contraction section entrance is located $3350mm$ from the nearest wall. Rubber vibration isolators were installed between the wind tunnel section and the supporting frames to minimize the vibration noise transmitted from the floor. An accelerometer was secured to the empty test section, and while the wind tunnel was operated at 50% of its capacity, no major vibration signal could be detected by the accelerometer.

4.2 Model Design

4.2.1 Tube Array Geometry

The analysis of open literature data, as discussed in Chapter 3, informed the design and construction of a new test rig which was employed in the present research. It was found that a parallel triangular array provides the most consistent single flexible tube behavior. Moreover, the stability threshold for a single flexible tube in a rigid parallel triangular array was found to be essentially the same as that for the fully flexible array. Thus, this array geometry was chosen to conduct the experimental part of this study. The tube array design had three main objectives:

1. To have a sufficient number of columns and rows of tubes to properly model tube bundle behavior. Weaver and Elkashlan (1981b) investigated the effect of

array dimensions on the fluidelastic stability threshold, and it was concluded that at least five rows and three columns of tubes are required to model the fluidelastic instability in tube arrays.

2. To have enough tube spacing to permit interstitial flow measurements.

3. To be able to examine a fully flexible array as well as a single flexible tube at any row location in a rigid tube array.

The tube array dimensions, i.e. number of columns and rows, were determined based on test section dimensions, tube dimensions, and array pitch ratio. The test section dimensions are constrained by the wind tunnel sectional area, while the array pitch can be obtained from the test section width as follow:

$$P = \frac{W}{(2n)cos(\alpha)} \tag{4.1}$$

where P is the array pitch, W is the test section width ($306mm$), n is the number of tubes in each row (must be integer), and α is the array pitch angle ($\alpha = 30^\circ$ for a parallel triangular array). Equation 4.1 has two unknown parameters (P) and (n) which can be iterated to obtain the desired design.

The tube diameter was selected to facilitate sufficient tube spacing for interstitial flow measurements and based on the available standard tube sizes. Thin aluminum tubes were selected as they have a relatively lower mass and higher structural stiffness. As a result, the array consisted of seven rows and five columns of tubes arranged with a pitch ratio of 1.54 as shown in Figure.4.2. The aluminum tubes properties were: diameter $D = 57mm$, length $H = 305mm$, thickness $t = 1.2mm$, and mass $m = 240 \pm 5gm$.

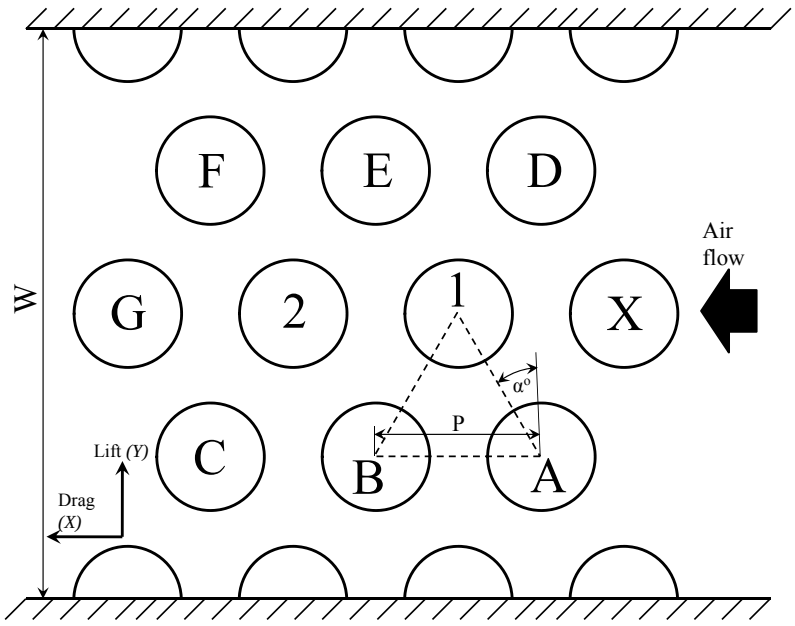

Figure 4.2: Array geometrical configuration.

As an extra feature of this array, the first tube row which contains the tube marked X and the two half tubes on the test section walls was designed to be removable. This idea enables examining the same tube at different tube row locations, which eliminates the tube to tube variability and provides more flexibility in the experimentation.

4.2.2 Tube Dynamic Control

The term *tube dynamics* refers to the tube natural frequency and mode shapes, and the total damping. It was required in the present array design to have a precise geometrical configurations, as recommended in Chapter 3, and to facilitate fine tuning of the tubes dynamic properties. In order to achieve these two objectives, a piano wire arrangement was selected to support the tubes. The tubes were suspended on piano wires tensioned on a steel frame. Details of the steel frame designed to support

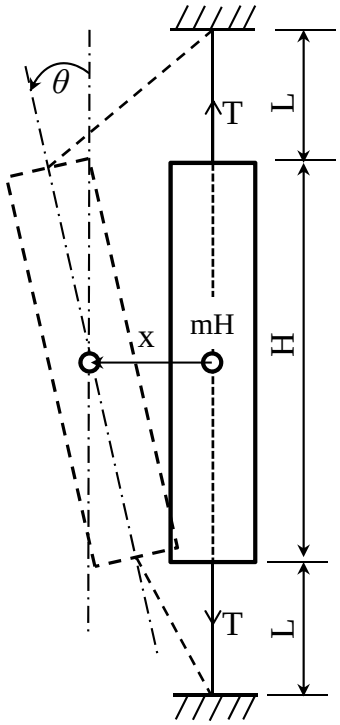

Figure 4.3: General vibrations of a rigid tube suspended on a piano wire.

the test section are discussed in Appendix A.

The general vibrations of a rigid tube suspended on a piano wire can be modeled as shown in Figure 4.3. The equations of motion can be written as follow:

$$mH\ddot{x} + \frac{2T}{L}x = 0 \tag{4.2}$$

$$\frac{mH^3}{12}\ddot{\theta} + \frac{TH(H+2L)}{2L}\theta = 0 \tag{4.3}$$

where m is the tube mass per unit length, T is the piano wire tension, and L is the piano wire free length. The tube general vibration is assumed to be planar, and a combination of a translational motion x and a rotational motion θ, which were assumed to have small values such that the piano wire tension T is constant. By

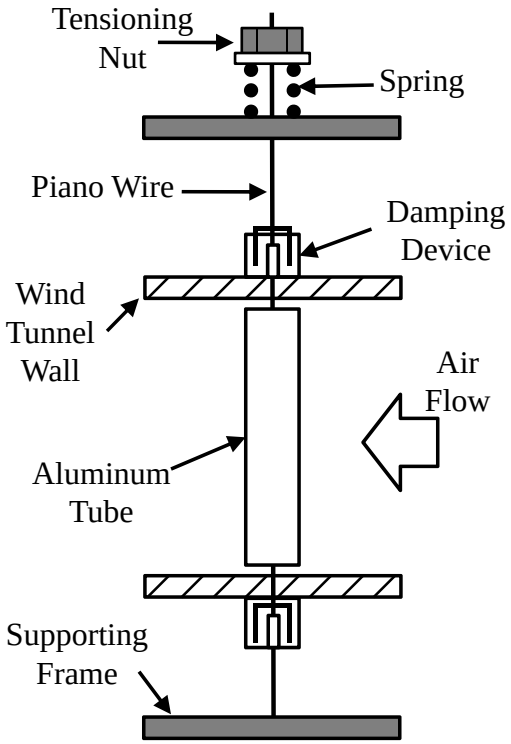

Figure 4.4: Sketch of the tube support arrangement.

solving the equations of motion, the tube natural frequencies were obtained as follow:

$$\omega_1 = \sqrt{\frac{2T}{mHL}} \tag{4.4}$$

$$\omega_2 = \sqrt{\frac{6T(H+2L)}{mLH^2}} \tag{4.5}$$

where ω_1 is the translational mode frequency, and ω_2 is the rocking mode frequency. The piano wire tension T was regulated using a tensioning mechanism which facilitates precise tuning of the tube natural frequency with a precision of $0.1Hz$. Such precision was considered important for obtaining reliable and repeatable results.

A damping device that consists of cups and paddles was used to adjust the tube total damping. The cups are filled with oil, and the paddles are mounted on the

piano wire such that they have the same motion as the tube. The amount of damping added to the tube can be regulated by adjusting the level and viscosity of the oil used in the cups. A sketch of the tube support arrangement used in this study is shown in Figure 4.4.

4.2.3 Test Section

The wind tunnel test section was modified according to the requirements of the present research. The side walls were equipped with half tubes to properly model flow across tube arrays. The top and bottom of the test section were manufactured to facilitate the following functions:

- Providing tight air sealing of the test section.
- Providing anchors to hold the tubes rigid when needed, such that each tube in the array could be examined as a single flexible tube in a rigid array.
- Providing a platform for conducting interstitial flow measurements.

An isometric view of the test section solid model is shown in Figure 4.5. The location of each tube on the test section top and bottom had a recess for securing the damping devices. Two holes at each tube location were used to anchor the tube with screws when needed. A wavy channel was opened on the test section top, and was used as a platform for conducting interstitial flow measurements. The shape of this wavy channel was determined based on the flow visualizations of Scott (1987) as shown in Figure 3.13.

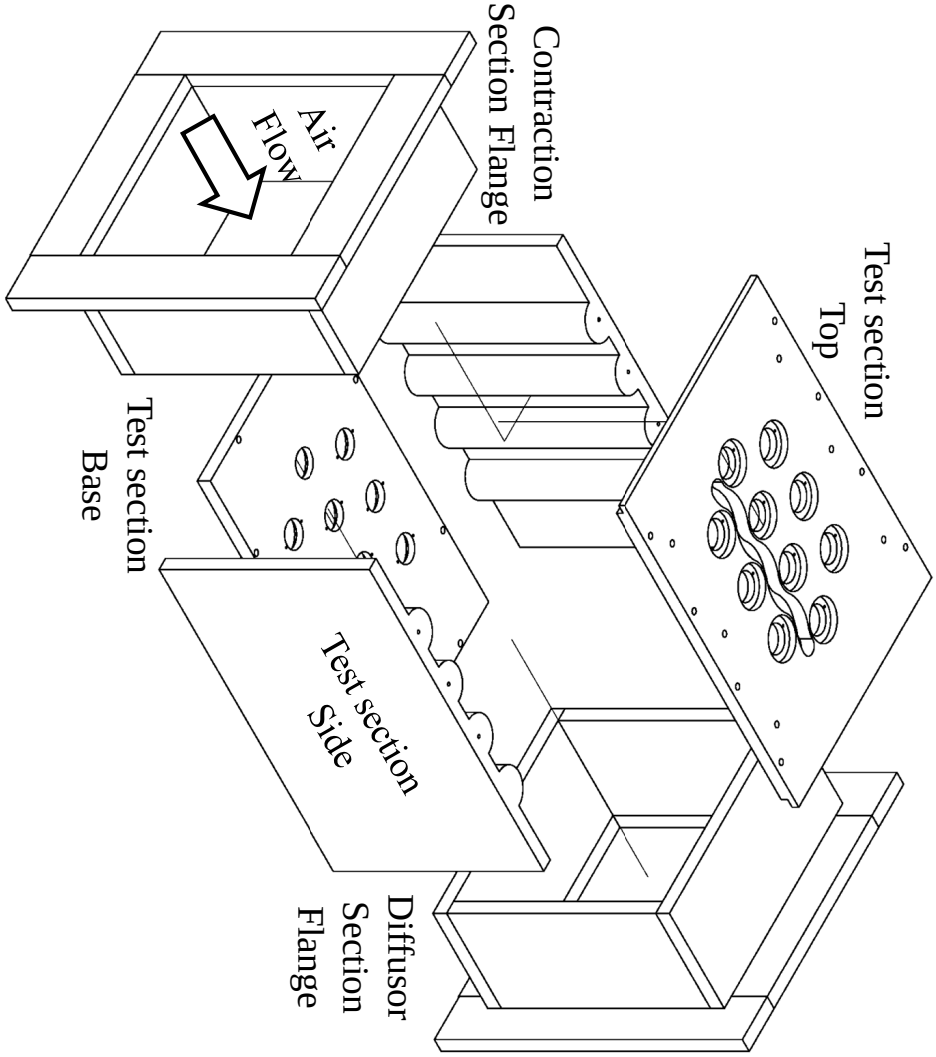

Figure 4.5: Exploded view of the test section.

4.3 Instrumentation

The instrumentation was designed to provide detailed and clear measurements of the interaction between fluid flow and tube vibrations. A set of quantities was required to be monitored in order to obtain more comprehensive measurements namely, upstream flow velocity, interstitial flow perturbations, tube response, and fluid pressures acting on the tubes.

Instrumenting all the array tubes was not feasible, thus two tubes were instrumented during experimentation, namely tubes 1 and 2 which are located in the third and fifth row, respectively, as seen in Figure 4.2. These particular two tubes were selected as tubes 1 and 2 are located in the middle of the array where the effect of test section side walls is minimized. Removal of the first row upstream, i.e. the tube marked X and the two half tubes on the test section walls in Figure 4.2, moves the monitored tubes 1 and 2 to the second and fourth rows respectively.

The upstream turbulence level in the wind tunnel is less than 1% which means that flow disturbances caused by tube motion in the very early tube rows should be detectable over turbulence. It is known that turbulence generated by the tube bundle increases to about the third or fourth tube row and that this tends to obscure flow disturbances created by small tube motion (Polak and Weaver, 1995). At the same time, third row tubes typically have the lowest fluidelastic stability threshold (Weaver and Elkashlan, 1981a). Thus, there is a tradeoff between obtaining a good signal to noise ratio and monitoring a tube with behavior typical of a full tube bundle. The present arrangement supports such an investigation.

4.3.1 Flow Velocity Instrumentation

The air flow velocity was measured using a Pitot tube placed $150mm$ upstream of the array and connected to a digital differential pressure transducer to display the flow dynamic head. Details of the differential pressure transducer and the calibration curves are included in Appendix B. The flow velocity can be obtained knowing the dynamic head through Bernoulli's equation as follows

$$U_o = \sqrt{\frac{2\Delta P}{\rho}} \tag{4.6}$$

where ΔP is the dynamic head, and ρ is the air density. The air flow velocities covered through this research were typically less than $30m/s$ with an average temperature in the laboratory of about $22°C$. Thus, the air flow was assumed to be incompressible, and the air density was considered to be $1.21kg/m^3$.

Constant-temperature hot-wire anemometry was used for studying the interstitial flow details. The small probes limit the flow interference and allow small spatial resolution, while the low thermal inertia of the sensing element enables high frequency sampling. It follows that hot-wire anemometry can provide valuable details of the flow perturbations through the array. Details of the hot-wire anemometry system are included in Appendix B.

The constant-temperature hot-wire anemometer detects the instantaneous flow velocity by determining the voltage needed to maintain the wire temperature. The output voltage signal of the anemometer was calibrated to obtain the flow velocity. The relationship between the anemometer output voltage and the flow velocity can be obtained as follow (Bruun, 1995):

$$E^2 = A + BU^n \tag{4.7}$$

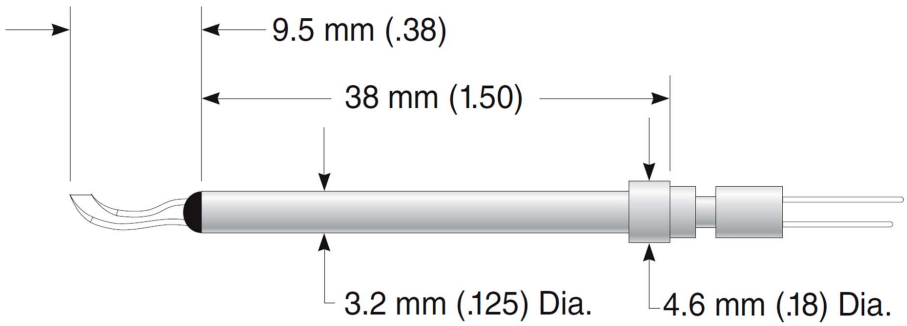

Figure 4.6: 90° Hot-wire probe. (TSI Measurement Tools)

where A, B, and n are constants, E is the anemometer output voltage, and U is the flow velocity normal to the wire. The hot-wire probe can detect only the velocity component of the flow normal to the wire, which requires a prior knowledge of the flow direction to orient the hot-wire probe correctly. The flow directional effect was eliminated in the present research by using a 90° or *Boundary layer* probe as shown in Figure 4.6. The wire in this probe is oriented normal to the plane of measurements, thus it can detect the flow velocity with no directional effects.

Two rigs were designed to support the hot-wire probe as shown in Figure 4.7. The round rig allows traversing the hot-wire probe across the flow channels, while the square rig locates the hot-wire probe accurately along the flow wavy path. The rigs have a clearance fit with the wavy channel in the test section top. The hot-wire was mounted on the rig which was secured at the desired measurement location while the remaining of the wavy channel was sealed. The use of a linear traversing mechanism to move the hot-wire probe was not possible in the present arrangement. Instead, the probe was visually located, since high spatial resolution was not required. With care, the probe can be located within $2mm$ of the desired location in the array.

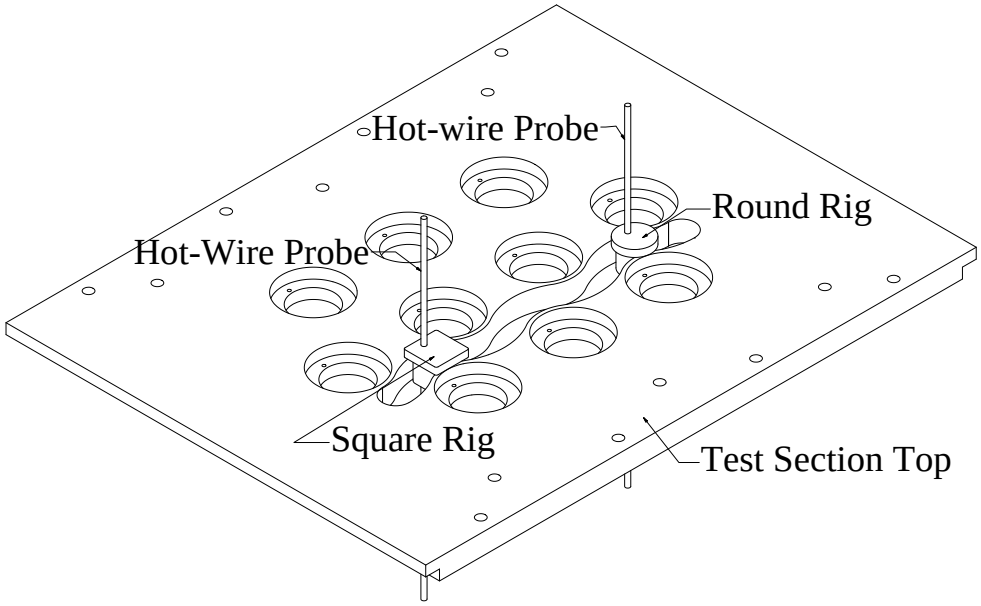

Figure 4.7: Diagram of the hot-wire rigs installed in the wavy channel of the test section top.

4.3.2 Tube Instrumentation

Tubes 1 and 2 were instrumented to measure tube motion and fluid forces. The fluid forces acting on the tube can be obtained by integrating the pressure field around the tube. As the present research is concerned with the interaction between tube motion and fluid forces, the fluid forces magnitude need not to be known. Rather, an indication of the fluid forces acting on the tube is sufficient. As such, each tube was instrumented with two pressure transducers, one on each side, and the difference between these two pressure signal was considered to represent the fluid forces.

In order to eliminate any time delay or pressure dissipation caused by connecting the point of measurement to a pressure transducer, flush mounted miniature pressure transducers were mounted inside the tubes. The sensors were selected to have a light weight such that they did not affect the tube dynamics. The pressure transducers have a sensitivity of $217.5mV/KPa$ and a range up to $1720KPa$. The

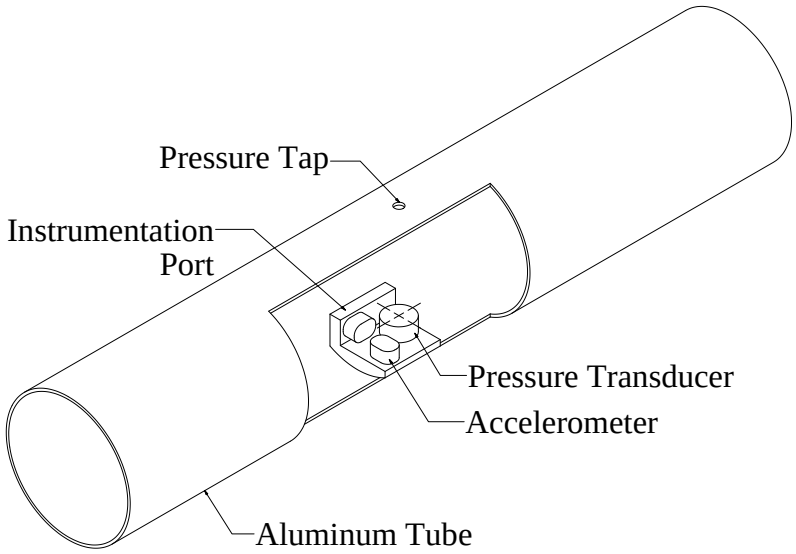

Figure 4.8: Sectional view of an instrumented tube.

acceleration sensitivity of the pressure transducers is $0.35Pa/(m/s2)$, and this value was used to compensate for vibration effects on the acquired pressure signals.

Two uni-axial accelerometers oriented in the stream-wise and cross-stream directions were installed in tubes 1 and 2 to obtain the two normal components of tube motion. The accelerometers have a sensitivity of $10.2mV/(m/s^2)$ and range up to $500m/s^2$ which corresponds to vibration amplitudes up to 50% of the tube diameter.

The pressure transducers and accelerometers were mounted on a platform inside the instrumented tube as shown in Figure 4.8. The platform was designed to be rigid and to maintain the tube mass uniform. The instrumented tube total mass was $275gm$ while the un-instrumented tube mass was $240 \pm 5gm$, and the small difference in mass was compensated for by tuning the tensioning mechanism and damping devices described earlier.

A uni-axial accelerometer was attached to a special rig which could be used to monitor the cross-stream response of any non-instrumented tube in the array. A

photograph of the experimental facility is shown in Figure 4.9.

4.4 Signal Processing Techniques

A total of 8 sensors were used in the experiments in addition to the hot-wire anemometry and Pitot tube anemometer. A list of the sensors function and channel name is included in Table 4.1. The signals were collected simultaneously from the eight channels by a National Instruments data acquisition card $NI - DAQ6015$ controlled via a MATLAB program from a personal computer. Using this arrangement enabled collecting a large amount of data which was quite useful for subsequent off-line signal processing.

Table 4.1: Sensors locations and functions

Channel	*Sensor Type*	*Measured Property*
1	Accelerometer	Cross-stream vibrations of tube (1)
2	Accelerometer	Stream-wise vibrations of tube (1)
3	Pressure Transducer	Pressure fluctuation on tube (1) right side
4	Pressure Transducer	Pressure fluctuation on tube (1) left side
5	Accelerometer	Cross-stream vibrations of tube (2)
6	Accelerometer	Stream-wise vibrations of tube (2)
7	Pressure Transducer	Pressure fluctuation on tube (2) right side
8	Pressure Transducer	Pressure fluctuation on tube (2) left side

4.4.1 Amplitude and Frequency

Any fluctuating time signal can be decomposed to a summation of an infinite harmonic signals based on Equation 4.8, where each harmonic has a certain frequency and amplitude. This process is called Fourier Transformation and produces a frequency spectrum which shows the amplitude and frequency of each harmonic.

Figure 4.9: Photograph of the experimental facility.

$$F(\omega) = \hat{f}[f(t)] = \int_1^{\infty} f(t)\, e^{-i\omega t} dt \tag{4.8}$$

The collected signals are transformed from the time domain to the frequency domain using the Fast Fourier Transform (FFT) algorithm. Instead of considering the FFT of one long time signal, an ensemble averaging of frequency spectra was considered to improve the repeatability of measurements and to reduce ambient noise effects. The time signal is divided into a number of filtered windows with a certain overlap percent, and an ensemble average of the frequency spectrum for each window is performed.

Sampling frequencies ranging from $512Hz$ to $4096Hz$ were adopted in the present research. The maximum frequency that can be detected is determined by the sampling frequency. Each window of the time signal has a length of $10(sec)$ which provides a frequency resolution of $0.1Hz$. It was found that the signal Root Mean Square (RMS) value asymptotes after averaging 50 windows, therefore about 50 averages were collected from each sensor signal. A sample of the tube response time signal and the corresponding frequency spectrum are shown in Figure 4.10. In the present case, the time signal shows essentially a single vibration frequency with some amplitude modulations. The frequency spectrum shows the tube natural translational frequency at $20Hz$, a very small rocking mode at $44Hz$, and line noise at $60Hz$.

4.4.2 Damping

Damping is an important parameter in determining the stability threshold of tube arrays subjected to cross flow. It follows that great care must be taken in determining the tube damping. The damping represents the amount of energy lost per oscillation, and viscous damping can be presented by an exponential decay function

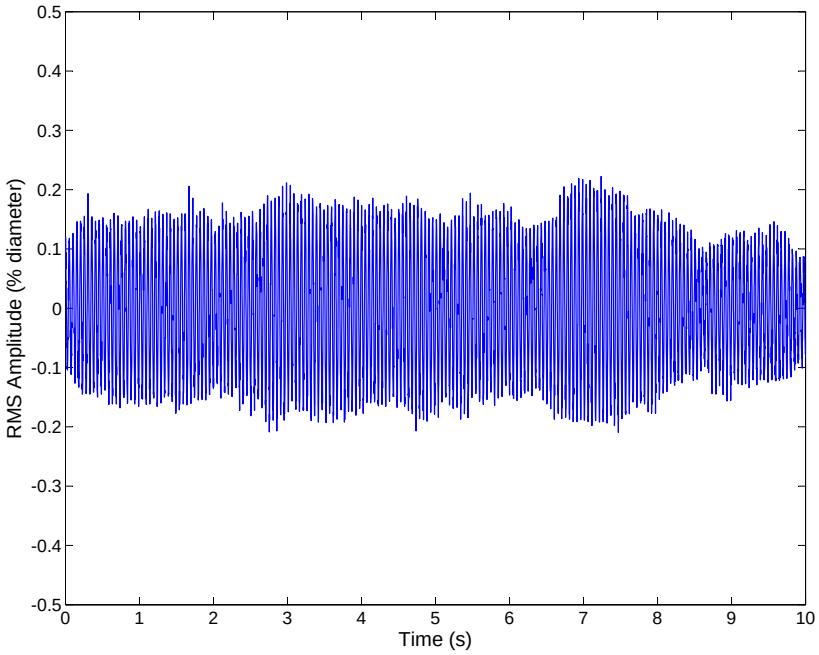

(a) Sample of tube response time signal.

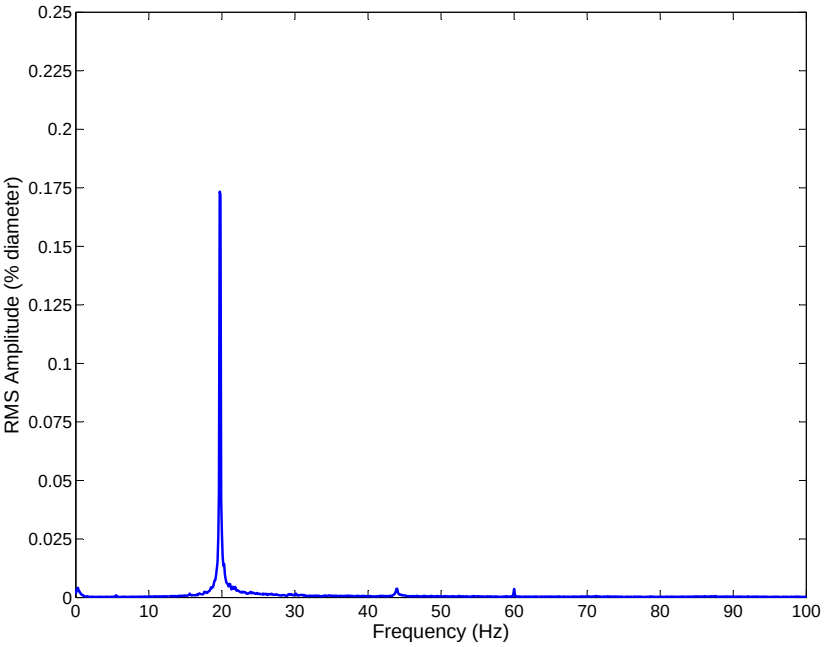

(b) Corresponding averaged frequency spectrum.

Figure 4.10: Sample of the cross-stream response of tube (1) in time and frequency domains.

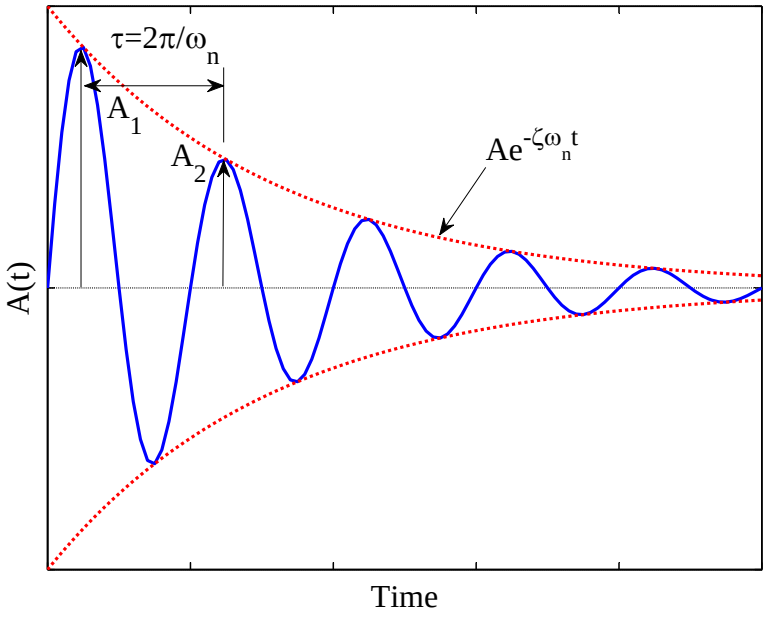

Figure 4.11: General free response of a damped system.

as shown in Figure 4.11.

where ζ presents the amount of damping in the system relative to the critical damping and is called the damping ratio. The damping can be expressed also using the logarithmic decrement δ which represents the ratio between oscillation peaks as follows

$$\delta = \frac{1}{n} ln(\frac{A_1}{A_{n+1}}) \tag{4.9}$$

where A_1 is the first oscillation amplitude, and A_{n+1} is the oscillation amplitude after n cycles. The relation between damping ratio and logarithmic decrement can be expressed for small damping ratios ($\zeta < 4\%$) as follows

$$\zeta = \frac{\delta}{2\pi} \tag{4.10}$$

The tube damping in the present research was evaluated primarily using the exponential decay method while the half-power bandwidth method was used for ver-

ification. The logarithmic decrement was calculated based on the exponential decay method by fitting an exponential envelope curve on the tube free response. The decay trace was captured using a MATLAB program that detects the oscillation peaks as shown in Figure 4.12(a), and fits an exponential envelope curve to these peaks as shown in Figure 4.12(b).

The exponential curve was fitted over a tube response range from $0.25\%D$ to $3\%D$. This range ensures that the response is not so large that non-linear effects are significant, and not so small that the signal is overwhelmed by noise. During the experimental setup tuning it was found that averaging five damping measurements was sufficient to produce a repeatable data.

The calculated damping values were verified by comparison to the damping values obtained using the half-power bandwidth method. The damping ratio ζ can be calculated from the power spectrum by calculating the quality factor Q as follows

$$Q = \frac{1}{2\zeta} = \frac{\omega_n}{\omega_2 - \omega_1} \tag{4.11}$$

where the quality factor Q represents the width of the response peak at an amplitude of $A_{max}/\sqrt{2}$ as shown in Figure 4.13(a). Due to the relatively small tube damping and frequency resolution limitation ($0.1Hz$), the width of the response peak was quite narrow as shown in Figure 4.13(b), which affected the accuracy of the damping ratios obtained using this method. Thus, the half-power bandwidth method was used for verification purposes only.

4.4.3 Coherence and Phase

Phase and coherence measurements were carried out using a MATLAB program that employs the cross-spectral analysis to obtain the phase and coherence. The

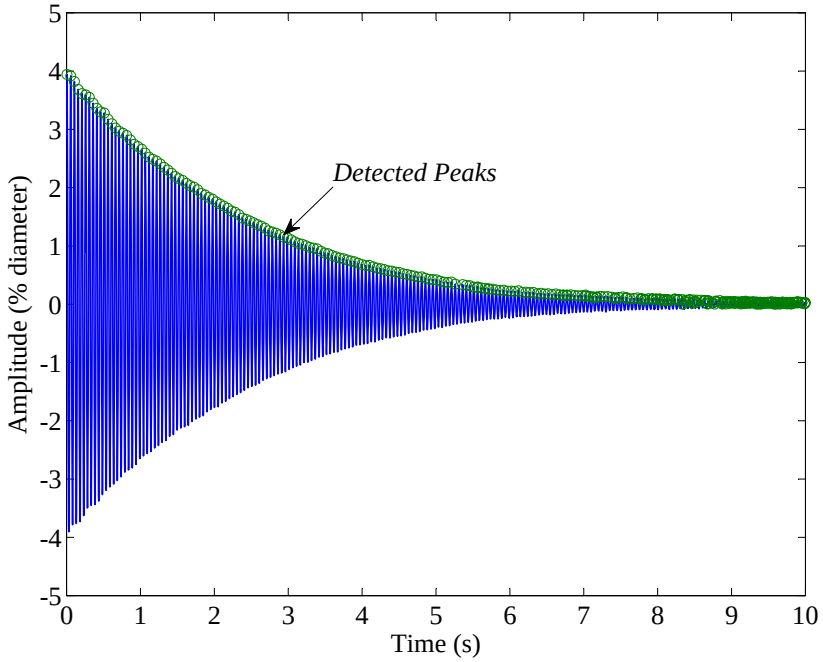

(a) Detected oscillation peaks.

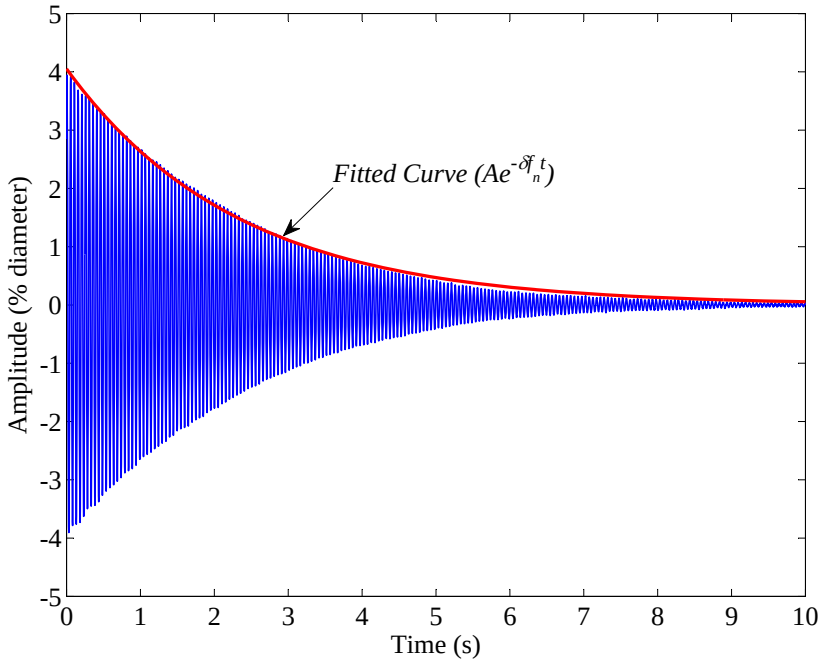

(b) Fitted exponential decay curve.

Figure 4.12: Exponential decay method for evaluating the logarithmic decrement of tube (1) free response.

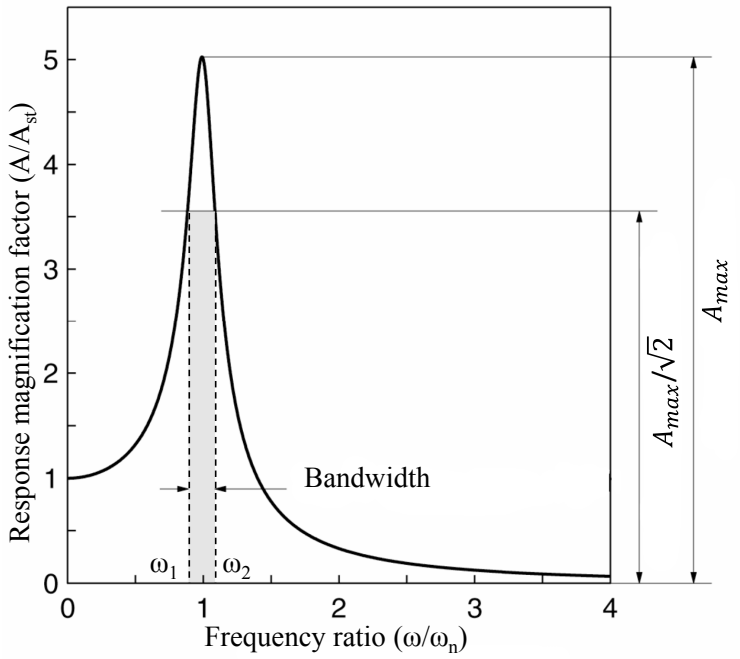

(a) Half-power bandwidth method.

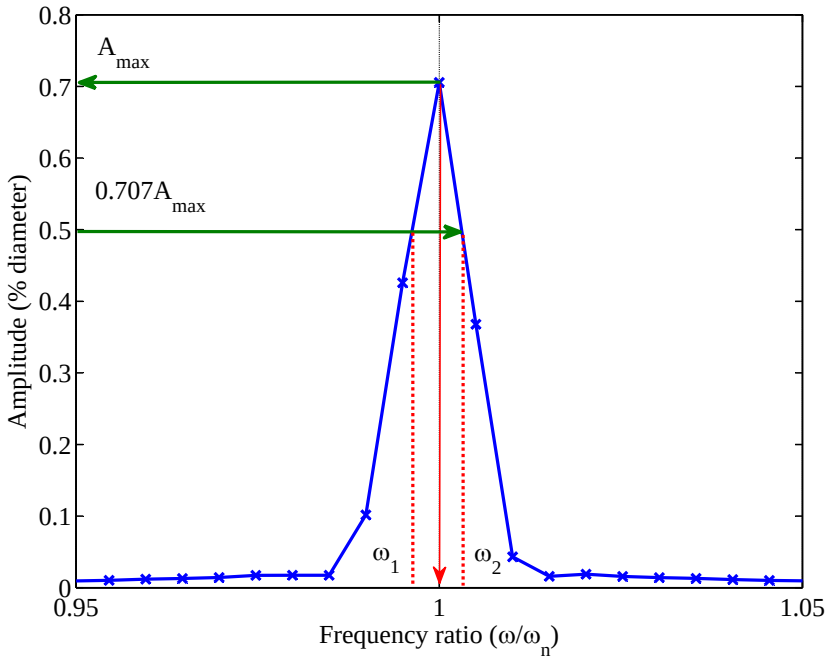

(b) Half-power method applied on present frequency spectrum.

Figure 4.13: Evaluation of damping ratio using the half-power bandwidth method.

program produces first the complex Fourier Transform of two signals $M(t)$ and $N(t)$ as follows

$$M(f) = a + ib \tag{4.12}$$

$$N(f) = c + id \tag{4.13}$$

where $i = \sqrt{-1}$. The power spectral density of the signals, which is the power content of each frequency component, is then obtained as follows

$$G_{MM} = M(f) \times M(f)^* = a^2 + b^2 \tag{4.14}$$

$$G_{NN} = N(f) \times N(f)^* = c^2 + d^2 \tag{4.15}$$

where $M(f)^*$ and $N(f)^*$ are the conjugates of $M(f)$ and $N(f)$ respectively. The next step is to calculate the cross-power spectrum of the two signals as follows

$$G_{NM} = N(f) \times M(f)^* = (ac + bd) + i(ad - bc) \tag{4.16}$$

The real part of Equation 4.16 is called the *co-linear term* while the imaginary part is called the *quadrate term*. The relative phase between the signals can be calculated as

$$\phi = tan^{-1}\left(\frac{Quadrate}{Co - linear}\right) = tan^{-1}\left(\frac{Img(\overline{G_{NM}})}{Re(\overline{G_{NM}})}\right) \tag{4.17}$$

while the coherence function is calculated as:

$$\eta = \frac{|\overline{G_{NM}}|^2}{\overline{G_{MM}} \times \overline{G_{NN}}} \tag{4.18}$$

where $\overline{G_{NM}}$, $\overline{G_{MM}}$, and $\overline{G_{MM}}$ are the averaged cross spectrum, averaged power spectrum for signal (M), and averaged power spectrum for signal (N) respectively. The coherence and phase are both functions of frequency, and are ensemble averaged during the analysis. The coherence function is employed to express the degree of linear dependence of two signals and has a value between *zero* and 1.0. As the coherence level approaches 1.0, this indicates that the measured phase relationship is valid, while as the coherence approaches *zero*, the measured phase relationship is not valid.

In the present research, the calculated phase relationship is considered valid if the coherence is more than 0.5. This threshold was selected based on preliminary experimental observations which showed that phase measurements became repeatable for a coherence more than 0.5.

4.4.3.1 Sign Convention

The phase angle presents the time elapsed between two dependent events. To explain the sign convention adopted in the present study, consider a harmonic time function $F(t)$ as follows

$$F(t) = ASin(\omega t) \tag{4.19}$$

where A is the harmonic amplitude, ω is the harmonic frequency, and t is the time. Now, consider another time function $G(t)$ which is frequency dependent of $F(t)$ as follows

$$G(t) = BSin(\omega t - \phi) \tag{4.20}$$

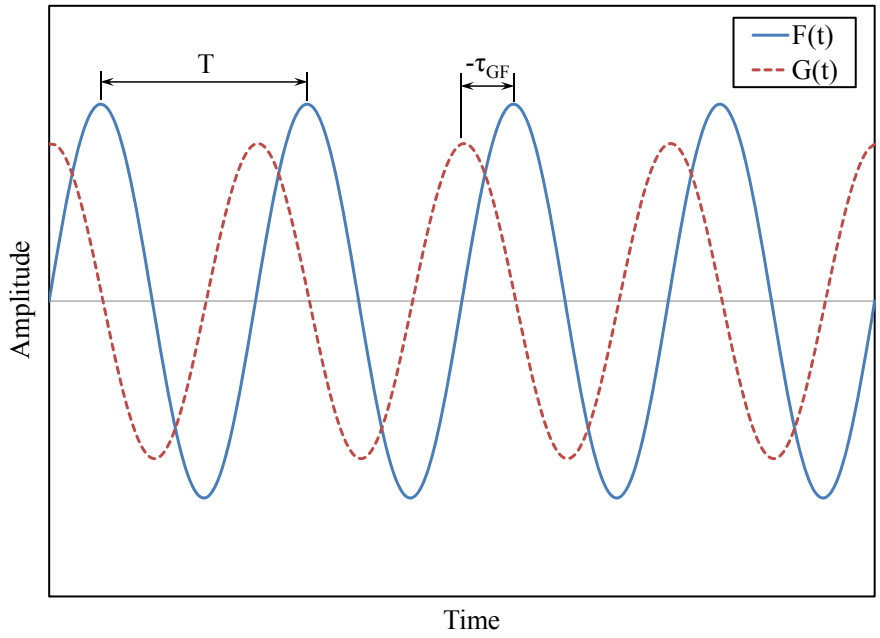

Figure 4.14: General sign convention adopted in the present study.

where B is the amplitude, and ϕ is the phase angle. The function $G(t)$ takes place prior to the reference function $F(t)$ by a time $(-\tau_{GF})$ as shown in Figure 4.14, and in this case, the function $G(t)$ is considered *leading* the function $F(t)$ by a phase of (ϕ) such that

$$\phi = 2\pi\frac{\tau}{T} \tag{4.21}$$

where T is the function period, and τ is the phase lead or lag time. It follows that, a negative phase angle means that the dependent function $G(t)$ *leads* the reference function $F(t)$ in time, while a positive phase angle means that the dependent function *lags* the reference function.

4.5 Tube Array Tuning

The experimental part of this research was conducted in three stages:

Table 4.2: Logarithmic decrement of the array tubes before and after tuning

Tube	(δ) *Before tuning*	(δ) *After tuning*
A	0.0211	0.0234
B	0.0114	0.0216
C	0.0154	0.0240
D	0.0124	0.0214
E	0.0077	0.0218
F	0.0081	0.0229
G	0.0224	0.0233
X	0.0195	0.0221
1	0.0173	0.0209
2	0.0147	0.0226
Mean	0.0150	0.0224
St. Deviation %	34	4.5

1. Tube array tuning, where the tube natural frequency and total damping are adjusted to essentially the same value for each tube. This was performed when fully flexible tube array was tested.

2. Stability behavior study, where the behavior of a single flexible tube in a rigid array is investigated and compared to the behavior of a fully flexible array.

3. Interstitial flow measurements, where the interaction between tube vibration and fluid perturbation is investigated.

Each tube in the array was tuned to the desired frequency using the tensioning mechanism. The tube free response to a given excitation was recorded and the natural frequency was obtained from the frequency spectrum. The tubes were tuned to a mean natural frequency of $19.8Hz$ with a standard deviation of less than $0.1Hz$.

The tube damping was adjusted using the damping devices installed for each tube. The tubes were given a certain displacement and the tube free response was analyzed to obtain the damping. The damping was calculated using the exponential

decay method, and an average of five runs for each tube was considered. The damping calculated using the exponential decay method was verified by comparison to the calculated damping using the half-power bandwidth method, and the calculated logarithmic decrement δ values agreed within 10%. A list of logarithmic decrement for the tubes before thinning and after tuning is shown in Table 4.2.

Chapter 5

Experimental and Numerical Results

This Chapter presents the experimental and numerical results of this research. In order to validate the approach of using a single flexible tube in a rigid array for the present study, the single flexible tube has to have essentially the same stability threshold as for the fully flexible array. Thus, the stability of a single flexible tube located at several tube row locations in a rigid array was investigated and compared to the stability behavior of the fully flexible tube array.

Once the approach of using a single flexible tube in a rigid array to study fluidelastic instability was validated for the present study, interstitial flow measurements were carried out and analyzed to investigate the interaction between tube vibrations and the associated flow perturbations. The effect of flow and structural parameters on the interaction between tube motion and fluid perturbation was investigated. A computational Fluid Dynamics (CFD) model was developed and validated to conduct parametric studies and to help understand the experimental trends.

5.1 Tube Array Stability Analysis

The general experimental procedure in this section consists of three steps:

1. The flow velocity is increased by increasing the wind tunnel fan speed incrementally until the desired flow velocity is reached. Then, the wind tunnel is held at the same flow velocity for about ($30s$) to reach steady state based on the differential pressure measurements of the upstream flow velocity.

2. Once the flow velocity is steady, simultaneous measurements from tube (1) and tube (2) are collected for ($65s$) while recording the upstream flow velocity every 10 seconds.

3. The flow velocity is increased to the next step and the procedure is repeated until the tube becomes fluidelastically unstable. At least two measurement points are taken in the post stability region to establish the post stability trend.

On-line analysis of the tube cross-stream response was carried out to establish a preliminary response curve, while a detailed analysis of the signals was carried out off-line due to the equipment memory limitations. Each experiment reported in this section was repeated at least four times to ensure the results repeatability.

5.1.1 Fully Flexible Tube Array

Experiments were conducted first on a fully flexible tube array to determine the fluidelastic stability threshold as the reference case. The effect of the monitored tube row location was investigated by removing the first row upstream, which moves the instrumented tubes 1 and 2 from the third and fifth rows to the second and fourth rows respectively. The purpose of locating the instrumented tube 1 in the second row

of the array was an attempt to obtain fluidelastic instability at a location that has low turbulence level and thus higher signal-to-noise ratio.

Two sets of experiments were conducted, one with the row of tube X removed and the other with tube X in place. The response of tube 1 in the second row is shown in Figure 5.1(a), while that for the same tube in the third row is shown in Figure 5.1(b). Over the range of mean gap velocity $U_g = 2 - 6m/s$, the RMS response of tube 1 in the second row Figure 5.1(a) is small, typically less than 0.2% of the tube diameter. The excitation mechanism in this region is turbulent buffeting, and the very small amplitudes can be attributed to the low turbulence level. At about $U_g = 6.6m/s$, the RMS vibration amplitude in the transverse direction suddenly increased to about 3.5% of the tube diameter and the tube is considered to have become fluidelastically unstable. At about $7.5m/s$, the RMS response of tube 1 dropped slightly while violent vibrations of the adjacent tubes in the array were observed and the experiment was terminated at $8.2m/s$.

A straight line drawn through response peaks in the frequency spectra which increase with flow velocity is shown in Figure 5.1(a). It is seen that the point of flow oscillation frequency coincidence with tube natural frequency occurs at a flow velocity of about $U_g = 4.6m/s$. Clearly, no tube resonant response is observed and the point of frequency coincidence is well removed from the fluidelastic stability threshold. Ziada and Oengoren (2000) reported extensive experiments for parallel triangular tube arrays and computed Strouhal numbers using the actual mean flow velocity in the minimum gap between tubes for this array geometry rather than the commonly used Equation 2.2. Based on continuity, the equation relating upstream velocity and minimum gap velocity for parallel triangular array is

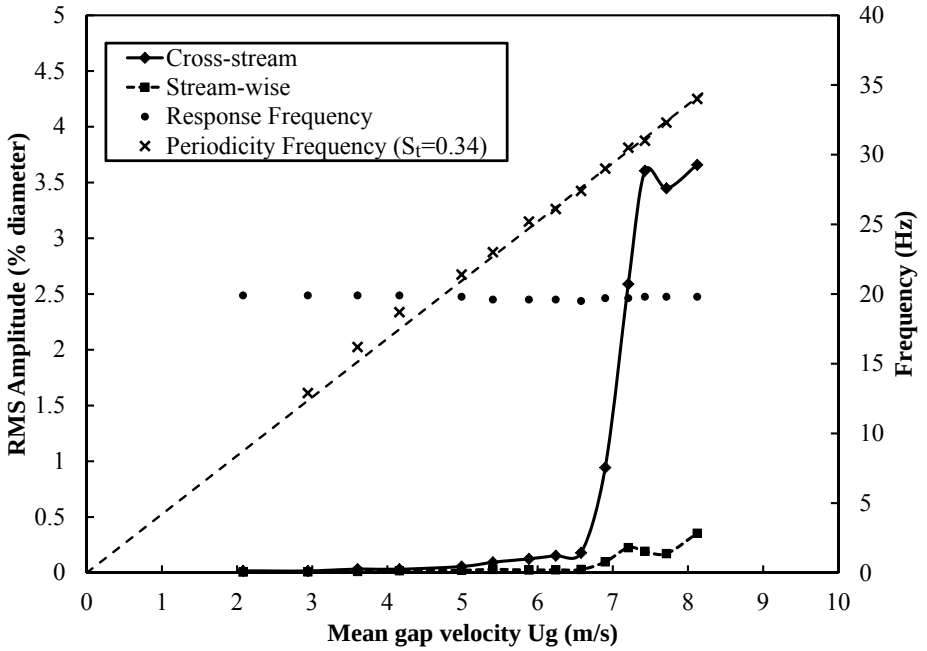

(a) Tube 1 located in the second row.

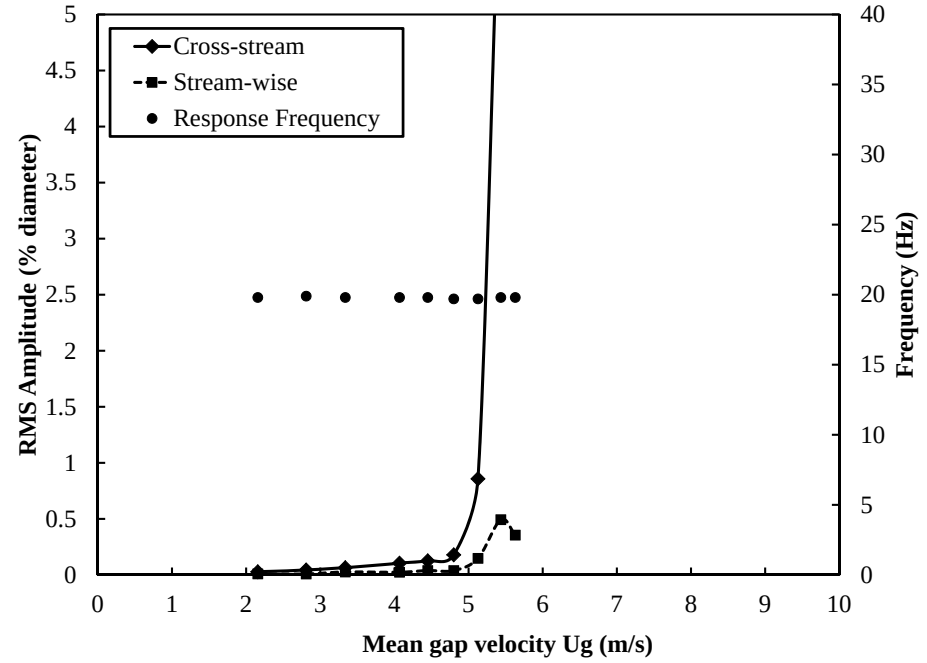

(b) Tube 1 located in the third row.

Figure 5.1: The response of tube 1 in a fully flexible parallel triangular array $P_r = 1.54$.

$$U_g = \frac{2P_r cos(\alpha)}{2P_r cos(\alpha) - 1} U_o. \tag{5.1}$$

The resulted value of $S_t = 0.34$ agrees reasonably well with the Strouhal number of $S_t = 0.32$ reported by Ziada and Oengoren (2000) for the same array pattern and pitch ratio.

The response pattern of tube 1 when it was in the third row is shown in Figure 5.1(b). In the range of mean gap velocity $U_g = 2 - 4.8m/s$, small vibration amplitudes are observed and caused by turbulent buffeting. At a mean gap velocity of about $U_g \approx 5.0m/s$, a sudden increase in the transverse RMS tube response took place, indicating that the tube has become fluidelastically unstable. A further increase in flow velocity produces RMS vibration amplitudes in excess of $15\%D$ and the experiment was terminated.

The response of tube 2 shows a similar behavior to tube 1 as seen in Figure 5.2. When tube 2 was located in the fourth row, it became unstable at about $6.6m/s$ and reached RMS amplitudes of about $4\%D$ as shown in Figure 5.2(a). Then, the amplitude dropped for velocities above $U_g = 7m/s$. For higher velocities, the tube tended to whirl, with large amplitudes in the stream-wise direction. When the first row upstream is placed back in position, tube 2 is in the fifth tube row and its response is shown in Figure 5.2(b). In this case the tube is observed to become fluidelastically unstable at about $U_g = 5.2m/s$. The experiments were repeated four times to determine the repeatability and it was found that the general behavior was similar in all cases, and the stability threshold was repeatable within 6%.

In summary, when the first row upstream is in place, tubes 1 and 2 are in the third and fifth rows respectively, the stability threshold is about $U_g \approx 5.2m/s$, and the post stability response is typical of that expected from previous experiments with

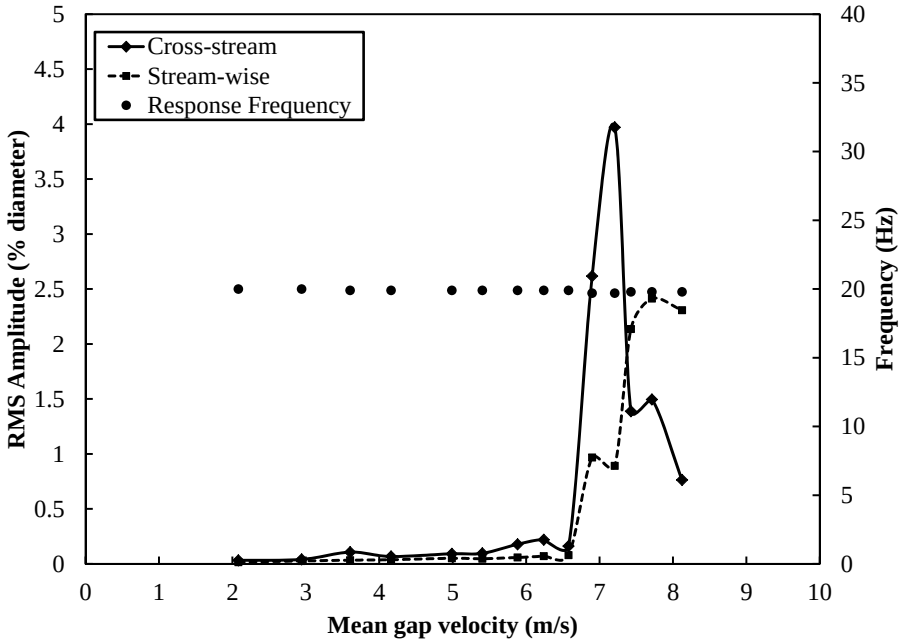

(a) Tube 2 located in the fourth row.

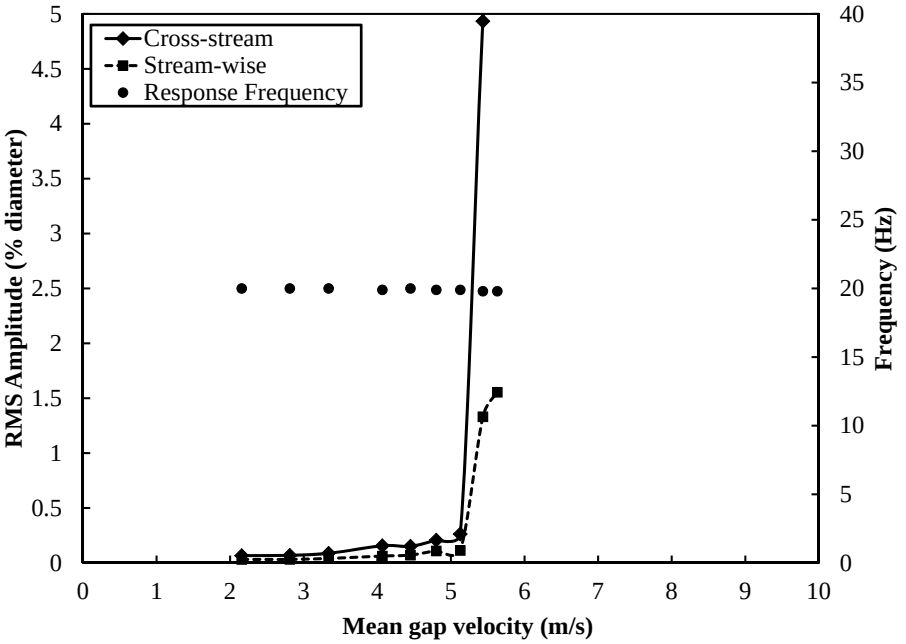

(b) Tube 2 located in the fifth row.

Figure 5.2: The response of tube 2 in a fully flexible parallel triangular array $P_r = 1.54$.

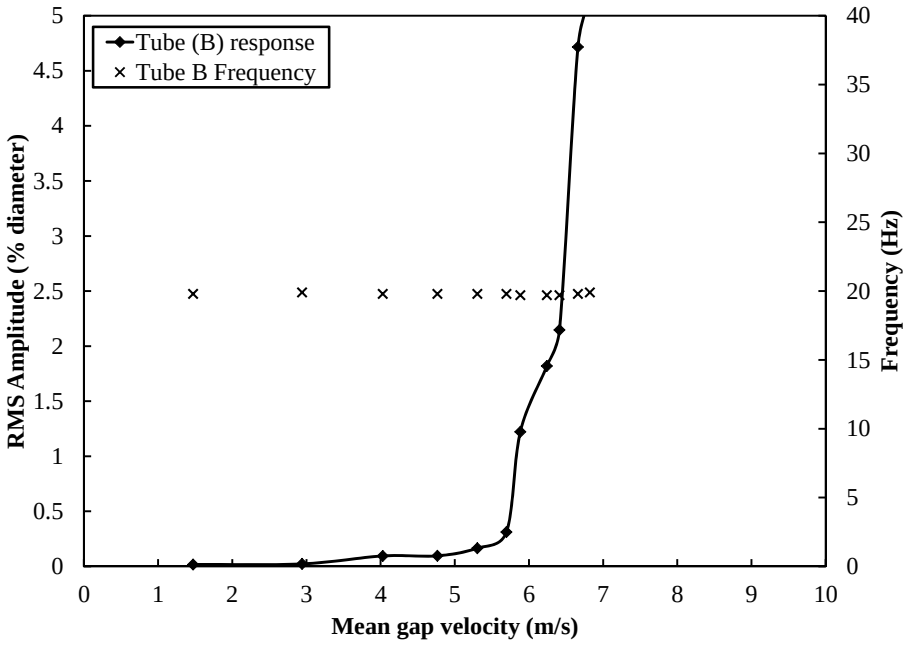

Figure 5.3: The response of tube B as located in the third row of a fully flexible array.

fully flexible arrays. When the first row is removed, tubes 1 and 2 become now in the second and fourth rows respectively, and the stability threshold is not only delayed to about $U_g \approx 6.6m/s$, but also the post stability response is limited and irregular. In other words, the same tube behaves differently depending on whether or not an upstream row is in place.

In order to understand better why the stability threshold for the same tube varies significantly based on its location in the array, the response of the other tubes in the array was monitored. It was found that when the first tube row upstream was removed, the tubes in the third row, either tube B or tube E as seen in Figure 4.2, always became fluidelastically unstable first followed by the rest of the array tubes. The response of tube B as located in the third row of a fully flexible array is shown in Figure 5.3 and is seen to become fluidelastically unstable at about $U_g \approx 5.8m/s$. This corresponds to the experiments where tubes 1 and 2 were located in the second and

fourth rows and became unstable at about $U_g \approx 6.6m/s$ as observed in Figure 5.1(a) and Figure 5.2(a) respectively. Thus, it appears that the third row tube becomes unstable to large amplitudes and then triggers instability in other tubes in the array.

When the first row is installed in place, such that tube 1 is in the third row, tube 1 became unstable at about $5.2m/s$ as observed in Figure 5.1(b). When the first tube row upstream is removed, the third row tube is located beside the wall which could explain the slightly delayed stability threshold observed in Figure 5.1(a) and Figure 5.2(a). In order to investigate this behavior further, the response of a single flexible tube was investigated at different locations in an otherwise rigid tube array.

5.1.2 A Single Flexible Tube in a Rigid Array

The same experimental procedure discussed in the previous section was adopted to carry out the experiments for studying the behavior of a single flexible tube in a rigid array. The purpose of these experiments was to determine the response of a single flexible tube at different locations in a rigid array. The response of tube 1 as a single flexible tube located in the second and third rows is shown in Figure 5.4(a) and Figure 5.4(b) respectively. When tube 1 was in the second row, no instability was observed up to a mean gap velocity of $U_g = 11m/s$ which is double the critical velocity found for the fully flexible array.

The response of the same tube located at the third row, by adding the upstream row of tube X, is completely different. Clear fluidelastic instability, primarily in the cross-flow direction, occurred at a mean gap velocity of about $U_g = 5.2m/s$ as shown in Figure 5.4(b). It seems that when tube 1 is the only flexible tube in the otherwise rigid array, it is stable when in the second row and unstable when it is in the third row. Furthermore, the stability threshold in the latter case is equal to the value of

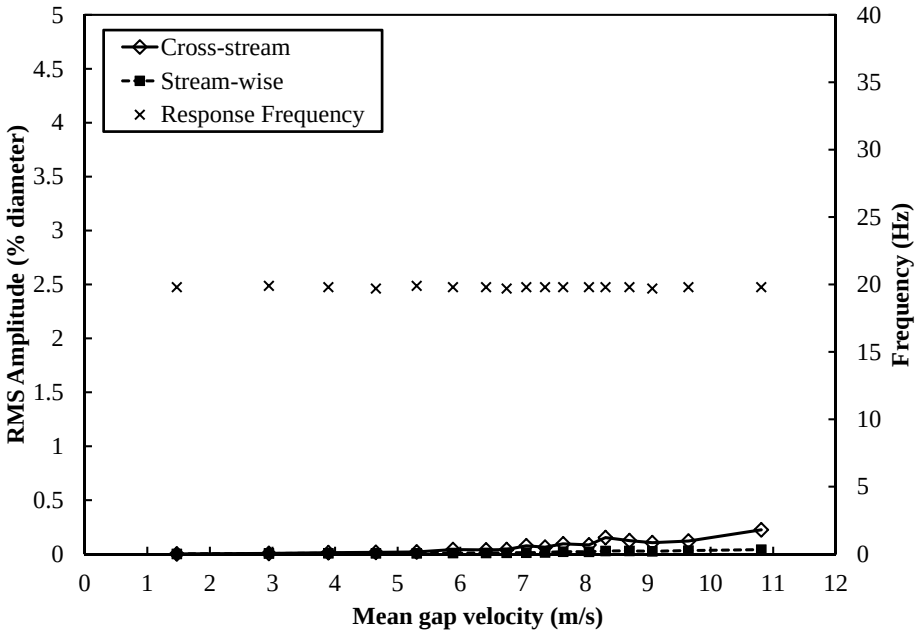

(a) Tube 1 located in the second row

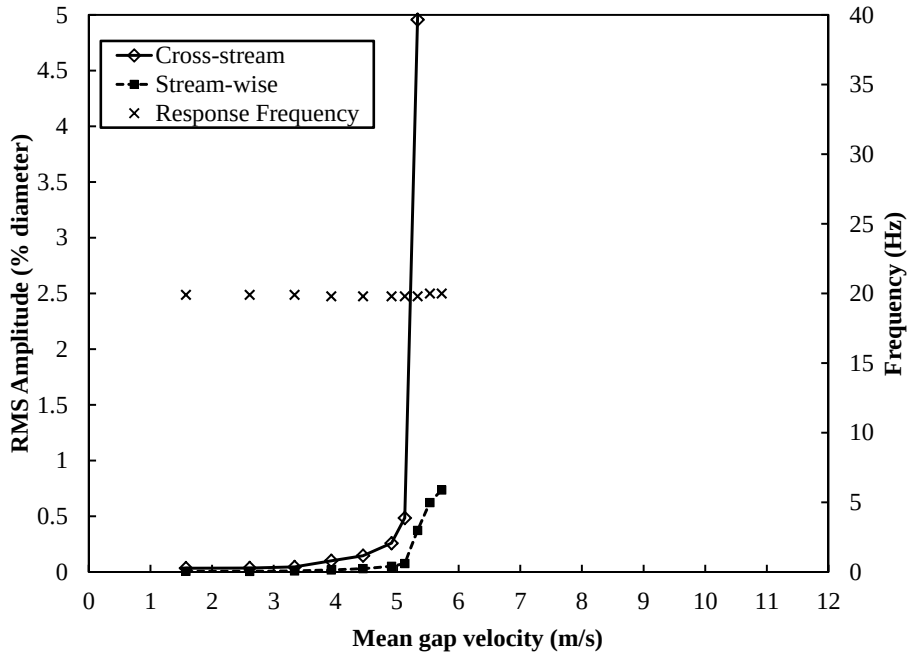

(b) Tube 1 located in the third row

Figure 5.4: The response of tube 1 as a single flexible tube in a rigid parallel triangular array $P_r = 1.54$.

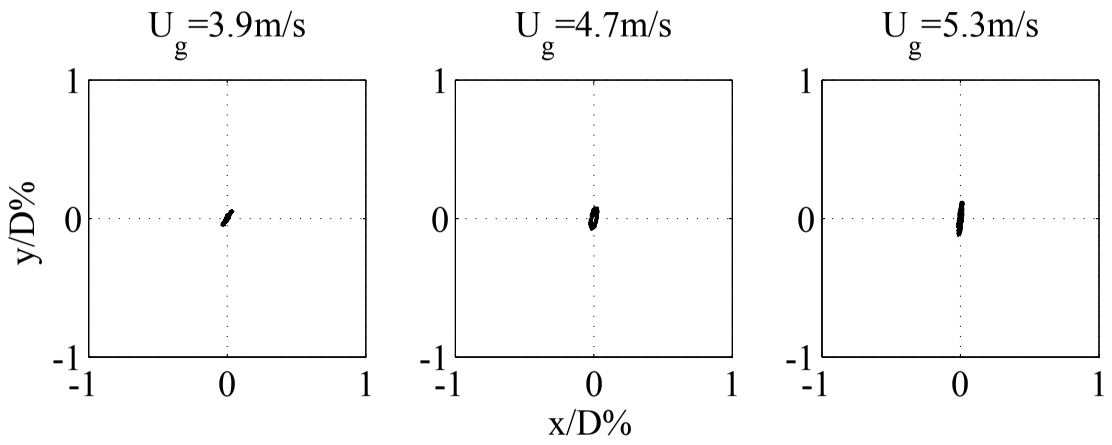

(a) Tube 1 located in the second row

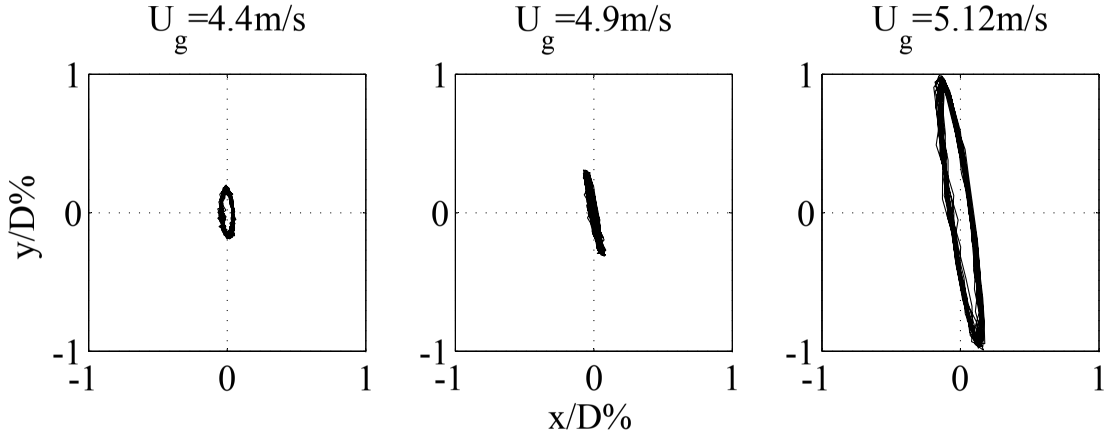

(b) Tube 1 located in the third row

Figure 5.5: Response pattern of tube 1 as a single flexible tube in a rigid parallel triangular array $P_r = 1.54$ at different mean gap velocities.

$5.2m/s$ found for the case of a fully flexible array.

The vibration patterns of tube 1 as a single flexible tube in a rigid array located at the second and third rows are shown in Figure 5.5. When tube 1 was in the second row, the RMS vibration amplitudes increased gradually with flow velocity but remained less than about $0.2\%D$. Interestingly, it does seem to oscillate primarily in the direction transverse to the flow. The response pattern of tube 1 located in the third row is shown in Figure 5.5(b) for several flow velocities. At $4.4m/s$, the small amplitude motions are due to turbulent buffeting. By a velocity of $5.1m/s$, the tube has become fluidelastically unstable predominantly in the transverse direction.

To ensure that this behavior was not tube specific, similar experiments were carried out with other tubes, varying the location of each tube by adding or removing the upstream tube row. For example, tube B and E, as seen in Figure 4.2, were studied as a single flexible tube located in the third row when the first row upstream was removed, and in the fourth row when the first row upstream was installed. The response of tube B in the third and fourth tube rows is shown in Figure 5.6. At a mean gap velocity of about $5m/s$, tube B became fluidelastically unstable when in the third row as shown in Figure 5.6(a). This is about the same critical velocity as found for tube 1 when it was in the third row. The change of slope of the post stable RMS amplitude response around $6m/s$ may be attributable to wall confinement effects as this tube is adjacent to the half tubes on the test section wall.

When the first row upstream is installed, tube B is now in the fourth tube row and shows quite different behavior. While the RMS amplitude rises to about $1\%D$ in the transverse direction near $8m/s$, no clear fluidelastic instability is observed up to a mean gap velocity of $12m/s$. These amplitudes are well above the buffeting amplitudes observed for this array and suggest that some fluidelastic forces exist but are unable to overcome the system damping to produce large amplitude instability.

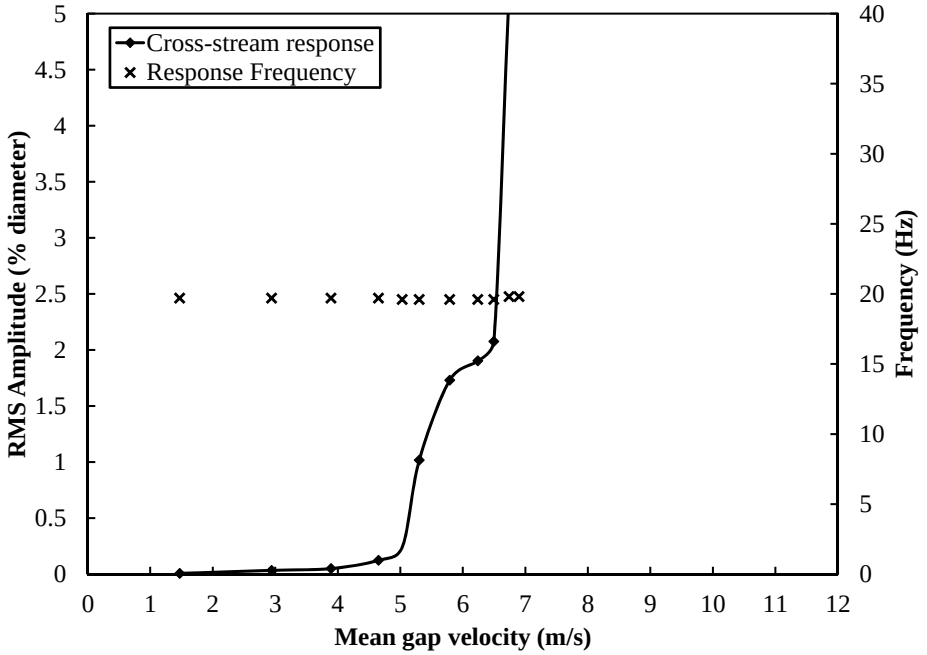

(a) Tube B located in the third row

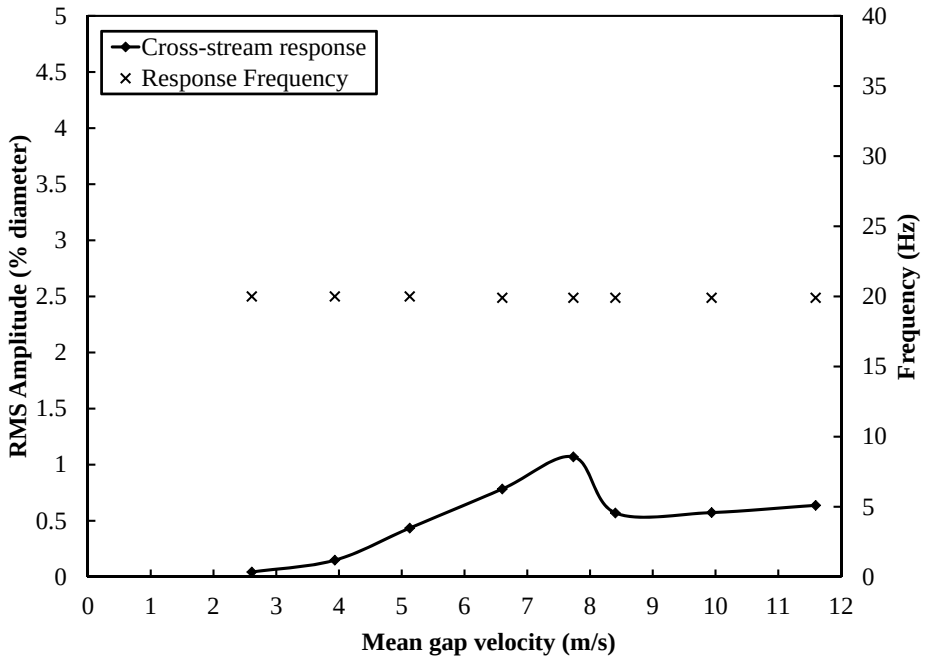

(b) Tube B located in the fourth row

Figure 5.6: The response of tube B as a single flexible tube in a rigid parallel triangular array $P_r = 1.54$.

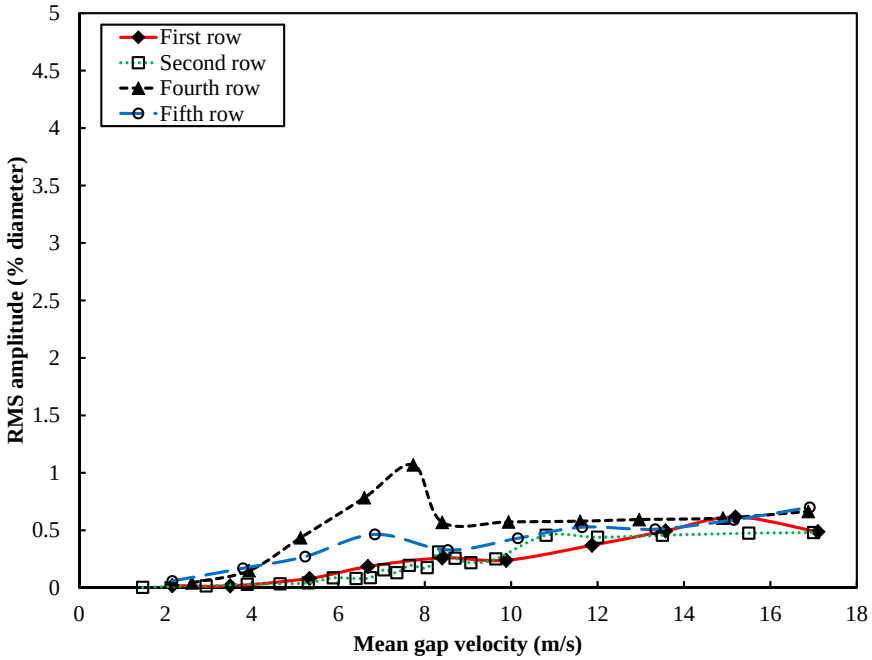

Figure 5.7: The vibration response of a single flexible tube located at different positions in a rigid parallel triangular array $P_r = 1.54$.

Similar experiments were conducted on a single flexible tube located in the first, second, fourth, and fifth tube rows and similar trends were observed. Relatively small response amplitudes were detected in all cases up to a mean gap velocity of $U_g = 17m/s$. Changing the location of the single flexible tube in the array did not significantly affect its response behavior unless it is located at the third row. The responses of a single flexible tube located at the first, second, fourth, and fifth rows of the array are shown in Figure 5.7. These experiments imply that, at least for this array pattern and pitch ratio, a single flexible tube in a rigid array only develops large amplitude fluidelastic instability if it is located in the third tube row.

5.1.3 Effect of Restraining the Third row tube in flexible array

It is clear that a single flexible tube in a rigid array can only become fluidelastically unstable through the negative damping mechanism. The present experiments have shown that, at least for the particular array pattern and pitch ratio under consideration, a single flexible tube in a rigid array can only become unstable to large amplitudes if it is located in the third tube row. This suggests that third row tubes may have a dominant role in the fluidelastic mechanism for these arrays. To examine this idea further, another experiment was carried out in which a third row tube in a flexible array was restrained.

The fully flexible tube array was subjected to a cross flow velocity of $U_g = 7m/s$, which is above the critical flow velocity. Then, while the tubes were oscillating at significant amplitudes, the third row tube was suddenly held rigid and the responses of other tubes were monitored. The cross-stream RMS response of tubes 1 and 2 are plotted against time in Figure 5.8. While tube 1 in the third row was oscillating at an RMS amplitude of about $5\%D$, it was suddenly stopped at about $t = 3sec.$ as in Figure 5.8(a). This results in tube 2 becoming stabilized within about 7 seconds as in Figure 5.8(b), although a small amplitude modulated response is still observed.

Figure 5.9 shows the behavior when tube 1 is released from rest at about $t = 1sec.$ After about 5 seconds its amplitude begins to grow, and within 22 seconds, large unstable amplitudes have developed as shown in Figure 5.9(a). Moreover, the other tubes in the array also become fluidelastically unstable with amplitude modulations typical of fluidelastic instability in tube bundles. In the case of tube 2, as seen in Figure 5.9(b), the response amplitude modulations are associated with change in relative tube motion.

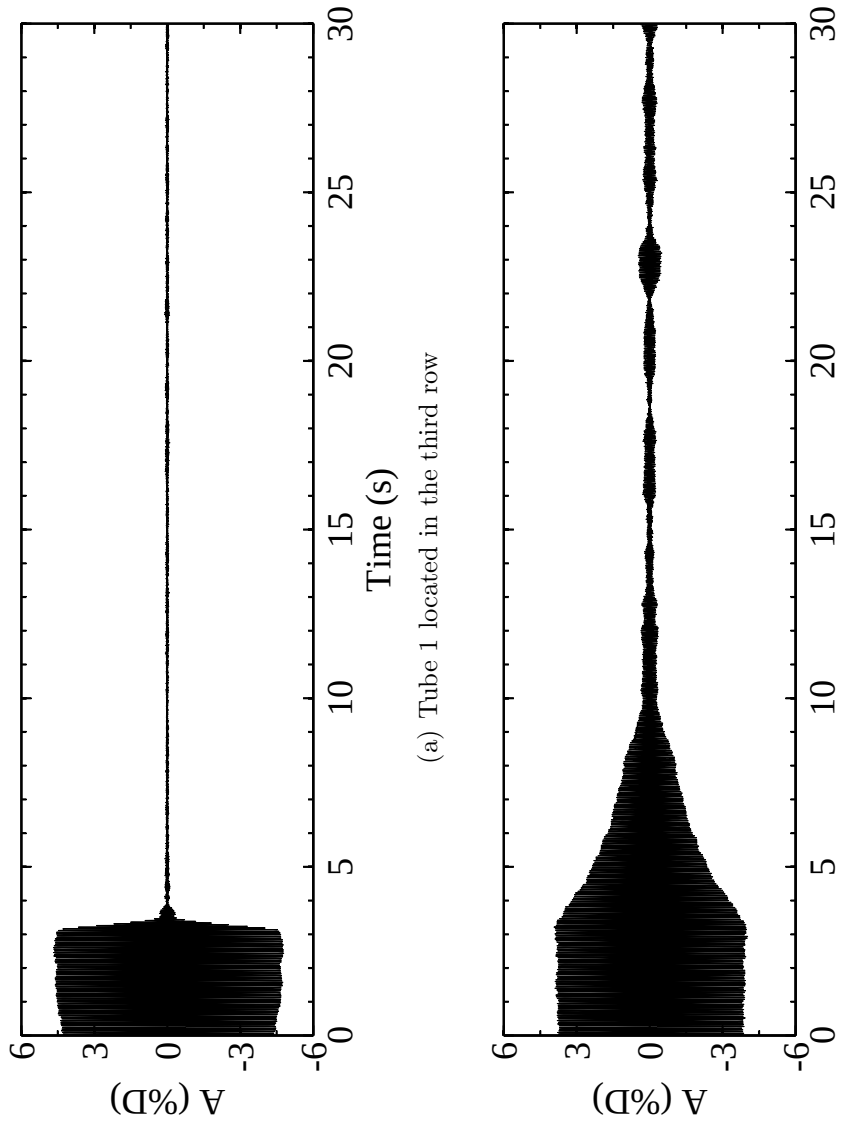

(a) Tube 1 located in the third row

(b) Tube 2 located in the fifth row

Figure 5.8: The effect of holding the third row tube rigid during instability onset of a fully flexible parallel triangular array $P_r = 1.54$ array at $U_g = 7m/s$.

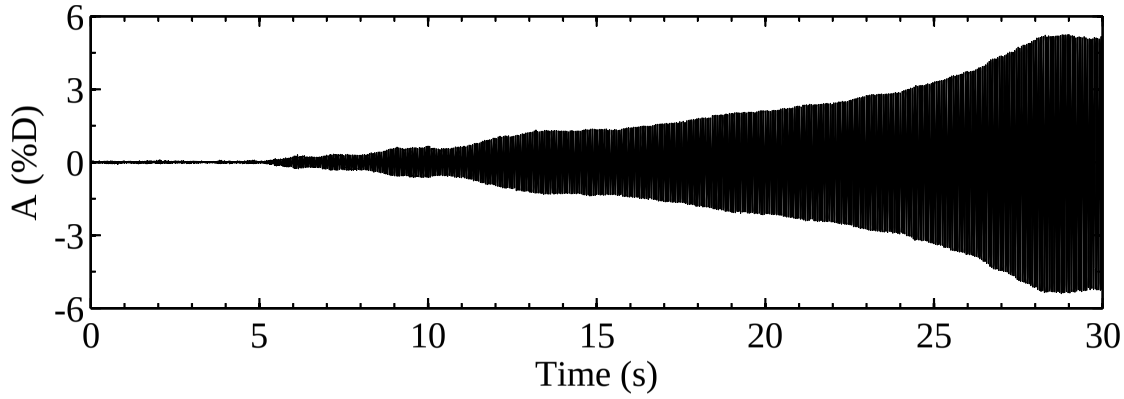

(a) Tube 1 located in the third row

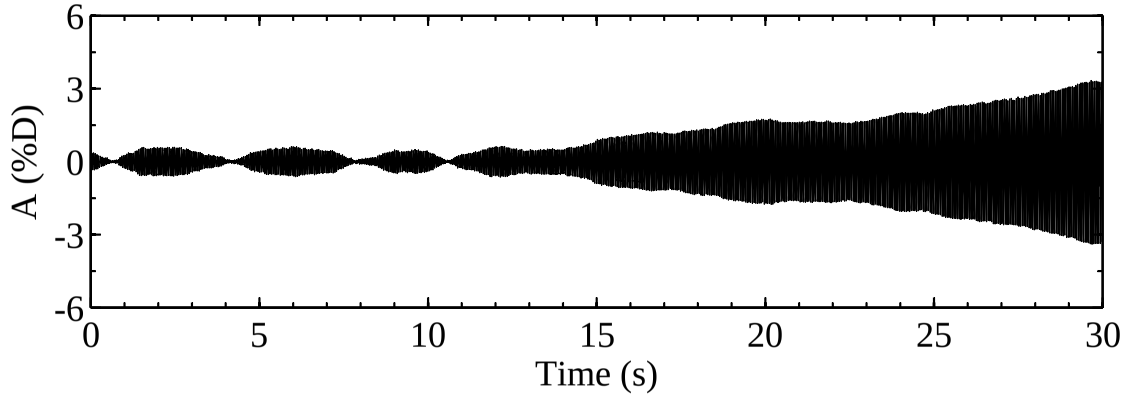

(b) Tube 2 located in the fifth row

Figure 5.9: The effect of releasing the third row tube during instability onset of a fully flexible parallel triangular array $P_r = 1.54$ array at $U_g = 7m/s$.

In summary, a single flexible tube in a rigid array only became fluidelastically unstable if it was located in the third row of the array. By monitoring the same tube and changing its location in the array, the effect of tube-to-tube variability was removed and the observed effect on stability can only be attributed to tube row location. Furthermore, as seen in Figure 5.10, the stability threshold for tube 1 in the third row of a rigid array is essentially the same as that for tube 1 in the third row of the fully flexible array. These results support the observation made while testing a fully flexible array that the instability seems to develop in the third row of tubes first and then propagates through the array.

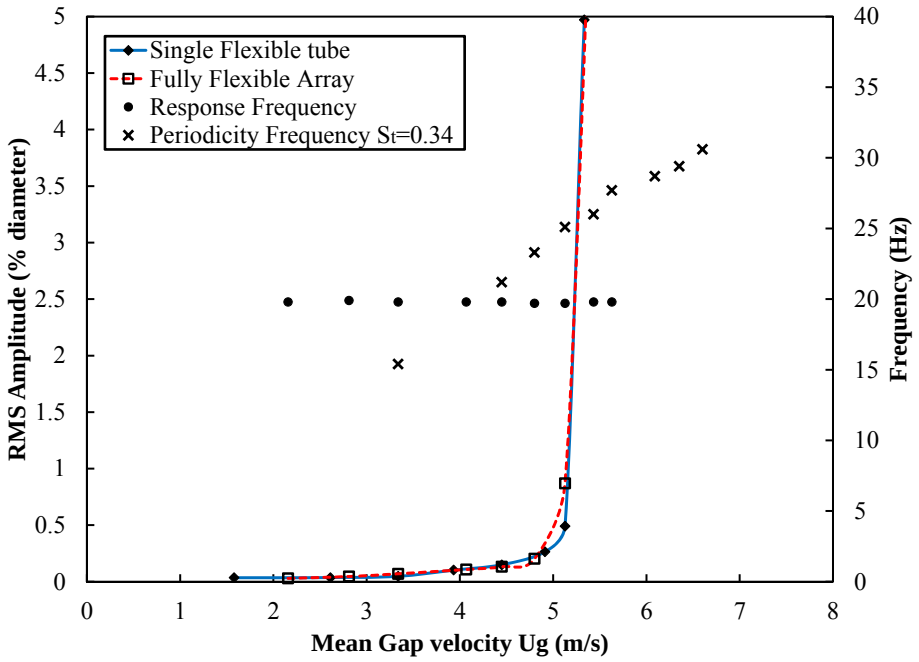

Figure 5.10: The stability behavior of tube 1 located in the third row of both single flexible tube and fully flexible cases for parallel triangular array $P_r = 1.54$.

A similar behavior was reported by Austermann and Popp (1995) when studying a parallel triangular array with a pitch ratio of 1.25. They found that a single flexible tube did not become fluidelastically unstable when located at the second, third, or fourth row of a rigid array. However, when located at the first row of the

rigid array, it became unstable. The same study showed that for a parallel triangular array with pitch ratio 1.375, a single flexible tube located at the first, second, third, or fourth row of a rigid array became fluidelastically unstable. They also determined experimentally that the least stable tube was the third row tube, which agrees with the observations of Lever and Weaver (1986b) for a pitch ratio of 1.375. Thus, it appears that the stability of a single flexible tube in a rigid array is not only dependent on the array geometry, pitch ratio, and mass ratio, but is also dependent on the tube row location in the array.

5.1.4 Discussion

The results reported in this section showed that a single flexible tube in a rigid parallel triangular array of tubes with a pitch ratio of 1.54 can only become fluidelastically unstable if it is located in the third tube row. It was also found that a third row tube in a fully flexible array is the least stable and, when it becomes unstable, it appears to trigger the instability of the other tubes.

This result suggests that, at least for this particular array geometry, fluid coupling of adjacent tube motion *"stiffness mechanism"* is an essential component of the fluidelastic mechanism except for the third row tubes which can become unstable by the damping mechanism alone. Thus, the relative importance of the damping and stiffness mechanisms of fluidelastic instability depend not only on array geometry, pitch ratio, and mass ratio, but also on tube location in the array.

When the third tube row in the present tube array was tested as a single flexible tube it became unstable at essentially the same stability threshold for the dully flexible tube array. It follows that, the dominant mechanism causing the fully flexible tube array to become fluidelastically unstable is the same mechanism casing this tube

to become unstable. Thus, the third row tube was considered for investigating the interaction between tube motion and flow perturbation.

5.2 Tube Surface Pressure Measurements

Fluid forces were obtained using the two flush-mounted pressure transducers inside each of tubes 1 and 2. The signals collected from the pressure transducers were vibration compensated using the accelerometers signals, and were calibrated to obtain the pressure on both sides of the tube. The summation of pressures on tube surface was anticipated to provide the fluctuation pattern of the fluid forces, which is the concern of this study. However, such measurement cannot provide the fluid force amplitudes since this would require integration of the dynamic pressure measured around the tube circumference. Fluid forces measurements were conducted at several tube row locations in both fully flexible array as well as a single flexible tube in a rigid array.

5.2.1 Fully Flexible Array

The relative phase between tube vibrations and fluid forces was measured at the second and third tube row locations in a fully flexible array. The phase between tube motion and fluid forces acting on tube (1) in the second row is shown in Figure 5.11(a) and the tube response is shown in Figure 5.11(b).

A relatively small tube response amplitude, typically $< 0.5\%D$, was observed over the range of mean gap velocity $U_g = 1.5 - 4.8m/s$. While a lower turbulence level was expected at the second tube row, the coherence over this range of mean gap velocity was less than 0.5. Thus, the phase measurements for $U_g < 4.8$ were considered unreliable in this case. As the mean gap velocity increased above $U_g = 4.8m/s$, there

was a sudden increase in the coherence to values about 0.9, which was associated with the increase in tube vibration amplitude. Over the range of mean gap velocity $U_g = 4.8 - 8.2m/s$, the phase angle between fluid forces and tube vibrations increased gradually in the positive direction indicating gradual increase in the phase lag to a value of about $\phi = 75°$ at $U_g = 8.2m/s$. The increasing trend of phase lag was not affected by the fluidelastic stability threshold at about $U_g = 6.4m/s$.

The phase between tube motion and fluid forces acting on tube (1) in the third row of a fully flexible array is shown in Figure 5.12(a) and the tube response is shown in Figure 5.12(b). The general phase trend was similar to that observed for tube (1) when located in the second row of the array. However, when tube (1) is located in the third tube row, better coherence was measured at lower mean gap velocities, $U_g = 2.1 - 4.8m/s$. The phase value increased gradually to a value of about $\phi = 48°$ at a mean gap velocity of $U_g = 6.9m/s$.

5.2.2 Single Flexible Tube in a Rigid Array

The same experimental procedure discussed in the previous section was adopted to investigate the fluid forces acting on a single flexible tube located in the second and third tube rows of a rigid array. The phase lag between tube motion and fluid forces acting on a single flexible tube located in the second row of a rigid array is shown in Figure 5.13(a). It was observed that the phase lag values were generally less than 10° and no apparent trend was detected. The lack of any definable trend in this case was attributed to the absence of any significant tube vibrations as shown in Figure 5.13(b)

When the single flexible tube was located in the third row of a rigid array, the phase trend changed significantly as shown in Figure 5.14(a). The phase lag was

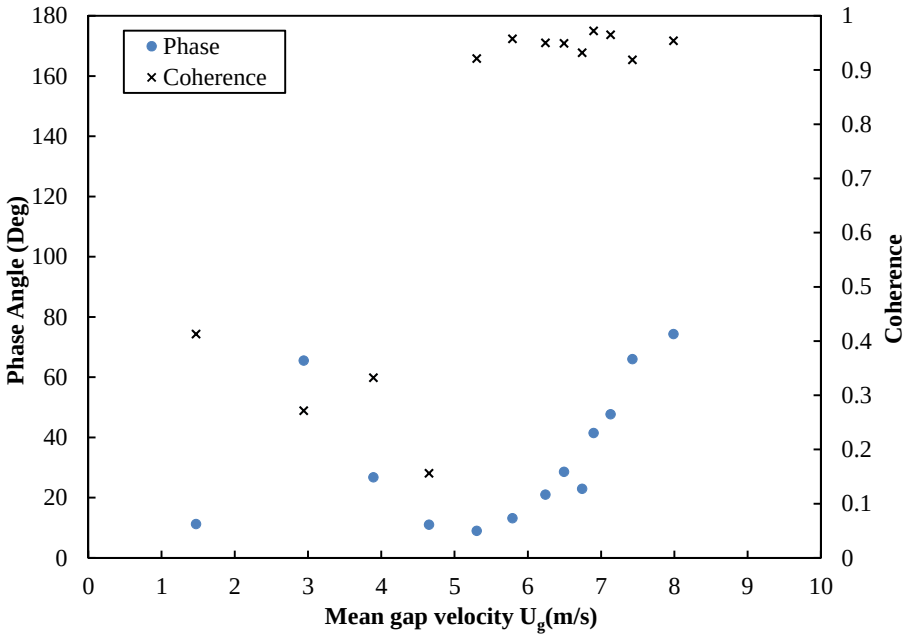

(a) Phase and Coherence.

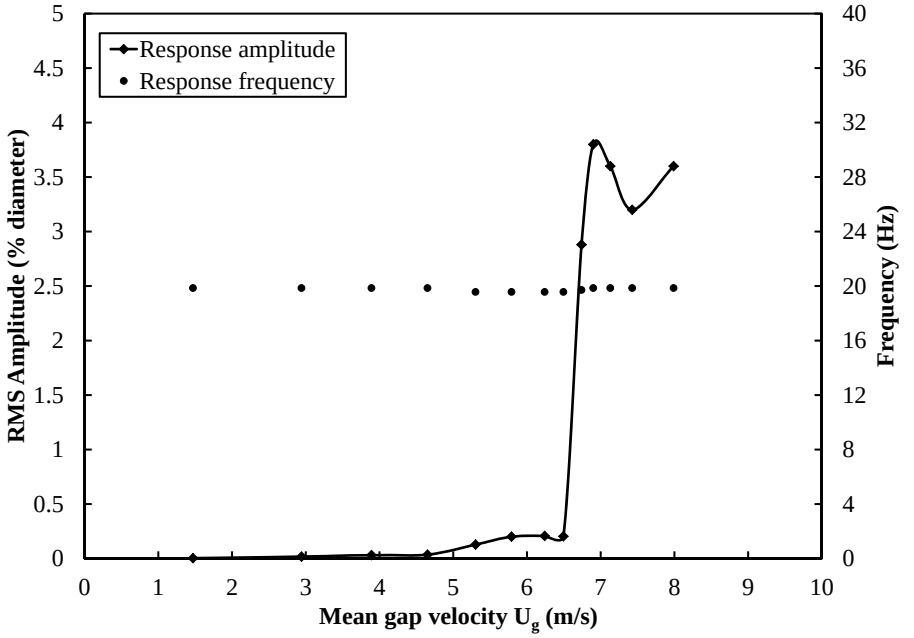

(b) Response amplitude and frequency.

Figure 5.11: The phase lag between tube motion and fluid forces acting on tube (1) when located in the second row of a fully flexible array.

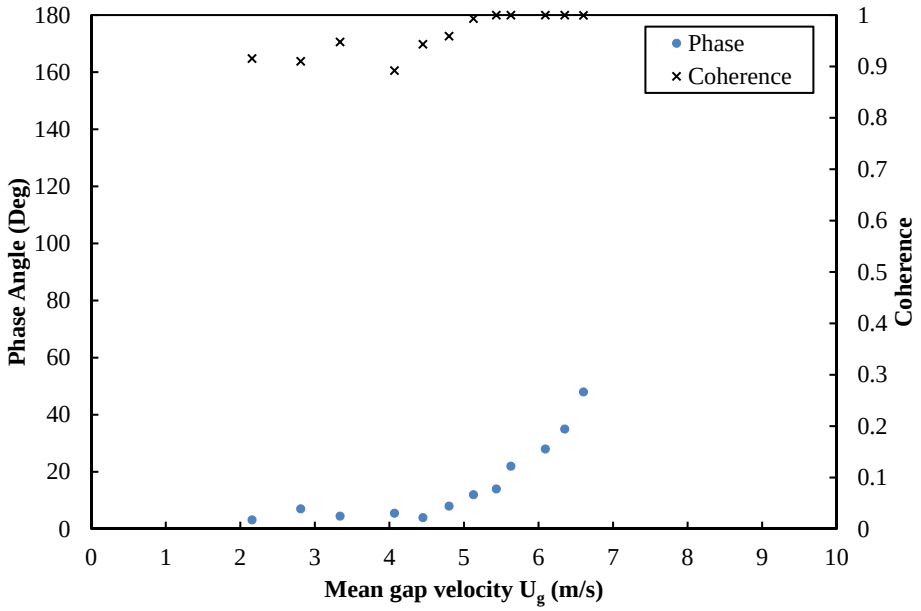

(a) Phase and Coherence.

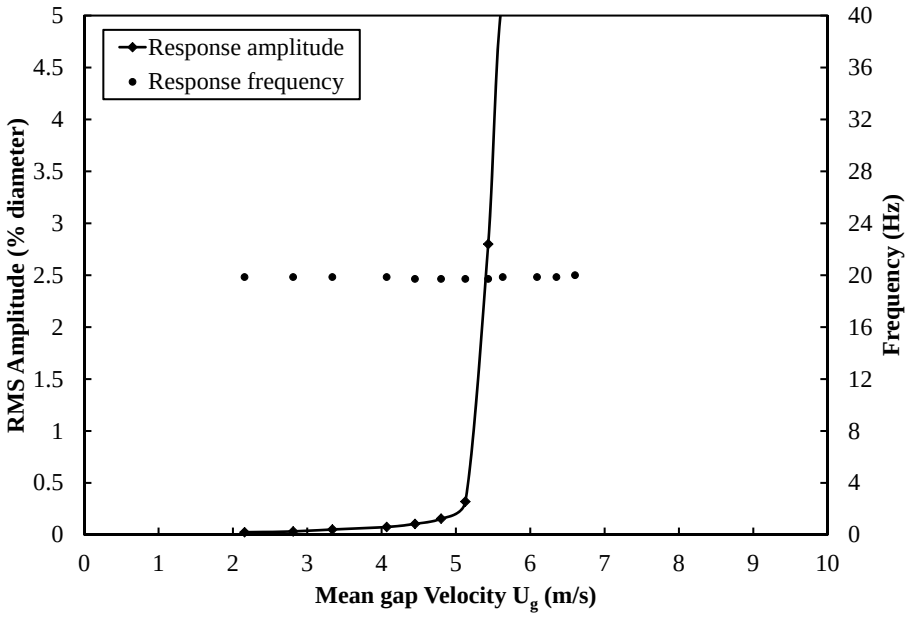

(b) Response amplitude and frequency.

Figure 5.12: The phase lag between tube motion and fluid forces acting on tube (1) when located in the third row of a fully flexible array.

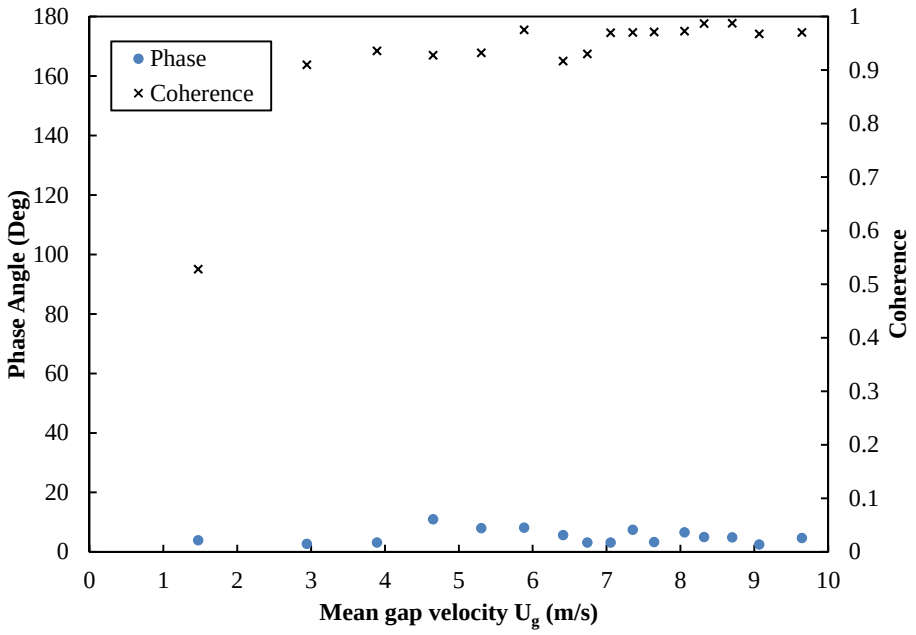

(a) Phase and Coherence.

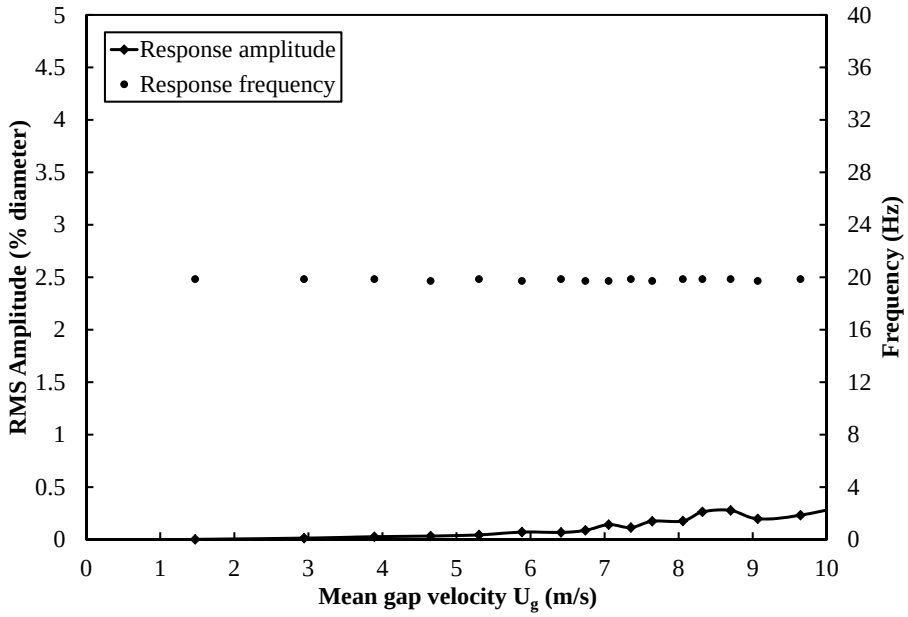

(b) Response amplitude and frequency.

Figure 5.13: The phase lag between tube motion and fluid forces acting on tube (1) when located in the second row of a rigid array.

observed to be relatively constant over the mean gap velocity range $U_g = 1.5-4.0m/s$ which was associated with a relatively high coherence, typically > 0.7. At a mean gap velocity of about $U_g = 5.1m/s$ a sudden change in the rate of phase lag increase took place associated with fluidelastic instability of the tube response as shown in Figure 5.14(b). The phase lag reached a maximum value of about $\phi = 86°$ at a mean gap velocity $U_g = 5.9m/s$ where the experiment was terminated due to the large tube oscillation amplitudes.

5.2.3 Discussion

Comparison of the fluid force phase measurements from a single flexible tube in a rigid array and those from a fully flexible array are quite revealing. It seems that a gradual increase in the phase lag between fluid forces and tube motion is associated with the correlation of flow field around the tube leading to fluidelastic instability. The single flexible tube located in the second row of a rigid array did not experience fluidelastic instability, and in this case no clear phase trend between fluid forces and tube motion was detected. Rather, relatively small phase lag values, $< 10°$, were observed in that case.

The delay time between tube motion and induced fluid forces can be scaled with the vibration frequency to produce the phase (ϕ), and can be scaled as well with the mean gap velocity and tube diameter to produce scaled time (τ^*) as follow:

$$\tau^* = \frac{\tau U_g}{D} \tag{5.2}$$

The scaled-times τ^* for the cases where fluidelastic instability took place are shown in Figure 5.15. The scaled times seem to follow the same trend in all three examined cases indicating that the same interaction mechanism between tube motion

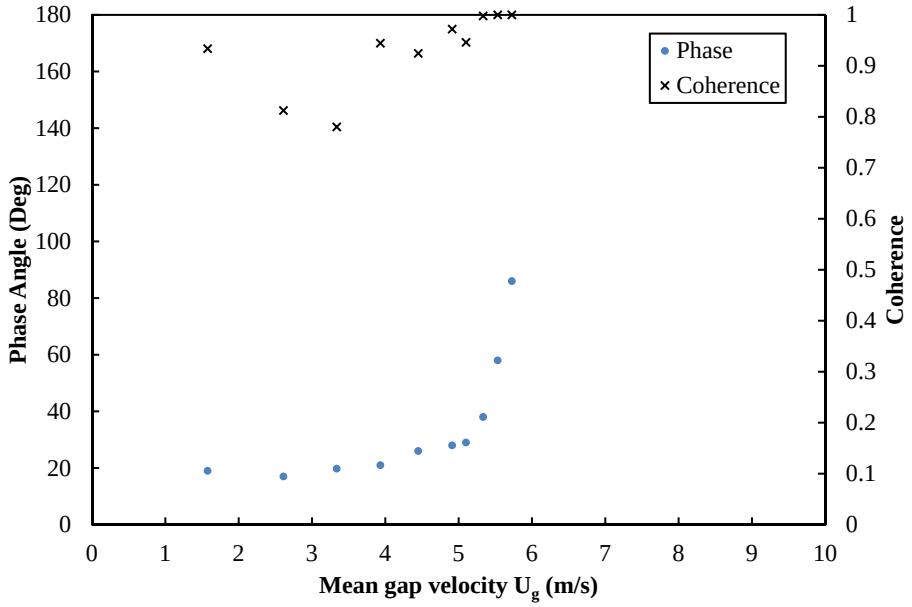

(a) Phase and Coherence.

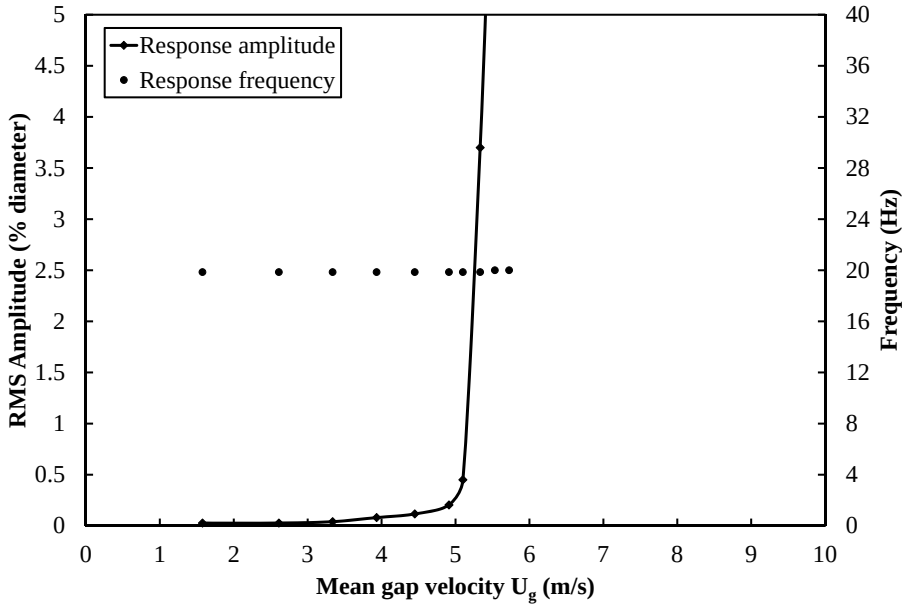

(b) Response amplitude and frequency.

Figure 5.14: The phase lag between tube motion and fluid forces acting on tube (1) when located in the third row of a rigid array.

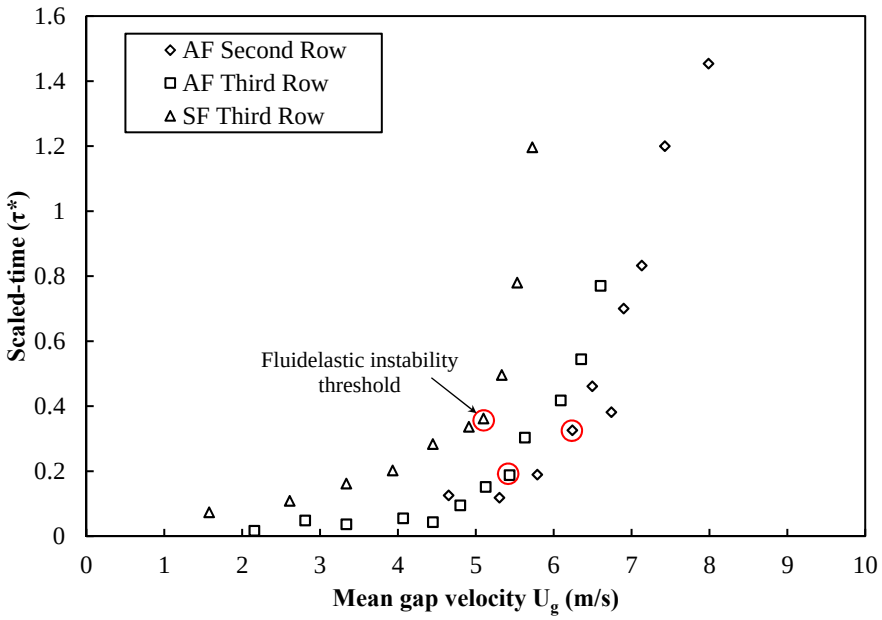

Figure 5.15: The scaled time between tube motion and induced fluid forces on tube (1).

and fluid forces is dominant in all cases. The points of fluidelastic instability threshold are marked with red circles in Figure 5.15, and these points correspond to scaled-times of *(0.35, 0.34, and 0.18)*. These values agree reasonably reasonably with the scaled time measurements of (0.3) reported by Mahon and Meskell (2010a).

5.3 Flow Perturbation Amplitude

This section presents experiments conducted to measure the amplitude of flow perturbations related to tube vibrations along the flow channel in the array. The experiments were conducted using a single flexible tube located in the third row of a rigid array. A hot-wire probe was positioned along the flow channel as shown in Figure 5.16 to monitor the flow. The locations of measurements and flow channel shape were selected based on the flow visualizations of Scott (1987) which are shown in Figure 3.13.

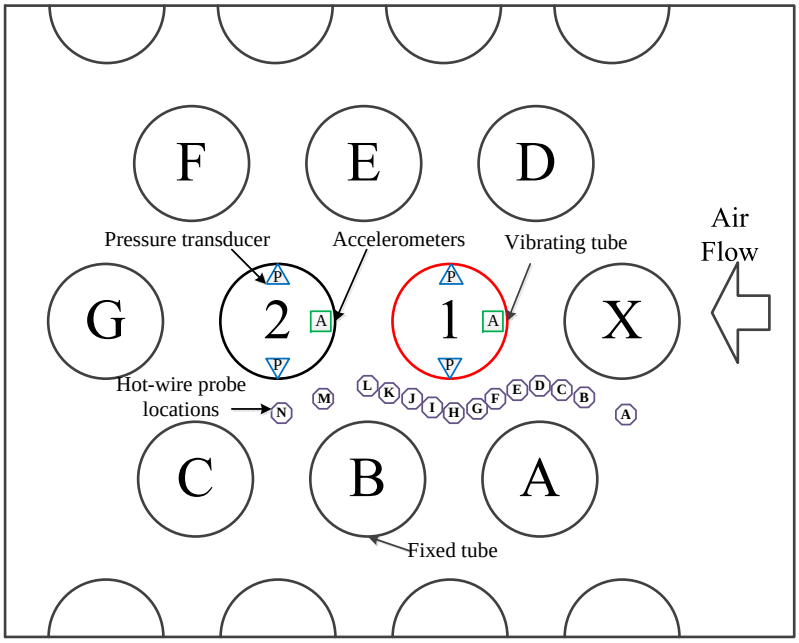

Figure 5.16: Locations of hot-wire measurements along an assumed flow channel

The wind tunnel flow velocity was increased incrementally to the desired value and left for about ($30s$) to reach a steady-state. Then, the hot-wire probe was traversed through all location to collect measurements. The flow velocity was increased incrementally and the procedure was repeated until the tube became fluidelastically unstable. The hot-wire time signal was used to obtain the mean flow velocity and turbulence level at each location as shown in Figure 5.17(a), while the averaged frequency spectrum of the hot-wire measurements was used to measure the flow perturbation amplitude as shown in Figure 5.17(b). The spectra used were the results of 50 sample averages and the velocity perturbation component is the RMS amplitude of such a spectrum at the tube natural frequency.

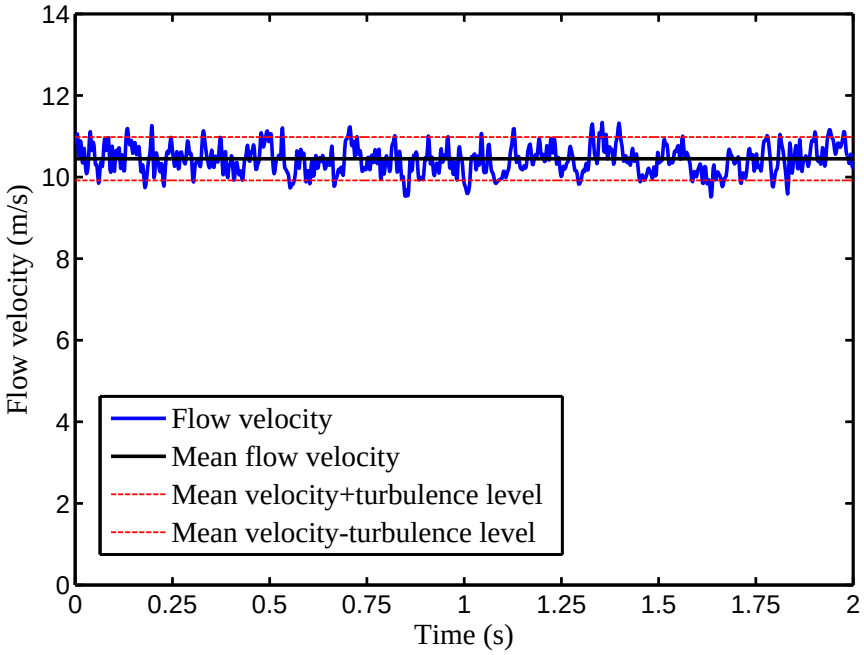

(a) Hot-wire time signal.

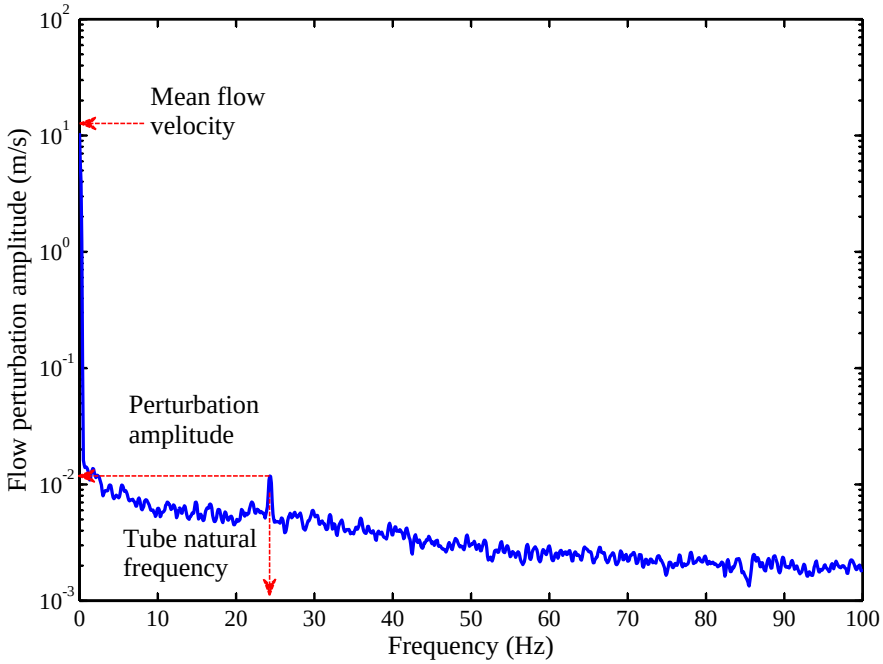

(b) Corresponding frequency spectrum.

Figure 5.17: Hot-wire measurements signal at point (H), tube vibration amplitude 1%D.

5.3.1 Tube Vibrations Amplitude Effect

The amplitudes of flow perturbations caused by tube vibrations along a flow channel are shown in Figure 5.18(a) for tube vibration amplitudes of *0.5%D, 1%D, and 5%D*. These three amplitudes were selected to present the typical tube response due to turbulent buffeting *0.5%D*, the tube response just prior to instability *1%D*, and the tube response just after instability *5%D*. The locations of measurements are presented using the curvilinear coordinate (s) which follows the sinuous flow path along the stream channel centerline and takes a value of zero at the transverse line through the center of the vibrating tube. The coordinate (s) positive direction is downstream from the tube while the negative direction is upstream. The location index (s^*) shown in Figure 5.18(b) is the measurement coordinate (s) scaled with the tube diameter (D).

It is observed that the flow perturbations followed the same general trend, and the flow perturbation amplitudes are proportional to the tube vibration amplitude. The flow perturbation amplitudes increased gradually as the hot-wire probe approached the vibrating tube in the third row. The minimum flow perturbation amplitude was detected at point *(A)* which is two tube rows upstream of the vibrating tube. This finding agrees with the findings of Tanaka and Takahara (1981) which showed that the effects of tube vibrations were dissipated by about two tube rows away.

A local maximum of the perturbation amplitude was detected at point *(F)* in all three cases, and this peak is associated with the flow attachment point on the vibrating tube. The flow visualizations by Scott (1987) showed that, for a parallel triangular array, the flow attaches at an angle $\beta_a \approx 40^\circ$ and separates at an angle $\beta_s \approx 40^\circ$ as shown in Figure 5.18(b). The maximum perturbation amplitude was detected at point *(K)*, and this peak is associated with the flow separation from

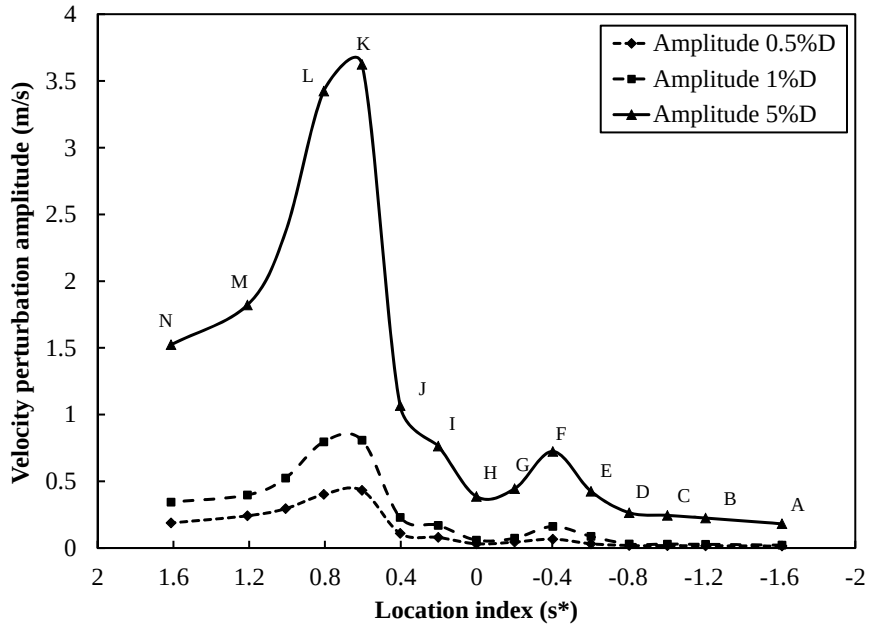

(a) Flow perturbation velocity.

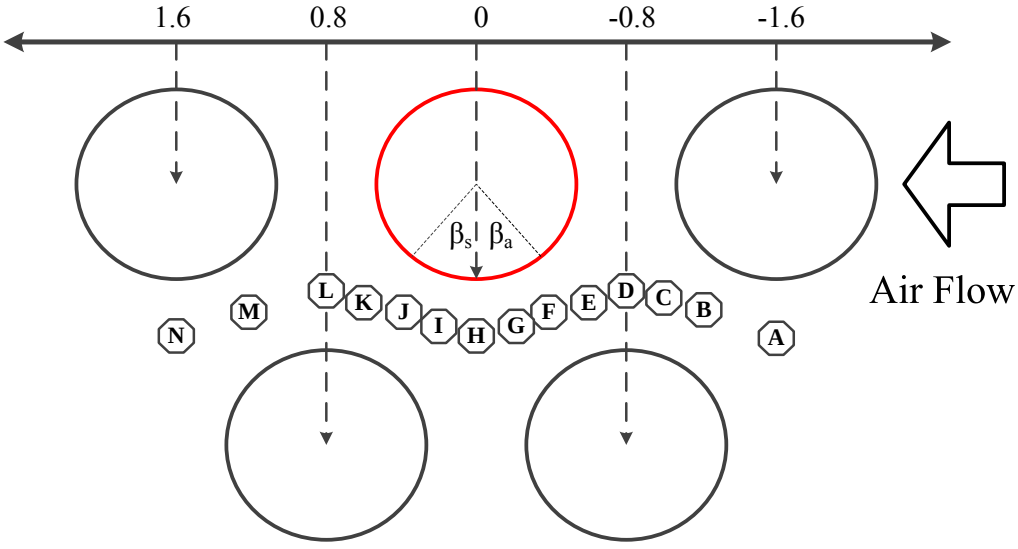

(b) Location index scheme.

Figure 5.18: Flow velocity perturbation amplitude along flow channel.

the tube. The perturbation amplitude was dissipated quickly as the measurements proceeded downstream as shown in Figure 5.18(a). Over this region, the vorticity generated by a tube will impinge on the next tube downstream and be stretched out and dissipated as it passes the tube.

5.3.2 Scaling and Data Analysis

In order to verify that the perturbation amplitude peaks were associated with flow attachment and separation from the vibrating tube, the hot-wire probe was traversed along the flow channel but closer to the tubes. The amplitudes of flow perturbations caused by a tube vibrations amplitude of $1\%D$ is shown in Figure 5.19(a), and the locations of measurements are shown in Figure 5.19(b). It was observed that the flow perturbation amplitudes followed the same trend shown in Figure 5.18(a), and the peaks at points *(E)* and *(I)* aligned well with the flow attachment and separation points on the vibrating tube respectively.

The flow perturbation amplitude was scaled using the tube velocity and a good collapse of the data is achieved as shown in Figure 5.20. The amplitude trends show a maximum value near the separation point indicating that the source of flow perturbation is not directly the tube vibrations, but rather the flow separation from the tube. The same rate of decay in perturbation amplitude is observed for the three investigated cases. The upstream amplitude decay rate is reasonably represented using a function of the form

$$\psi(s^*) = \frac{a}{s^* + b} \tag{5.3}$$

where $\psi(s^*)$ is the amplitude decay function upstream of the separation point, and (a) and (b) are constants determined using two boundary conditions. First, the

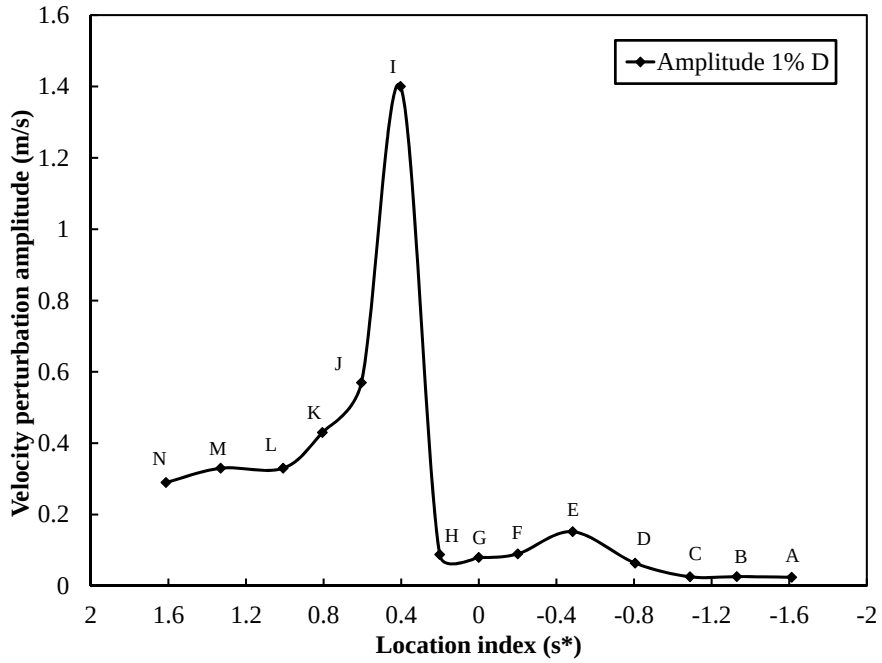

(a) Flow perturbation velocity.

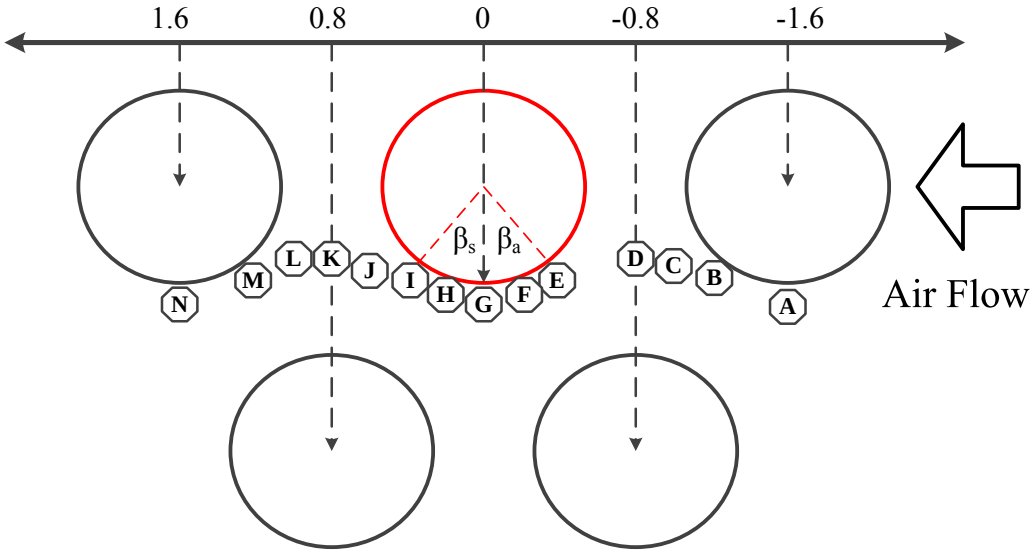

(b) Location index scheme.

Figure 5.19: Flow velocity perturbation amplitude along flow channel and near the tubes.

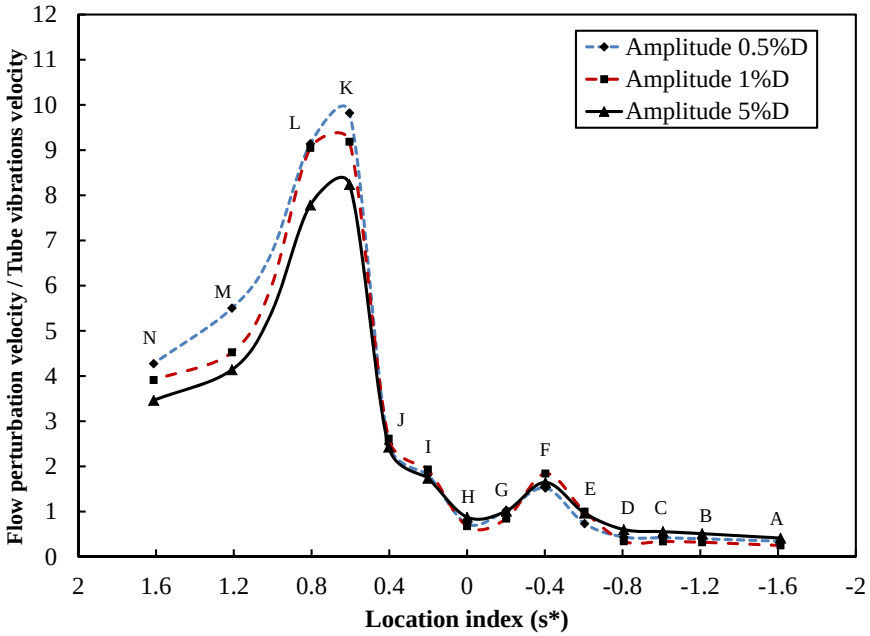

Figure 5.20: Scaled flow velocity perturbation amplitude along the middle of a flow channel.

maximum amplitude is assumed to occur at the separation point (s_s^*), and second, the perturbation amplitude at the flow channel entrance (s_i^*) is taken as about 4% of the maximum amplitude. This produces values of ($a = -0.904$) and ($b = -0.64$) which are used in Equation 5.3 to produce the decay curve shown in Figure 5.21. This fits the experimental data quite well, a goodness if fit value $R^2 = 0.986$.

5.4 Phase Lag Between Tube Motion and Induced Flow Perturbation

The experiments discussed in this section were designed to obtain the phase lag between tube vibration and the associated flow perturbation. The wind tunnel was set to the desired flow velocity and left for about 30 seconds to obtain steady flow before collecting measurements. Simultaneous measurements of tube accelerations and flow

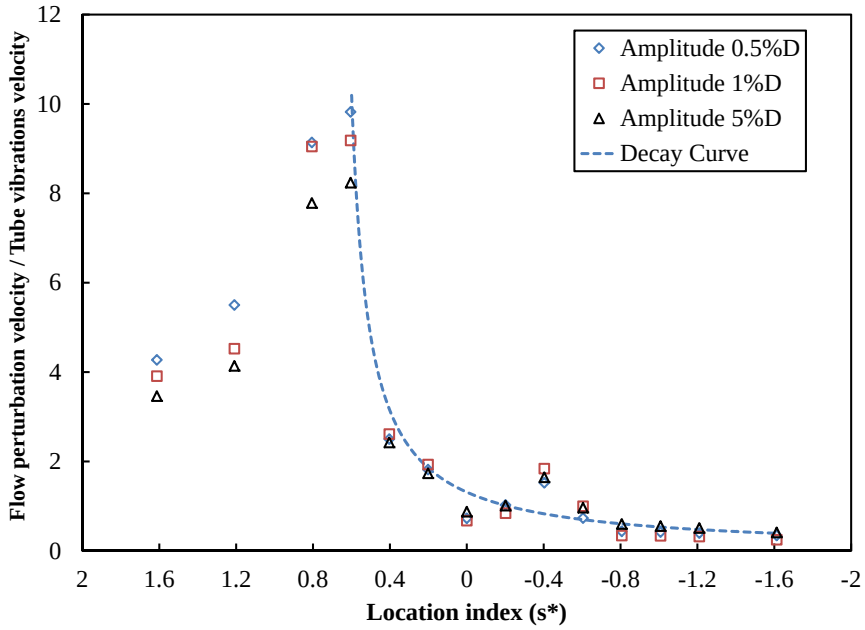

Figure 5.21: Decay function of the velocity perturbation amplitude.

perturbations were collected from the accelerometers and hot-wire respectively. The acceleration signal was integrated over time to obtain the tube velocity, and the hot-wire signal was calibrated to obtain the flow velocity.

The relative phase was obtained by correlating the flow velocity perturbation to the tube vibration velocity using cross spectral analysis at each measurement location. The parameters affecting the phase measurements were investigated first to obtain more comprehensive measurements

5.4.1 Effect of Turbulence Level

.

It is known that, as the flow turbulence level increases, detecting flow structures becomes more difficult. Thus, the effect of turbulence level on the coherence obtained at any given location of measurements in the array was investigated. The hot-wire probe was traversed through the measurement locations shown in Figure

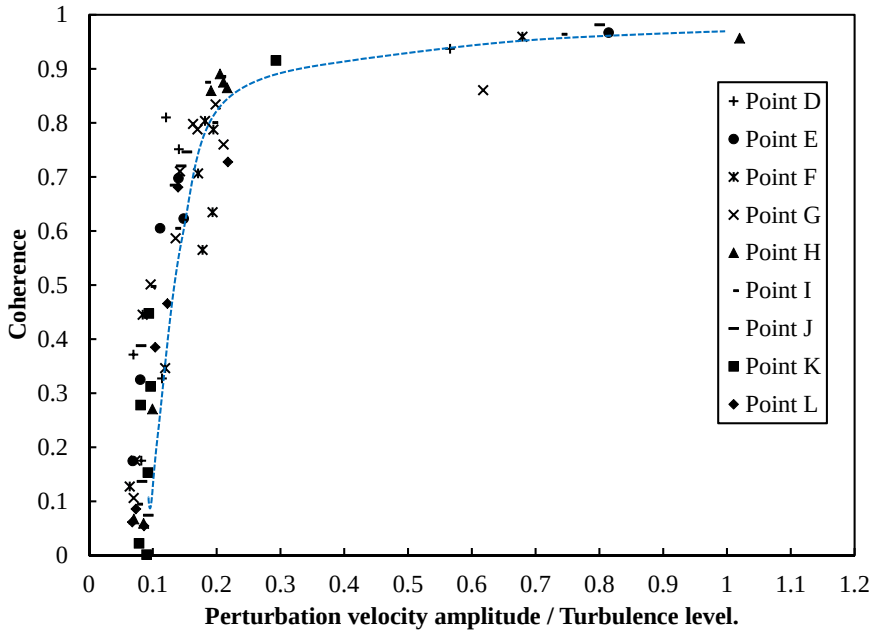

Figure 5.22: Effect of turbulence level on the coherence between tube vibrations and flow perturbations signal.

5.18(b), and, at each measurement point, phase and coherence measurements were collected. The flow velocity was increased gradually, and the measurement procedure was repeated until the tube became unstable.

It was found that the coherence depends on the ratio between flow velocity perturbation amplitude at tube vibration frequency indicated in Figure 5.17(b) and the turbulence level indicated in Figure 5.17(a). The measurements taken along the flow channel are shown in Figure 5.22, where each symbol type presents measurements at one location for several mean gap velocities. It is important to note here that the turbulence level refers to the total RMS of the flow velocity spectrum.

The collapse of all data points on a single curve shows that when the ratio between flow velocity perturbation amplitude and turbulence level was less than about 0.1, the coherence was very low. This case was associated with a relatively high turbulence level which completely veils the effect of tube vibration. This was typical

for measurements taken deeper in the array where the turbulence level is high or at relatively small tube vibration amplitudes. As the ratio increased from 0.1 to 0.2, a dramatic increase in the coherence level was detected. This increase in the coherence level indicates that the effect of tube vibration on the flow becomes more discernible and can be reliably quantified. It was found that in order to obtain reliable phase measurements, the flow velocity perturbation amplitude should be more than about 15% of the turbulence level.

5.4.2 Effect of Tube Vibration Frequency

The effect of tube vibration frequency was investigated by measuring the relative phase between tube vibration velocity and flow perturbation at a fixed location for several tube natural frequencies while maintaining the tube vibration amplitude to a constant value. The experimental setup was designed to investigate the tube natural response, and setting the tube response amplitude to a constant value was achieved by adjusting the mean gap velocity.

It was found that as the tube natural frequency increases, a higher mean gap velocity is required to obtain the same tube response amplitude. When the mean gap velocities are scaled to the corresponding tube frequencies, the reduced velocities (U_g/fD) were found to be nearly constant. It follows that, the tube response amplitude is directly related to the reduced velocity as seen in Figure 5.23, and the tube response amplitude can be controlled by adjusting the reduced velocity.

As the tube vibration amplitude was kept constant, the effect of tube vibrations on the flow was assumed to be constant. Thus, the resulting variation of measurements is due to frequency changes only. It was found that the relative phase was almost constant for all the tube vibration frequencies tested as shown in Figure

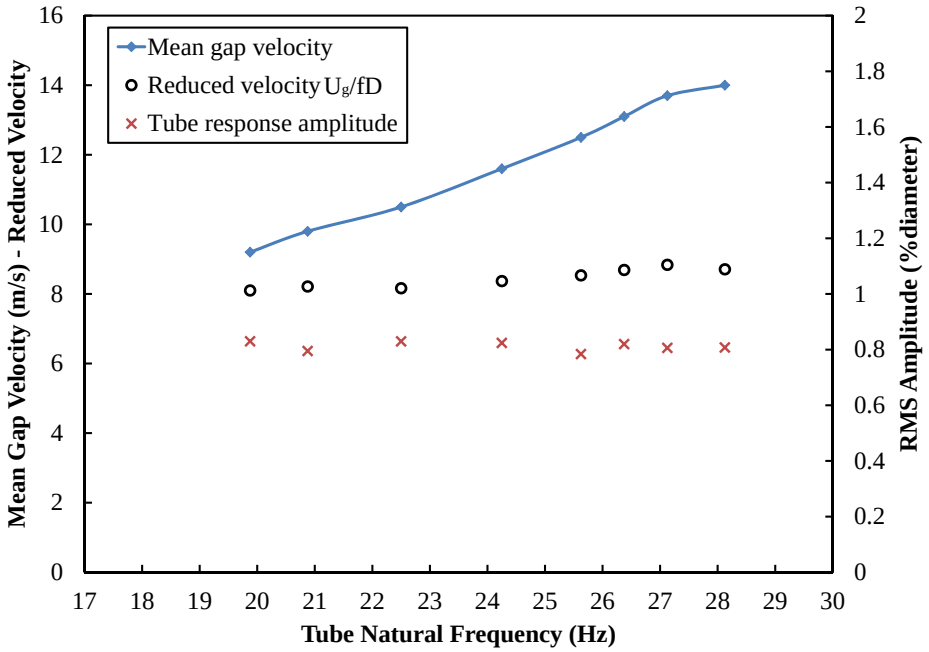

Figure 5.23: Variation of mean gap velocity with tube natural frequency to obtain constant vibration amplitude.

5.24.

The time delay between tube vibration and flow perturbation is related to the relative phase by Equation 4.21. When the phase measurements were transformed to time delay in milliseconds (ms), it was found that the time delay decreased with the vibration frequency increase as shown in Figure 5.25. The time delay data was fitted to a linear trend and the goodness of the fit is $R^2 = 0.91$.

The time delay term τ can be normalized also using the mean gap velocity U_g and the tube diameter D, and the resulting scaled-time is $\tau U_g/D$. The effect of tube vibration frequency on the scaled-time $\tau U_g/D$ is shown in Figure 5.26. It was found that the scaled delay time $\tau U_g/D$ increased linearly as the tube vibration frequency increased. This behavior can be associated with the increase in mean gap velocity to obtain constant vibration amplitude at all frequencies. It can be noted here that as the tube frequency increased, the coherence level decreased. This was also associated

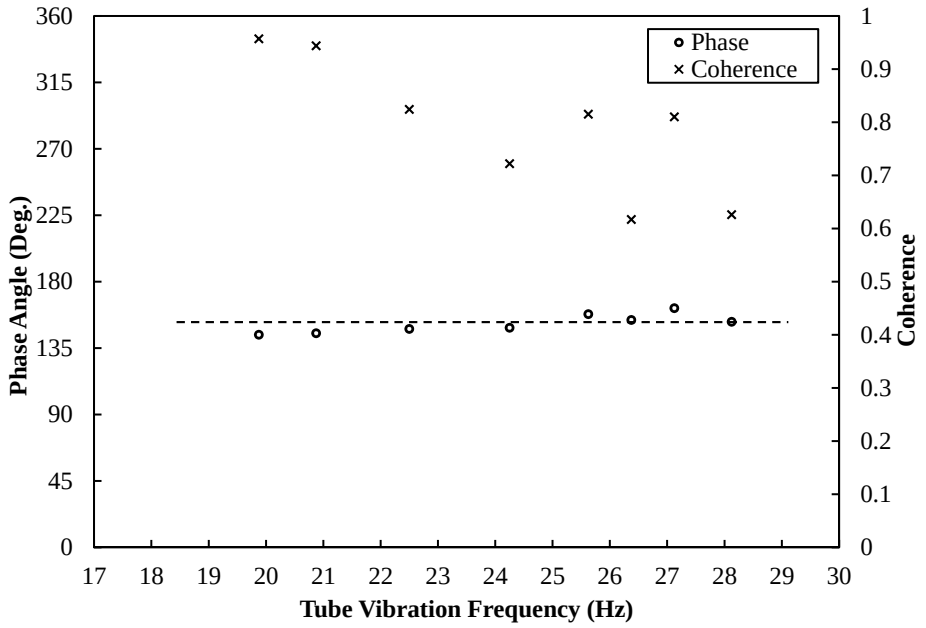

Figure 5.24: Phase lag between tube vibration and flow perturbation at point (D), tube vibration amplitude $0.8\%D$.

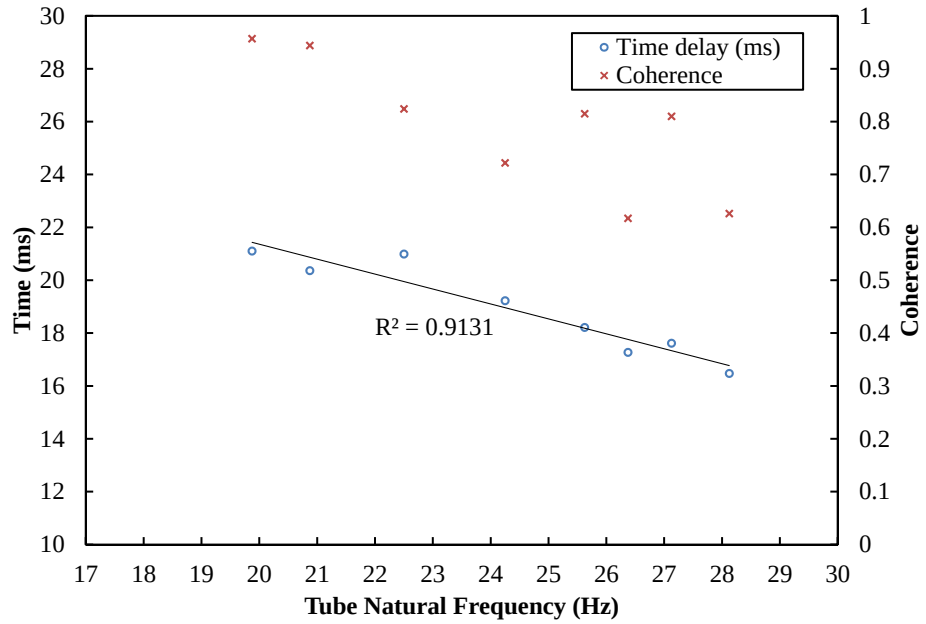

Figure 5.25: Time delay between tube vibration and flow response at point (D), tube vibration amplitude $0.8\%D$.

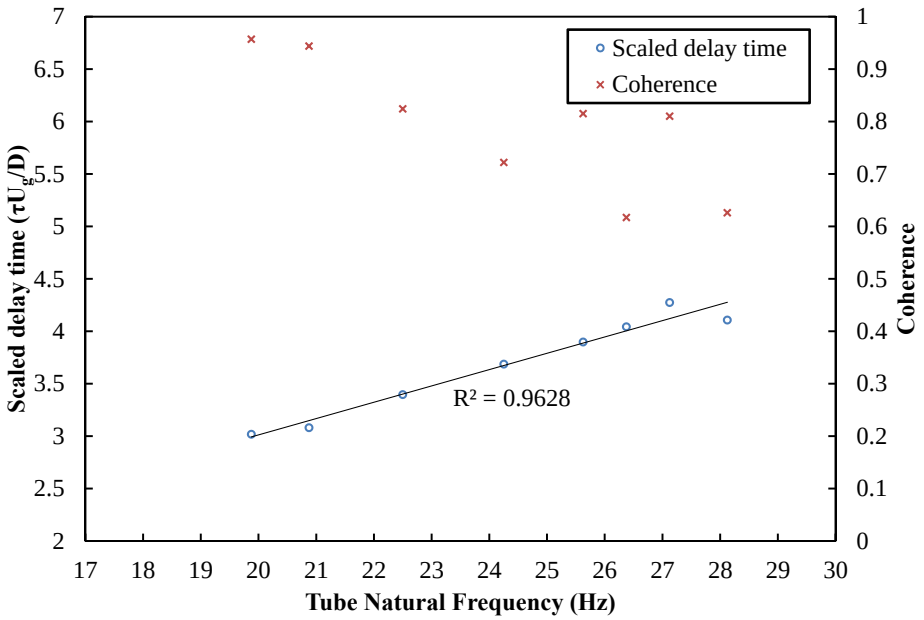

Figure 5.26: Effect of tube frequency on normalized time $\tau U_g/D$ at point (D), tube vibration amplitude $0.8\%D$.

with the increase in the turbulence level with mean gap velocity.

In summary it can be seen from these measurements that the time delay is linearly related to the tube vibration frequency, and the effect of tube vibration frequency can be compensated for when scaling the delay time with vibration frequency to obtain the relative phase angle.

5.4.3 Tube Tuning

The critical flow velocity is dependent on tube frequency and logarithmic decrement of damping. It follows that the fluidelastic stability threshold can be delayed by adjusting the tube damping and natural frequency. Delaying the stability threshold increased the number of measurements points which could be collected as the experiments were bounded by the stability threshold. However, it was found, as

shown in Figure 5.24, that the coherence level decreased with the mean gap velocity. The decrease in coherence level was attributed to the increase in turbulence level associated with increase in mean gap velocity.

Thus, there was a trade off between obtaining a high coherence level and delaying the stability threshold which gave more measurement points. A preliminary investigation of the interaction between tube vibration and flow response at several conditions was carried out to guide the selection of tube natural frequency and total damping.

As a result of this preliminary investigation, the tube logarithmic decrement was increased from $\delta = 0.0224$, as indicated in Table 4.2, to $\delta = 0.0289$ which is equivalent to about 30% increase in the damping value. The natural frequency of the tubes were also increased to about $25Hz$. As a result to these changes, the mass damping parameter increased from $m\delta/\rho D^2 = 1.56$ to $m\delta/\rho D^2 = 2.01$ and the critical reduced velocity increased from $U_g/fD = 4.5$ to $U_g/fD = 9$.

The typical response of tube (1) as a single flexible tube in a rigid array is shown in Figure 5.27. A gradual increase in tube response is associated with the mean gap velocity increase to a value of about $U_g = 11.1m/s$ where the tube response amplitude was about $1\%D$. A significant increase in tube response takes place at about $U_g = 11.8m/s$ where the tube is becoming fluidelastically unstable. The pressure spectra measurements show a small frequency peak which increased with flow velocity, also plotted on Figure 5.27. The associated Strouhal number based on mean gap velocity is $S_g = 0.34$ which agrees reasonably well with the value of $S_g = 0.32$ reported in the literature for the same array geometry (Ziada and

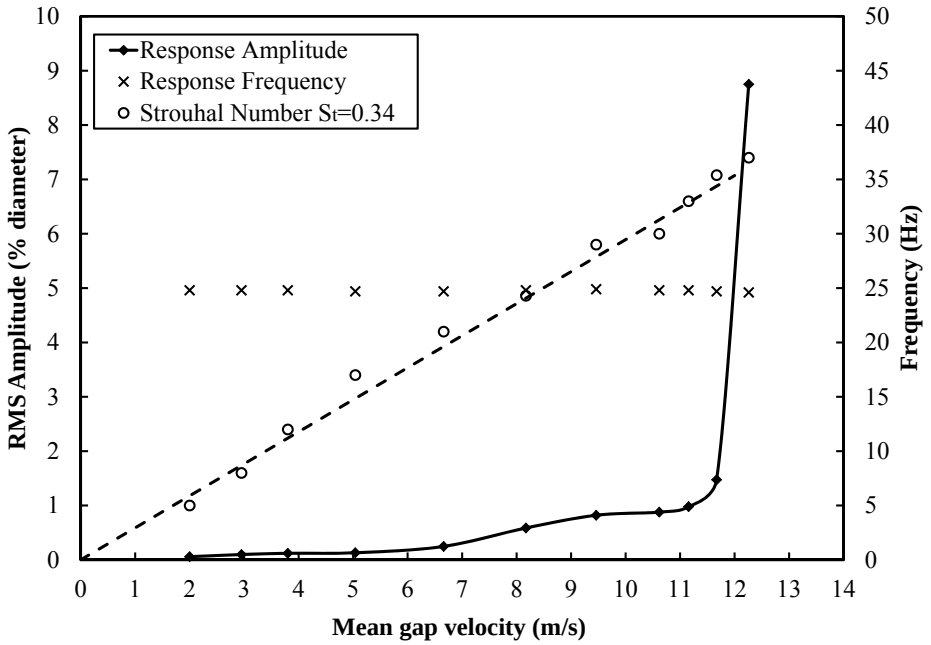

Figure 5.27: Tube (1) response as a single flexible tube in a rigid array.

Oengoren, 2000). At the coincidence of vorticity peak with tube frequency near a mean gap velocity of $U_g = 8m/s$, no clear resonance was detected.

5.4.4 Phase Measurements Along Flow Channel

In order to investigate the propagation rate of disturbances caused by tube vibrations, the relative phase was measured along the flow channel indicated in Figure 5.18(b) using two experimental procedures. The first procedure is referred to as *"fixed location"*, in which the hot-wire probe was fixed at one location and the flow velocity was increased gradually until the tube became fluidelastically unstable. Then, the probe was moved to the next measurement point and the procedure was repeated. The second procedure is referred to as *"constant velocity"*, in which the flow velocity was set to a constant value while the hot wire probe was traversed through all locations to collect the measurements. Then the velocity was increased incrementally and the

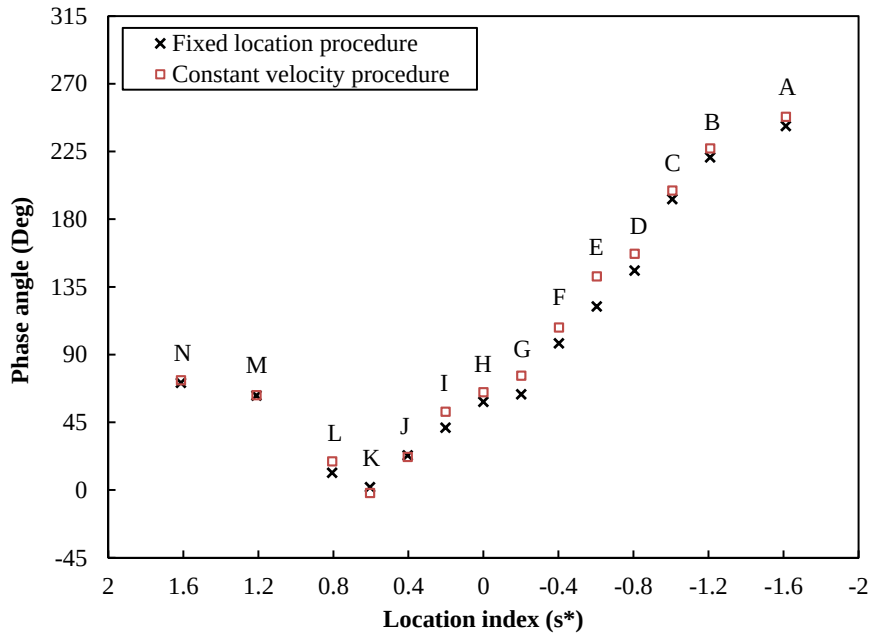

Figure 5.28: Relative phase along flow path at tube frequency $25Hz$ and response amplitude $1\%D$.

hot-wire probe was traversed again through all locations.

The phase values measured using both procedures collapsed well on the same trends for constant vibration amplitude. The phase lag between tube vibration and induced flow perturbation along the flow channel is shown in Figure 5.28, where the squares present measurements using the *fixed location* procedure and crosses present measurements using the *constant velocity* procedure for tube response amplitude of $1\%D$. It should be noted that in the present study a positive phase angle means that the flow perturbation is lagging the tube vibration and vice versa.

Analyzing the phase measurements along the flow channel reveals some interesting insights. Two distinct trends for the phase measurements are observed. From the point (K) at about $s^* \approx 0.6$, the phase lag shows a nearly constant slope to the point (N) where $s^* \approx 1.6$ at about two rows downstream. On the other hand, upstream from the point (K) to the point (B) where $s^* \approx 1.2$ at about two tube rows

upstream, the phase lag shows a different near constant slope.

The two trends intersect at a location index of about 0.6, i.e. point (K), where the phase lag was almost zero. Point (K) was considered to be the source of the observed perturbations in the flow as the phase at this location is about zero. It was shown earlier that the maximum perturbation amplitude took place at point (K), as shown in Figure 5.18(a), and was caused by the vorticity separation from the vibrating tube. Thus, based on the amplitude and phase measurements it seems that the flow perturbations are caused by the flow separation and the associated vorticity generation from the vibrating tube. The phase lag trends shown in Figure 5.28 seem to be linear both upstream and downstream from the separation point (K). A linear phase lag trend means that the disturbance is propagating at a constant speed.

In order to study the propagation velocity of perturbations both downstream and upstream more fully, the phase lag trends were obtained at different mean flow velocities. A comparison between the relative phase trends obtained for a range of mean gap velocities is shown in Figure 5.29(a). The data obtained at all flow velocities followed reasonably the same trend both upstream and downstream of the flow separation point (K). When the data are scaled using the mean gap velocity U_g and the tube diameter D, the normalized delay time $\tau U_g/D$ showed a reasonable collapse to a single curve both upstream and downstream of the tube as seen in Figure 5.29(b).

The linear trends obtained in Figure 5.29(b) were analyzed to obtain the propagation velocity of flow perturbations. The slope, C, of the data linear fit can be expressed as Equation 5.4, while the propagation velocity of the perturbation, U_p, scaled to mean gap velocity, U_g, can be expressed as Equation 5.5.

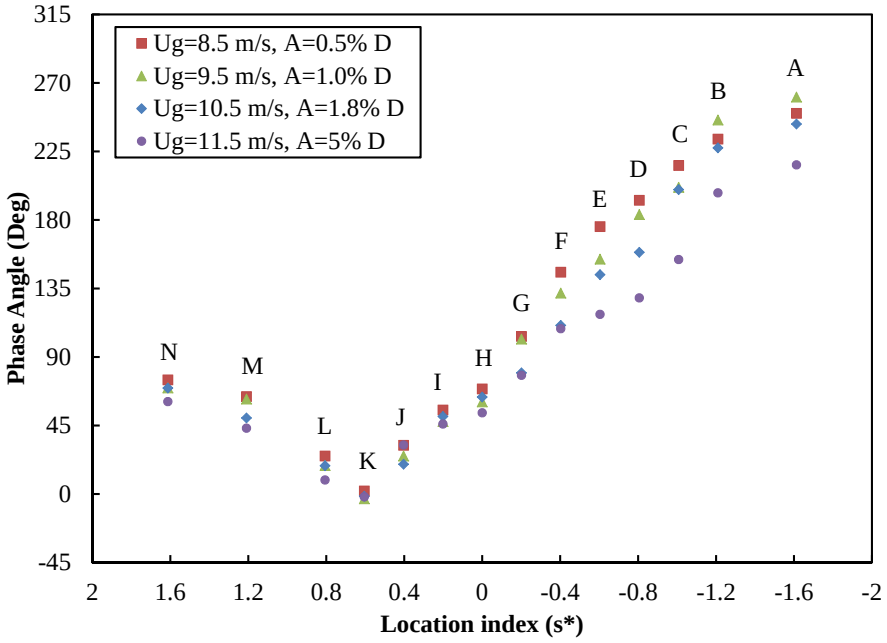

(a) Phase angle.

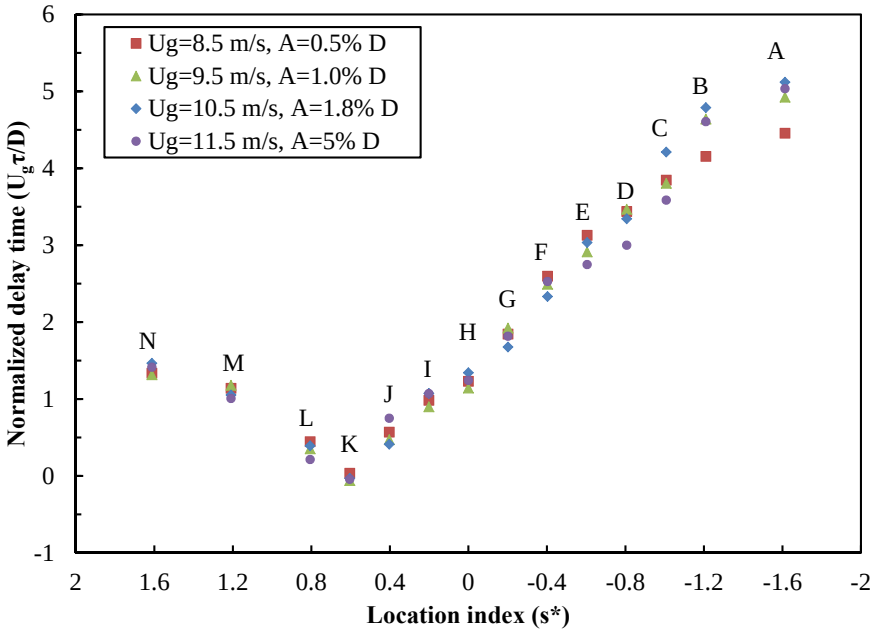

(b) Scaled-time $\tau U_g/D$.

Figure 5.29: Effect of mean gap velocity on phase lag value at tube frequency $25Hz$.

Table 5.1: Fitting data and propagation velocities upstream of point (K).

$U_g(m/s)$	$C_{upstream}$	R^2	*Upstream* U_p/U_g
8.5	-2.26	0.97	0.44
9.5	-2.4	0.99	0.42
10.5	-2.5	0.98	0.4
11.5	-2.3	0.98	0.43

Table 5.2: Fitting data and propagation velocities downstream of point (K).

$U_g(m/s)$	$C_{downstream}$	R^2	*Downstream* U_p/U_g
8.5	1.28	0.94	0.78
9.5	1.31	0.91	0.76
10.5	1.36	0.98	0.74
11.5	1.34	0.98	0.75

$$C = \frac{d\left(\tau U_g/D\right)}{d\left(s/D\right)} = \left(\frac{d\tau}{ds}\right) U_g \tag{5.4}$$

$$\left(\frac{U_p}{U_g}\right) = \frac{\left(ds/d\tau\right)}{U_g} = \frac{1}{C} \tag{5.5}$$

5.4.5 Discussion

The normalized time delay data can be divided into two regions, one upstream and the other downstream from the flow separation point (K). For each flow velocity the upstream and the downstream regions were fit to straight lines which present the propagation velocity of flow perturbations. The values for the linear fit slope, goodness of the fit, and propagation velocities are shown in Table 5.1 and Table 5.2 for upstream and downstream trends respectively.

The propagation velocity of the perturbations downstream was found to remain approximately constant at a value of about 0.76 of the mean gap velocity. This

ratio approximates to the vorticity convection velocity obtained experimentally from a single cylinder subjected to cross flow as reported in the literature by Zhou and Antonia (1992) and Lin and Hsieh (2003). Lin and Hsieh (2003) found the convection velocity of vorticity shed from a cylinder to be 0.85 the mean flow velocity. Thus the linear trend of normalized time delay in the downstream direction seems to be caused by the convection of vorticity from the vibrating cylinder.

The propagation velocity upstream shows the same behavior but with a smaller slope. Based on the data listed in Tables 5.1 and 5.2, it is difficult to define a clear trend for the disturbances propagation velocity with the mean gap velocity. However, the upstream propagation velocity was found to be less than the downstream propagation velocity by approximately a factor of 2. This behavior could be related to the fact that the perturbation is traveling upstream against the mean flow which results in a larger time delay. The physical nature of this upstream propagating disturbances is unknown.

The range of mean gap velocity investigated in the present study was limited by the minimum tube vibration amplitude required to produce coherence level adequate for reliable phase measurements and by the fluidelastic instability onset beyond which measurements were not possible. These limitations resulted in investigating a relatively small range of mean gap velocity, i.e. from $U_g = 8.5m/s$ where the vibration amplitude $A = 0.5\%D$ to $U_g = 11.5m/s$ where $A = 5\%D$.

In summary, the downstream disturbances propagation could be associated with convection of vorticity. The upstream propagation rate of disturbances from the vibrating tube is linear and has an average value of 0.42 of the mean gap velocity. However, the physical nature of this propagation mechanism is not understood.

5.5 Computational Fluid Dynamics Modeling

The problem of fluidelastic instability in tube bundles is associated with high turbulence levels which affect the signal-to-noise ratio and, in many cases, veils the physical phenomenon under investigation. In contrast, Computational Fluid Dynamics (CFD) modeling provides great flexibility in investigating problem parameters. However, due to the complex nature of fluidelastic instability and the present computational abilities, CFD modeling is not capable yet of providing quantitatively accurate predictions of the phenomena.

A CFD model for a tube array subjected to cross flow was developed to assist in understanding the interaction between tube motions and fluid response. The present CFD modeling was intended to examine at least qualitatively the ability to predict numerically the physical phenomenon observed experimentally. It follows that precise quantitative agreement with the experimental results was not considered essential. This section presents a brief description of the CFD model construction and validation as well as a comparison between the numerical and experimental results.

5.5.1 Model Details

Two dimensional tube array models were constructed using ANSYS-CFX. The flow response to harmonic tube vibrations in the cross-stream direction was monitored along the flow path which was obtained based on the flow visualizations of (Scott, 1987). The surface pressures on the vibrating tube were monitored to obtain the fluid forces, and the time-signals of pressure and flow velocity at each monitored point were transferred to the frequency domain to obtain the amplitude and phase with tube vibrations.

The first array model had a normal triangular geometry and a pitch ratio of

$P_r = 1.32$. The array consisted of five rows and five columns of $30mm$ diameter tubes with half tubes on both sides of the model as shown in Figure 5.30(a). The second array model had a parallel triangular geometry and a pitch ratio of $P_r = 1.54$. The array consisted of seven rows and three columns of $57mm$ tubes with half tubes on the model sides as shown in Figure 5.30(b). These particular geometrical configurations were selected to match the arrays where experimental data are available for validation (Mahon and Meskell, 2009, 2010b).

ANSYS CFX-Mesh module was used to produce the model meshing where tetrahedra and prism elements were used to capture the circular curvature of the tubes. The tube diameter was considered to be the length scale, and the standard element size was selected to be below 5% of the tube diameter as shown in Figure 5.31(a). The elements were refined around the tubes and near the walls to about 1% of the tube diameter, and an expansion factor of 1.2 between the fine and the standard elements was adopted.

Inflated boundary layer elements were used at the model walls and on the tubes surfaces to properly model the boundary layer development. The number and size of the inflated boundary layer elements were determined based on the non-dimensional distance from the wall($y+$), the Reynolds number R_e, and the length scale D, and an expansion factor of 1.2 was used for the transition from the fine inflated elements to the standard tetrahedral elements as shown in Figure 5.31(b).

Symmetry boundary conditions were assigned to the domain plans to handle the problem as two dimensional. The inlet region was set to have a uniform flow, while an opening boundary condition was assigned to the outlet region. The opening boundary condition allows the fluid to flow out or into the domain, and as such the flow is not forced to go in the outlet direction. The domain sides and the tube surfaces

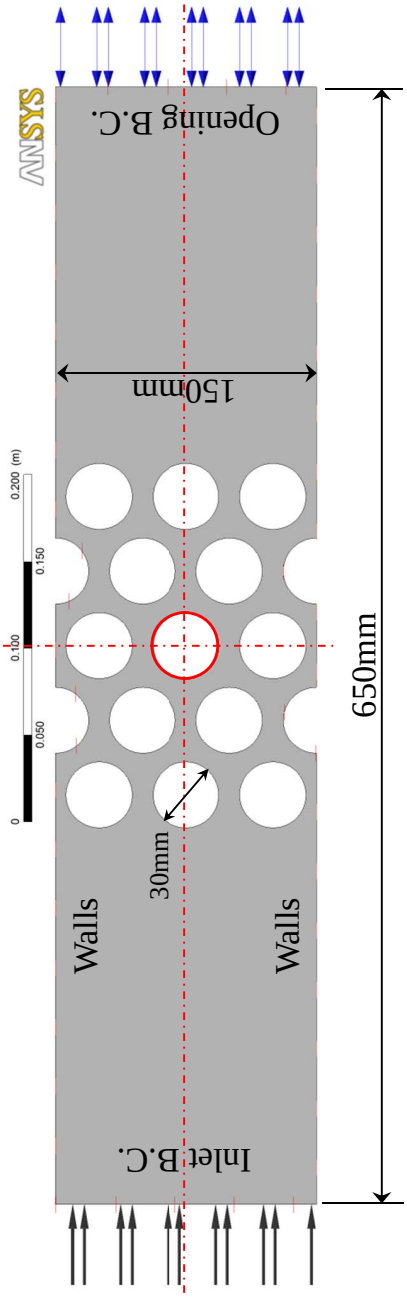

(a) Normal triangular array model, $P_r = 1.32$.

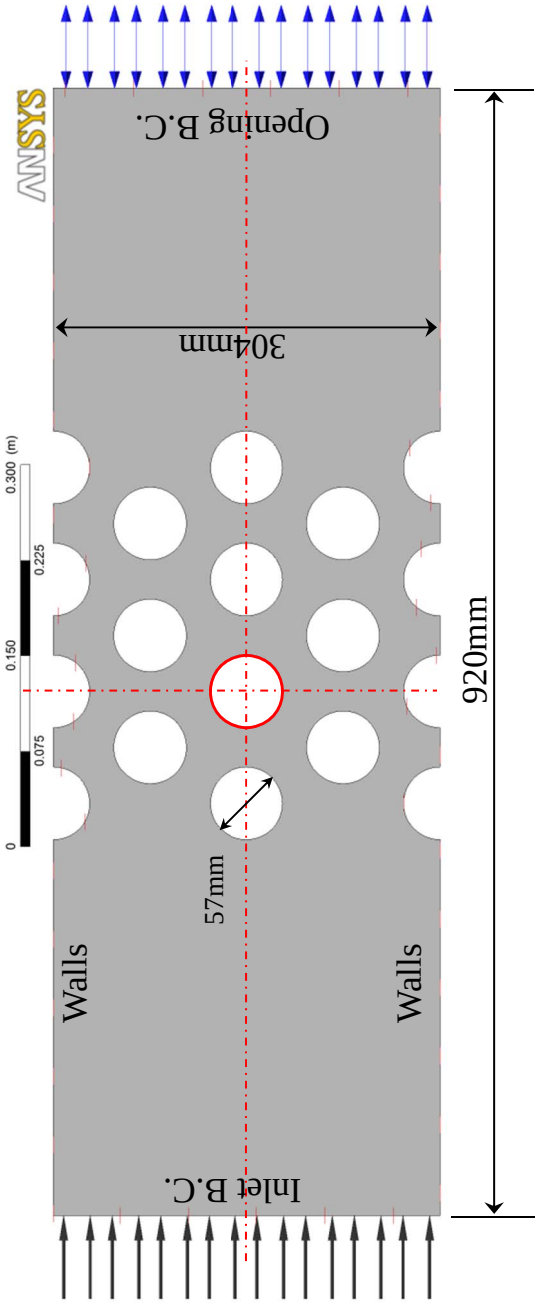

(b) Parallel triangular array model, $P_r = 1.54$.

Figure 5.30: Geometrical configurations of the present CFD models.

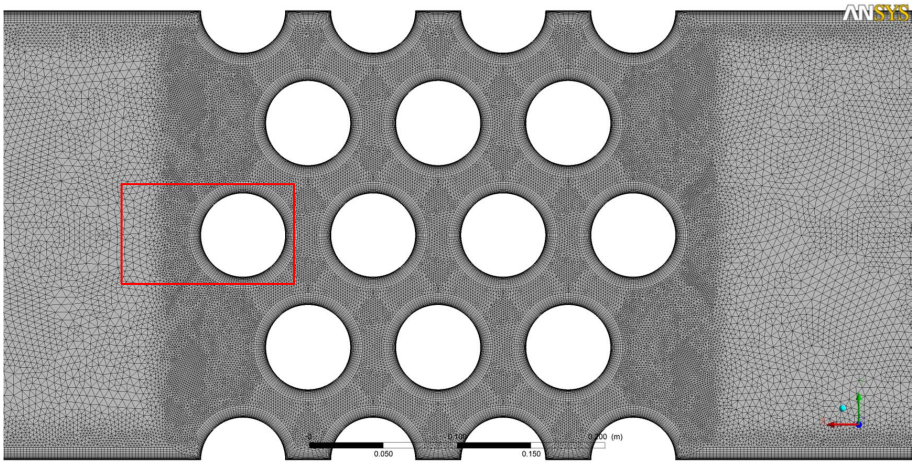

(a) Meshing of a parallel triangular array, $P_r = 1.54$.

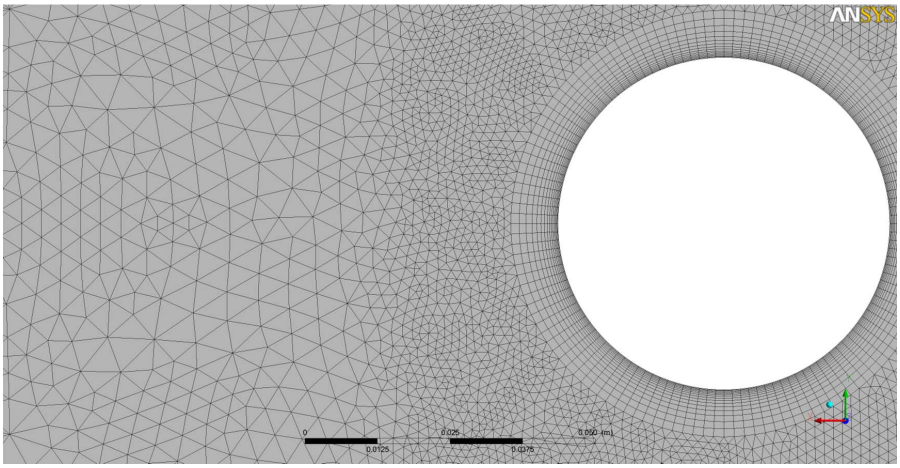

(b) Detailed view of the meshing.

Figure 5.31: Meshing details for a parallel triangular array, $P_r = 1.54$.

were treated as stationary no slip walls except for the third row central tube which was treated as a harmonically moving wall. The Reynolds number R_e in the present simulations was in the range of $R_e = 2e3$ to $R_e = 6 \times 10^4$ depending on the mean gap flow velocity.

A domain size independence study showed that at least six length scales are required upstream of the tube array for the results to asymptote within $\pm 2\%$. A grid independence study was conducted to determine the number of meshing elements above which the results are not affected by meshing size. The time step was selected to maintain an RMS Courant number in the simulations below $C_r = 5$. The number of time steps was adjusted to provide about 100 cycles of tube vibrations which is enough for frequency analysis. An investigation of the turbulence modeling effect showed that the Shear Stress Transport model SST performed best for the present geometry. Details of the meshing, boundary conditions, and independence studies are provided in Appendix E.

5.5.2 Model Validation

The CFD models were validated first by comparing the predicted pressure distribution around the vibrating tubes to the experimental data reported by Mahon and Meskell (2009, 2010b). The pressure coefficient C_p at each position angle on the tube surface was defined as

$$C_p = 1 - \frac{P_o - P_\theta}{\frac{1}{2}\rho U_g^2} \tag{5.6}$$

where P_o is the mean pressure at ($\theta = 0^\circ$), P_θ is the mean pressure at any surface position angle (θ), and U_g is the mean gap velocity. The surface pressure distribution

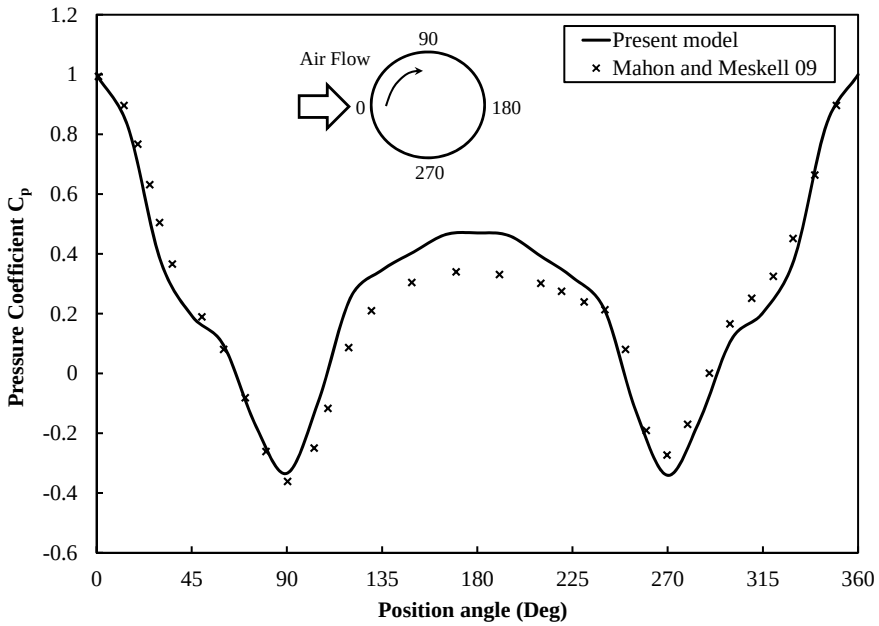

Figure 5.32: Surface pressure distribution on a flexible tube located in the third row of a rigid normal triangular array, $P_r = 1.32$ and $R_e = 57000$.

for a tube in the normal triangular array is shown in Figure 5.32 for a Reynolds number of $R_e = 57000$. The present CFD model provided good agreement with the experimental results over the ranges of position angle $(0^\circ - 120^\circ)$ and $(240^\circ - 360^\circ)$ where the agreement with the experimental results was within 6%. The model was capable of predicting the separation points on both sides of the tube correctly at about 120° and 240°, however the predicted pressure coefficient values over the wake region were within 15% of the experimental values.

The surface pressure distribution on a tube located in the parallel triangular array showed a lack of symmetry on both sides of the tube for both the experimental and numerical data as shown in Figure 5.33 for a Reynolds number of $R_e = 39000$. The present model provided good prediction of the surface pressure coefficient values over the ranges of position angle $(0^\circ - 120^\circ)$ and $(240^\circ - 360^\circ)$ where the agreement with the experimental results was within 7%. The flow separation points were pre-

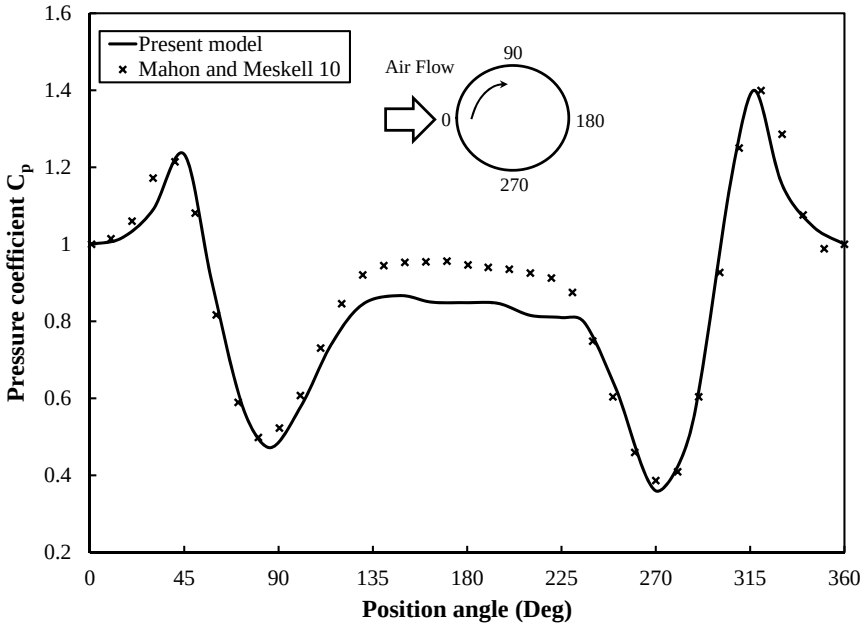

Figure 5.33: Surface pressure distribution on a flexible tube located in the third row of a rigid parallel triangular array, $P_r = 1.54$ and $R_e = 39000$.

dicted correctly by this model at angles of 125° and 240° while the agreement with the experimental data over the wake region ($125° - 240°$) was within 14%.

Comparison of the surface pressure distribution showed that the models are capable of capturing the mean flow behavior in the arrays. Detailed discussion of pressure distribution lack of symmetry in both the numerical and experimental results is included in Appendix E. In order to similarly validate the unsteady behavior of the flow, the Strouhal numbers S_t obtained from both arrays were compared the the values reported in literature for similar array geometries. The normal triangular array simulations resulted in a Strouhal number based on upstream flow velocity of $S_t = 2.05$, which agrees well with the corresponding values reported in literature by Polak and Weaver (1995) as shown in Figure 5.34. The parallel triangular model resulted in a Strouhal number based on the mean gap velocity of $S_t = 0.31$ While the present experiments showed a Strouhal number of $S_t = 0.34$ and Ziada and Oengoren

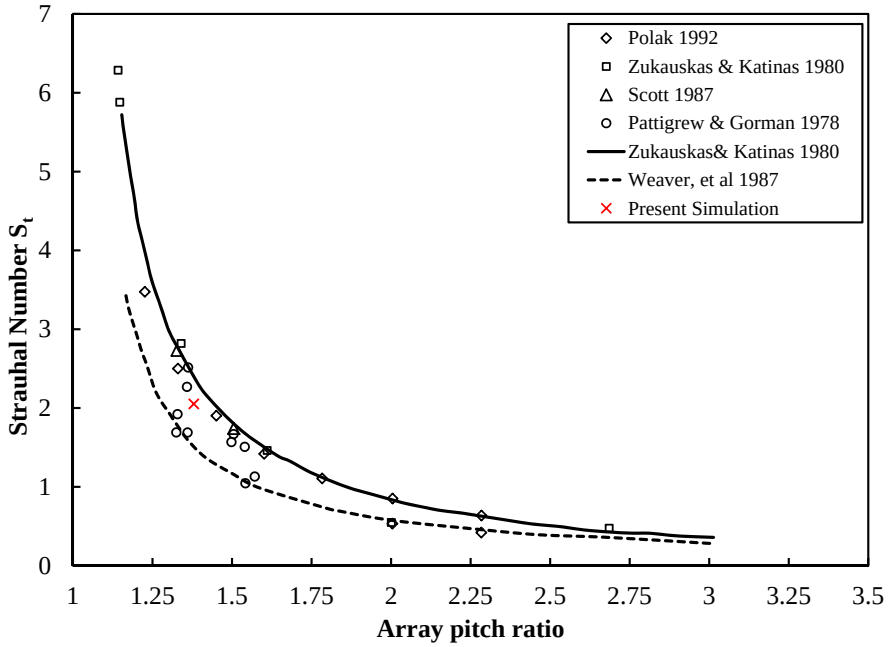

Figure 5.34: Comparison of present model Strouhal number prediction to the data reported in literature by Polak and Weaver (1995).

(2000) reported a Strouhal number for this array geometry of $S_t = 0.32$.

5.5.3 Parallel Triangular Array Results

Having been satisfied that the CFD model can reasonably predict the pressure distribution and vortex shedding in a tube array, simulations using the parallel triangular array model were carried out to predict the experimental phase observations. The first simulation was conducted using air flow at a Reynolds number of $R_e = 30500$ which corresponds to a mean gap velocity of $U_g = 8.8m/s$. The third row tube was harmonically displaced in the cross-stream direction with an amplitude of $1\%D$ at a frequency of $25Hz$ which results in a reduced velocity $U_r = 6.2$. These particular flow characteristics were selected based on the experimental values reported earlier in this chapter.

The transient simulations were conducted using a time step of $\Delta t = 0.3ms$ over

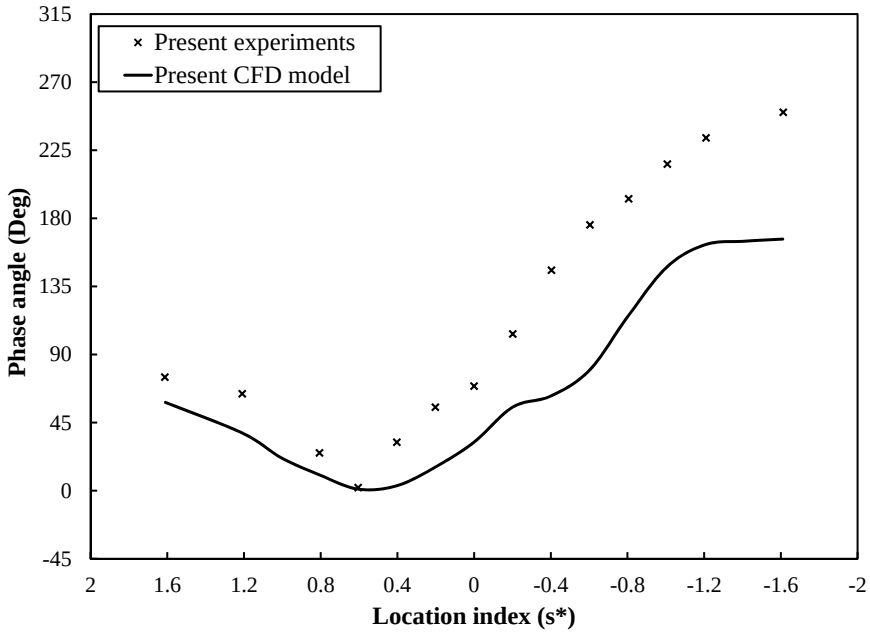

Figure 5.35: Comparison between numerical and experimental phase between tube vibrations and flow perturbation along the flow channel for a parallel triangular array, $P_r = 1.54$, $R_e = 30500$, and $U_r = 6.2$.

a period of $(6sec)$ which produced 150 tube oscillations over 20000 time steps. The fine time step was selected to produce a RMS Courant number of $C_r < 8$ as recommended by ANSYS-CFX manual. The flow velocities and pressures were monitored along the flow channel at comparable locations to the experimental data. The relative phase between tube velocity and flow velocity perturbations were compared to the experimental data for the same reduced velocity as shown in Figure 5.35.

The numerical phase trend agreed qualitatively with the experimental data over the entire range of measurements. Two distinct phase trends were obtained from the numerical simulations and a minimum relative phase was observed at the flow separation point. While the quantitative agreement with the experimental data was within about 45°, the fact that the present CFD modeling captured the phenomenon physics, means that further refinement of the CFD modeling might produce better agreement with the experimental data. As the CFD part of the present study

Table 5.3: CFD Simulations data for low range of reduced velocity.

U_g/fD	U_g	Reynolds number
1	0.57	2000
2	1.14	4000
3	1.71	6000
4	2.28	8000
5	2.85	10000
6	3.43	12000

was intended for qualitative analysis of the physics only and not for quantitative prediction, such refinement was not carried out and the model was employed in investigating the effect of reduced velocity on the phase trends.

The reduced velocity $U_r = U_g/fD$ effect on the phase between tube vibrations and velocity perturbation was investigated over the range of $(U_r = 1-6)$. In order to reduce the simulation time, the tube vibration frequency was reduced to $10Hz$ which resulted in a significant reduction of the flow velocities. It follows that the time step was increased to $\Delta t = 1ms$ and about 10000 time steps were solved. The details of this set of simulations are listed in Table 5.3.

The phase trends obtained from the CFD simulations for reduced velocities $U_r = 1$ through $U_r = 6$ are shown in Figure 5.36. It is observed that the phase trends for $U_r = 1$ and $U_r = 2$ as shown in Figures 5.36(a) and 5.36(b) respectively are quite similar. The flow velocity perturbations at the upstream points , i.e. location index $s^* < 0$, have a phase lag of about 180° with the tube velocity, while the velocity perturbations at the downstream points, i.e. for location index $s^* > 0$, are in-phase with the tube velocity ($\phi = 0°$). Fundamental changes in the phase trends both upstream and down stream of the tube take place at about $U_r = 3$ as shown in Figure 5.36(c). Two trends for the phase lag start to form and a minimum phase lag value is observed at a location index of about $s^* = 0.6$ which is the flow separation

point as indicated in the previous sections. Examining the phase trends obtained for $U_r = (4, 5, 6)$ as shown in Figures 5.36(d), 5.36(e), and 5.36(f) respectively, show that the two phase trends exist in all cases indicating that the phenomenon physics are not changing. However, the rate of flow perturbation propagation upstream and downstream increase with the increase in the reduced velocity.

The present simulations for $U_r > 2$ showed trends for the phase between tube velocity and flow perturbation velocity that agree in concept with the experimental results. The phase trends predicted for $U_r = 6$ and $U_r = 7$ were compared to the experimental data for $U_r = 6.2$ and $U_r = 7.0$ as shown in Figure 5.37. It is found that, the CFD results agree well with the experimental results over the downstream region, while the agreement was within 45° for the upstream region. It seems that the present CFD modeling is able to capture the physical phenomenon causing the phase lag between tube vibration and flow perturbation.

In order to understand the fundamental change in the phase behavior between $U_r = 2.0$ and $U_r = 3.0$, the pressure fields in both cases were examined. The pressure images showed a fundamental change in the excitation and fluid response mechanisms. At reduced velocity of $U_r = 2.0$, the flow followed a regular path in the array, no vorticity separation from the tube was detected and the flow field in this case was similar to the potential flow around a cylinder at relatively low Reynolds numbers $R_e \leq 4000$. The pressure field images showed that a high and low pressure regions are formed as the tube vibrates as shown in Figure 5.38. It follows that, the flow perturbations were caused by the pressure pulse associated with the tube vibration which travels at the speed of sound. This propagation time is essentially instantaneous, which explains the zero slopes of the phase angle for upstream and downstream propagating disturbances.

It is also observed that a phase shift of 180° takes place between the upstream

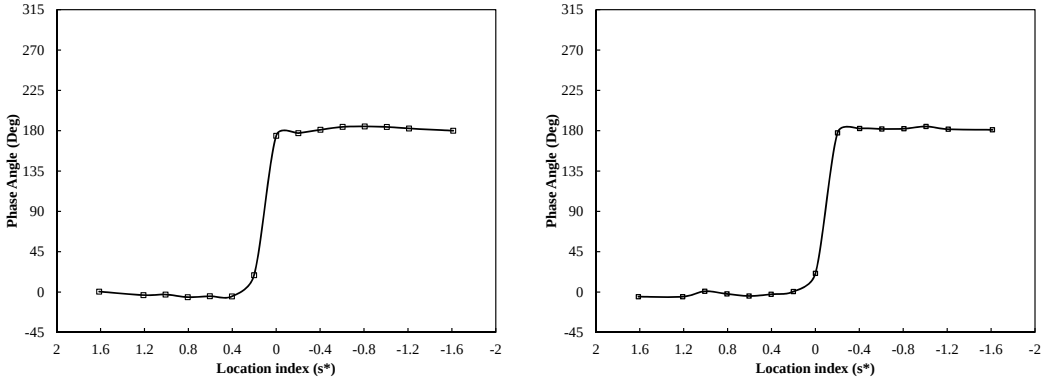

(a) $U_r = 1$.

(b) $U_r = 2$.

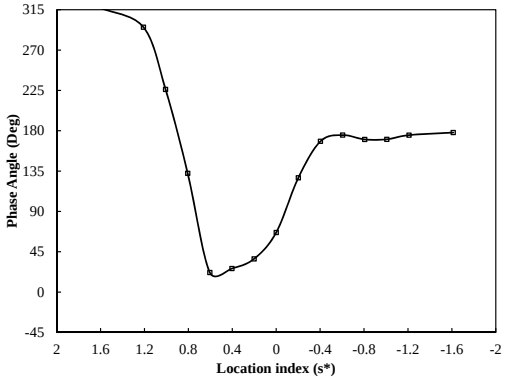

(c) $U_r = 3$.

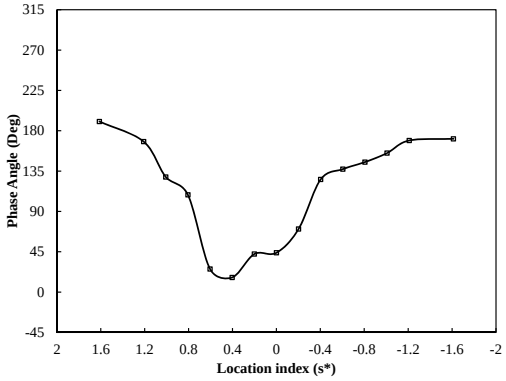

(d) $U_r = 4$.

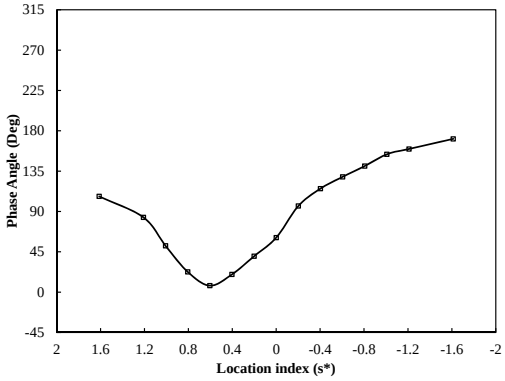

(e) $U_r = 5$.

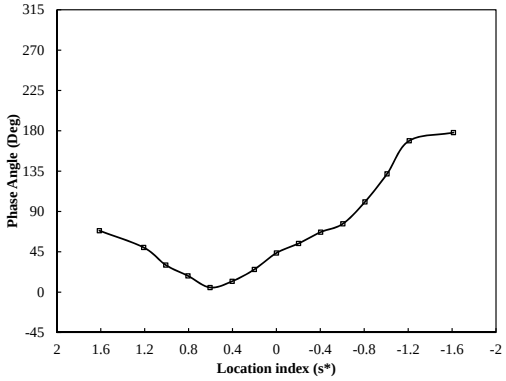

(f) $U_r = 6$.

Figure 5.36: Development of the phase lag trends with reduced velocity over the range of $U_r = 1 - 6$.

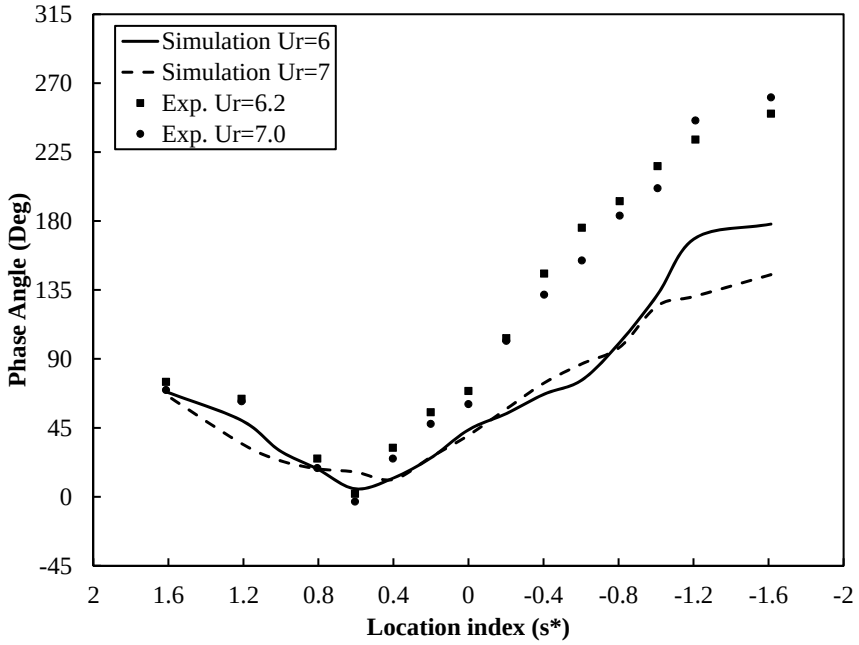

Figure 5.37: Comparison between numerical and experimental phase between tube vibrations and flow perturbation along the flow channel for a parallel triangular array, $P_r = 1.54$. Experimental ($U_r = 6.2$,$R_e = 30500$, and $U_r = 7.0$,$R_e = 33200$), numerical ($U_r = 6.0$,$R_e = 12000$, and $U_r = 7.0$,$R_e = 14000$).

and downstream directions. This behavior is associated with the effect of tube vibration on the flow such that, when the tube moves in one direction, this reduces the interstitial gap area and thus the flow decelerates upstream and accelerates downstream of the vibrating tube. This opposite reaction results in a phase shift of 180° between the upstream and downstream signals.

Examining the flow pattern at $U_r = 3.0$ reveals a fundamental change in the flow as vorticity shedding from the tube occurs. The pressure field images show that high and low pressure regions are associated with the flow separation from the tube as shown in Figure 5.39. In this case the flow perturbation is caused by the flow separation and the associated generation of wake vorticity. Thus, the phase behavior is governed by vorticity convection downstream and the associated effect upstream from the tube under consideration.

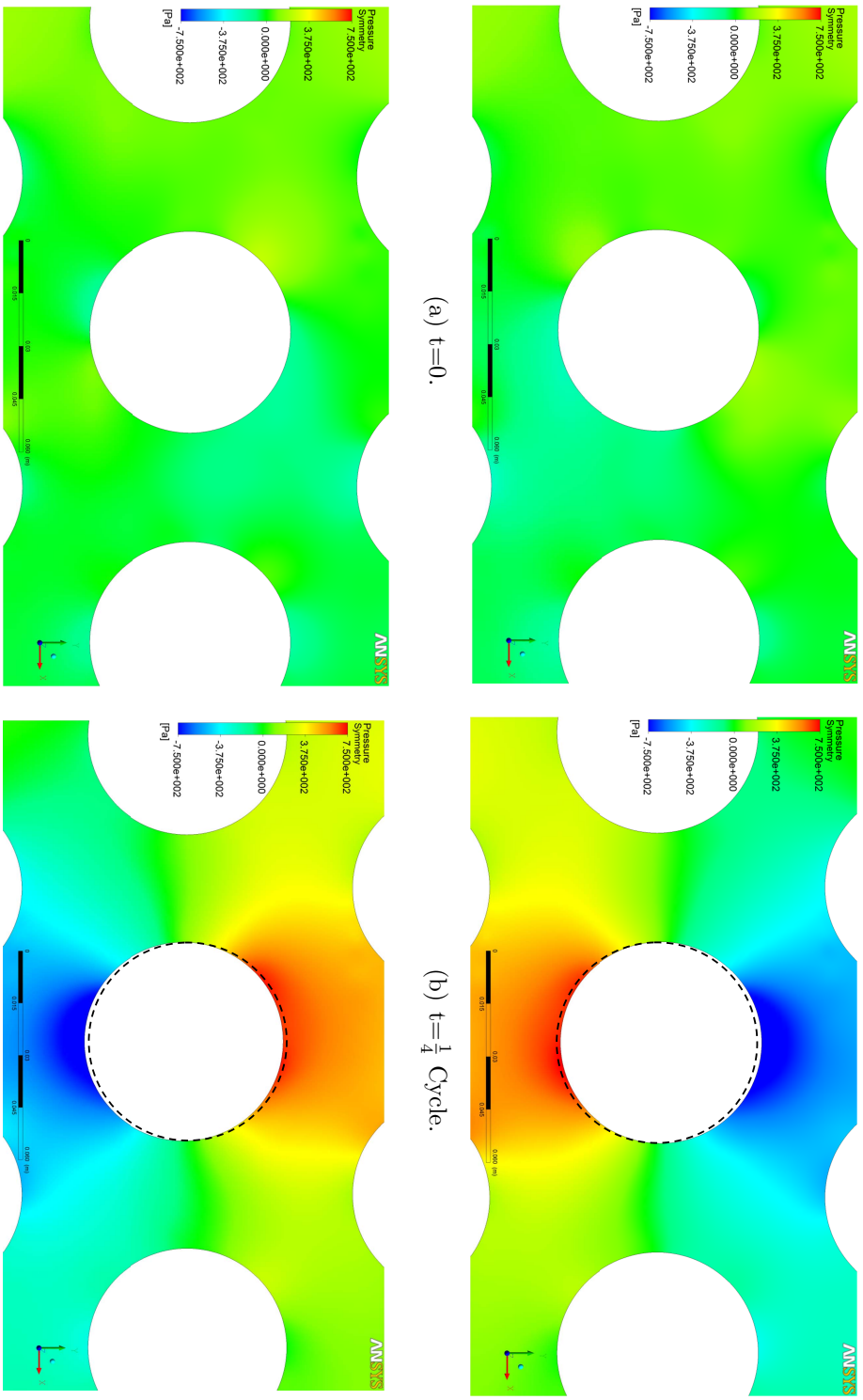

(a) t=0. (b) t=$\frac{1}{4}$ Cycle.

(c) t=$\frac{1}{2}$ Cycle. (d) t=$\frac{3}{4}$ Cycle.

Figure 5.38: Pressure field variation over one cycle of tube vibration, $P_r = 1.54$, $U_r = 2$, and $R_e = 4000$.

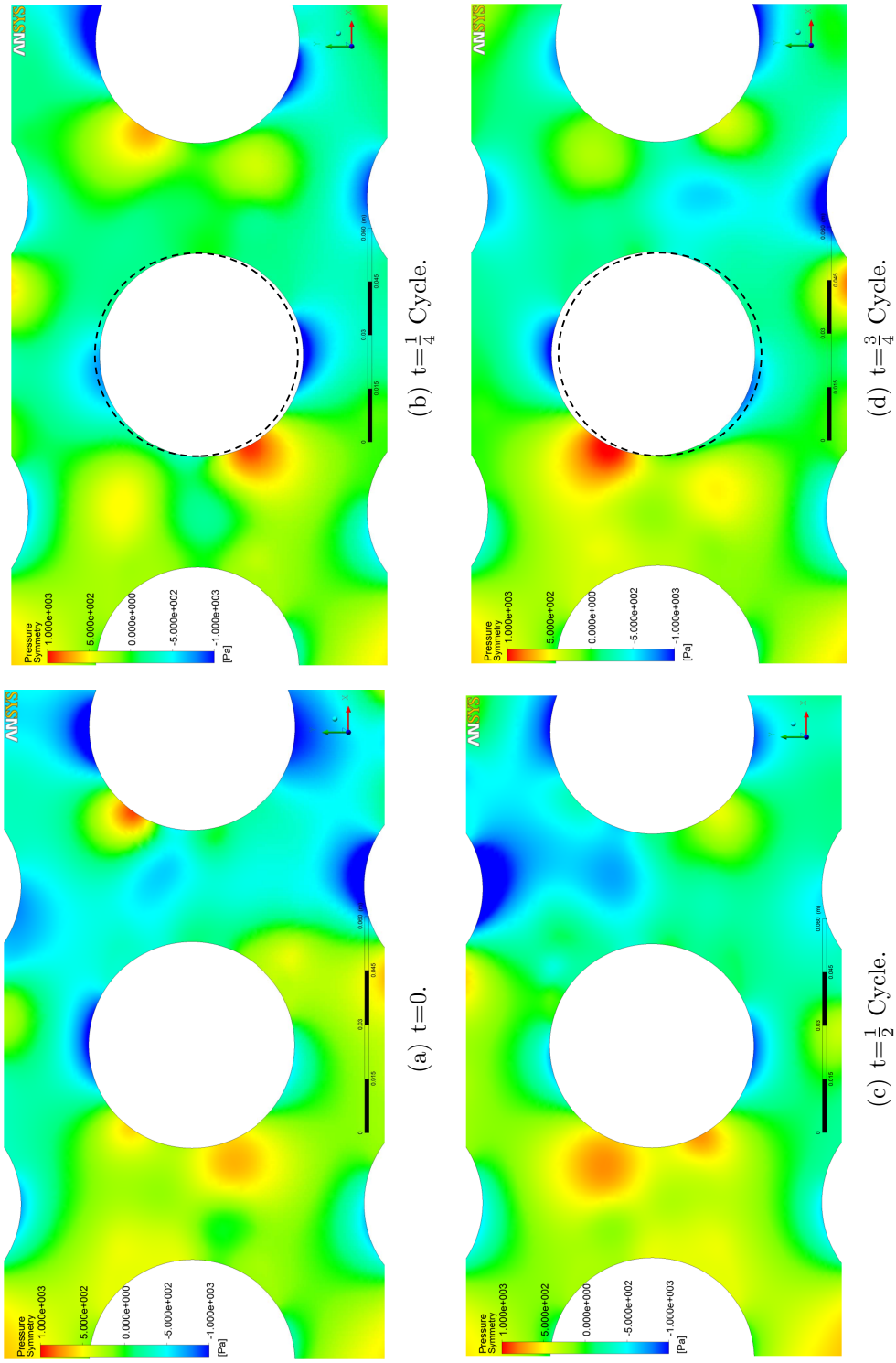

(a) t=0. (b) t=$\frac{1}{4}$ Cycle.

(c) t=$\frac{1}{2}$ Cycle. (d) t=$\frac{3}{4}$ Cycle.

Figure 5.39: Pressure field variation over once cycle of tube vibration, $P_r = 1.54$, $U_r = 3$, and $R_e = 6000$.

5.5.4 Discussion

In summary, CFD simulations of a parallel triangular array subjected to air cross flow at Reynolds numbers from $R_e = 2000$ to $R_e = 60000$ have been conducted. The tube surface pressure distribution and Strouhal number predicted numerically were compared to the experimental values and a relatively good agreement was achieved. The present CFD model was found to be capable of predicting the physical phenomenon causing the phase lag trends observed in the experiments between tube velocity and flow velocity perturbations.

Investigation of the flow response to tube vibrations at relatively low reduced velocity $U_r = 1 - 6$ showed a fundamental change in the source of flow perturbations associated with tube vibrations. It was found that for a reduced velocity $U_r \leq 2$, the flow perturbation was caused by the pressure pulsation associated with tube vibrations, and thus, the flow perturbations propagate at the speed of sound. As the reduced velocity increases $U_r > 2$, the flow separating from the vibrating tube forms vortices which are convected downstream and also produces disturbances which propagate upstream at a lower velocity. The flow perturbation caused by flow separation and associated vorticity convection seem to overwhelm the flow perturbations propagating at the speed of sound, which agrees with the experimental observations.

Chapter 6

Theoretical Modeling

This Chapter presents mathematical modeling of the experimental and numerical results for the interaction between tube vibration and flow perturbations. The *semi-analytical* model developed by Lever and Weaver (1986a,b) is summarized first which forms the basis of the present study. The geometrical aspects of each array pattern are discussed and the mathematical modeling equations are presented. A series of modifications are introduced to the semi-analytical model based on the present experimental and numerical results as discussed in Chapter 5. Theoretical modeling of the amplitude and phase lag of flow perturbations along the flow channel are introduced and coupled with the modified theoretical model. The numerical solution technique is discussed and the present predictions of fluidelastic instability are compared with the experimental data available in the literature.

6.1 Theoretical model development

It was shown in Section 5.1 that a single flexible tube in a rigid parallel triangular array can have the same stability threshold as for the fully flexible array. Thus,

the concept of a single flexible tube in a rigid array is adopted in the present analysis. As the theoretical model is intended to account for the array geometry and pitch ratio effect, which is currently ignored by the ASME design guidelines, the common array geometrical parameters are discussed first.

Four common tube array geometries are used in Heat exchangers. The flow path through these geometries can be defined based on the flow visualization (Scott, 1987) as shown in Figure 6.1 where the letter (A) marks the flow attachment point, while the letter S marks the flow separation point.The flow images show that symmetrical flow channels are formed on both sides of the tubes leaving a wake region behind the tubes. The flow channels in staggard arrays follow a wavy path as shown in Figures 6.1(a), 6.1(b), and 6.1(c), while the flow in an in-line array follows essentially a straight path as shown in Figure 6.1(d). The difference between the flow patterns in staggard and in-line arrays have been discussed by Ziada and Oengoren (1992). It follows that two geometrical groups are introduced, the first group is for parallel triangular array, inline array, and rotated square array with $P_r \leq 1.7$, and the stream tube scaled area A_o in this group can be presented as

$$A_o = P_r - 1 \tag{6.1}$$

The second geometrical group is for normal triangular arrays and rotated square arrays with $P_r > 1.7$, and the A_o can be presented as:

$$A_o = P_r cos(\alpha) - \frac{1}{2} \tag{6.2}$$

The modeling concept is the same for all array geometries. However, the parameters are pattern and pitch ratio dependent. Therefore, the modeling equations and parameters are developed for a parallel triangular array in the following section,

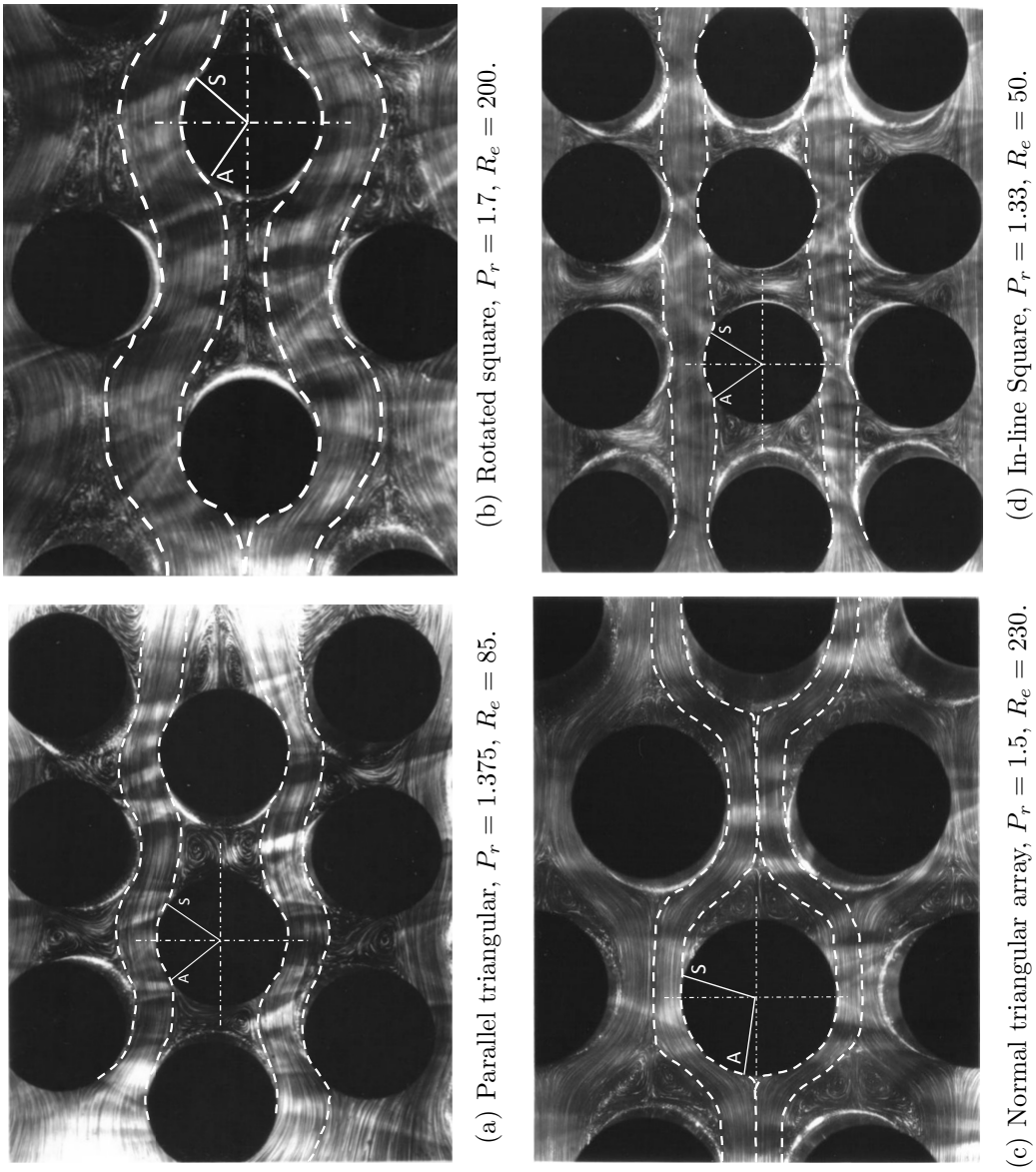

(a) Parallel triangular, $P_r = 1.375$, $R_e = 85$.

(b) Rotated square, $P_r = 1.7$, $R_e = 200$.

(c) Normal triangular array, $P_r = 1.5$, $R_e = 230$.

(d) In-line Square, $P_r = 1.33$, $R_e = 50$.

Figure 6.1: Geometrical parameters of the flow in the four main array geometries, flow visualizations by Scott (1987)

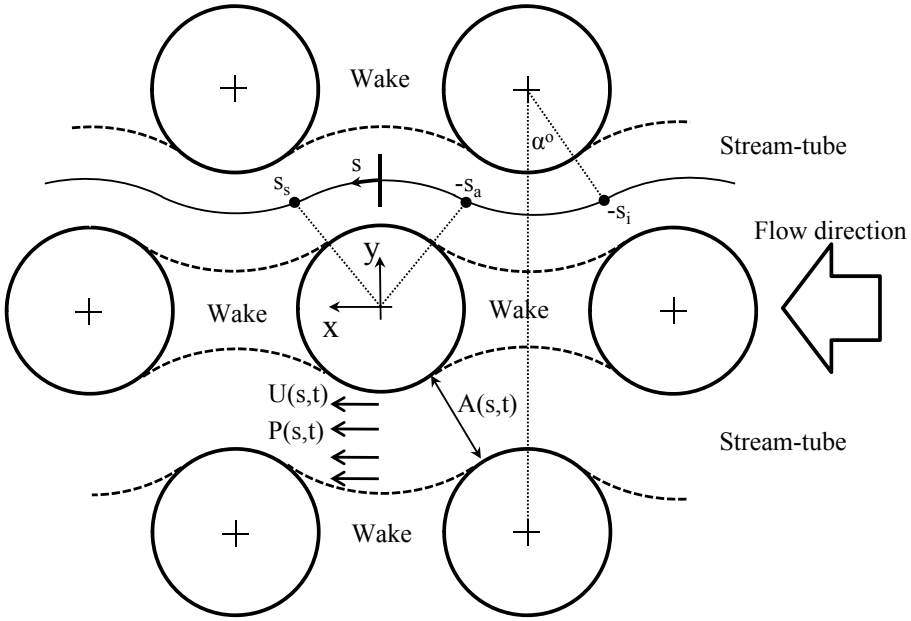

Figure 6.2: Idealized flow in a parallel triangular array.

while the parameters for the other configurations are discussed later in this chapter.

6.1.1 Theoretical Model Fundamentals

Based on past flow visualization (Abd Rabbo and Weaver, 1986; Scott, 1987), the flow in a parallel triangular array can be idealized as shown in Figure 6.2. The stream tubes are assumed to present the fluid flow regions, while the wake regions are assumed to have a minimum effect which can be neglected. A curvilinear coordinate (s) is introduced to present the length along the stream tube. The coordinate (s) of any point presents the summation of circular arcs leading to this point.

The modeled length of the stream tube starts from point $-s_i$ at about one and a half rows upstream and ends at the flow separation point s_s while the flow attaches on the tube at point $-s_a$. These settings were selected as it was found by Tanaka et al. (1982) that the tube vibrations effects on the flow are dissipated beyond two rows from the vibrating tube.

It is assumed that the mean area of the stream tube A_o is constant along the modeled length, while a small harmonic area perturbation $a(s,t)$ is associated with tube vibrations such that the stream tube area $A(s,t)$ can be presented as follows

$$A(s,t) = A_o + a(s,t) \tag{6.3}$$

Due to the fluctuating change in stream tube area, the flow velocity and pressure will have fluctuation components. It follows that, the flow velocity $U(s,t)$ and pressure $P(s,t)$ can be presented using mean values (U_o, P_o) and perturbation components $[u(s,t), p(s,t)]$ as follow

$$U(s,t) = U_o + u(s,t) \tag{6.4}$$

$$P(s,t) = P_o + p(s,t) \tag{6.5}$$

where U_o is the mean gap velocity. The stream area perturbation associated with tube vibrations is assumed to propagate at a certain rate, and as such, there will be a finite time delay (τ) between tube vibration and flow perturbation at any point along the stream tube. This time delay when scaled with the tube frequency presents a phase difference $\phi(s)$. Due to the flow viscous dissipation, the flow perturbations decay with distance from the tube. This decay phenomenon is modeled using a decay function $\psi(s)$ such that

$$\lim_{s\to\infty} \psi(s) = 0 \tag{6.6}$$

Therefore, the area perturbation at any location $a(s,t)$ can be defined based on the area perturbation at the tube as follows

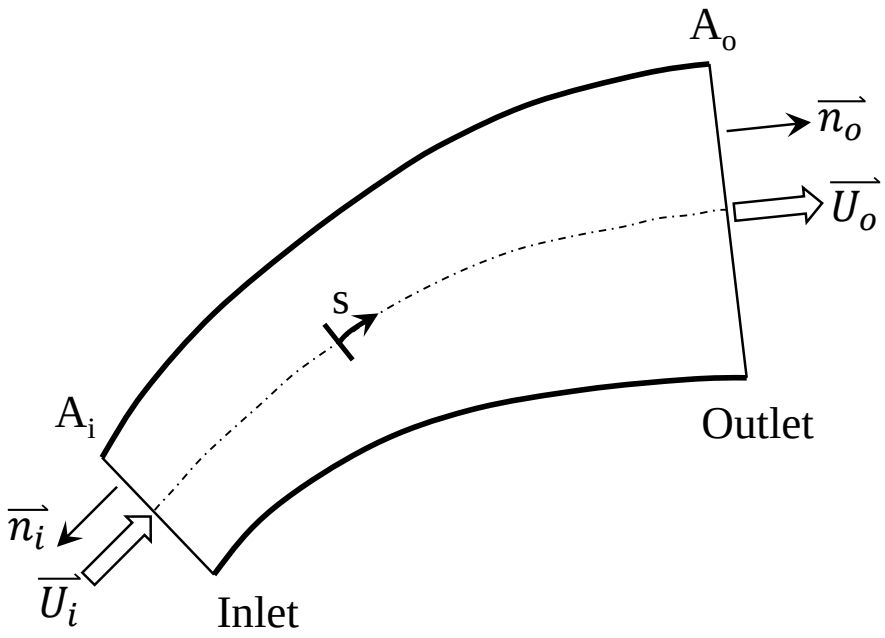

Figure 6.3: The element control volume.

$$a(s,t) = a(-s_m,t)\psi(s)e^{i\phi(s)} \tag{6.7}$$

where $-s_m$ is the location of minimum gap, and $i = \sqrt{-1}$. The flow along the idealized stream tube is solved using one dimensional unsteady Bernoulli's equation to obtain the pressure at any location s. The flow pressures are then integrated over the attachment length on the tube to obtain the fluid forces. These fluid forces are coupled with the tube equation of motion to define the instability conditions.

6.1.2 Conservation of Mass

The problem is modeled as one dimensional, unsteady, incompressible, and inviscid flow in a channel with a variable cross-sectional area. Considering an element control volume as shown in Figure 6.3, the continuity equation along the coordinate s can be written as

$$\frac{\partial}{\partial t}A(s,t) + \frac{\partial}{\partial s}A(s,t)U(s,t)\cdot\bar{n}(s) = 0 \tag{6.8}$$

where $\bar{n}(s)$ is the unit vector normal to the surface of the control volume. The first term on the left hand side of Equation 6.8 represents the rate of mass accumulation in the control volume, while the second term represents the net mass flux across the control volume boundaries. Substituting the flow velocity from Equation 6.4 into Equation 6.8, and integrating from $-s_i$ to s_s leads to

$$\int_{-s_i}^{s_s}\frac{\partial}{\partial t}[A_o + a(s,t)]ds + \int_{-s_i}^{s_s}\frac{\partial}{\partial s}[(A_o + a(s,t))(U_o + u(s,t))]\cdot\bar{n}(s)ds = 0 \tag{6.9}$$

Eliminating the steady-state and higher order terms yields to

$$\int_{-s_i}^{s_s}\frac{\partial}{\partial t}a(s,t)ds + \int_{-s_i}^{s_s}\frac{\partial}{\partial s}[A_o u(s,t) + U_o a(s,t)]\cdot\bar{n}(s)ds = 0 \tag{6.10}$$

Assuming a unit length in the spanwise direction, the terms of Equation 6.10 are scaled as follow

$a^*(s,t)$ $= a(s,t)/D$, where D is the tube diameter.

A_o^* $= A_o/D$

$u^*(s,t)$ $= u(s,t)/U_o$

s^* $= s/D$

t^* $= \omega t$, where ω is the complex frequency of tube response.

U_o^* $= U_o/(\omega_n L_o)$, where ω_n is the tube natural frequency, and L_o is the modeled stream tube length.

L_o^* $= L_o/D$.

Equation 6.10 can be written after performing the integration and scaling the terms as

$$\frac{1}{U_o^*}\frac{\omega}{\omega_n}\int_{-s_i^*}^{s_s^*}\frac{\partial}{\partial t}a^*(s,t)ds^* + L_o^*A_o^*\left[u^*\left(s_s^*,t^*\right)-u^*\left(s_i^*,t^*\right)\right] + L_o^*\left[a^*\left(s_s^*,t^*\right)-a^*\left(s_i^*,t^*\right)\right]=0 \tag{6.11}$$

6.1.3 Conservation of Linear Momentum

The linear momentum equation for unsteady, incompressible, and inviscid flow in a channel with a variable cross-sectional area can be written as

$$\frac{\partial}{\partial t}\left(\int_{cv}U(s,t)\rho dV\right)+\oint_{cs}\left[\rho U(s,t)\left(U(s,t)\cdot\bar{n}(s)\right)\right]dA=\sum F_{ext} \tag{6.12}$$

The first term on the left hand side of Equation 6.12 represents the rate of change of the control volume linear momentum, while the second term represents the net momentum flux across the control surfaces. The right hand side of Equation 6.12 represents the summation of the external forces acting on the control volume. The external forces include gravity forces, shear forces due to viscosity, and pressure forces acting on the control volume. In the present model, the gravity and shear forces are neglected, and the pressure distribution parallel to the stream tube is assumed uniform. Therefore, the external forces can be written as

$$\begin{aligned}\sum F_{ext} &= -\oint_{cs}P(s,t)\cdot n(s)dA \\ &= -A(s_i,t)P(s_i,t)\cdot\bar{n}(s_i)+A(s_s,t)P(s_s,t)\cdot\bar{n}(s_s)\end{aligned} \tag{6.13}$$

Substituting Equations 6.3 and 6.5 into 6.13, the summation of external forces can be written as

$$\begin{aligned}\sum F_{ext} &= -[A_o + a(s_i,t)][P_o + p(s_i,t)] - [A_o + a(s_s,t)][P_o + p(s_s,t)] \\ &= -A_o[p(s_s,t)\cdot\bar{n}(s_s) + p_i(i,t)\cdot\bar{n}(s_i)] - P_h\end{aligned} \tag{6.14}$$

where P_h represents the pressure drop due to flow losses along the modeled stream tube length. The pressure drop term was introduced by Lever and Weaver (1986a) to be proportional to the flow velocity squared. The flow pressure and the pressure drop term can be scaled as follows

$$\begin{aligned}P_h^* &= \frac{hL_o^*U_o^*}{s_i^*}\int_{s_i}^{s_s} u^*(s^*,t^*)ds^* \\ P^* &= \frac{P}{\rho U_o D\omega_n} = \frac{P}{\rho U_o^* D L_o \omega_n^2}\end{aligned} \tag{6.15}$$

where h is a loss coefficient term adopted from the experimental work of Pierson (1937). Eliminating the steady-state and higher order terms and scaling the parameters, the momentum equation can be written as

$$\begin{aligned}&\frac{\omega}{\omega_n}\int_{-s_i}^{s_e}\frac{\partial u^*(s^*,t^*)}{\partial t^*}ds^* + \frac{\omega}{\omega_n A_o^*}\int_{-s_i}^{s_e}\frac{\partial a^*(s^*,t^*)}{\partial t^*}ds^* \\ &+ \frac{U_o^*L_o^*}{A_o^*}[(a^*(s_s^*,t^*) - a^*(s_i^*,t^*)) + 2A_o^*(u^*(s_s^*,t^*) - u^*(s_i^*,t^*))] \\ &+ P_h^* = p^*(s_s^*,t^*) - p^*(s_i^*,t^*)\end{aligned} \tag{6.16}$$

6.1.4 Equations of Motion

The fluid forces acting on the tube are calculated by integrating the pressures over the attachment region on the tube surface. Solution of the continuity and momentum equations show that the velocity and pressure perturbations are directly

related to the magnitude of area perturbation. Therefore, the fluid forces acting on the tube can be calculated for a unit area perturbation at the minimum gap. It follows that the scaled fluid forces in the stream-wise F_L^* and the cross-stream F_T^* can be presented as follow

$$\begin{aligned} F_L^*(t^*) &= \int_{-s_a}^{s_s} p^*(s^*,t^*) Cos\beta(s^*) ds^* \\ F_T^*(t^*) &= \int_{-s_a}^{s_s} p^*(s^*,t^*) Sin\beta(s^*) ds^* \end{aligned} \tag{6.17}$$

where the subscripts L and T denotes the longitudinal and transverse directions respectively, and β denotes the angle corresponding to location s^* on the tube surface. The total forces acting on the tube can be calculated by multiplying the fluid forces due to unit area perturbation F by the area perturbation a. The fluid forces F are scaled as follows

$$F^* = \frac{F}{\rho \omega_n^2 D^2 L_o U_o^*} \tag{6.18}$$

The tube is assumed to behave like a two degree of freedom forced system where the natural frequency is the same in the two directions. The equations of motion can be written as

$$\begin{aligned} m\ddot{x} + c\dot{x} + kx &= F_L a_1(-s_m,t) + F_L a_2(-s_m,t) \\ m\ddot{y} + c\dot{y} + ky &= F_T a_1(-s_m,t) + F_T a_2(-s_m,t) \end{aligned} \tag{6.19}$$

where x and y are the longitudinal and transverse directions respectively, m is the tube equivalent mass per unit length including the fluid added mass, c is the equivalent

system damping, and k is the equivalent system stiffness. The subscripts 1 and 2 on the right hand side of Equation 6.19 refer to stream channel 1 and stream channel 2 on both sides of the tube, and subscripts L and T refer to the longitudinal and transverse directions respectively, while $-s_m$ is the location of minimum gap.

6.2 System Parameters

In Equations 6.11, 6.16, and 6.19, U_o^* is used to represent the mean gap velocity, while the conventional stability maps are referenced to the reduced velocity term $U_r = U_g/fD$. The relationship between U_o^* and U_r is given by

$$U_o^* = \frac{U_o}{2\pi f_n L_o} = U_r \frac{(P_r - 1)cos(\alpha)}{2\pi L_o^* A_o^*} \tag{6.20}$$

6.2.1 Geometrical Aspects

The flow visualizations reported by Scott (1987) showed that the flow attachment and separation points are not symmetrical as assumed by Lever and Weaver (1986a), rather the location of flow attachment and separation are array geometry and pitch ratio dependent. These observations agree well with the present analysis reported in Chapter 3, that the stability behavior is strongly dependent on array geometry and pitch ratio. It follows that the geometrical parameters used in the theoretical model are array geometry and pitch ratio dependent.

The geometrical parameters adopted in Lever and Weaver (1986a) are listed in Table 6.1, where β_a and β_s are the flow attachment and separation angles on the tube surface. The coordinate s^* can be obtained as follow

$$s_a^* = -\frac{sin(\beta_a)}{2}$$
$$s_s^* = \frac{sin(\beta_s)}{2} \tag{6.21}$$

The geometrical parameters are modified in the present study based on the flow visualization reported in the literature. The parameters adopted in the present study are listed in Table 6.2. It is important to note here that the new values for flow attachment, flow separation, and modeled stream channel length are evaluated based on the flow visualizations for a certain pitch ratio. The exact relation between these parameters and the pitch ratio can be the subject of future studies.

6.2.2 Area Perturbation Phase Function

Lever and Weaver (1986a) assumed that the area perturbation associated with tube vibrations does not take place at all points in the stream channel instantaneously. It was assumed that the stream channel area perturbation over the attachment region is in phase with tube vibration, and due to the finite fluid inertia, there is a finite time delay between the perturbations at the tube and the perturbations at any location along the stream channel. This finite time delay when scaled with the tube vibration frequency was modeled by a phase delay function as follows

$$\phi(s^*) = \begin{cases} \dfrac{\omega_n L_o}{U_g}\left(\dfrac{s^*+s_a^*}{s_i^*-s_a^*}\right) = \dfrac{1}{U_o^*}\left(\dfrac{s^*+s_a^*}{s_i^*-s_a^*}\right) & , \quad s^* < -s_a^*; \\ 0 & , \quad -s_a^* \leq s^* \leq s_s^*. \end{cases} \tag{6.22}$$

A comparison between the phase lag predictions using Equation 6.22 and the present experimental results is shown in Figure 6.4. The phase lag theoretical pre-

Table 6.1: Geometrical parameters adopted in Lever and Weaver (1986a) theoretical model

Parameter	α	β_a	β_s	L_o^*	A_o^*	s_i^*
In-line Square	0°	11.5°	11.5°	$4s_i^*$	$P_r - 1$	$1.0P_r$
Parallel Triangular	30°	α/P_r	α/P_r	$8/3s_i^*$	$P_r - 1$	$1.5\alpha P_r$
Rotated Square, $P_r \leq 1.7$	45°	α/P_r	α/P_r	$8/3s_i^*$	$P_r - 1$	$1.5\alpha P_r$
Rotated Square, $P_r > 1.7$	45°	α/P_r	α/P_r	$8/3s_i^*$	$P_r cos(\alpha) - 1/2$	$\frac{P_r sin(\alpha)}{\pi} \int_0^{\pi} \left[1 + \left(\frac{\pi}{4P_r sin(\alpha)}\right)^2 sin^2\beta\right]^{0.5} d\beta$
Normal Triangular array	60°	α/P_r	α/P_r	$8/3s_i^*$	$P_r cos(\alpha) - 1/2$	$\frac{P_r sin(\alpha)}{\pi} \int_0^{\pi} \left[1 + \left(\frac{\pi}{4P_r sin(\alpha)}\right)^2 sin^2\beta\right]^{0.5} d\beta$

Table 6.2: Geometrical parameters adopted in the present study

Parameter	α	β_a	β_s	L_o^*	A_o^*		s_i^*
In-line Square	$0°$	$25°$	$25°$	$4s_i^*$	$P_r - 1$		$1.0P_r$
Parallel Triangular	$30°$	$40°$	$40°$	$8/3s_i^*$	$P_r - 1$		$1.5\alpha P_r$
Rotated Square	$45°$	$65°$	$55°$	$8/3s_i^*$	$P_r - 1$		$1.0\alpha P_r$
Normal Triangular array	$60°$	$80°$	$25°$	$8/3s_i^*$	$P_r cos(\alpha) - 1/2$	$\frac{P_r sin(\alpha)}{\pi} \int_0^{\pi} \left[1 + \left(\frac{\pi}{4P_r sin(\alpha)} \right)^2 sin^2\beta \right]^{0.5} d\beta$	

diction has a linear trend similar to the experimental results. However, the slopes of the theoretical model predictions are different from the experimental results, and the theoretical model assumes a phase of $\phi = zero^{\circ}$ over the attachment region which does not agree with the measurements. It is important to note here that, based on Equation 6.22, the phase lag approaches ∞ as the reduced velocity approaches $U_o^* = zero$. This trend is not physically accurate, as it means that the effect of tube vibrations at a given cycle can still have an effect after infinite number of cycles later.

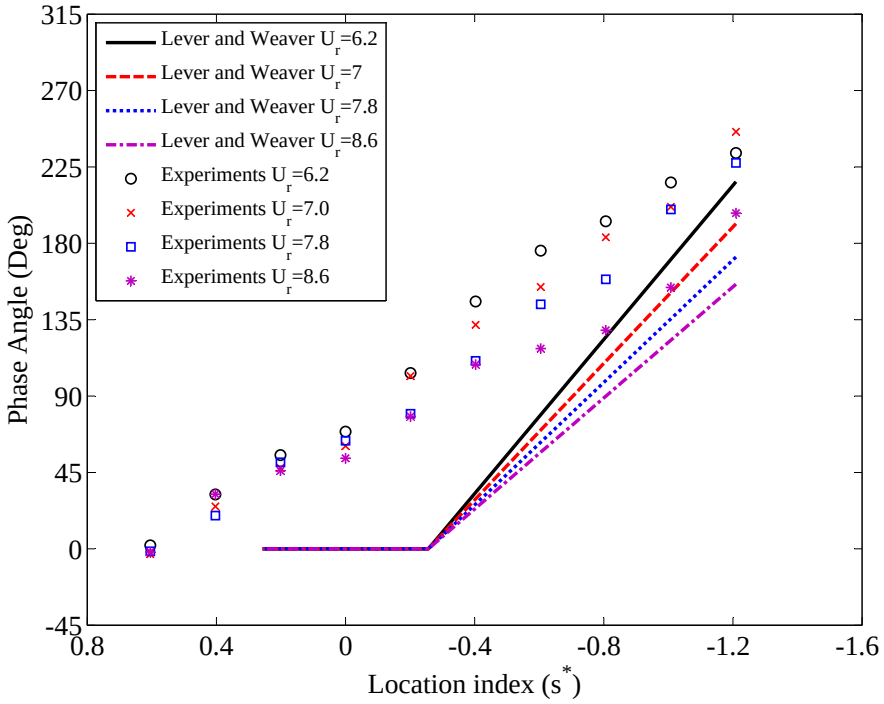

Figure 6.4: Comparison between Lever and Weaver (1986a) theoretical phase prediction and the present experimental results for a parallel triangular array, $P_r = 1.54$.

The experimental results discussed in Section 5.4 suggest that the source of perturbation in the stream channel is the flow separation from the tube. The effect of this perturbation is found to propagate upstream at a rate of $0.42U_g$ as shown in Table 5.1. Considering these two findings, the time between perturbation at the flow

separation point s_s and the same perturbation at any location s can be expressed as

$$\tau = \frac{s - s_s}{U_p} = \frac{s - s_s}{0.42U_g} \tag{6.23}$$

where U_{up} is the propagation rate of flow perturbation upstream. Scaling the terms in Equation 6.23 leads to

$$\frac{\tau^*}{\omega_n} = \frac{(s^* - s_s^*)D}{0.42U_r f_n D} \tag{6.24}$$

which can be reduced to

$$\phi(s^*) = \frac{s^* - s_s^*}{0.42U_r} 2\pi \tag{6.25}$$

A comparison between the phase predictions using Equation 6.25 and the experimental results is shown in Figure 6.5. The present phase predictions are obtained using the geometrical parameters listed in Table 6.2. The present model provides a relatively good agreement with the experimental results for the range of reduced velocity $U_r = 6.2 - 8.6$. The predicted phase trends at all reduced velocities meet at a location index of $s^* = 0.604$ which presents the flow separation point where the perturbation is in phase with tube vibrations.

While the model presented in Equation 6.25 agrees relatively well with the experimental data, it predicts infinite phase lag at small reduced velocity.

$$\lim_{U_r \to 0} \phi(s^*) = \infty$$

However, the numerical simulations discussed in Section 5.5 show that, as the reduced velocity goes below $U_r = 2$, the mechanism of flow perturbation changes fundamentally. It is observed also from the numerical results that there is a continuous

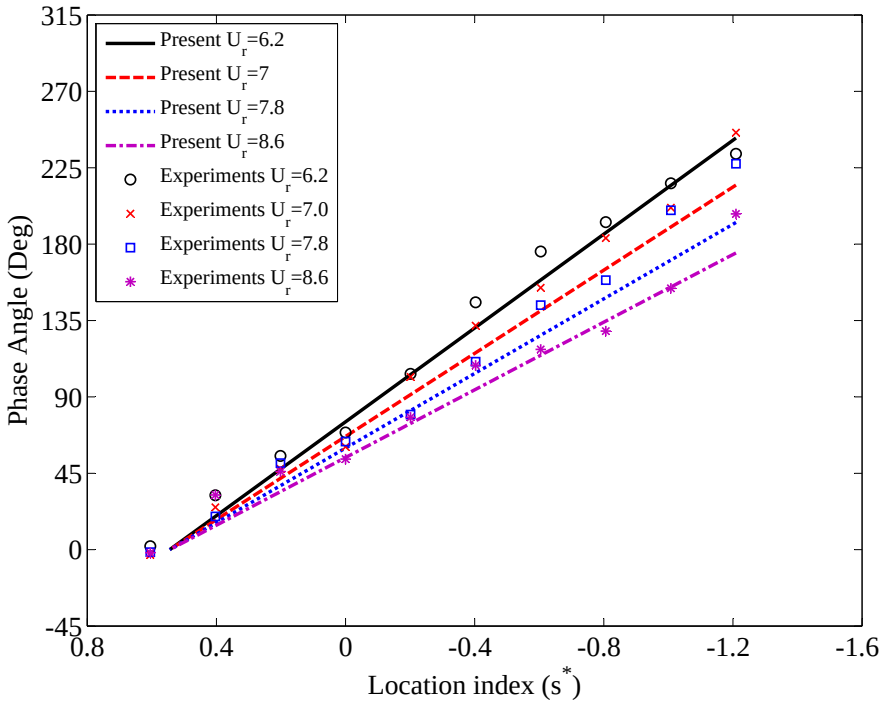

Figure 6.5: Comparison between present phase prediction and the experimental results for a parallel triangular array, $P_r = 1.54$.

transition between the two mechanisms. It seems that both mechanisms are active at all reduced velocities but the relative effect of each mechanism is determined by the reduced velocity. At low reduced velocity, the perturbations caused by pressure pulsations associated with tube vibrations are dominant, and thus, they propagate at the speed of sound. Therefore, all upstream points have a phase of $\phi \approx \pi$ while the downstream points are in phase with tube vibrations as shown in Figure 5.36(a).

This phase trend can be modeled using a transcendental function called the error function which has the form

$$erf(x) = \frac{2}{\sqrt{\pi}} \int_0^x e^{-t^2} dt \tag{6.26}$$

This function can be used to fit the phase trend observed at low reduced velocities numerically as shown in Figure 6.6, where the employed function has the

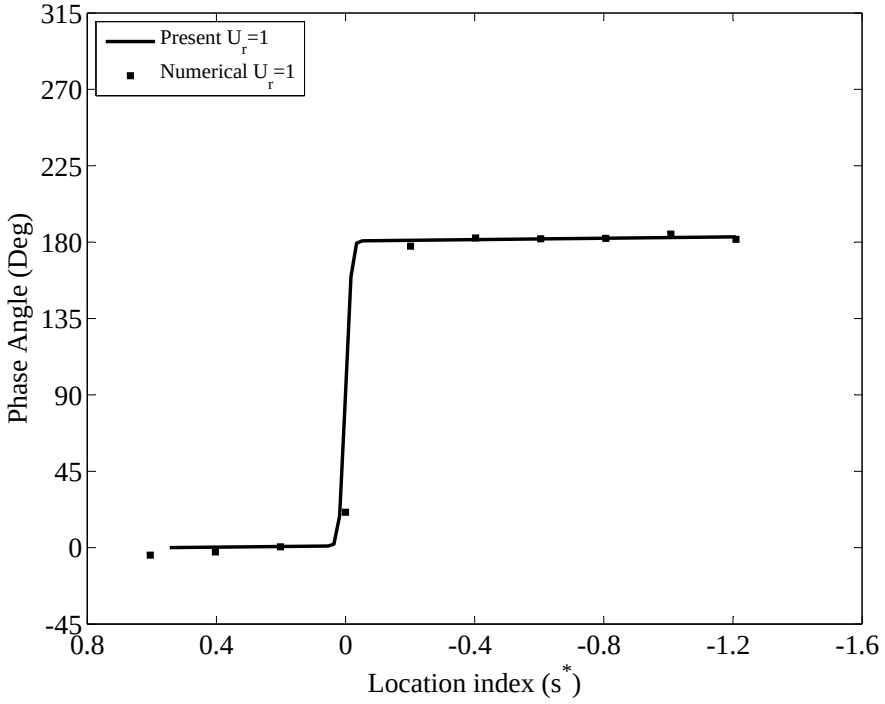

Figure 6.6: Comparison between present phase prediction and the numerical results for a parallel triangular array, $P_r = 1.54$, and $U_r = 1$.

form

$$\phi_1(s^*) = [erf(50s^*) + 1]\,\frac{\pi}{2} \tag{6.27}$$

It follows that, the phase lag term can be represented by two function based on the reduced velocity as

$$\begin{aligned} \phi_1(s^*) &= [erf(50s^*) + 1]\,\frac{\pi}{2}, \qquad && U_r \leq 2 \\ \phi_2(s^*) &= \frac{s^* - s_s^*}{0.42U_r}2\pi, && U_r >> 2 \end{aligned} \tag{6.28}$$

The numerical simulations discussed in Section 5.5 show that there is a continuous transition between the two perturbation propagation mechanisms. This con-

tinuous transition seems to be more realistic as physical phenomena in general tend to be continuous. In order to model the continuous transition between the two mechanisms,a controller (γ) is introduced. The parameter γ takes values from 0 to 1 and acts as a weight factor between the two functions ϕ_1 and ϕ_2 in Equation 6.28. The parameter γ has the following mathematical form

$$\gamma = \frac{erf[2(U_r - 2)] + 1}{2} \tag{6.29}$$

Combining Equations 6.29 and 6.28 leads to

$$\Phi(s^*) = (1 - \gamma)\phi_1(s^*) + (\gamma)\phi_2(s^*) \tag{6.30}$$

where $\Phi(s^*)$ represents the phase function employed in the present model. The phase predictions using Equation 6.30 are compared to the experimental and numerical results as shown in Figure 6.7.

6.2.3 Flow Perturbation Decay Function

The term *"decay"* here refers to the dissipation of flow perturbation along the modeled flow channel. This term is introduced to account for the viscous dissipation in the flow which is neglected in the modeling equations. Lever and Weaver (1986a) ignored this decay term in their model and assumed that the perturbation at the tube propagates with the same amplitude at all points. Later, Yetisir and Weaver (1993a) introduced an arbitrary mathematical function to account for this decay, however this function was based on heuristic argument only.

The present flow perturbation measurements as discussed in Section 5.3 show that a maximum flow perturbation amplitude is observed at the flow separation point.

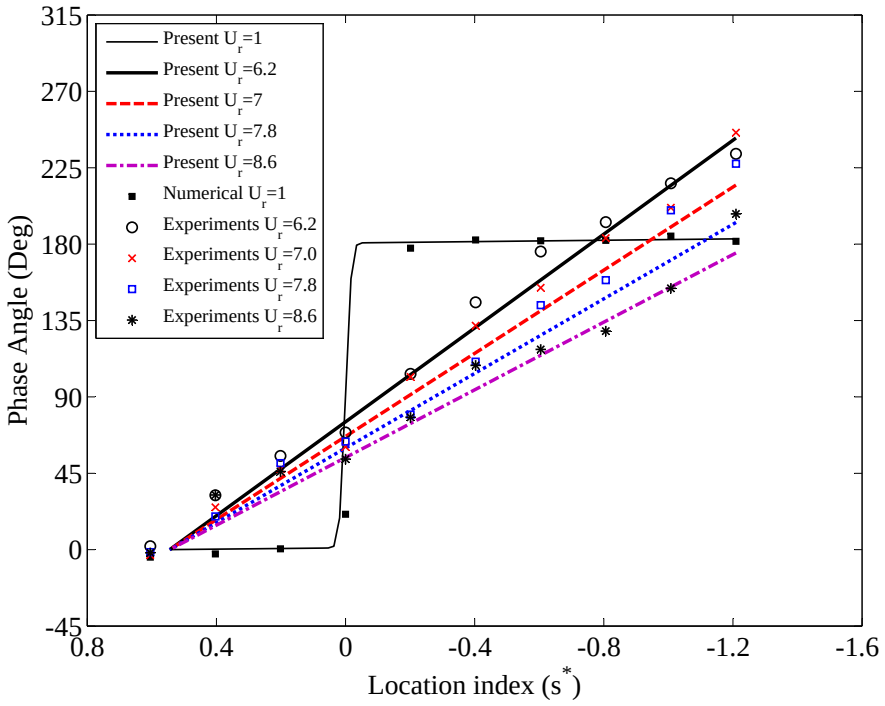

Figure 6.7: Comparison between present phase prediction and the numerical and experimental results for a parallel triangular array, $P_r = 1.54$.

The flow perturbation amplitude along the modeled stream channel, as shown in Figure 5.21 can be represented in the following form

$$\psi(s^*) = \frac{-0.904}{s^* - 0.64} \tag{6.31}$$

The constants in Equation 6.31 are obtained based on the experimental data fitting with a goodness of the fit $R^2 = 0.986$. The goodness of fit parameter R^2 indicates the degree of agreement between the fitted function and the data, such that it has a value of 1 when all the data are 100% represented by the fitting function has a value of *zero* when the data are not presented by the fitting function.

6.3 Solution Procedure

The effect of adjacent tubes vibration, i.e. stiffness mechanism, has been investigated by Yetisir and Weaver (1993a). It was shown that the tube equations of motion in the transverse and longitudinal directions are uncoupled, and thus, the tube stability can be solved for each direction independently. Furthermore, constrained mode analysis has shown that transverse instability is more critical (Price and Paidoussis, 1986a). Therefore, the analysis discussed in this section is for a single flexible tube in a rigid array vibrating in the transverse direction only, while the effect of tube arbitrary motion and adjacent tubes vibrations is a direct extension which can be included in the future.

The mathematical model solution introduced here is based on a unit area perturbation at the minimum gap along the stream channel (a_m^*). Thus, the stream tube area perturbation associated with harmonic tube vibrations in the transverse direction $y(t)$ is evaluated first. Lever and Weaver (1986a) assumed that, the area perturbation along the stream channel is constant and equal to tube vibration amplitude $a_m^* = a^* = y(t)$. Yetisir and Weaver (1993a) assumed that, the area perturbation at the minimum gap in the stream tube is array geometry dependent.

In the present model, the solution is based on a unit area perturbation at the flow separation point s_s^*, and the area perturbations along the stream tube are evaluated using Equation 6.31. Assuming harmonic tube vibrations in the transverse direction of form

$$y(t) = Y e^{i\omega t} \tag{6.32}$$

where Y is the tube vibration amplitude, ω is the tube vibration frequency, and $i = \sqrt{-1}$. The resulting area perturbation at the flow separation point can be written as

$$\begin{aligned} a^*(s_s*,t) &= y(t)cos(\alpha) \\ &= Ycos(\alpha)e^{i\omega t} \end{aligned} \tag{6.33}$$

where α is the array pitch angle. The area perturbation along the stream tube can be calculated as

$$a^*(s^*) = a^*(s_s^*)\psi(s^*)e^{i\omega t+\Phi(s^*)} \tag{6.34}$$

where $\psi(s^*)$ is the area perturbation decay function as indicated in Equation 6.31, and $\Phi(s^*)$ is the phase function as indicated in Equation 6.30. Knowing the stream tube area from Equation 6.34, and solving the continuity Equation 6.11, the velocity perturbation can be expressed as

$$u^*(s^*) = -\frac{a^*(s^*) - a^*(s_i^*)}{A_o^*} - \frac{1}{U_o^*}\frac{\omega}{\omega_n}\frac{1}{L_o^*A_o^*}\int_{s_i^*}^{s^*}\frac{\partial a^*(s^*)}{\partial t^*}ds^* \tag{6.35}$$

Equation 6.35 can be reduced to

$$u^*(s^*) = u_1^*(s^*) + \frac{1}{U_o^*}\frac{\omega}{\omega_n}u_2^*(s^*) \tag{6.36}$$

where u_1^* and u_2^* are functions only of the stream tube area perturbation. It is important to note here that the frequency ratio ω/ω_n is considered unknown in the analysis, which means that the tube response is not forced to be at the tube natural frequency.

The velocity perturbations terms obtained from Equation 6.36 are substituted in the momentum Equation 6.16 to solve for the pressure field. The pressure perturbations can be expressed as

$$p^*(s^*) = U_o^* \left[\frac{L_o^*}{A_o^*} \left(a^*(s^*) - a^*(s_i^*) \right) + 2L_o^* u_1^*(s^*) + \frac{hL_o^*}{s_o^*} \int_{s_i^*}^{s^*} u_1^*(s^*) ds^* \right] + \frac{\omega}{\omega_n} \left[\int_{s_i^*}^{s^*} \frac{\partial u_1^*(s^*)}{\partial t^*} ds^* + \frac{1}{A_o^*} \int_{s_i^*}^{s^*} \frac{\partial a^*(s^*)}{\partial t^*} ds^* + 2L_o^* u_2^*(s^*) + \frac{hL_o^*}{s_o^*} \int_{s_i^*}^{s^*} u_2^*(s^*) ds^* \right] + \left(\frac{\omega}{\omega_n} \right)^2 \frac{1}{U_o^*} \left[\int_{s_i^*}^{s^*} \frac{\partial u_2^*(s^*)}{\partial t^*} ds^* \right] \tag{6.37}$$

Equation 6.37 can be reduced to

$$p^*(s^*) = U_o^* p_1^*(s^*) + \frac{\omega}{\omega_n} p_2^*(s^*) + \frac{1}{U_o^*} \left(\frac{\omega}{\omega_n} \right)^2 p_3^*(s^*) \tag{6.38}$$

where the terms p_1^*, p_2^*, and p_2^* are dependent on the stream tube area and velocity perturbation. By solving Equation 6.38, the pressure field along the stream tube length is calculated. The unsteady fluid forces acting on the tube can be obtained by integrating the pressure along the tube flow attachment line.

$$F^* = \int_{-s_a^*}^{s_s^*} \left[U_o^* p_1^*(s^*) + \frac{\omega}{\omega_n} p_2^*(s^*) + \frac{1}{U_o^*} \left(\frac{\omega}{\omega_n} \right)^2 p_3^*(s^*) \right] ds^* \tag{6.39}$$

Then, the unsteady fluid forces from one stream tube can be expressed as

$$F^* = U_o^* F_1^* + \frac{\omega}{\omega_n} F_2^* + \frac{1}{U_o^*} \left(\frac{\omega}{\omega_n} \right)^2 F_3^* \tag{6.40}$$

The next step is to substitute the unsteady fluid forces into the tube equation of motion. The tube equation of motion in the transversa direction is written as

$$m\ddot{y}(t) + c\dot{y}(t) + ky(t) = 2F(t)Cos(\alpha) \tag{6.41}$$

The right hand side of Equation 6.41 is multiplied by 2 since the unsteady

fluid forces acting on the tube are produced by two identical stream tubes, one on each side of the tube and 180° out of phase with one another. By introducing the system equivalent damping c and stiffness k in the forms

$$c = \frac{m\omega_n\delta}{\pi} \qquad\qquad k = m\omega_n^2$$

where (δ) is the system logarithmic decrement of damping. Scaling the terms in Equation 6.41 leads to

$$-m\omega^2 e^{i\omega t} + \frac{i\omega m\omega_n\delta}{\pi}e^{i\omega t} + m\omega_n^2 e^{i\omega t} = 2F^*\rho\omega_n^2 D^2 L_o U_o^* Cos(\alpha)e^{i\omega t} \tag{6.42}$$

which can be reduced to

$$-\frac{m}{\rho D^2}\left(\frac{\omega}{\omega_n}\right)^2 + \frac{i}{\pi}\frac{m\delta}{\rho D^2}\frac{\omega}{\omega_n} + \frac{m}{\rho D^2}^2 = 2F^* L_o U_o^* Cos(\alpha) \tag{6.43}$$

For simplicity, the right hand side of Equation 6.43 can be presented as

$$\begin{aligned}\bar{F} &= 2F^* L_o U_o^* Cos(\alpha) \\ &= U_o^*\bar{F}_1 + \frac{\omega}{\omega_n}\bar{F}_2 + \frac{1}{U_o^*}\left(\frac{\omega}{\omega_n}\right)^2\bar{F}_3\end{aligned} \tag{6.44}$$

By substituting Equation 6.44 into Equation 6.43, the tube equation of motion can be written as

$$\frac{m}{\rho D^2} = \frac{U_o^*\bar{F}_1 + \frac{\omega}{\omega_n}\bar{F}_2 + \frac{1}{U_o^*}\left(\frac{\omega}{\omega_n}\right)^2\bar{F}_3}{\left[1-\left(\frac{\omega}{\omega_n}\right)^2\right] + i\left[\frac{\delta}{\pi}\frac{\omega}{\omega_n}\right]} \tag{6.45}$$

Equation 6.45 presents the characteristic equation for the present model. By knowing the geometrical parameters for a given array, the unsteady fluid force terms $\bar{F}_1$, $\bar{F}_2$, and $\bar{F}_3$ can be calculated and the characteristic equation can be solved based on the dimensionless velocity U_o^*. The solution of Equation 6.45 provides the frequency ratio (ω/ω_n) and the mass ratio $(m/\rho D^2)$, and thus, the stability map can be plotted using the reduced velocity U_r and the mass damping parameter $(m\delta/\rho D^2)$.

It is important to note here that the tube response frequency in the present model is a complex number in the following form

$$\omega = \omega_R + i\omega_I \tag{6.46}$$

where ω_R represents the oscillatory frequency of the vibration, and ω_I represents the decay or growth rate of the vibration amplitude. The tube vibration behavior associated with the different complex frequency values is demonstrated in Figure 6.8. When the real frequency component $\omega_R = 0$, the response pattern is non-oscillatory. In such case, if the imaginary component has a positive sign $\omega_I > 0$, the response amplitude decays and the system is considered statically stable. On the other hand, if the imaginary component has a negative sign $\omega_I < 0$, the response amplitude increases and the system is considered statically unstable or divergent.

When the real frequency component is non-zero $\omega_R \neq 0$, the response pattern is oscillatory with a frequency of $|\omega_R|$. In such cases, if the imaginary component is positive, the vibration amplitude decays and the system is considered dynamically stable, while if the imaginary component is negative, the vibration amplitude increases and the system is considered dynamically unstable as shown in Figure 6.8. It follows that, the imaginary frequency component switches from a positive value to a negative value or $\omega_I = 0$ at the stability threshold. Therefore the frequency ratio

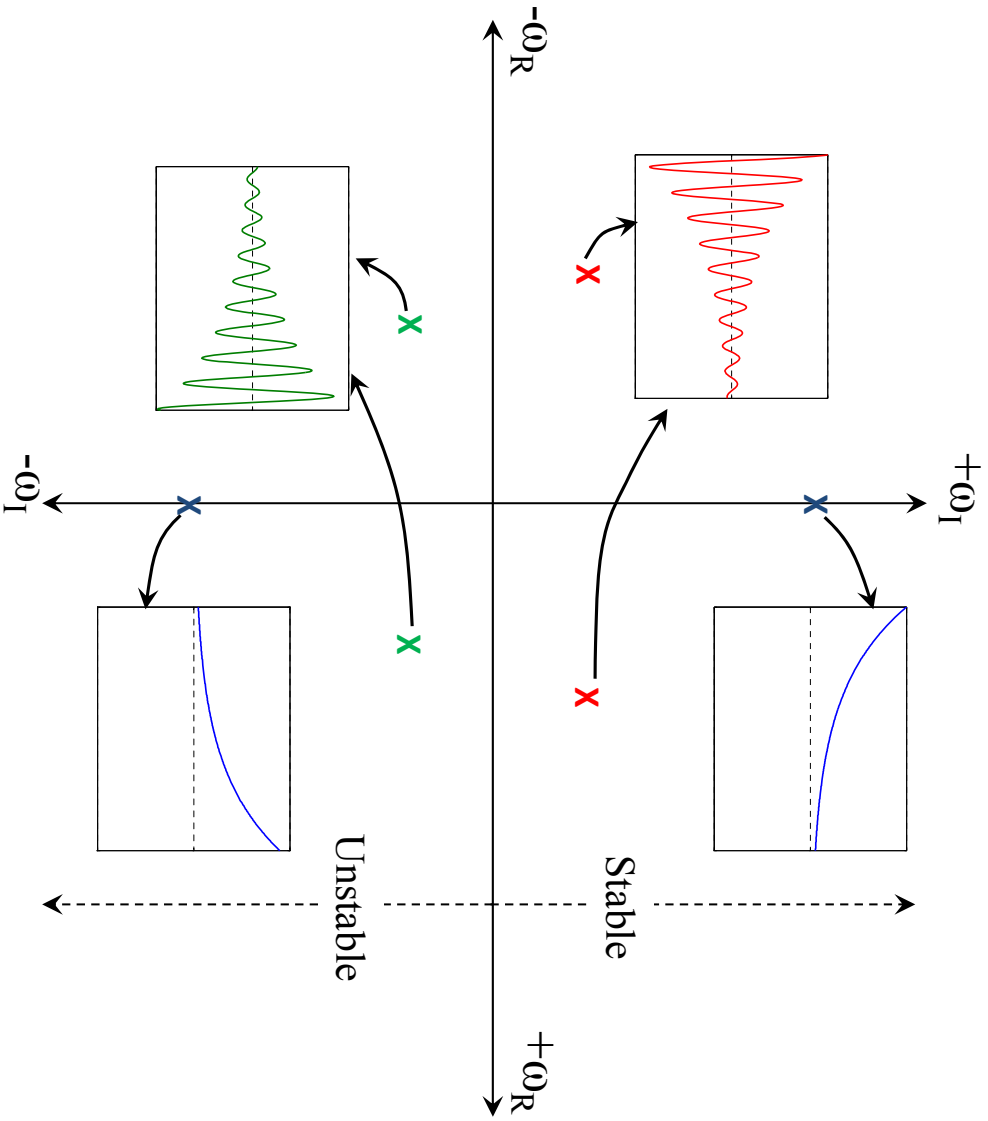

Figure 6.8: Vibration patterns associated with different combination of complex frequencies.

becomes ω_R/ω_n which is a real number. The solution of the Equation 6.45 can then be obtained by setting the velocity and searching for solutions for which the mass ratio and frequency ratio are real numbers.

An iterative solver was developed using MATLAB to solve Equation 6.45. Equation 6.44 is solved first using a frequency ratio of 1 and an assumed U_o^* to obtain the unsteady fluid forces. The calculated unsteady fluid forces are then substituted into Equation 6.45 to calculate the mass ratio and the updated frequency ratio. If the updated frequency ratio is different from the initial value the procedure is repeated until the difference between the old and the updated frequency ratio is $\leq 0.01\%$.

6.4 Stability of a Parallel Triangular Array

6.4.1 Semi-Analytical Model (Lever and Weaver, 1986a)

The solution procedure is used first to check its accuracy by computing the stability maps using the geometrical parameters of the Lever and Weaver (1986a) theoretical model. The dynamic stability boundaries for a parallel triangular array $P_r = 1.375$, a rotated square array $P_r = 1.375$, a normal triangular array $P_r = 1.4$, and an in-line square array $P_r = 1.33$ are shown in Figure 6.9. When the present numerical solution is compared with the analytical solution of Lever and Weaver (1986a), the stability boundaries are identical within 0.5%.

The Lever and Weaver (1986a) stability predictions for a parallel triangular array were in reasonable qualitative agreement with the experimental results reported by Weaver and Fitzpatrick (1988) as shown in Figure 6.9(a). It is observed that the agreement between the stability predictions and the experimental data is not as good for the rotated square and normal triangular array as shown in Figures 6.9(b),

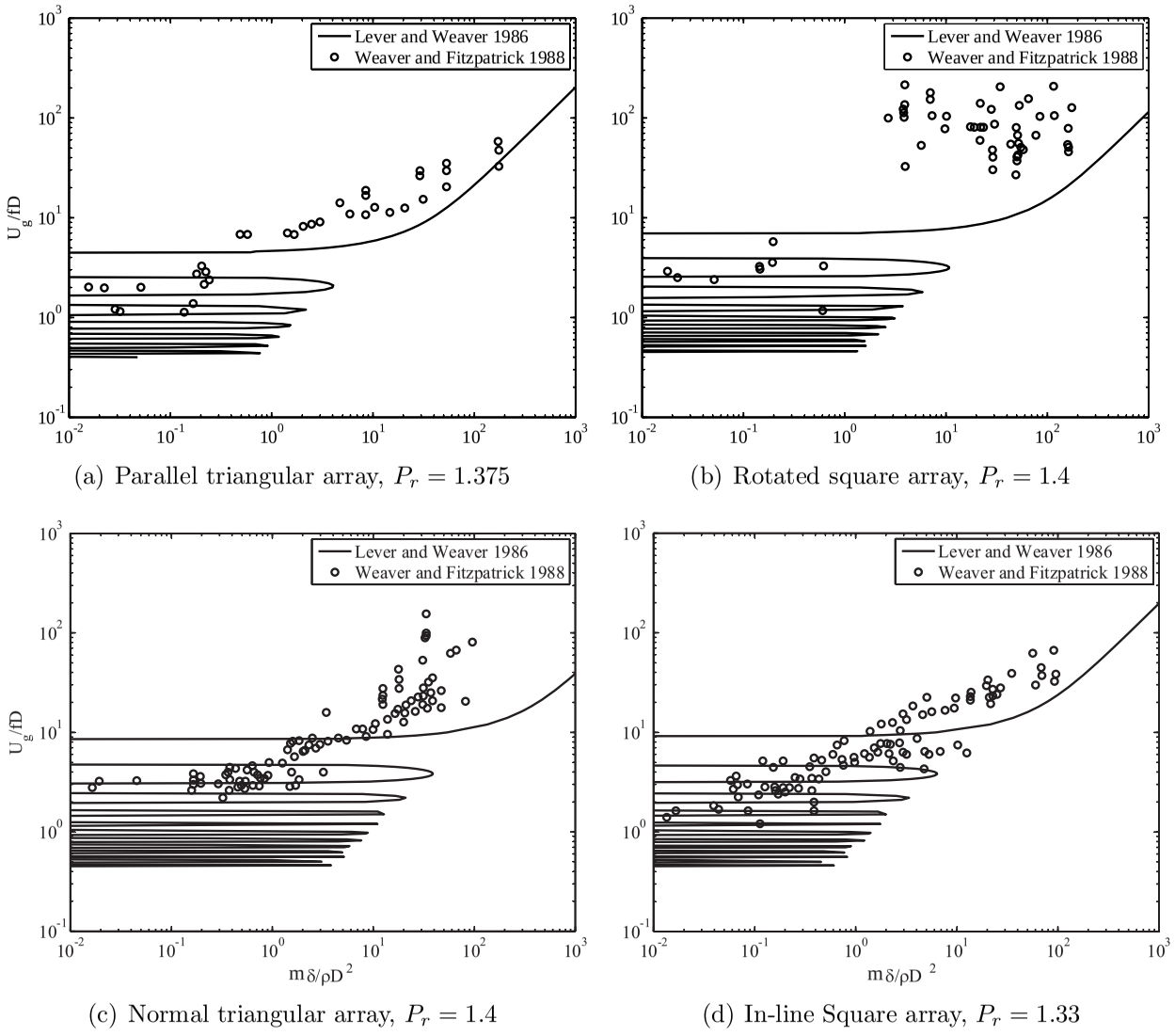

(a) Parallel triangular array, $P_r = 1.375$

(b) Rotated square array, $P_r = 1.4$

(c) Normal triangular array, $P_r = 1.4$

(d) In-line Square array, $P_r = 1.33$

Figure 6.9: Stability maps for the common tube array configurations developed using the geometrical parameters adopted by Lever and Weaver (1986a).

and 6.9(c) respectively. However, a relatively good agreement with the experimental results is observed for the in-line square array as shown in Figure 6.9(d).

It is important to note here that the Lever and Weaver (1986a) theoretical stability maps for all array geometries show multiple stability loops at lower mass damping and reduced velocity parameters. While the existence and physical nature of these multiple stability loops remain unresolved, they are predicted by all the theoretical models developed to date. It is known that these multiple stability loops are associated with large values of the phase between tube motion and fluid response. As such, Lever and Weaver (1986a) considered only two stability loops arguing that the disturbances caused by tube motion must be completely dissipated within two cycles of vibrations.

6.4.2 Present Model

In this section the modifications proposed in the previous sections are applied to develop new stability maps for the common array geometries. The proposed modifications are recaped here as follows

- The geometrical parameters such as flow attachment and separation locations have been modified based on the flow visualization for different array patterns (Scott, 1987). The geometrical parameters adopted in the present model for the common array patterns are listed in Table 6.2
- The flow perturbation decay rate has been modeled based on the present measurements discussed in Section 5.3. Equation 6.31 presents the flow perturbation decay model.
- The time delay between tube vibrations and the associated flow perturbations has been modeled as a phase function based on the present measurements

and simulations discussed in Sections 5.4 and 5.5 respectively. Equation 6.30 presents the relative phase between flow perturbation at the flow separation point and the flow perturbations at any location along the stream tube.

The predicted stability boundaries and tube response frequency for a parallel triangular array with $P_r = 1.375$ are shown in Figure 6.10. The present stability boundaries follow well the experimental data reported by Weaver and Fitzpatrick (1988) for mass damping parameter range $m\delta/\rho D^2 \approx 0.6 - 200$. It is observed that the present stability boundary asymptotes as the experimental data asymptote for $m\delta/\rho D^2 \leq 10$ at a reduced velocity of about $U_g/fD \approx 9.5$.

Only one instability loop is predicted by the present model in contrast with most of the theoretical models in the literature which predict an infinite number of instability loops. The instability loop occurs at reduced velocity range $U_g/fD = 1.5 - 2$ and for mass damping parameters $m\delta/\rho D^2 \leq 3$. It must be noted here that the existence of this stability loop is theoretical only, as once the tube becomes fluidelastically unstable, increasing the reduced velocity will not stabilize the tube. It follows that the practical stability boundaries follows the lower bound of both loops. The prediction of a single stability loop as shown in Figure 6.10 may explain the sudden drop in the experimental fluidelastic stability data for a parallel triangular array at a mass damping parameter $m\delta/\rho D^2 \approx 0.3$.

Examining the tube response frequency as shown in Figure 6.10 is quite revealing. The response frequency ratios for reduced velocities $U_g/fD \leq 40$ are about 1 ± 0.03, except at a reduced velocity of about $U_g/fD \approx 9.5$ where the discontinuity in response frequency ratio corresponds to the theoretical gap between the two stability boundaries. This result agrees with most of the experimental observations reported in the literature that the tubes become fluidelastically unstable at a frequency ratio

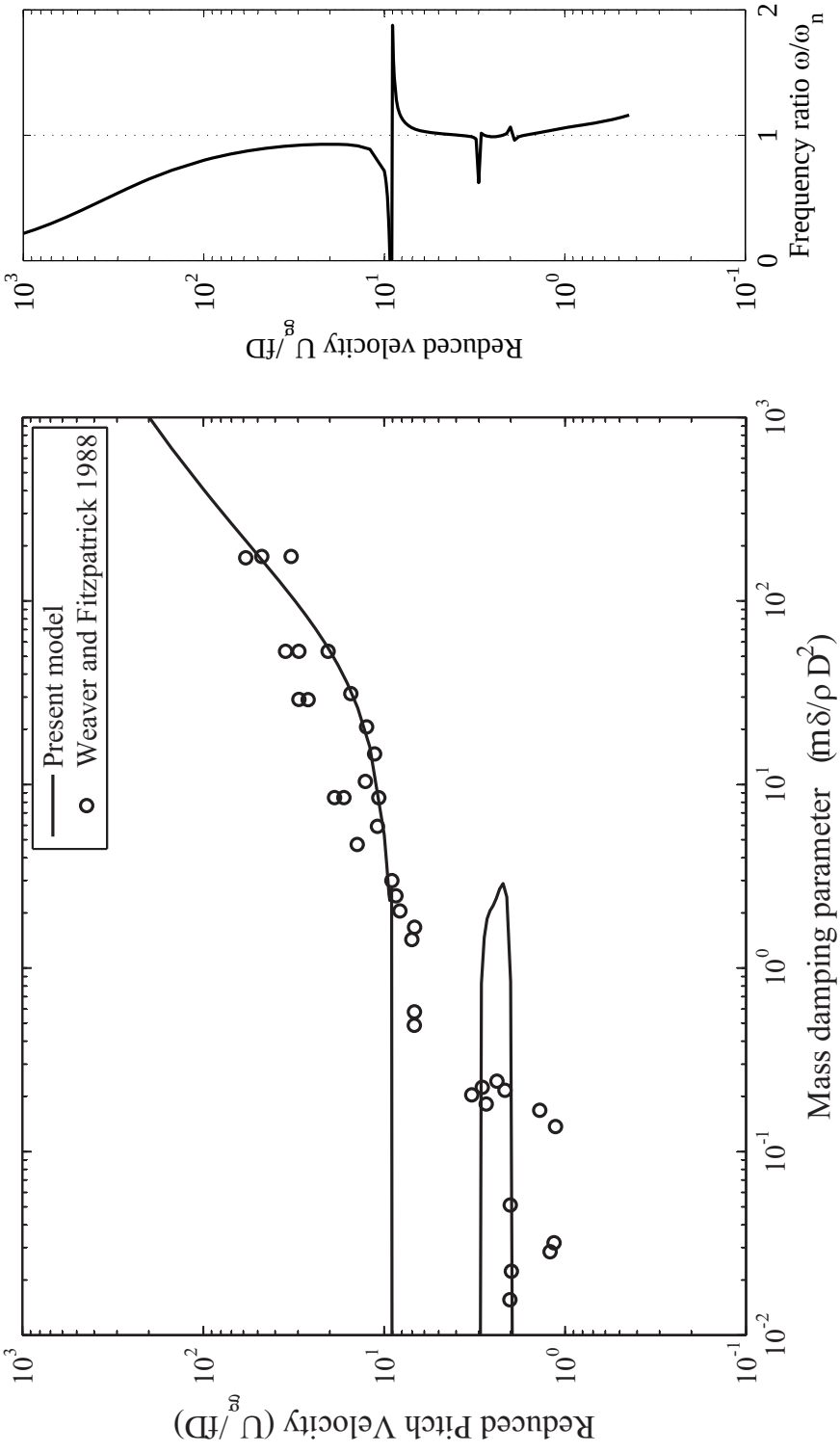

Figure 6.10: Stability map and response frequency for a parallel triangular tube array with $P_r = 1.375$.

of about 1. The predicted response frequency ratio starts to shift down towards *zero* for reduced velocities $U_g/fD > 40$ indicating that over this region, the single flexible tube model, i.e. the damping mechanism model, is not sufficient to properly predict fluidelastic instability. The stability boundary at a reduced velocity of $U_g/fD \approx 40$ corresponds to a mass damping parameter of $m\delta/\rho D^2 \approx 200$. It follows that modeling of the stiffness mechanism, i.e. coupling of adjacent tubes vibrations, becomes essential to predict fluid elastic instability at higher mass damping parameters. This outcome agrees with the analysis reported by Paidoussis and Price (1988) and Yetisir and Weaver (1993a).

6.5 Sensitivity Analysis

It is important when introducing a new theoretical model to investigate the sensitivity of the model predictions to the numerical values of the different parameters involved. Lever and Weaver (1986a) conducted a detailed sensitivity analysis on the model parameters, and therefore, the present sensitivity analysis is concerned only with the phase lag function (Equation 6.30) and the flow perturbation decay function (Equation 6.31), the terms newly introduced to the model. The sensitivity analysis is conducted to investigate the effect of parameter variations within $\pm 10\%$ on the quantitative predictions of the model. The effect of perturbation propagation velocity upstream U_p, reduced velocity of switching between the two flow perturbation propagation mechanisms, and the flow perturbation decay rate are investigated in this section.

6.5.1 Perturbation Propagation Rate U_p

Figure 6.11 shows the effect of varying the flow perturbation propagation rate by ±10%. Increasing the propagation rate U_p by 10% as shown in Figure 6.11(a) resulted in a reduction of the stability boundary less than 4% at a mass damping parameter $m\delta/\rho D^2 = 20$. The stability boundary for mass damping parameter $m\delta/\rho D^2 \geq 40$ is not affected by increasing the perturbation propagation rate. The reduced velocity range of the lower stability loop is reduced by about 8%. However, the stability loop lower bound which is the practical stability boundary is slightly increased by about 2%.

A reduction of the flow perturbation propagation rate increases, as expected, the stability boundaries as shown in Figure 6.11(b). The critical reduced velocity corresponding to a mass damping parameter of $m\delta/\rho D^2 = 20$ is shifted up by about 4%. Similar to the previous case, the stability boundary for mass damping parameter $m\delta/\rho D^2 \geq 40$ is not affected by decreasing the propagation rate. The stability loop span on the reduced velocity axis was increased by about 8%, however the lower bound of the stability loop was shifted down by about 1%. It is observed that a 'notch' is formed in the stability loop as shown in Figure 6.11(b), as a result of the slower perturbation propagation rate. Slower perturbation propagation rates result in larger phase lag values at lower reduced velocities and ultimately multiple stability loops.

6.5.2 Mechanisms of Perturbation Propagation

As discussed in Section 6.2.2, two different perturbation propagation mechanisms are believed to exist depending on the reduced velocity. Based on the CFD

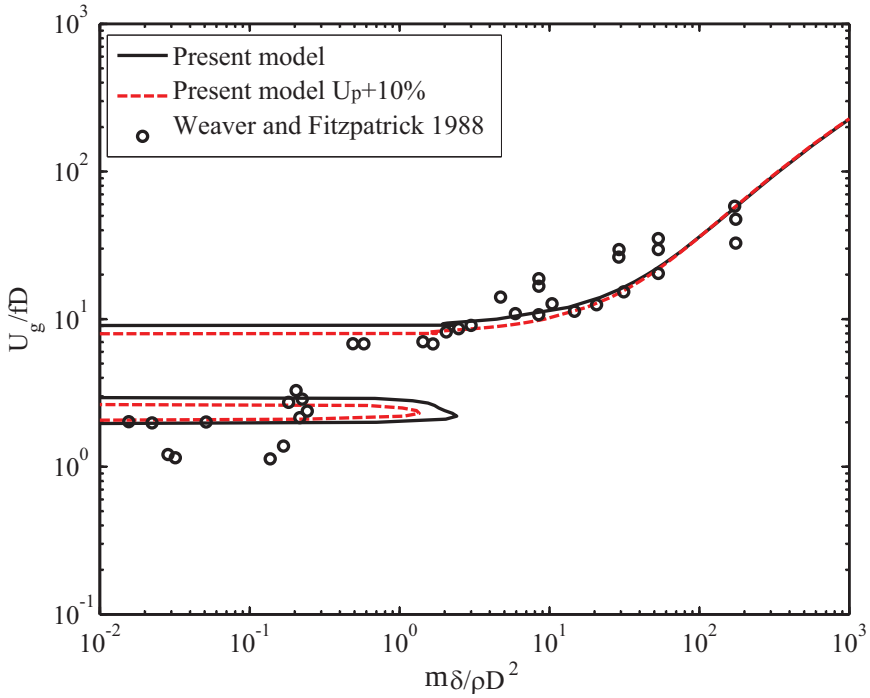

(a) Propagation velocity $U_p + 10\%$

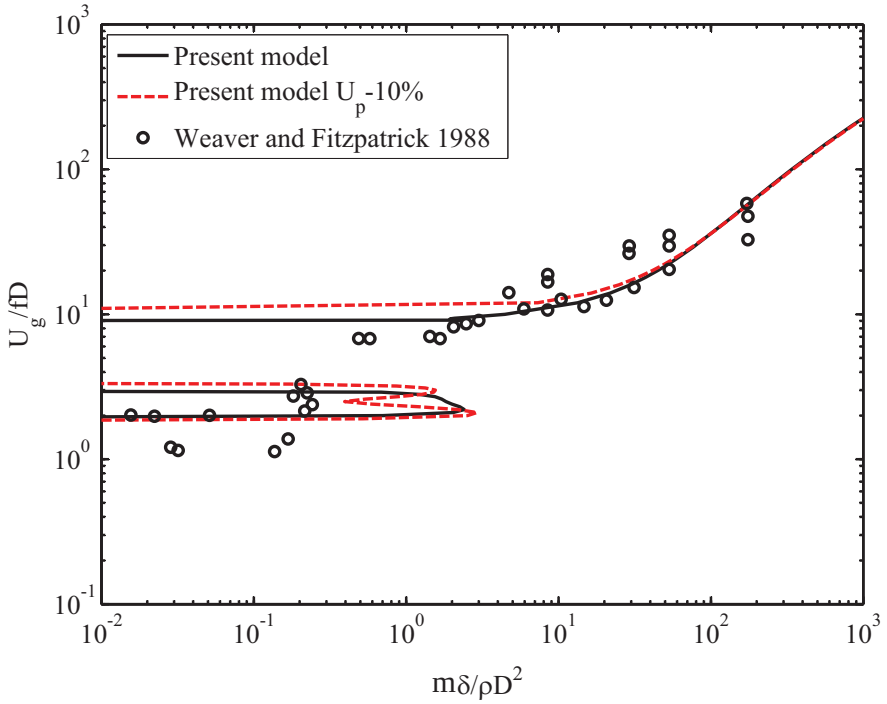

(b) Propagation velocity $U_p - 10\%$

Figure 6.11: Effect of varying flow perturbation propagation rate on the stability boundaries for a parallel triangular array $P_r = 1.375$.

simulations, it was found that below a reduced velocity of $U_r \leq 2$ the dominant mechanism is the pressure wave propagation at the speed of sound while for higher reduced velocity values $U_r > 4$, the dominant mechanism is caused by flow separation and vorticity generation at the tube. In order to investigate the model sensitivity to this transition point, both small ($\pm 10\%$) and large ($\pm 50\%$) variations of the transition point value are examined.

The effect of varying the transition point by $\pm 10\%$ is shown in Figure 6.12. Increasing the transition point by 10% as shown in Figure 6.12(a) shifted the lower bound of the lower stability loop by about 10% without affecting the upper bound of the stability loop. Decreasing the transition point by 10% as shown in Figure 6.12(b)results in a change in the second stability loop shape similar to that produced by decreasing the flow propagation rate. The lower bound of the stability loop is shifted down by about 15% without affecting the upper bound. The change in the stability loop is attributed to the larger phase lag values predicted at lower reduced velocities.

In order to investigate the quantitative effect of large variations in the transition point between the two propagation mechanisms, large variations $\pm 50\%$ are examined as shown in Figure 6.13. Shifting the transition reduced velocity from $U_r = 2$ to $U_r = 3$ as shown in Figure 6.13(a) results in the elimination of the lower stability loop for reduced velocity $U_r \leq 3$ with no effect on the stability boundary above $U_r = 3$. On the contrary, decreasing the reduced velocity of switching from $U_r = 2$ to $U_r = 1$ results in the generation of a second and third stability loop as shown in Figure 6.13(b).

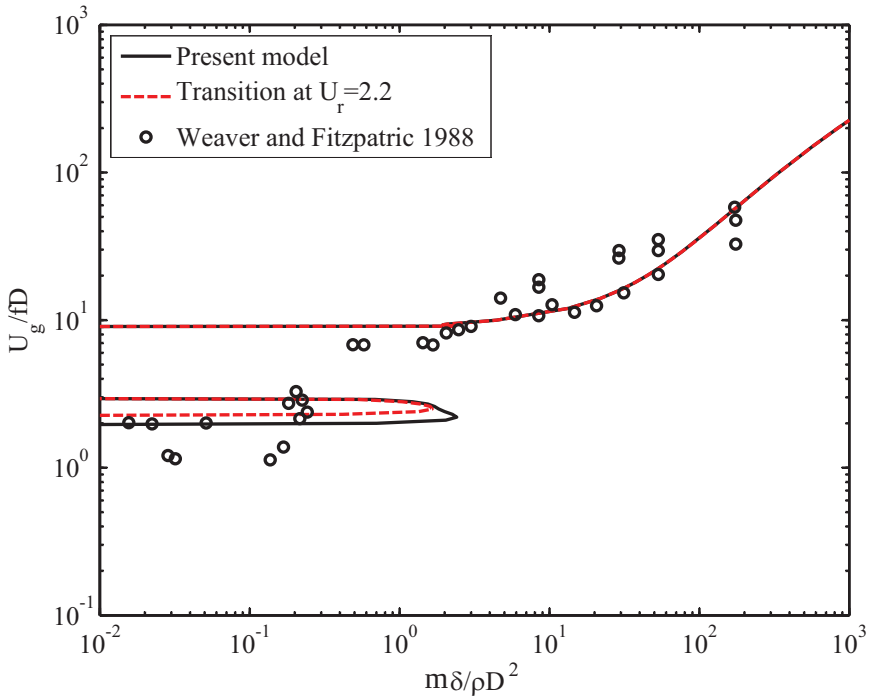

(a) Transition +10%

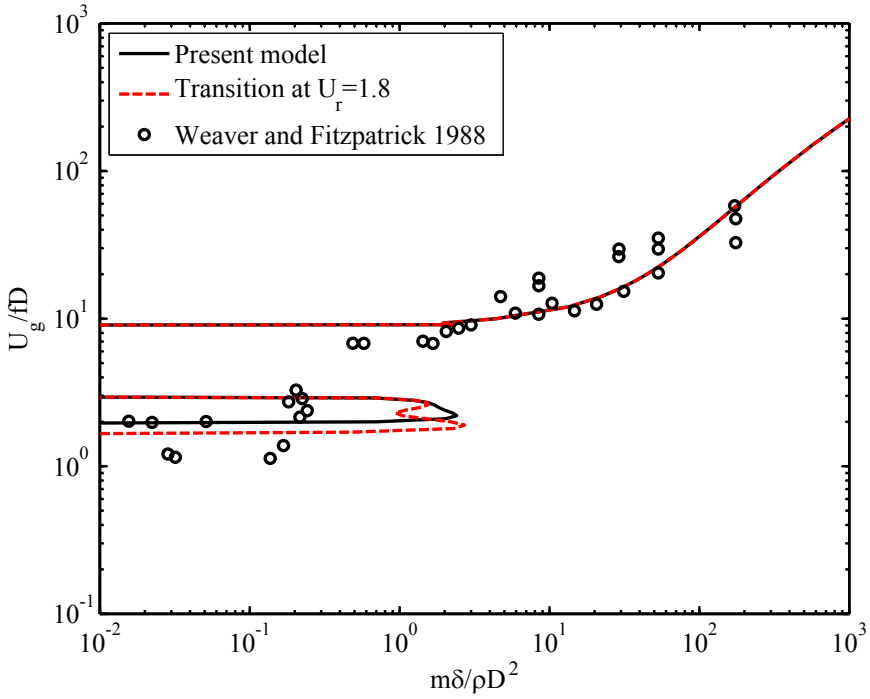

(b) Transition −10%

Figure 6.12: Effect of varying slightly the relative importance of phase lag mechanism on the stability boundaries for a parallel triangular array $P_r = 1.375$.

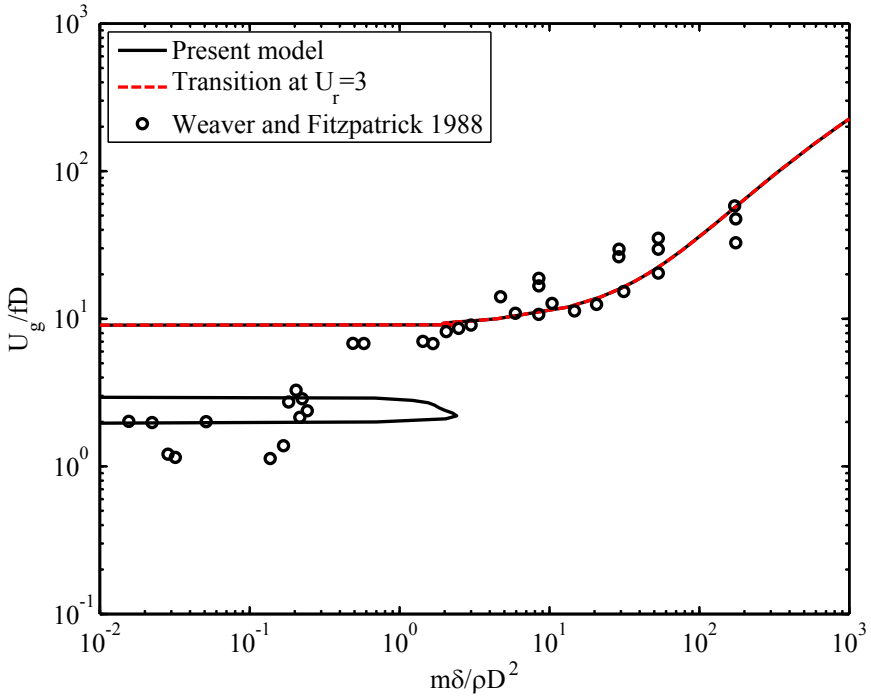

(a) Transition +50%

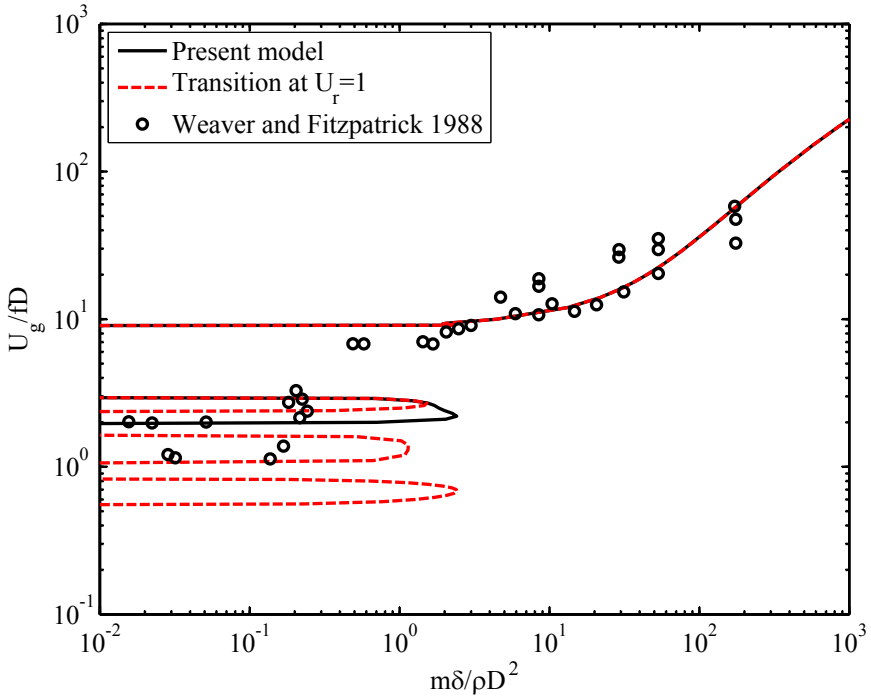

(b) Transition −50%

Figure 6.13: Effect of varying significantly the relative importance of phase lag mechanism on the stability boundaries for a parallel triangular array $P_r = 1.375$.

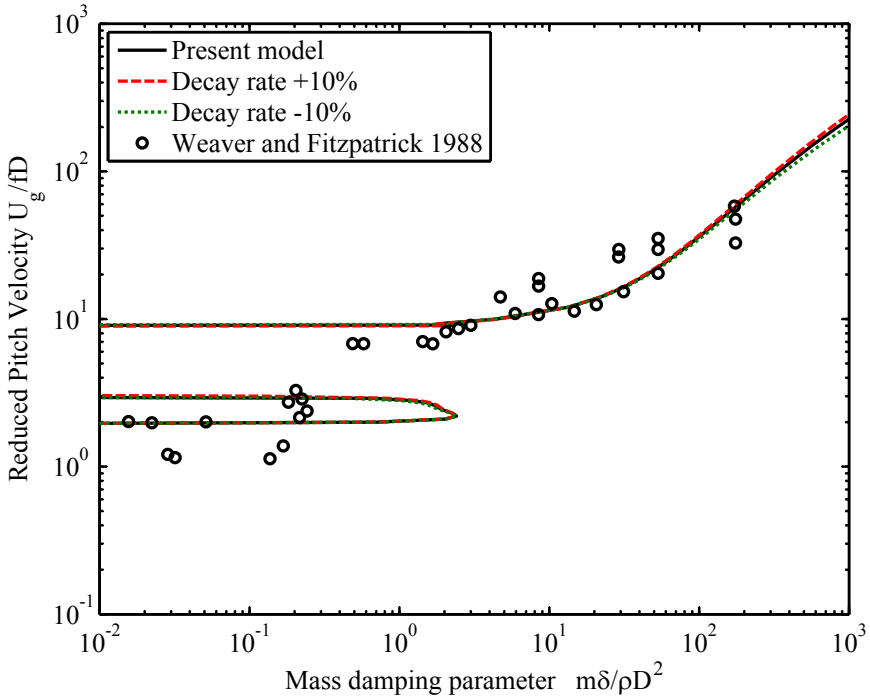

Figure 6.14: Effect of flow perturbation decay rate on the stability map for a parallel triangular tube array $P_r = 1.375$.

The existence of these stability loops is directly related to the phase lag values, such that large phase lag values ($\Phi > n\pi$) produce multiple stability loops, and the number of stability loops depends on the number of lagging cycles (n). It follow that, for smaller phase lag values ($\Phi < \pi$), only one stability boundary is predicted as shown in Figure 6.13(a).

6.5.3 Flow Perturbation Decay Rate

The effect of variations of the flow perturbation decay rate, as in Equation 6.31, by $\pm 10\%$ is investigated. It is found that small increase or decrease in the decay rate by 10% has a negligible effect on the stability boundaries as shown in Figure 6.14. It is found that varying the decay rate up to $\pm 20\%$ has minimum effects on the predicted stability boundaries.

6.6 Stability of Other Tube Array Patterns

In this section, the stability boundaries for the common array geometries are calculated using the present phase function as in Equation 6.30, the present flow perturbation decay function as in Equation 6.31, and the geometrical parameters listed in Table 6.2.

6.6.1 In-line Square Array

The stability map and tube response frequency ratio for an in-line square array with $P_r = 1.33$ are shown in Figure 6.15. The present stability boundary agrees reasonably well with the experimental data provided by Weaver and Fitzpatrick (1988) for the entire range of mass damping parameter except between $m\delta/\rho D^2 = 2-10$ where the large experimental data scatter makes it difficult to define a physical trend for the phenomenon. The presence of a stability loop at a reduced velocity of about $U_r = 1.5$ agrees qualitatively with the trend of the experimental data.

The response frequency ratio has a value of about $(\omega/\omega_n = 1 \pm 0.04)$ for a reduced velocity range $U_r = 0.4 - 60$ except for the points of discontinuity between the lower stability loop and the upper boundary. This outcome agrees with the observations reported in the literature for fluidelastic instability at relatively low mass damping parameters as discussed in Chapter 3. The response frequency ratios for reduced velocities $U_r > 60$, which corresponds to mass damping parameter $m\delta/\rho D^2 > 200$, shift down towards *zero* indicating that modeling the damping mechanism only is not sufficient to predict the fluidelastic instability at a relatively high mass damping parameters. It is important to note here that the flow perturbation phase and decay functions used to develop this stability map are based on the experimental data for a parallel triangular array.

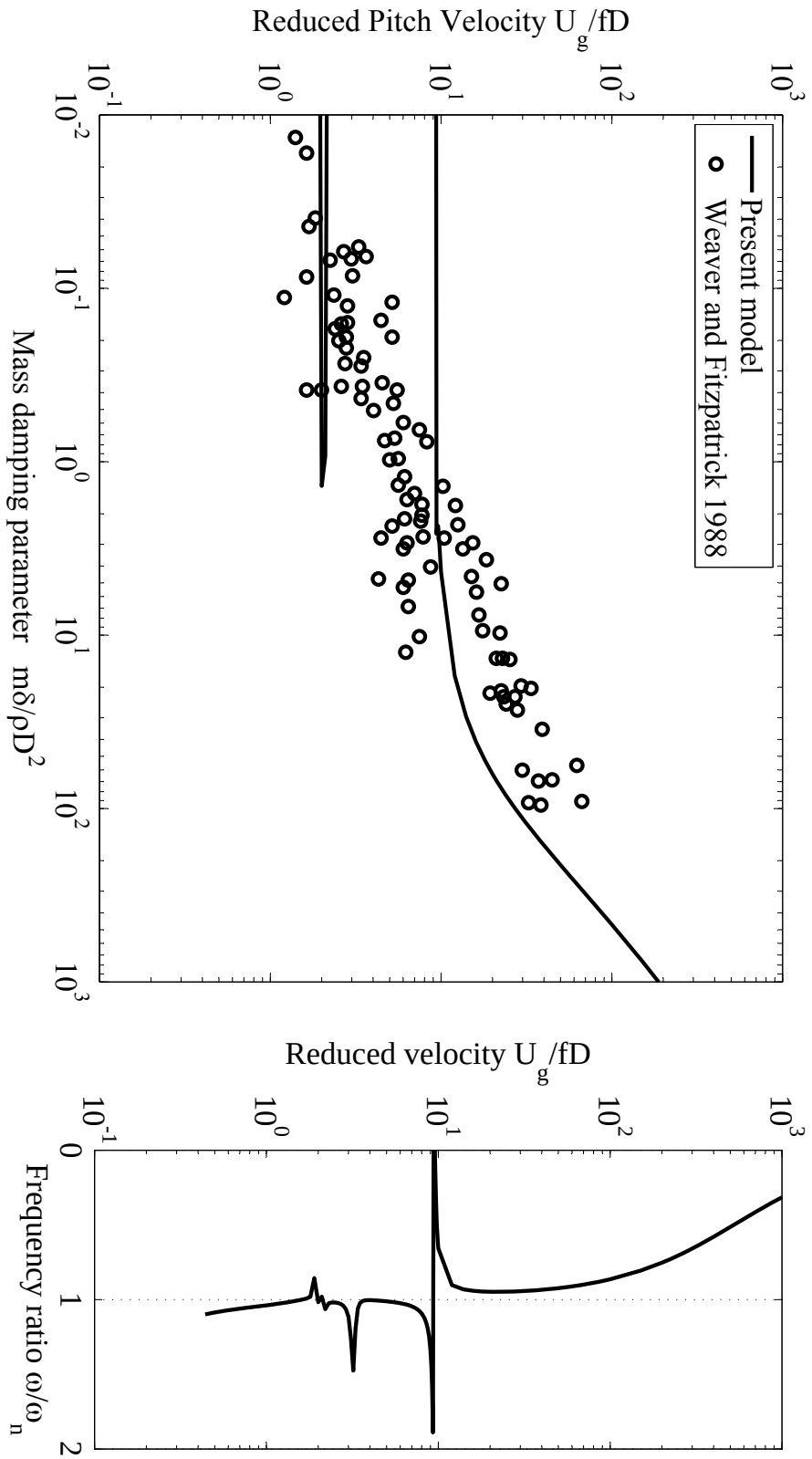

Figure 6.15: Stability map and response frequency for an in-line square tube array with $P_r = 1.33$.

6.6.2 Normal Triangular Array

The stability map and tube response frequency ratio for a normal triangular tube array with $P_r = 1.4$ are shown in Figure 6.16. Similar to the parallel triangular and in-line square arrays, one theoretical stability loop is predicted. It is observed that the lower stability loop spans the mass damping parameter between $m\delta/\rho D^2 = 0.01 - 1.5$ where the experimental data asymptote at a reduced velocity value of about $U_r \approx 2$, while the upper stability boundary follows well the mean trend of the experimental data. Considering the amount of scatter in the literature data, the present model predicts reasonably well the data trend.

The response frequency ratio for the normal triangular array pattern has a value of about 1 ± 0.04 over the range of reduced velocity $U_r = 0.4 - 60$. The frequency ratios for reduced velocity $U_r > 60$, which corresponds to mass damping parameters $m\delta/\rho D^2 > 150$, shift down towards *zero* indicating the need for modeling the stiffness mechanism, i.e. the adjacent tubes vibrations, to properly predict fluidelastic instability.

The stability boundaries shown in Figure 6.16 are developed using the flow perturbation decay and phase functions for a parallel triangular array. A relatively good agreement with the experimental results is achieved which indicates that the actual phase and decay functions for a normal triangular array may not be much different from those for a parallel triangular array.

6.6.3 Rotated Square Array

The stability map and tube response frequency ratio for a rotated square array with $P_r = 1.4$ are shown in Figure 6.17. A single theoretical stability loop is predicted as for the cases of the other array geometries. Because of the large scatter

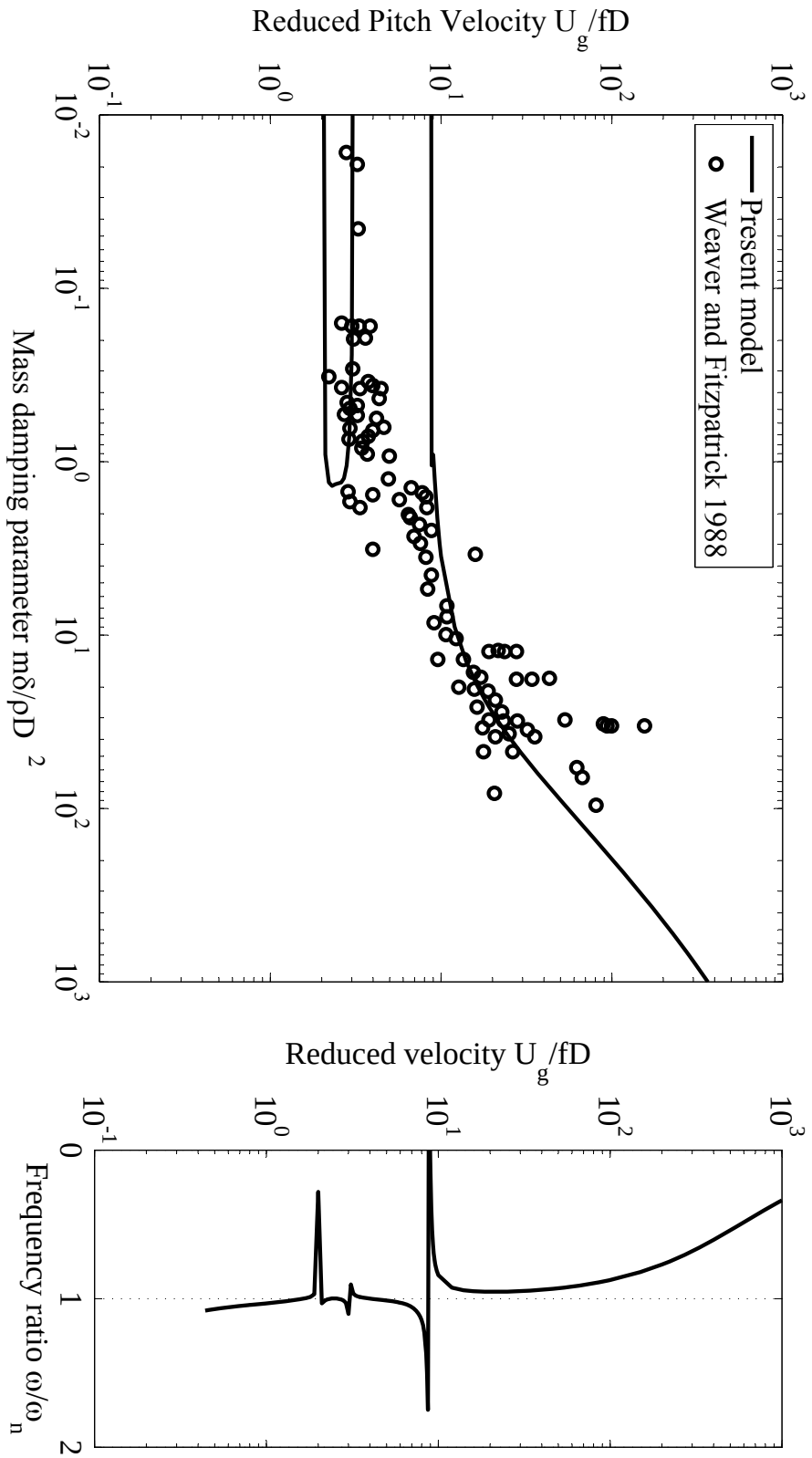

Figure 6.16: Stability map and response frequency for a norma triangular tube array with $P_r = 1.4$.

in the literature data reported by Weaver and Fitzpatrick (1988), it is difficult to define a physical trend to establish a clear comparison. The data scatter is greater than that for other arrays and less data is available. However, the predictions provide a reasonable lower bound to the available data and are a definite improvement over previous models.

6.7 Discussion

The theoretical model introduced in this study presents an improvement to the theoretical model developed by Lever and Weaver (1986a) and modified later by Yetisir and Weaver (1993a). The stream tube geometrical parameters have been modified in the present model based on the flow visualizations of Scott (1987). The flow perturbation phase and decay functions have been modeled based on the experimental measurements, coupled with further insights generated by the CFD model. Sensitivity analysis has been conducted to investigate the effect of varying the modeled parameters on the model performance.

The stability predictions for the parallel triangular array are in a relatively good agreement with the experimental results. It is important to note here that the stability boundaries are developed based on the single flexible tube in a rigid array model. It is anticipated that including the coupling of adjacent tube vibrations will produce better agreement with the experimental results, especially at higher mass damping parameter.

It is shown through the sensitivity analysis that the existence and number of stability loops are directly related to the flow perturbation phase values. It follows that, great care must be taken in determining the flow perturbation propagation rates. This outcome may explain why both the semi analytical model by Lever and Weaver

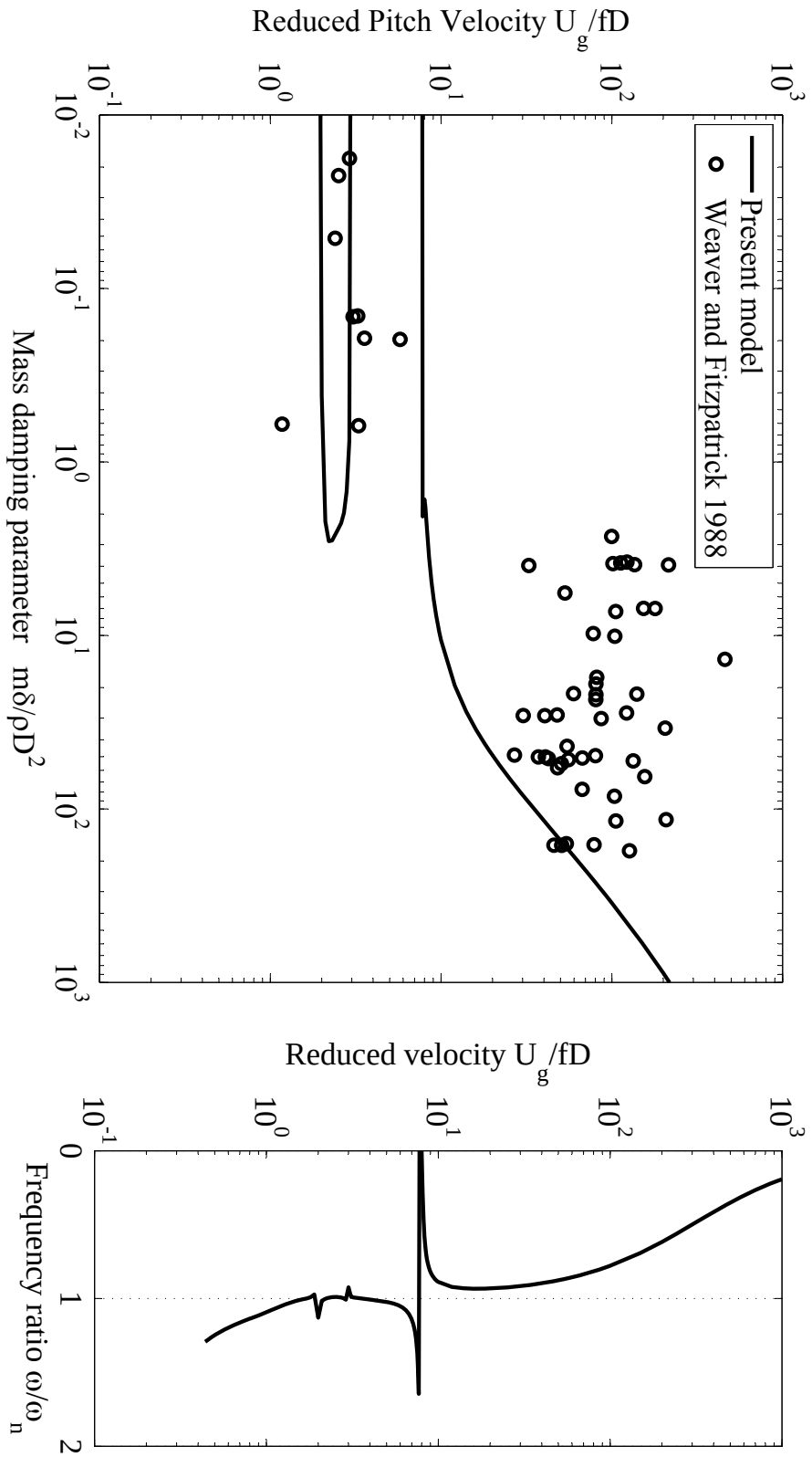

Figure 6.17: Stability map and response frequency for a rotated square tube array with $P_r = 1.4$.

(1986a) and the quasi-steady model by Price and Paidoussis (1984) predicted infinite number of stability loops while the unsteady model by Chen (1983a) which is based on experimental fluid forces measurements of Tanaka and Takahara (1981) predicted only one stability loop similar to the present model.

In summary, despite the simplifying assumptions made in the present model, it is capable of predicting the phenomenon of fluidelastic instability in tube arrays reasonably well. The present model considers the effects of array pattern and pitch ratio which are not considered by the present ASME design guidelines. Furthermore, it shows clearly the effect of the different fluidelastic instability mechanisms and advances the present understanding of the fluidelastic instability phenomenon.

Chapter 7

Conclusions and Recommendations

The fluidelastic instability in tube and shell heat exchangers was investigated with an intent to gain better understanding of the phenomenon physics. A critical review of the literature has provided some answers and raised a few questions regarding the stability behavior of a single flexible tube in a rigid array and its theoretical modeling. A new experimental study was carried out along with numerical and analytical investigations of the phenomenon to shed light on some of the unresolved issues in the fluidelastic instability in tube arrays.

7.1 Conclusions

A critical review of the stability behavior of a single flexible tube in a rigid array as compared to that of a tube in a fully flexible array was carried out in an attempt to understand the apparently contradictory results. It was found that the relative importance of the *fluid damping* and *fluid stiffness* mechanisms of fluidelastic

instability is strongly dependent on array geometry, pitch ratio, and mass ratio. The analysis showed that as the staggered array pitch angle (α) increases from ($\alpha = 30°$) through ($\alpha = 45°$) to ($\alpha = 60°$), the stability behavior of a single flexible tube in a rigid array becomes less consistent due to the change in the interstitial flow patterns. It follows that the most consistent results for a single flexible tube in a rigid array are for the parallel triangular array. It was shown that in order to obtain reliable and repeatable fluidelastic instability results from a tube array, great care needs to be taken to ensure the array geometrical precision and to fine tune the natural frequency of array tubes within 1%. It was concluded that simplified models such as single flexible tube in a rigid array can have a substantial benefits for developing a better understanding of the underlying fluid excitation mechanisms of fluidelastic instability. However, great care must be taken in interpreting the results and in making generalizations about the observed behavior. In particular, experiments used to establish the fluidelastic stability threshold of tube arrays for design purposes should use fully flexible tube array with sufficient rows and columns of tubes to properly model the array behavior.

A new experimental program was developed to provide more comprehensive and accurate measurements of the interaction between tube vibrations and the associated flow perturbations. The new experimental rig design and construction was informed by the critical review outcomes. A parallel triangular array was designed and constructed such that the tubes were suspended on piano wires to ensure precise array geometry as well as fine tuning of natural frequency and damping. The array was designed to facilitate the addition or removal of tube rows, such that the same tube can be studied at different row depths in the array. Simultaneous interstitial flow velocity, tube vibration, and tube surface pressures were collected to study the interaction between tube vibration and the associated flow perturbations along the

stream tube. Such an experimental study has never been carried out before in tube bundles and provides new results which help to improve our understanding of the interaction mechanisms between the tubes and the fluid flow.

Investigation of the stability behavior showed that a single flexible tube in a rigid parallel triangular array of tubes with a pitch ratio of 1.54 can only become fluidelastically unstable if it is located in the third tube row. It was also found that a third row tube in a fully flexible array is the least stable and, when it becomes unstable, it appears to trigger the instability of the other tubes. This result suggests that, at least for this particular array geometry, fluid coupling of adjacent tube motion, the *"stiffness mechanism"*, is an essential component of the fluidelastic mechanism except for the third row tubes which can become unstable by the damping mechanism alone. Thus, the relative importance of the damping and stiffness mechanisms of fluidelastic instability depends not only on array geometry, pitch ratio, and mass ratio, but also on tube location in the array.

The present results show that, the interaction between tube vibrations and the fluid forces acting on the tube can be studied by monitoring the surface pressures on both sides of the tube. It was found that a gradual increase in the phase lag between tube motion and fluid forces was associated with the mean gap velocity increase, such that the fluid forces are in phase with tube velocity, i.e. 90° with tube displacements, at the onset of instability. This finding provides physical evidence that the damping mechanism for fluidelastic instability is caused by fluid forces in phase with tube velocity. Further analysis of the measurements shows that, the dimensionless time delay $\tau^* = \tau U_g/D$ between tube vibrations and fluid forces at the onset of instability is about $\tau^* \approx 0.3$.

State of the art measurements of the amplitude and phase of flow perturbations associated with tube vibrations along the stream tube have been carried out. The

measurements showed that the source of flow perturbations in the stream tube is likely the effect of flow separation and the associated vorticity generation and convection. Two distinct propagation mechanisms were observed; the first is associated with the downstream vorticity convection, while the second mechanism is associated with the propagation of perturbations upstream of the vibrating tube. The rate of downstream perturbation convection was found to be about 0.76 of the mean gap velocity, which agrees with literature data for vorticity convection velocity. The rate of propagation upstream was found to be less than the rate of downstream convection at about 0.42 of the mean gap velocity.

Computational Fluid Dynamics (CFD) modeling of the present tube array was developed using ANSYS-CFX, and validated using experimental data from both the present measurements and the literature. The model was employed to investigate the interaction between tube motion and fluid flow at lower reduced velocities ($U_r = 1 - 6$). The results showed that there are two mechanisms associated with the propagation of perturbations. The first mechanism is that found for ideal fluids where disturbances propagate at the speed of sound which is effectively infinite if the fluid is incompressible. The second mechanism is caused by the flow separation from the vibrating tube and the associated vorticity generation and convection. The flow perturbations caused by this mechanism propagate at different rates upstream and downstream and are proportional to the mean gap velocity. It was found that the sound propagation mechanism is dominant at low reduced velocities, in the present case ($U_r \leq 2$), where the flow separation effect is relatively weak. As the reduced velocity increases ($U_r > 2$), the effects of flow separation from the tube become dominant, and the flow perturbation propagation rate becomes dependent on the mean gap velocity. It follows that both flow perturbation propagation mechanisms have to be modeled to properly predict the fluidelastic stability threshold.

The present measurements guided the development of a new mathematical model for the decay rate and phase angle of the flow perturbations along the stream tube. In order to predict the fluidelastic instability in tube arrays considering the present study new findings, the semi-analytical model developed by Lever and Weaver (1986a) and modified later by Yetisir and Weaver (1993a) was adopted. The geometrical parameters were modified to better represent the flow stream tubes observed in the flow visualizations provided by Scott (1987). The semi-analytical model was coupled with the new empirical model for flow perturbations propagation and decay rates to improve the predictive model for fluidelastic instability in tube and shell heat exchangers. The present model accounts for array geometry, pitch ratio, and the effect of mass ratio on the stability threshold.

The stability maps developed using the present theoretical model are in relatively good agreement with the experimental results reported in the literature for parallel triangular, normal triangular and in-line square arrays. The present model predicts a single stability loop for all array geometries unlike the infinite number of stability loops predicted by all the previous theoretical models. It was found that the existence and number of stability loops are directly related to the flow perturbation phase values. The number of stability loops depends on the number of lagging cycles while for small phase lag values ($\Phi < \pi$), only one stability boundary is predicted. This outcome explains why both the semi analytical model by Lever and Weaver (1986a) and the quasi-steady model by Price and Paidoussis (1984) predict an infinite number of stability loops while the unsteady model by Chen (1983a), which is based on experimental fluid forces measurements of Tanaka and Takahara (1981), predicted only a single stability loop, similar to the present model.

Despite the relative simplicity of the present model, it is capable of predicting the phenomenon of fluidelastic instability in tube arrays relatively well. The

present work has advanced the current understanding of the fluidelastic instability phenomenon, and can be used to improve the future design guidelines for tube and shell heat exchangers.

7.2 Research Contributions

The contributions of the present research to the current state of knowledge in the field of fluidelastic instability in tube and shell heat exchangers are summarized as follows:

1. The apparent contradictions and scatter of the experimental data reported in the literature for a single flexible tube in a rigid array were investigated and explained. Recommendations have been made regarding the parameters to be controlled in order to improve the repeatability and reliability of future experimental investigations.

2. The stability behavior of a single flexible tube in a rigid array has been thoroughly investigated. It was shown that array geometry, pitch ratio, mass ratio, and tube location in the array affect significantly the relative importance of the fluidelastic instability mechanisms.

3. An innovative experimental program was designed and carried out to facilitate conducting state of the art measurements of the interaction between tube vibrations and the associated flow response. This is significant as this experimental setup provided data that were not available before. Such new measurements have advanced the current state of knowledge in the field of fluidelastic instability in tube arrays.

4. The decay rate and relative phase of flow perturbations associated with tube vibrations were investigated both experimentally and theoretically. It was found that the flow perturbations are related to the flow separation and the associated vorticity shedding from the vibrating tube and propagate upstream and downstream at different rates relative to the mean gap velocity.

5. CFD simulations showed that two distinctive mechanisms are associated with the propagation of disturbances. At low reduced velocities, the dominant perturbation propagation mechanism is acoustic, and the disturbances travel at the speed of sound. At high reduced velocities, the perturbation propagation is dominated by vorticity generation and convection. The transition from one mechanism to the other occurs near ($U_r \approx 2$).

6. A semi-analytical model was modified by considering the geometrical parameters based on flow visualizations, and coupled with the present phase lag and perturbation decay models. The improved theoretical model shows the relative importance of the damping and stiffness mechanisms, and provides improved predictions of the fluidelastic instability phenomenon when compared with the experimental data in the literature.

7.3 Recommendations for Future Work

Based on the analysis reported in this thesis, there are several areas that require future research. These include:

1. The models for flow perturbation phase and decay rate from the present study are based on experimental measurements for a specific parallel triangular tube array. It is known that, as the array pitch angle increases, the flow channel geom-

etry changes which affects the nature of the interaction between tube vibrations and fluid flow. It would be very instructive to investigate experimentally the flow perturbation propagation and decay rates in different array geometries. It is anticipated that the use of array specific perturbation propagation and decay rates will improve the present predictions of fluidelastic instability.

2. The relative importance of the mechanisms related to flow perturbation propagation at different reduced velocities have been investigated numerically only. Investigating this phenomenon experimentally will validate the present findings and improve the present modeling of flow perturbation relative phase.

3. The present improved semi-analytical model is based on a single flexible tube in a rigid array. However, the array tubes are flexible in the real steam generators. The effect of adjacent tubes vibrations can be included in the present model which will improve the fluidelastic instability prediction for higher mass damping parameters where the stiffness mechanism becomes dominant.

References

Abd Rabbo, A., Weaver, D., 1986. A flow visualization study of flow development in a staggered tube array. Journal of Sound and Vibration 106 (2), 241 – 256.

Andjelic, M., Austermann, R., Popp, K., 1992. Multiple stability boundariesof tubes in a normal triangular cylinder array. Journal of Pressure Vessel Technology 114, 336–343.

Annaratone, D., 2010. Handbook for Heat Exchangers and Tube Banks Design. Springer Publications, New York.

Austermann, R., Popp, K., 1995. Stability behaviour of single flexible cylinder in a rigid array of different geometry subjected to cross flow. Journal of Fluids and Structures 9, 303–322.

Axisa, F., Antunes, J., Villard, B., 1990. Random excitation of heat exchangertubes by cross-flows. Journal of Fluids and Structures 4 (3), 321 – 341.

Barsamian, H. R., Hassan, Y. A., 1997. Large eddy simulation of turbulent cross-flow in tube bundles. Nuclear Engineering and Design 172, 103–122.

Bearman, P. W., 1984. Vortex shedding from oscillating bluff bodies. Annual Review of Fluid Mechanics 16, 195–222.

Blevins, R., 1974. Fluid elastic whirling of a tube row. Journal of Pressure Vessel Technology 96 (4), 263 – 267.

Blevins, R. D., 1977. Fluidelastic whirling of tube rows and tube arrays. Journal of Fluids Engineering 99, 457 – 460.

Blevins, R. D., 1979. Fluid damping and the whirling instability of tube arrays. In:

Flow Induced Vibrations. American Society of Mechanical Engineers, pp. 35 – 39.

Blevins, R. D., 1994. Flow-Induced Vibrations, 2nd Edition. Krieger Publications, Malabar, Florida.

Bruun, H. H., 1995. Hot-Wire Anemometry: Principles and Signal Analysis. Oxford University Press, Oxford, New York, USA.

Chen, S. S., 1982. Flow induced vibration. In: Pressure Vessel and Piping: Design Technology A decade of Progress. ASME, New York, pp. 301–312.

Chen, S. S., 1983a. Instability mechanisms and stability criteria of a group of circular cylinders subjected to cross flow. i. theory. Journal of Vibration, Acoustics, Stress and Reliability in Design. 105, 51–58.

Chen, S. S., 1983b. Instability mechanisms and stability criteria of a group of circular cylinders subjected to cross flow. ii. numerical results and discussion. Journal of Vibration, Acoustics, Stress and Reliability in Design. 105, 253–260.

Coleman, H. W., Steels, W. G., 1998. Experimental and Uncertainty Analysis for Engineers, 2nd Edition. A Wiley-Interscience Publication, New York, USA.

Connors, H. J., 1970. Fluidelastic vibration of tube array excited by cross flow. In: Flow Induced Vibrations in Heat Exchangers. ASME, pp. 42 – 56.

Eisinger, F. L., Rao, M. S. M., Steininger, D. A., Haslinger, K. H., 1995. Numerical simulation of cross-flow induced fluidelastic vibration of tube arrays and comparison with experimental results. Journal of Pressure Vessel Technology 117, 31–39.

Gelbe, H., Jahr, M., Schroder, K., 1995. Flow-induced vibrations in heat-exchanger tube bundles. Chemical Engineering and Processing 34 (3), 289–298.

Goyder, H. G. D., 2002. Flow induced vibration in heat exchangers. Chemical Engineering Research and Design 80 (3), 226–232.

Granger, S., Paidoussis, M. P., 1996. An improvement to the quasi-steady model with application to cross -flow induced vibration of tube array. Journal of Fluid Mechanics 320, 163–184.

Grover, L., 1977. Cross flow induced vibration deep inside a closely packed tube bank. Ph.D. thesis, McMaster University, Hamilton, Ontario, Canada.

Hassan, M., Gerber, A., Omar, H., 2010. Numerical estimation of fluidelastic instability in tube arrays. Journal of Pressure Vessel Technology, Transactions of the ASME 132 (4), 1 – 11.

Hassan, M. A., Weaver, D. S., Dokainish, M. A., 2003. The effects of support geometry on the turbulence response of loosely supported heat exchanger tubes. Journal of Fluids and Structures 18 (5), 529 – 554.

Kassera, V., Strohmeier, K., 1997. Simulation of tube bundle vibrations induced by cross-flow. Journal of Fluids and Structures 11 (8), 909 – 928.

Lever, J. H., Weaver, D. S., 1982. A theoretical model for the fluidelastic instability in heat exchanger yube bundles. Journal of Pressure Vessel Technology 104, 147–158.

Lever, J. H., Weaver, D. S., 1986a. On the stability of heat-exchanger tube bundles .1. modified theoretical-model. Journal of Sound and Vibration 107 (3), 375–392.

Lever, J. H., Weaver, D. S., 1986b. On the stability of heat-exchanger tube bundles .2. numerical results and comparison with experiments. Journal of Sound and Vibration 107 (3), 393–410.

Liang, C., Papadakis, G., 2007. Large eddy simulation of cross-flow through a staggered tube bundle at subcritical reynolds number. Journal of Fluids and Structures 23, 1215–1230.

Liang, C., Papadakis, G., Luo, X., 2009. Effect of tube spacing on vortex shedding characteristics of laminar flow past an inline tube array: A numerical study. Journal of Computers and Fluids 38, 950–964.

Lin, C., Hsieh, S. C., 2003. Convection velocity of vortex structures in the near wake of a circular cylinder. Journal of Engineering Mechanics 129 (10), 1108–1118.

Little, J., 2003. The effect of damping on fluidelastic instability in heat exchanger tube array. Master's thesis, McMaster University, Hamilton, Ontario, Canada.

Longatte, E., Bendjeddou, Z., Souli, M., 2003. Methods for numerical study of tube bundle vibrations in cross-flows. Journal of Fluids and Structures 18 (5), 513 – 528.

Mahon, J., Meskell, C., 2009. Surface pressure distribution survey in normal triangular tube arrays. Journal of Fluids and Structures 25 (8), 1348–1368.

Mahon, J., Meskell, C., 2010a. Measurement of the time delay associated with fluid

damping controlled instability in a normal triangular tube array. In: Proceedings of the 7th international symposium on fluid-structure interaction. ASME, Montreal, Quebec, Canada.

Mahon, J., Meskell, C., 2010b. A validation database for flow in a parallel triangular heat exchanger tube array. In: Proceedings of the 7th International Symposium on Fluid-Structue Interaction. Montreal, Quebec, Canada.

Marn, J., Catton, I., 1990. Flow-induced vibration problem in a simple cylinder array. one dimensional unsteady integral approach. In: Winter Annual Meeting of the American Society of Mechanical Engineer. Vol. 102. Dallas, TX, USA, pp. 19 – 21.

Marn, J., Catton, I., 1991. Flow induced vibrations in cylindrical bundles. two dimensional analysis into normal modes. In: Proceedings of the 28th National Heat Transfer Conference. Vol. 165. Minneapolis, MN, USA, pp. 9 – 14.

Mathieu, J., Scott, J., 2000. An Introduction to Turbulent Flow, first edition Edition. Cambridge University Press, Cambridge, United Kingdom.

Menter, F. R., 1994. Two-equation eddy-viscosity turbulence models for engineering applications. AIAA 32 (8), 1598–1605.

Meskell, C., Fitzpatrick, J. A., 2003. Investigation of the nonlinear behaviour of damping controlled fluidelastic instability in a normal triangular tube array. Journal of Fluids and Structures 18 (5), 573–593.

Naudascher, E., Rockwell, D., 2005. Flow-Induced Vibrations an Engineering Guide. Dover Publications, Inc., Mineola, New York.

Paidoussis, M. P., 1983. A review of flow induced vibrations in reactors and reactor components. Journal of Nuclear Engineering and Design 74, 31–60.

Paidoussis, M. P., 2005. Some unresolved issues in fluid-structure interactions. Journal of Fluids and Structures 20 (6), 871–890.

Paidoussis, M. P., 2006. Real-life experiences with flow-induced vibration. Journal of Fluids and Structures 22 (6-7), 741 – 755.

Paidoussis, M. P., Price, S. J., 1988. The mechanisms underlying flow-induced instabilities of cylinder arrays in crossflow. Journal of Fluid Mechanics 187, 45–59.

Paidoussis, M. P., Price, S. J., Mureithi, N. W., 1996. On the virtual nonexistence of

multiple instability regions for some heat-exchanger arrays in cross flow. Journal of Fluids Engineering 118, 103–109.

Paidoussis, M. P., Price, S. J., Nakamura, T., Mark, B., Mureithi, W. N., 1989. Flow-induced vibrations and instabilities in a rotated-square cylinder array in cross-flow. Journal of Fluids and Structures 3 (3), 229–254.

Pettigrew, M. J., Taylor, C. E., 2003a. Vibration analysis of shell-and-tube heat exchangers: an overview–part 1: flow, damping, fluidelastic instability. Journal of Fluids and Structures 18 (5), 469–483.

Pettigrew, M. J., Taylor, C. E., 2003b. Vibration analysis of shell-and-tube heat exchangers: an overview–part 2: vibration response, fretting-wear, guidelines. Journal of Fluids and Structures 18 (5), 485–500.

Pierson, O. L., 1937. Experimental investigation of the influence of tube arrangement on convection heat transfer and flow resistance in cross flow of gases over tube banks. Transactions ASME 59, 563–572.

Polak, D. R., Weaver, D. S., 1995. Vortex shedding in normal triangular tube arrays. Journal of Fluids and Structures 9 (1), 1–17.

Price, S., Paidoussis, M. P., McDonald, R., Mark, B., 1987. The flow-induced vibration of a single flexible cylinder in a rotated square array of rigid cylinders with pitch-to-diameter ratio of 2.12. Journal of Fluids and Structures 1 (3), 359–378.

Price, S. J., 1995. A review of theoretical-models for fluidelastic instability of cylinder arrays in cross-flow. Journal of Fluids and Structures 9 (5), 463–518.

Price, S. J., Mark, B., Paidoussis, M. P., 1986. An experimental stability analysis of a single flexible cylinder positioned in an array of rigid cylinders and subjected to cross-flow. Journal of Pressure Vessel Technology 108, 62–72.

Price, S. J., Paidoussis, M. P., 1984. An improved mathematical model for the stability of cylinder rows subject to cross-flow. Journal of Sound and Vibration 97 (4), 615–640.

Price, S. J., Paidoussis, M. P., 1986a. A constrained-mode analysis of the fluidelastic instability of a double row of flexible circular cylinders subjected to cross-flow: A theoretical investigation of system parameters. Journal of Sound and Vibration 105 (1), 121–142.

Price, S. J., Paidoussis, M. P., 1986b. A single flexible cylinder analysis for the fluidelastic instability of an array of flexible cylinders in cross flow. Journal of Fluids Engineering 108, 193–199.

Price, S. J., Paidoussis, M. P., 1989. The flow-induced response of a single flexible cylinder in an in-line array of rigid cylinders. Journal of Fluids and Structures 3, 61–82.

Rao, S. S., 2004. Mechanical Vibrations, 4th Edition. Pearson Education, Inc., Upper Saddle River, New Jersey, USA.

Ridluan, A., Tokuhiro, A., 2008. Benchmark simulation of turbulent flow through a staggered tube bundle to support cfd as a reactor design tool. part ii: Urans cfd simulation. Journal of Nuclear Science and Technology 45 (12), 1305 – 1315.

Roberts, B. W., 1966. Low frequency, aeroelastic vibrations in a cascade of circular cylinders. In: Mechanical Engineering Science. Vol. 4. The Institute of Mechanical Engineers, London, pp. 1–28.

Rottmann, M., Popp, K., 2003. Influence of upstream turbulence on the fluidelastic instability of a parallel triangular tube bundle. Journal of Fluids and Structures 18, 595–612.

Rzentkowski, G., Lever, J. H., 1998. An effect of turbulence on fluidelastic instability in tube bundles: A nonlinear analysis. Journal of Fluids and Structures 12 (5), 561–590.

Schneider, K., Farge, M., 2005. Numerical simulation of the transient flow behaviour in tube bundles using a volume penalization method. Journal of Fluids and Structures 20 (4), 555 – 66.

Schroder, K., Gelbe, H., 1999. Two- and three-dimensional cfd-simulation of flow-induced vibration excitation in tube bundles. Chemical Engineering and Processing 38 (4-6), 621–629.

Scott, P., 1987. Flow visualization of cross-flow induced vibrations in tube arrays. Master's thesis, McMaster University, Hamilton, Ontario, Canada.

Seitanis, S. A., Anagnostpoulos, P., Bearman, P. W., 2005. An experimental study of the in-line oscillations of a closely spaced row of cylinders in cross-flow. Journal of Fluids and Structures 21 (2), 211–226.

Sweeney, C., Meskell, C., 2003. Fast numerical simulation of vortex shedding in tube arrays using a discrete vortex method. Journal of Fluids and Structures 18 (5), 501 – 512.

Tanaka, H., Takahara, S., 1980. Unsteady fluid dynamic forces on tube bundle and its dynamic effect on vibration. ASME Pressure Vessel and Piping Division 41, 77–92.

Tanaka, H., Takahara, S., 1981. Fluidelastic vibration of tube array in cross flow. Journal of Sound and Vibration 77 (1), 19–37.

Tanaka, H., Takahara, S., Ohta, K., 1982. Flow -induced vibrations of tube arrays with various pitch to diameter ratios. Journal of Pressure Vessel Technology 104 (3), 168–174.

Weaver, D. S., 1993. Technology For The 90's. ASME, New York, Ch. Vortex Shedding and Acoustic Resonance in Heat Exchanger Tube Arrays, pp. 775–810.

Weaver, D. S., 2008. Some thoughts on the elusive mechanism of fluidelastic instability in heat exchanger tube array. In: Proceedings of the 9th International Conference On Flow-Induced Vibration. Vol. 1. Prague, Czech Republic, pp. 290–297.

Weaver, D. S., Elkashlan, M., 1981a. The effect of damping and mass ratio on the stability of a tube bank. Journal of Sound and Vibration 76 (2), 283–294.

Weaver, D. S., Elkashlan, M., 1981b. On the number of tube rows required to study cross-flow induced vibrations in tube banks. Journal of Sound and Vibration 75 (2), 265–273.

Weaver, D. S., Feenstra, P., Eisinger, F. L., 2000a. An experimental study of the effect of tube-to-tube ties on fluidelastic instability in an in-line tube array. Journal of Pressure Vessel Technology 122, 50–54.

Weaver, D. S., Fitzpatrick, J. A., 1988. A review of cross-flow induced vibrations in heat exchanger tube arrays. Journal of Fluids and Structures 2 (1), 73–93.

Weaver, D. S., Grover, L. K., 1978. Cross-flow induced vibrations in a tube bank - turbulent buffeting and fluid elastic instability. Journal of Sound and Vibration 59 (2), 277–294.

Weaver, D. S., Koroyannakis, D., 1982. The cross flow response of a tube array in water - a comparison with the same array in air. ASME Journal of Pressure Vessel Technology 10 (2), 136–146.

Weaver, D. S., Lever, J. H., 1977. Tube frequency effect on cross flow induced vibrations in tube array. In: Proceedings of The Fifth Biennial Symposium on Turbulence. Vol. 1. Missouri, USA, pp. 323–331.

Weaver, D. S., Yeung, H. C., 1983. Approach flow direction effects on the cross-flow induced vibrations of a square array of tubes. Journal of Sound and Vibration 87 (3), 469–482.

Weaver, D. S., Yeung, H. C., 1984. The effect of tube mass on the flow induced response of various tube arrays in water. Journal of Sound and Vibration 93 (3), 409–425.

Weaver, D. S., Ziada, S., Au-Yang, M. K., Chen, S. S., Paidoussis, M. P., Pettigrew, M. J., 2000b. Flow-induced vibrations in power and process plant components-progress and prospect. Journal of Pressure Vessel Technology 122, 339–348.

White, F. M., 2008. Fluid Mechanics, 6th Edition. McGrow Hill Publications, Boston, Massachusetts, USA.

Yetisir, M., Weaver, D. S., 1993a. An unsteady theory for fluidelastic instability in an array of flexible tubes in cross-flow .1. theory. Journal of Fluids and Structures 7 (7), 751–766.

Yetisir, M., Weaver, D. S., 1993b. An unsteady theory for fluidelastic instability in an array of flexible tubes in cross-flow .2. results and comparison with experiments. Journal of Fluids and Structures 7 (7), 767–782.

Zdravkovich, M. M., 1997. Flow around circular cylinders : a comprehensive guide through flow phenomena, experiments, applications, mathematical models, and computer simulations. Vol. 1. Oxford University Press.

Zhou, Y., Antonia, R. A., 1992. Convection velocity measurements in a cylinder wake. Experiments in Fluids 13 (1), 63–70.

Ziada, S., 2006. Vorticity shedding and acoustic resonance in tube bundles. Journal of The Brazilian Society of Mechanical Science & Engineering 28 (2), 186–199.

Ziada, S., Oengoren, A., 1992. Vorticity shedding and acoustic-resonance in an in-line tube bundle .1. vorticity shedding. Journal of Fluids and Structures 6 (3), 271–288.

Ziada, S., Oengoren, A., 1993. Vortex shedding in an in-line tube bundle with large tube spacings. Journal of Fluids and Structures 7 (6), 661–687.

Ziada, S., Oengoren, A., 2000. Flow periodicity and acoustic resonance in parallel triangle tube bundles. Journal of Fluids and Structures 14 (2), 197–219.

Ziada, S., Oengoren, A., Buhlmann, E. T., 1989a. On acoustical resonance in tube arrays .1. experiments. Journal of Fluids and Structures 3 (3), 293–314.

Ziada, S., Oengoren, A., Buhlmann, E. T., 1989b. On acoustical resonance in tube arrays .2. damping criteria. Journal of Fluids and Structures 3 (3), 315–324.

Appendix A

Test Section

The present tube array model consists of 7 rows and five columns of aluminum tubes, $D = 57.15mm(2.25in)$, with a pitch ratio of $P_r = 1.54$. The test section was designed to have a precise geometry, and to facilitate more comprehensive measurements. Therefore, the array tubes were suspended on piano wires tensioned on a steel frame as shown in Figure A1. The details of piano wire selection, frame design, tensioning mechanism, and damping devices are discussed in this appendix.

A.1 Tube Assembly

Aluminum tubes were used in the present array due to their relatively low weight and high strength. The experimental setup was designed to facilitate tuning the tubes up to a natural frequency of $40Hz$ for the translational mode. Thus, according to Equation 4.4, and using an average tube mass of about $240gm$ and piano wire free length of $L = 152mm$, the piano wires were designed to withstand a tension force of $T = 1150N$. A stainless steel wire (Type304) with a diameter of $D = 1.2mm(0.047in)$ and a rated tension load of $T = 1500N$ was selected.

In order to adjust the wire tension force, the piano wire was passed through a hollow threaded rod and wrapped around a cross link. A (SPEC-D13840) spring was installed outside the threaded rod around an aluminum bushing to provide the required tension force. The bushing was designed to ensure vertical threaded rod motion, and to eliminate any sudden changes in the tube frequency due to misalignment. A set of a hexagon nut, and washers was assembled to the threaded rod to enclose the spring as shown in Figure A2.

By screwing the hexagon nut, more tension force is exerted on the piano wire leading to higher natural frequency. Therefore, a fine thread was used to fine tune the tube natural frequency. A comparison between the theoretical prediction of the tube natural frequency using Equation 4.4 and the experimental values is shown in

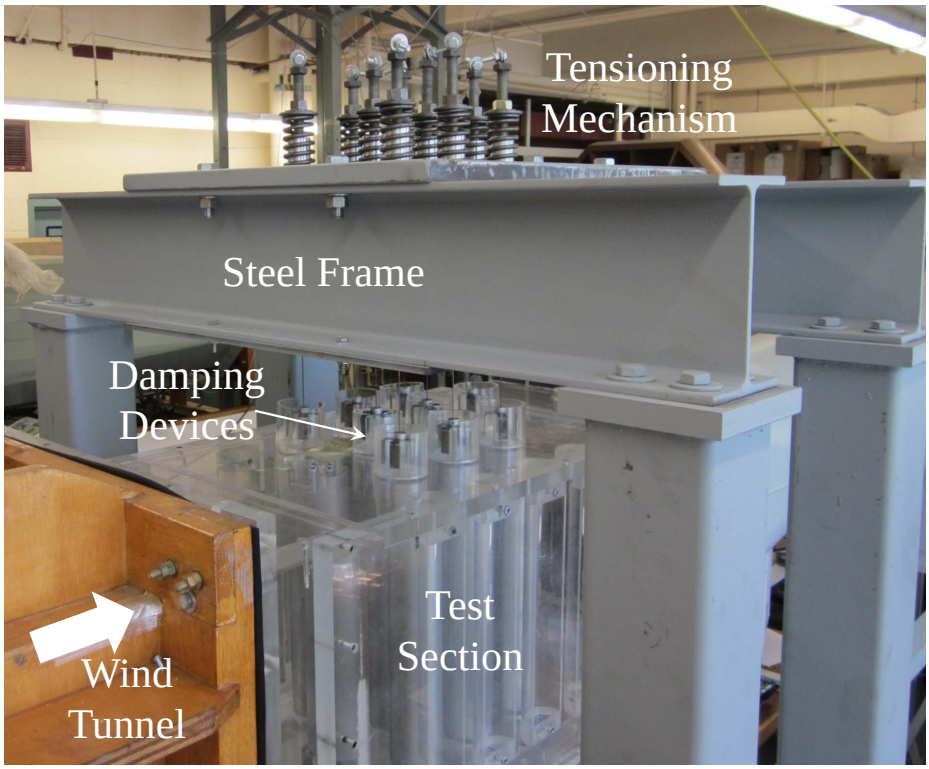

Figure A1: A picture of the test section assembly mounted on the wind tunnel.

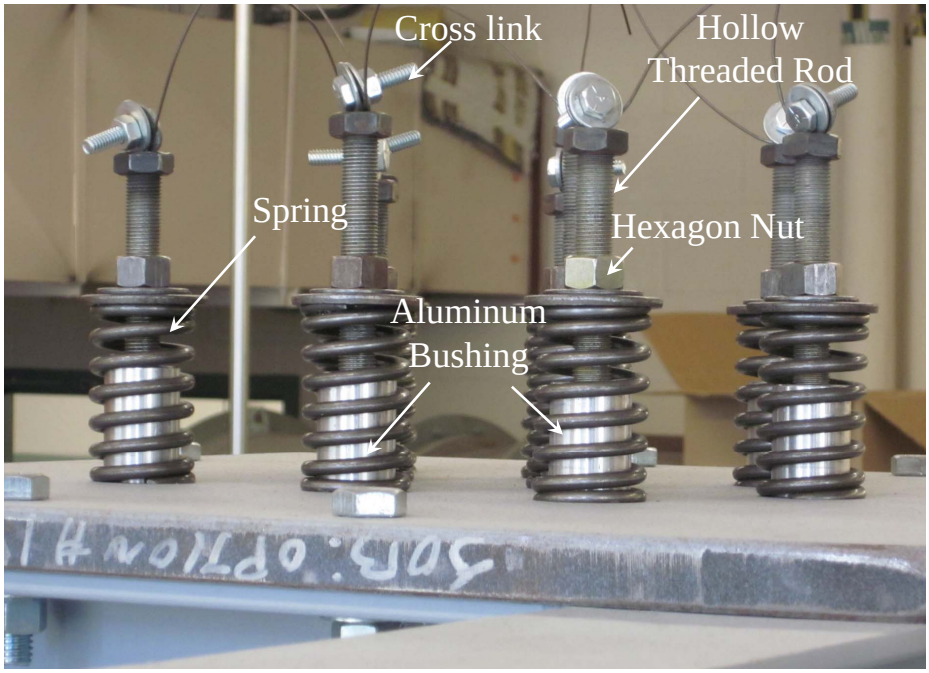

Figure A2: A picture of the tensioning mechanism.

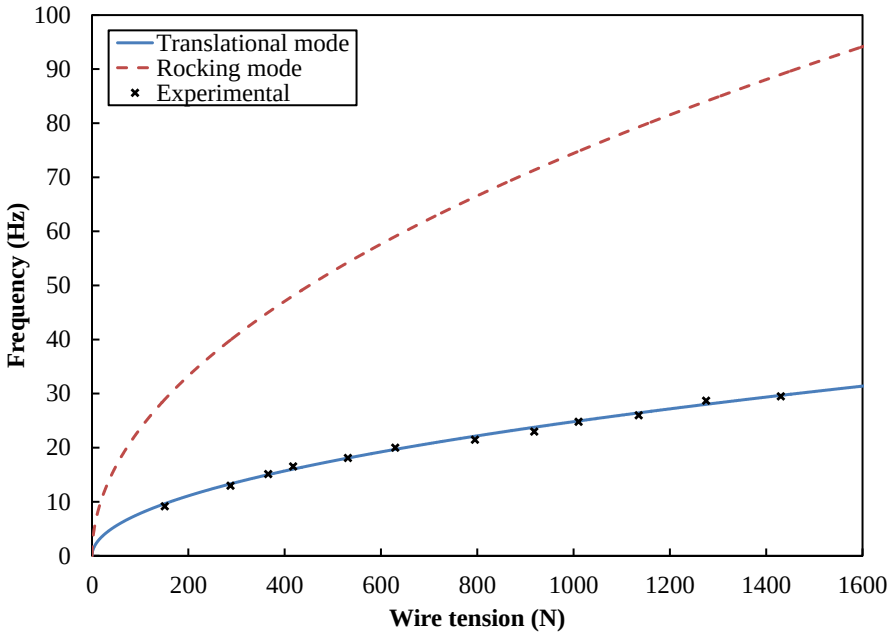

Figure A3: Theoretical and experimental prediction of the tube natural frequency variation with piano wire tension.

Figure A3.

Each tube in the array was equipped with two damping devices one on top and one on bottom of the test section to avoid exciting the rocking mode. The damping device consisted of a stationary cup and a paddle mounted on the piano wire as shown in Figure A4. The amount of added damping to the system is adjusted by varying the level and viscosity of the liquid used in the cups. The effect of fluid viscosity and level on the tube total damping is shown in Figure A5.

A.2 Supporting Frame

The piano wires were mounted on a steel frame designed to minimize the deflection due to wires tension. Excessive deflection of the steel frame could result in variations of tubes frequency, which may affect the experimental results [Weaver and Lever, 1977]. Thus, a finite element analysis of the steel frame was carried out to calculate the frame stresses and strains due to a maximum loading of $10 tubes \times 1.5KN = 15KN$. A maximum frame deflection of $5\mu m$ was predicted at the central tube (1) which corresponds to variation of about $0.1Hz$ in the tube frequency.

Modal analysis of the frame dynamic response was performed using ANSYS-12 to calculate the frame natural frequencies and mode shapes. The steel frame natural frequencies were measured by installing an accelerometer on the frame surface, and analyzing the frame response to a given excitation. It was possible to excite the first

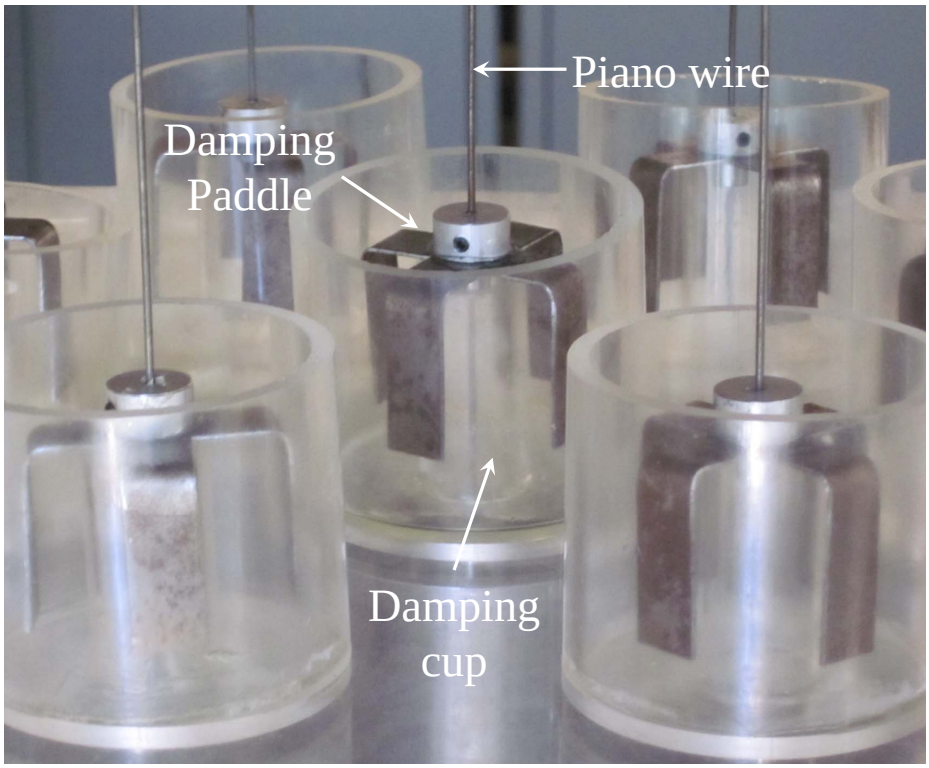

Figure A4: A picture of the damping devices.

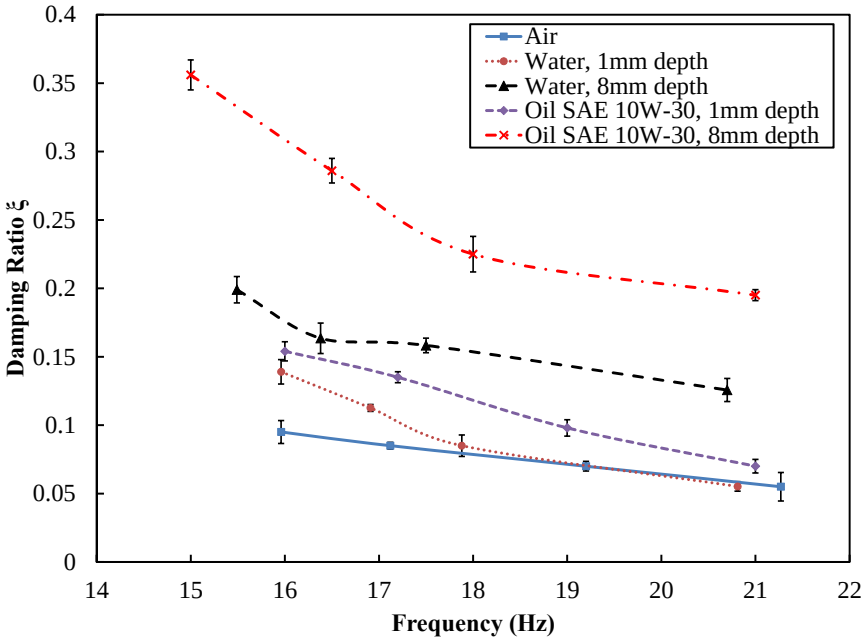

Figure A5: The effect of damping cup liquid level and viscosity on the tube total damping.

mode only using a simple hammer test on the frame which was used to validate the FEA results. Comparison of the frame predicted natural frequencies to the measured values is shown in Table A1.

Table A1: Natural frequencies and mode shapes of the steel frame

Mode	Numerical $f_n(Hz)$	Experimental $f_n(Hz)$	Mode shape
1	53	49	Bending
2	74	—	Bending
3	93.5	—	Torsion

Appendix B

Instrument Calibration

B.1 Pitot Tube

The flow velocity was measured using a Pitot tube located at about $150mm$ upstream of the test section. The Pitot tube was connected to a low range differential pressure transducer with a diaphragm number (DP45-14). This diaphragm has a pressure range of $0.22KPa$ which corresponds to an air flow velocity of $19m/s$. The pressure transducer signal was displayed on a Validyne digital transducer indicator with a model number (CD-23). Calibration of the flow velocity signal displayed on the digital indicator was performed using a micro-manometer, and the calibration curve is shown in Figure B1.

B.2 Accelerometer

The accelerometers selected for this research were used to monitor the longitudinal and transverse response of the tubes. Miniature accelerometers were selected due to their relatively small weight and simple installation procedure. Two (PCB-352 A24) accelerometers were installed in each instrumented tube, each accelerometer weighs $0.8gm$ and has a range of $50g$. The accelerometer specifications sheet is shown in Figure B2. The accelerometers were calibrated by the supplier, and the calibration certificate information was adopted in the present research.

B.3 Pressure Transducer

Tubes 1 and 2 in the present research were instrumented with two pressure transducers, one on each side, to monitor qualitatively the fluid forces acting on the tube. Miniature (PCB-103 B03) pressure transducers were flush mounted inside the

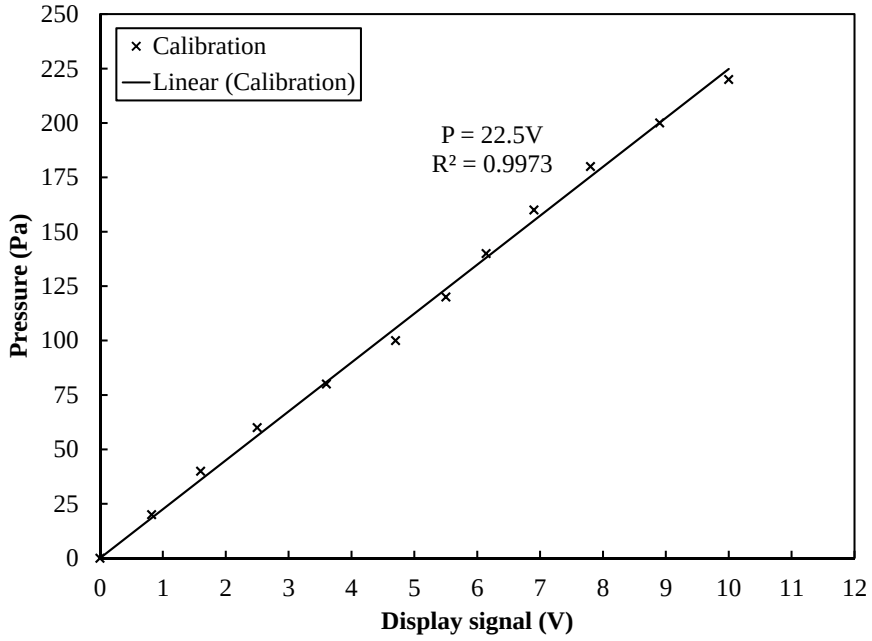

Figure B1: Calibration curve for the differential pressure transducer.

tubes. The transducers weigh $2.85gm$ each, and have a sensitivity of $217.4mV/KPa$. The pressure transducer specifications are shown in Figure B3. The transducers acceleration sensitivity as shown in the specifications sheet was used to compensate for the tube vibrations using the accelerometer's signal. Calibration of the transducer was performed by the supplier, and the calibration certificate information was adopted in the present research.

B.4 Hot-wire Anemometry

Constant temperature hot-wire anemometer was used in the present study. The hot-wire probe consists of an electrically heated thin wire ($5\mu m$ Dia.) strung across the tips of supporting needles. A boundary layer probe, as shown in Figure 4.6, was used such that the hot-wire axis is normal to the flow plane. The cooling effect caused by the flow passing on the wire is balanced by the electrical current, such that the wire is held at a constant temperature. The change in the wire current shows up as a change in the anemometer output voltage, which is calibrated to a flow velocity change.

A hot-wire probe model (Dantec-1211 Standard Probe) was connected to a Wheatstone bridge circuit as one arm of the bridge. The system has a frequency response of $250KHz$ which enables essentially rapid response time to flow velocity perturbations. The output voltage of the hot-wire anemometer is related to the flow velocity. However, the relation is not linear, and thus the anemometer has to be

Model Number 352A24	ACCELEROMETER, ICP®	Revision C ECN #: 27171

	ENGLISH	SI	
Performance			
Sensitivity (±10 %)	100 mV/g	10.2 mV/(m/s²)	
Measurement Range	±50 g pk	±490 m/s² pk	
Frequency Range (±5 %)	1.0 to 8000 Hz	1.0 to 8000 Hz	
Frequency Range (±10 %)	0.8 to 10000 Hz	0.8 to 10000 Hz	
Frequency Range (±3 dB)	0.4 to 12000 Hz	0.4 to 12000 Hz	
Resonant Frequency	≥30 kHz	≥30 kHz	
Broadband Resolution (1 to 10000 Hz)	0.0002 g rms	0.002 m/s² rms	[1]
Non-Linearity	≤1 %	≤1 %	[2]
Transverse Sensitivity	≤5 %	≤5 %	
Environmental			
Overload Limit (Shock)	±5000 g pk	±49050 m/s² pk	
Temperature Range (Operating)	-65 to +250 °F	-54 to +121 °C	
Temperature Response	See Graph	See Graph	
Electrical			
Excitation Voltage	18 to 30 VDC	18 to 30 VDC	
Constant Current Excitation	2 to 20 mA	2 to 20 mA	
Output Impedance	≤300 ohm	≤300 ohm	
Output Bias Voltage	8 to 12 VDC	8 to 12 VDC	
Discharge Time Constant	0.4 to 1.5 sec	0.4 to 1.5 sec	
Settling Time (within 10% of bias)	<8 sec	<8 sec	
Spectral Noise (1 Hz)	80 µg/√Hz	785 (µm/sec²/√Hz	
Spectral Noise (10 Hz)	15 µg/√Hz	147 (µm/sec²/√Hz	[1]
Spectral Noise (100 Hz)	4 µg/√Hz	39 (µm/sec²/√Hz	[1]
Spectral Noise (1 kHz)	1 µg/√Hz	9.8 (µm/sec²/√Hz	[1]
Electrical Isolation (Base)	≥10^8 ohm	≥10^8 ohm	
Physical			
Sensing Element	Ceramic	Ceramic	
Sensing Geometry	Shear	Shear	
Housing Material	Anodized Aluminum	Anodized Aluminum	
Sealing	Epoxy	Epoxy	
Size (Height x Length x Width)	0.19 in x 0.48 in x 0.28 in	4.8 mm x 12.2 mm x 7.1 mm	
Weight	0.03 oz	0.8 gm	[1]
Electrical Connector	3-56 Coaxial Jack	3-56 Coaxial Jack	
Electrical Connection Position	Side	Side	
Mounting	Adhesive	Adhesive	

CE[3]

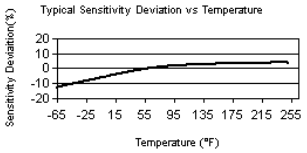

All specifications are at room temperature unless otherwise specified.
In the interest of constant product improvement, we reserve the right to change specifications without notice.

Optional Versions (Optional versions have identical specifications and accessories as listed for standard model except where noted below. More than one option maybe used.)

RH - RoHS Compliant
Supplied Accessory: Model RH030A10 Coax Cable, 10 ft (3 m), 3-56 plug to 10-32 plug, RoHS compliant. replaces Model 030A10

Notes
[1] Typical.
[2] Zero-based, least-squares, straight line method.
[3] See PCB Declaration of Conformance PS023 for details.

Supplied Accessories
030A10 Coax Cable, 10 ft (3 m), 3-56 plug to 10-32 plug. (1)
039A28 Removal Tool (1)
080A109 Petro Wax (1)
ACS-1 NIST traceable frequency response (10 Hz to upper 5% point). (1)

Entered: EB	Engineer: BAM			Spec Number:
Date: 08/23/2007	Date: 08/23/2007			**12320**

PCB PIEZOTRONICS VIBRATION DIVISION
3425 Walden Avenue
Depew, NY 14043
UNITED STATES
Phone: 888-684-0013
Fax: 716-685-3886
E-mail: vibration@pcb.com
Web site: www.pcb.com

Figure B2: Accelerometer specifications.

Model Number 103B03	ACOUSTIC ICP® PRESSURE SENSOR			Revision B ECN #: 20635
Performance	**ENGLISH**	**SI**		**Optional Versions** (Optional versions have identical specifications and accessories as listed for standard model except where noted below. More than one option maybe used.)
Measurement Range (± 5 V output)	3.33 psi	181 dB		**M** - Metric Mount
Useful Overrange (± 10 V output)	6.67 psi	187.2 dB	[1]	Supplied Accessory: Model M061A04 Clamp
Sensitivity (±15 %)	1500 mV/psi	217.5 mV/kPa		**Notes**
Maximum Pressure	250 psi	1724 kPa		[1] For +10 volt output, minimum 24 VDC supply voltage required. Negative 10 volt output may be limited by output bias.
Resolution	0.02 mpsi	77 dB		[2] Zero-based, least-squares, straight line method.
Resonant Frequency	≥13 kHz	≥13 kHz		[3] See PCB Declaration of Conformance PS023 for details.
Rise Time	≤25 µ sec	≤25 µ sec		
Low Frequency Response (-5 %)	5 Hz	5 Hz		**Supplied Accessories**
Non-Linearity	≤2.0 % FS	≤2.0 % FS	[2]	061A04 Sleeve clamp 4-40 cap screw (2)
Environmental				065A66 Adhesive Mounting Ring (3)
Acceleration Sensitivity	≤0.0005 psi/g	≤0.0035 kPa/(m/s²)		
Temperature Range (Operating)	-100 to 250 °F	-73 to 121 °C		
Temperature Coefficient of Sensitivity	≤0.2 %/°F	≤0.36 %/°C		
Maximum Flash Temperature	1000 °F	538 °C		
Maximum Shock	1000 g pk	9807 m/s² pk		
Electrical				
Output Polarity (Positive Pressure)	Positive	Positive		
Discharge Time Constant (at room temp)	≥0.1 sec	≥0.1 sec		
Excitation Voltage	20 to 30 VDC	20 to 30 VDC		
Constant Current Excitation	2 to 20 mA	2 to 20 mA		
Output Impedance	≤100 ohm	≤100 ohm		
Output Bias Voltage	7 to 13 VDC	7 to 13 VDC		
Physical				
Sensing Element	Ceramic	Ceramic		
Housing Material	Stainless Steel	Stainless Steel		
Diaphragm	316L Stainless Steel	316L Stainless Steel		
Sealing	Epoxy	Epoxy		
Electrical Connector	3-56 Coaxial Jack	3-56 Coaxial Jack		
Weight	0.10 oz	2.843 gm		

CE [3]

All specifications are at room temperature unless otherwise specified.
In the interest of constant product improvement, we reserve the right to change specifications without notice.
ICP® is a registered trademark of PCB group, Inc.

Entered: BLS	Engineer: RPF	Sales: DPC	Approved: MEM	Spec Number:
Date: 09/17/2004	Date: 09/17/2004	Date: 09/17/2004	Date: 09/20/2004	**24848**

PCB PIEZOTRONICS INC
PRESSURE DIVISION

3425 Walden Avenue
Depew, NY 14043
UNITED STATES
Phone: 888-684-0011
Fax: 716-686-9129
E-mail: pressure@pcb.com
Web site: www.pcb.com

Figure B3: Pressure transducer specifications.

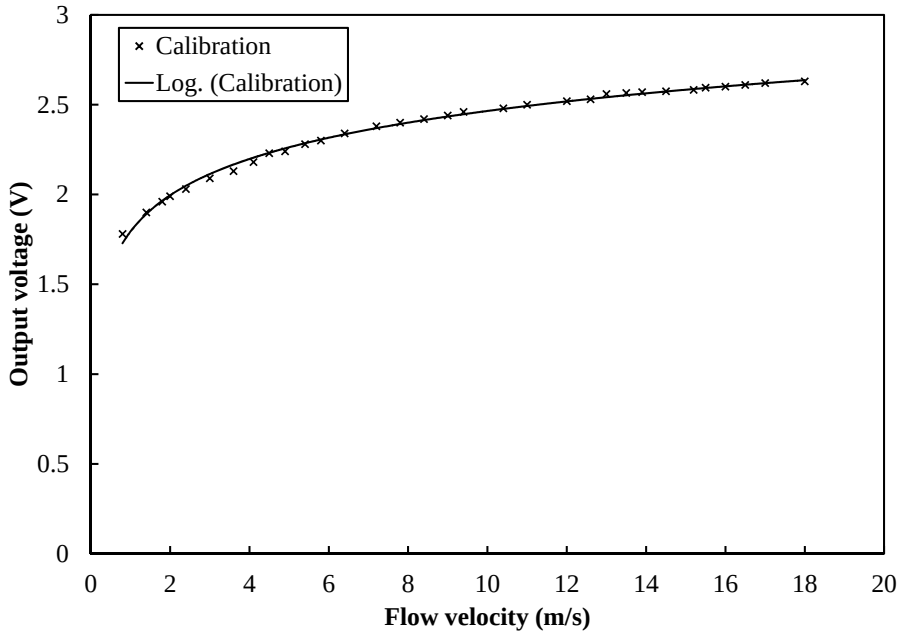

Figure B4: Hot-wire anemometer calibration curve.

calibrated for the desired flow velocity range. The calibration function for hot-wire anemometry can be given as

$$E^2 = A + BU^n \tag{B1}$$

where E is the anemometer output voltage in (Volt), U is the flow velocity in (m/s), and (A,B, and n) are constants. Equation B1 can be written as

$$ln(E^2 - A) = n[ln(U)] + ln(B) \tag{B2}$$

The constant A is obtained by measuring the bridge voltage in still air, and was found to be $A = 1.64$. The present hot wire anemometer was calibrated in the wind tunnel facility using a pitot tube anemometer to obtain the constants. The resulted calibration is shown in Figure B4 where the experimental data fitting has a goodness of $R^2 = 0.99$.
It follows that Equation B2 can be written as

$$E^2 = 1.64 + 6.008U^{0.292} \tag{B3}$$

It must be cautioned here that due to the long measurements period, typically 2-3 hours., the calibration curve was found to be slightly shifted at the end of measurements. Thus, calibration was averaged over the measurements period.

Appendix C

Uncertainty Analysis

The uncertainties associated with the present measurements are discussed in this appendix. For a given variable (X) which is a function of a set of independent measured variables (Y_i) such that

$$X = f(Y_1, Y_2, Y_3, ..., Y_i) \tag{C1}$$

The uncertainty in (X) can be expressed in terms of the uncertainties of the independent measured values (Y_i) using Kline and McClintock method [Coleman and Steels, 1998] as

$$\delta X = \sqrt{\sum_{i=1}^{N} \left(\frac{\partial X}{\partial Y_i} \delta Y_i \right)^2} \tag{C2}$$

where δY_i is the known uncertainty in each independent measured variable. The summation of the terms on the right hand side of Equation C2 gives the overall uncertainty in the dependent variable (X). Three principle quantities were monitored during the present experiments namely; flow velocity, frequency spectrum and relative phase angle, and the uncertainties associated with each parameter are discussed below.

C.1 Flow Velocity

The upstream flow dynamic head was measured using a Pitot tube, and by assuming one dimensional, incompressible, and inviscid flow, the flow velocity was calculated from Bernoulli's equation as follows

$$\Delta P = \frac{1}{2} \rho U^2 \tag{C3}$$

where ΔP is the pressure difference between the stagnation point and the free stream point on Pitot tube. Thus, the flow velocity can be calculated as

$$U = \sqrt{\frac{2\Delta P}{\rho}} \tag{C4}$$

where the air density ρ can be calculated as

$$\rho = \frac{P_o}{287 T_o} \tag{C5}$$

where P_o is the ambient pressure in (Pa) and T_o is the ambient temperature in (K°). It follows that, the flow velocity can be expressed as

$$U = \sqrt{\left(\frac{2\Delta P \times 287 T_o}{P_o}\right)} \tag{C6}$$

Substituting from Equation C6 in Equation C2 the relative uncertainty in flow velocity measurements can be written as

$$\frac{\delta U}{U} = \sqrt{\left(\frac{\delta(\Delta P)}{2\Delta P}\right)^2 + \left(\frac{\delta T_o}{2T_o}\right)^2 + \left(\frac{\delta P_o}{2P_o}\right)^2} \tag{C7}$$

The wind tunnel facility is located in a room where the temperature was controlled and monitored by a thermometer. The room temperature variations δT_o during experiments was between $(1 - 2K^\circ)$. The ambient air pressure was measured using a mercury barometer, and the variations in ambient air pressure δP_o were found to be $\leq 0.4KPa$. The two pressure ports of the Pitot tube were connected to a differential pressure transducer. The accuracy of the pressure transducer as indicated in the manual is $\pm 0.25\%$ of the full measured scale. The pressure transducer range was $(22-220Pa)$ which results in an uncertainty of differential pressure $\delta(\Delta P) = \pm 0.5Pa$. Using Equation C7, the overall uncertainty in flow velocity $(\delta U/U)$ was found to be 2.5%

Other sources of uncertainty in flow velocity measurements include the turbulence level, probe size, and wall proximity. In the present experiments, the upstream turbulence level was found to be less that 1% which has a negligible effect on the velocity measurements. The Pitot tube diameter was $4mm$ which presents an area blockage ratio of 0.01%. The Pitot tube probe was located well upstream of the test section in the mid span of the wind tunnel section to avoid the boundary layer effects.

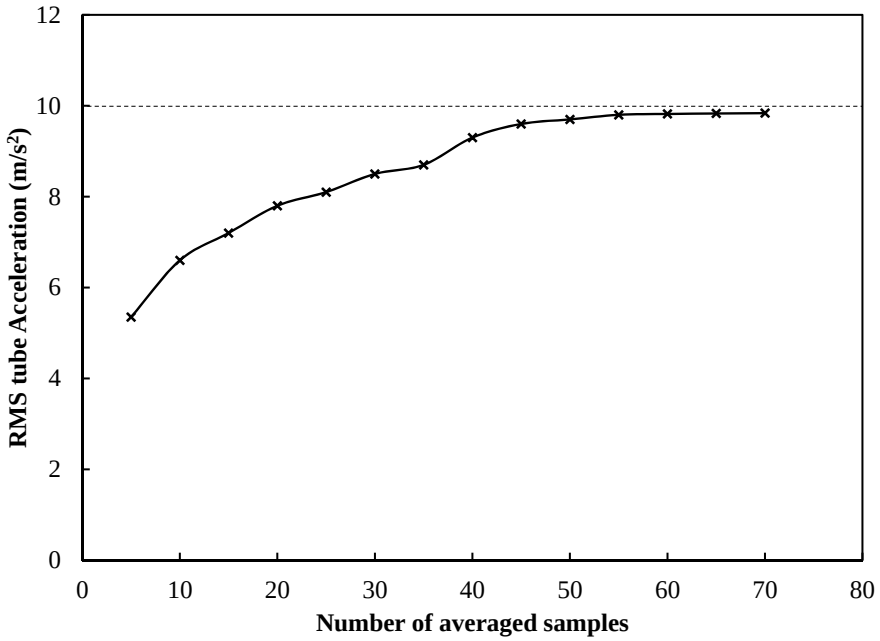

Figure C1: Effect of number of averages on the results RMS amplitude.

C.2 Frequency Spectrum

The RMS frequency components of a harmonic signal are affected by the sampling time, type of windowing, number of averages, and overlap percent. A sampling time of $10(s)$ was selected for the present measurements which resulted in a frequency resolution of $0.1Hz$. Thus, the uncertainty due to frequency resolution is $\pm 0.05Hz$. There are several types of signal windowing such as hamming, flat top window, cosine, and triangular,...etc. Each windowing type affects the RMS amplitude of the signal differently depending on a parameter called the leakage factor. A hamming window with 50% overlap was used in the present measurements as it has a leakage factor $\leq 2\%$.

The tube array response to cross flow is of modulating nature and not an ideal harmonic phenomenon. As such, the number of averaged samples affects the measured RMS amplitude to a certain number of averages after which the RMS amplitude asymptotes to a constant value. The effect of number of averages was investigated, and it was found that the RMS amplitude of the signal asymptotes within $\pm 0.5\%$ after about 50 averages as shown in Figure C1.

The frequency spectra for flow velocity and surface pressure measurements were used to calculate the Strouhal number which is given by

$$S_t = \frac{fD}{U} \tag{C8}$$

where (f) is the vortex shedding frequency, (D) is the tube diameter, and (U) is the flow velocity. Using Equation C2, the overall uncertainty in Strouhal number can be expressed as

$$\frac{\delta S_t}{S_t} = \sqrt{\left(\frac{\delta f}{f}\right)^2 + \left(\frac{\delta D}{D}\right)^2 + \left(\frac{\delta U}{U}\right)^2} \tag{C9}$$

where (δf) is the uncertainty in frequency measurements, and (δD) is the uncertainty in tube diameter measurements. The lowest measured frequency was $10Hz$ and the frequency resolution was $0.1Hz$, thus the maximum uncertainty in frequency measurements was 1%. Three random measurements of the diameter were taken for each tube using a vernier micrometer with an accuracy of $0.001in$ $(0.025mm)$. This resulted in a total of 30 random diameter measurements. The mean tube diameter was $D = 2.24in(56.9mm)$ and the standard deviation was $\delta D = 0.025in(0.64mm)$, thus the uncertainty in tube diameter $\delta D/D$ was 1.12%. Substituting the independent variables uncertainty values in Equation C9 results in an overall Strouhal number uncertainty $\delta S_t/S_t = 2.91\%$.

C.3 Phase Measurements

The uncertainties of phase measurements arise from sources such as the sampling rate and data acquisition system. In the present phase measurements, a sampling rate of $4096(Hz)$ was used. Considering that the investigated phenomenon has a frequency of $25Hz$ as discussed in Chapter 5, this means that 164 measurements were collected during each cycle. Thus, there was a phase angle uncertainty of $\pm 1.2^\circ$ due to the sampling frequency.

Most of the data acquisition systems collect measurements from the channels at the rated DAQ frequency, and delivers them according to the desired sampling frequency. It follows that an inherent time delay is introduced in the measurements due to the data acquisition system. The present experiments were conducted using a National Instrument (NI-DAQ6015) which has eight channels and a rated sampling rate of $250KHz$. Thus, the sampling frequency for each channel is $250/8 = 31.25(KHz)$ which introduces a phase angle uncertainty of $\pm 0.3^\circ$. It follows that, the inherent delay caused by the data acquisition system is negligible for such low frequency phenomenon.

Appendix D

Experimental Results

D.1 Tube Response

The tubes in the array were tuned precisely to the targeted frequency to improve the results repeatability. The tubes natural frequencies were measured again after six months to examine the effect of piano wire relaxation. A slight change in the natural frequencies, within ±1%, over a period of six months was observed as shown in Table D1.

The tube response pattern is affected by the directional natural frequency of the tube such that if the tube natural frequency in one direction is different from another direction, certain response patterns like elliptical, and figure 8 are observed. In order to role out this effect from the present study, the natural frequencies of tube 1 in the longitudinal and transversa directions were measured as shown in Table D2. It is shown that the differences in natural frequencies in both direction are $\leq 2.5\%$.

D.2 Tube Surface Pressure Measurements

The tube surface pressure measurements were repeated several times to ensure that the results are repeatable. It was found that the phase lag values between tube vibration and fluid forces are repeatable within ±20° which is equivalent to about 11% of the cycle time. The phase lag between tube vibrations and the fluid forces acting on a single flexible tube located in the third row of a rigid array is shown in Figure D1 with the error bars. These results correspond to the results shown in Figure 5.14(a).

Table D1: Natural frequencies of array tubes.

Tube name	$f_n(Hz)$	$f_n(Hz)$ *After 6 months*
A	19.8	19.9
B	19.8	19.9
C	19.8	19.9
D	19.8	19.7
E	19.8	19.7
F	19.8	19.8
G	19.8	19.8
X	19.8	19.8
1	19.8	19.8
2	19.8	19.8

Table D2: Tube (1) frequencies in the longitudinal and transverse directions

U_g (m/s)	$f_n(Hz)$ *Longitudinal*	$f_n(Hz)$ *Transverse*	*Difference %*
2.1	20.1	19.9	1
2.9	20.2	19.9	1.5
3.6	20.2	19.9	1.5
4.2	20.0	19.9	0.5
5.0	20.0	19.8	1
5.4	19.6	19.6	0
5.9	19.6	19.6	0
6.2	20.0	19.6	2
6.6	20.0	19.5	2.5
6.9	19.7	19.7	0
7.2	19.7	19.7	0
7.4	19.8	19.8	0
7.7	19.8	19.8	0
8.1	19.8	19.8	0

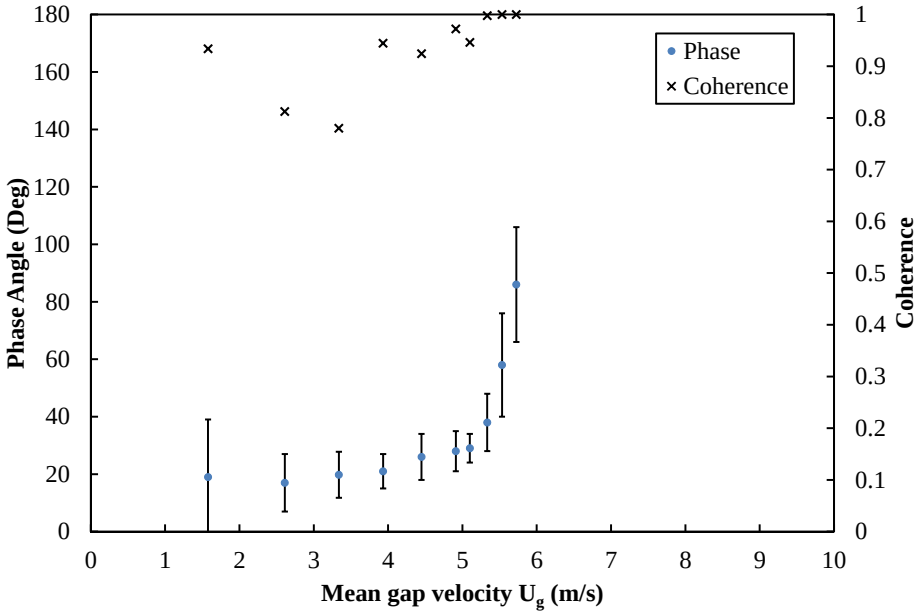

Figure D1: Phase lag between the fluid forces and tube (1) vibrations when located in the third row of a rigid array.

D.3 Phase Lag Between Tube Motion and Induced Flow Perturbation

Similarly, the phase lag measurements between tube vibrations and flow perturbations were repeated several times, and the results were found to be repeatable within $\pm 25°$ which represents about 12% of the cycle time. The phase lag measurements along the flow channel are shown in Figure D2 with the error bars.

In order to investigate the effect of hot-wire probe location across the stream channel, phase lag measurements were take near the tube and at the middle of the stream channel. It was found that the phase lag values are similar within $\pm 5°$ which corresponds to about 3% of the cycle time as shown in Figure D3. Therefore, all the consequent measurements were carried out at the stream channel middle, which facilitated studying larger tube vibration amplitudes.

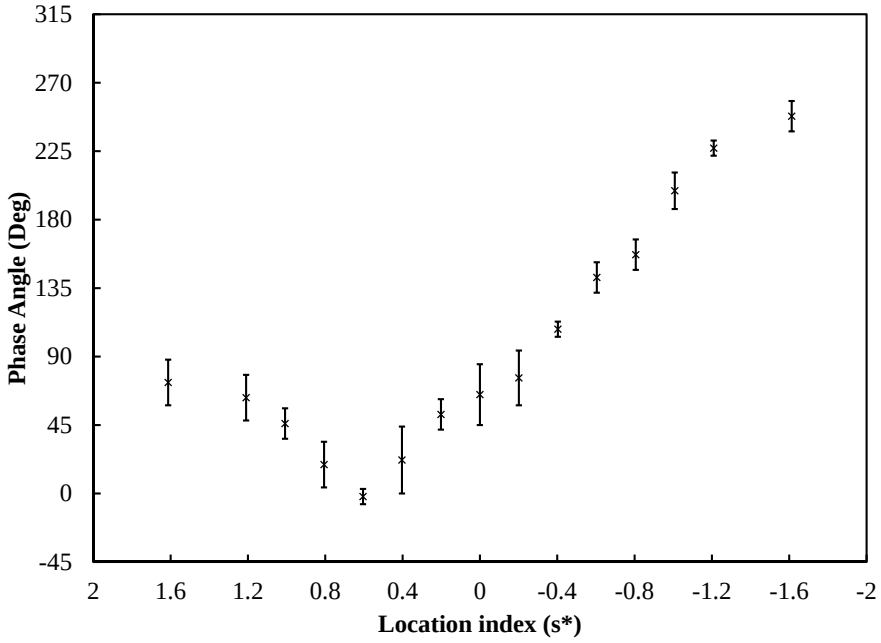

Figure D2: Phase lag between tube vibrations and flow perturbations along the stream channel.

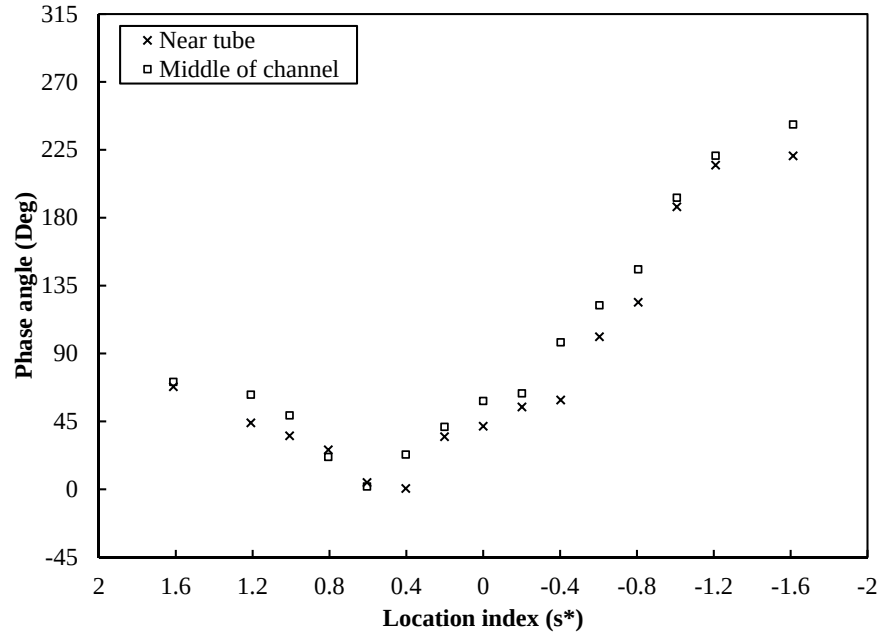

Figure D3: Effect of hot-wire probe location across the stream channel on the phase lag measurements.

Appendix E

Computational Fluid Dynamics Modeling

E.1 Meshing

The meshing process for the present models was performed using ANSYS-CFX mesh using tetrahedra and prism elements as they are more appropriate for curved surfaces. The default mesh size was selected to be about 5% of the tube diameter, and mesh refinement to about 1% was performed around the tubes and near the walls to capture the relatively higher velocity gradients in these regions. The expansion factor between the fine and coarse elements was selected to be 1.2 as recommended by ANSYS-CFX manual.

Inflated elements were used at the tubes and walls surface to properly model the velocity gradients in the boundary layer region. The height and number of inflated layers are dependent of Reynolds number, length scale, expansion ratio and ($y+$) value. Physically, the boundary layer flow is divided into outer and inner regions. The inner layer is also divided to a viscous sublayer close to the wall and a logarithmic layer further from the wall. The parameter ($y+$) in the boundary layer theory represents the scaled length of the viscous sublayer region as shown in Figure E1. The parameter ($y+$) in CFD modeling represents the scaled distance from the wall to the first grid point.

The recommended $y+$ value for the SST turbulence model by ANSYS-CFX manual is ≤ 1, thus a value of $y+ = 0.8$ was used in the present meshing. The number of inflated layers used was 15 layer with an expansion factor of (1.1). The surface mesh developed using the aforementioned properties was then extruded across the model thickness as the problem was solved as 2D. This procedure reduced the number of elements significantly and thus, reduced the solution time accordingly.

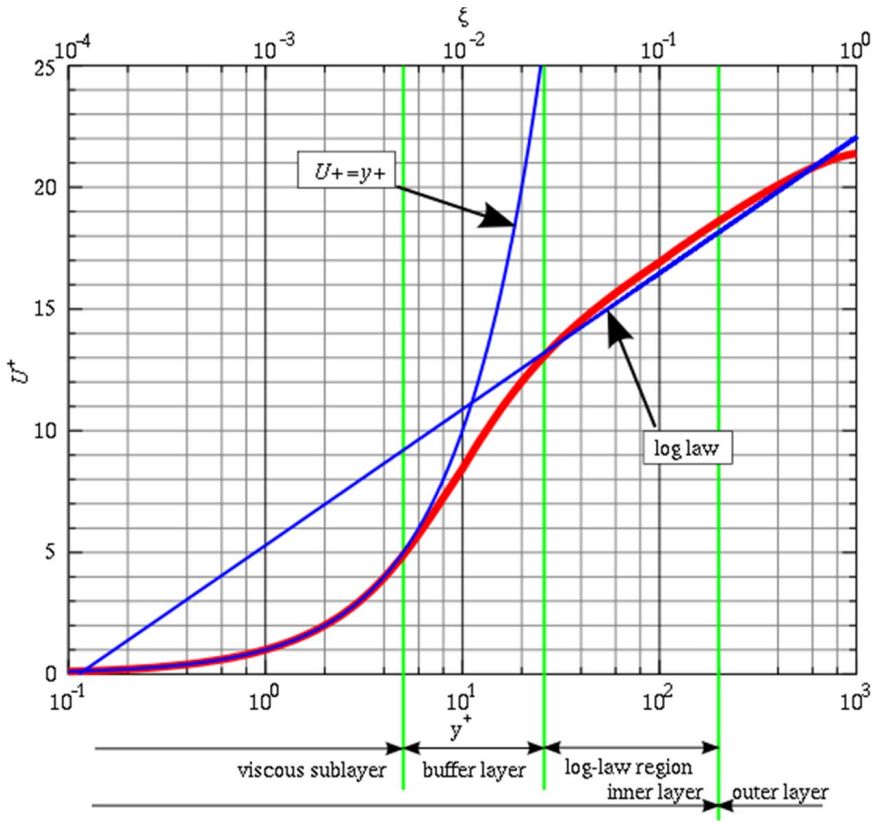

Figure E1: Typical behavior of scaled velocity $U+$ in the inner region of the boundary layer. Source(www.wikipedia.com)

E.2 Boundary Conditions

The inlet boundary condition defines the resultant normal velocity component at the entrance region. The turbulence intensity was selected to be $I = 1\%$ similar to the experimental value. An opening boundary condition was assigned to the outlet region such that the flow is free to go out or come into the modeled domain. An opening boundary condition means physically that the pressure gradient $(\partial p/\partial \bar{n} = 0)$ at this region. The tubes and test section sides were modeled as stationary no-slip walls, except for the third row central tube which was given a harmonic motion in the transverse direction. Symmetrical boundary condition was assigned to the model plan which means that solution is repeated along the tube length.

E.3 Domain size Independence Study

Domain size independence study was conducted to investigate the effect of flow entrance length on the surface pressure distribution results. Computational domains

with three, four, six, and ten length scales, (D), upstream were examined. It was found that the tube surface pressure distribution asymptotes within ±2% after six length scales upstream as shown in Figure E2. Therefore, the consequent simulations were built with six length scales upstream of the array.

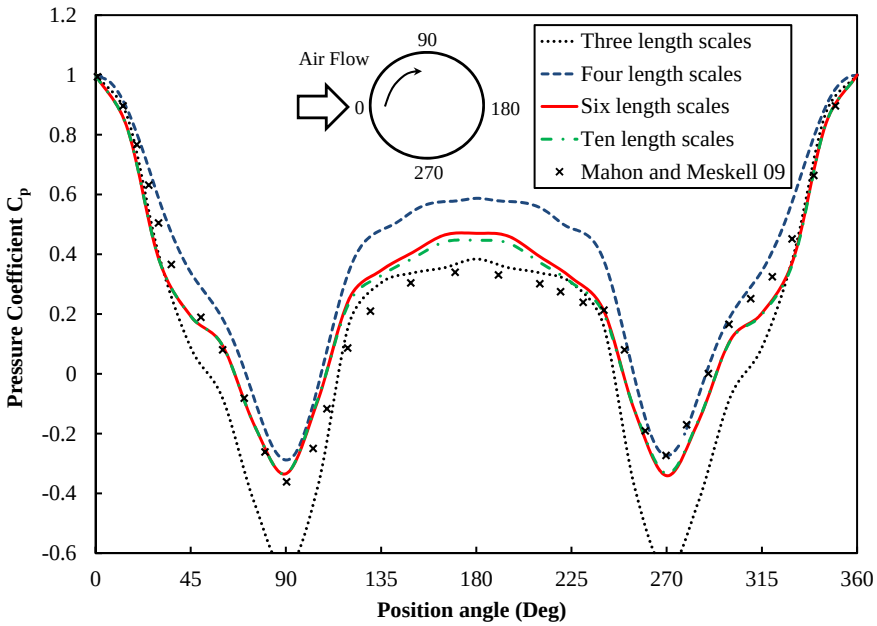

Figure E2: Predictions of surface pressure distribution using several domain sizes, NT array, $P_r = 1.32$, $R_e = 57000$.

E.4 Grid Independence Study

The grid refinement convergence is a basic step in CFD analysis. The present grid refinement study was performed on three successively finer grids. The default grid size, fine grid size, and number of elements used for each simulation are listed in Table E1. The tube surface pressure distributions from the simulations were compared to the experimental values as shown in Figure E3. It was found that, as the grid was refined, the simulation results were converging closer to the experimental values, and the pressure coefficient values asymptoted within ±2% between the second and third grid refinement. Therefore, the default grid size was selected to be 5%D while the fine grid size was select to be 1%D.

Table E1: Details of grid refinement study

Step	Default grid size (%D)	Fine grid size (%D)	Number of elements
1	9	2	50000
2	5	1	100000
3	3	0.6	180000

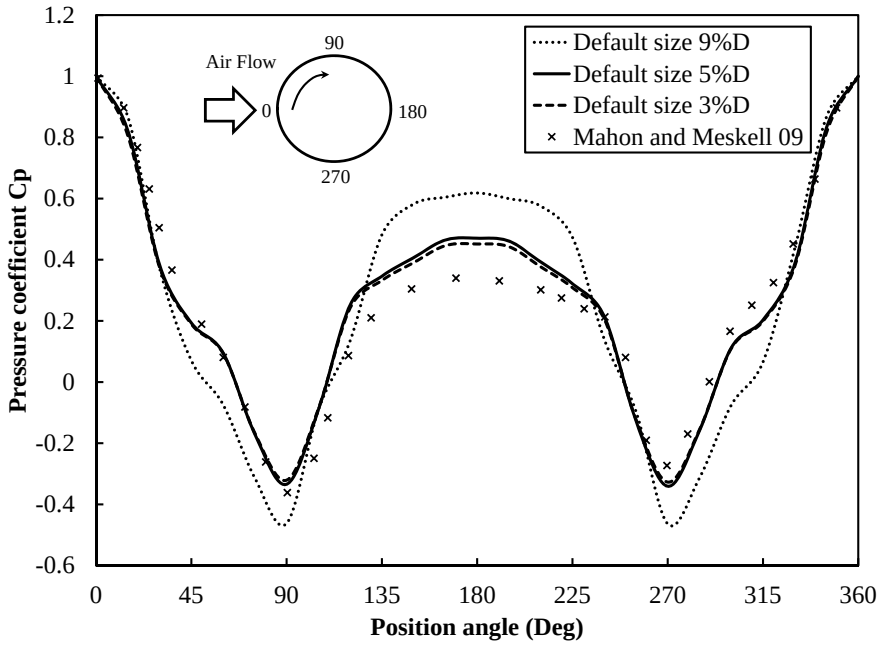

Figure E3: Predictions of surface pressure distribution using several grid sizes, NT array, $P_r = 1.32$, $R_e = 57000$.

E.5 Turbulence Modeling

Of the several turbulence models available in the literature [Mathieu and Scott, 2000], $(k-\epsilon)$ and $(k-\omega)$ are commonly used in most of engineering problems. These models are called two equation turbulence models where (k) is the turbulence kinetic energy and refers to the first equation, and the second equation is based on either (ϵ) which is the turbulence dissipation, or (ω) which is the specific dissipation.

The standard $(k-\epsilon)$ model is commonly used in many flow problems because of its robustness, economy, and reasonable accuracy. However, the model performs poorly when faced with non-equilibrium boundary layer such as flow separation. It follows that, problems with complex wall-fluid interaction present a challenge for the $(k-\epsilon)$ model. The Shear Stress Transport model (SST) was introduced by Menter [1994] to tackle such problems. The model works by solving the bulk flow using the standard $(k-\epsilon)$, and the turbulence frequency based model $(k-\omega)$ near the walls.

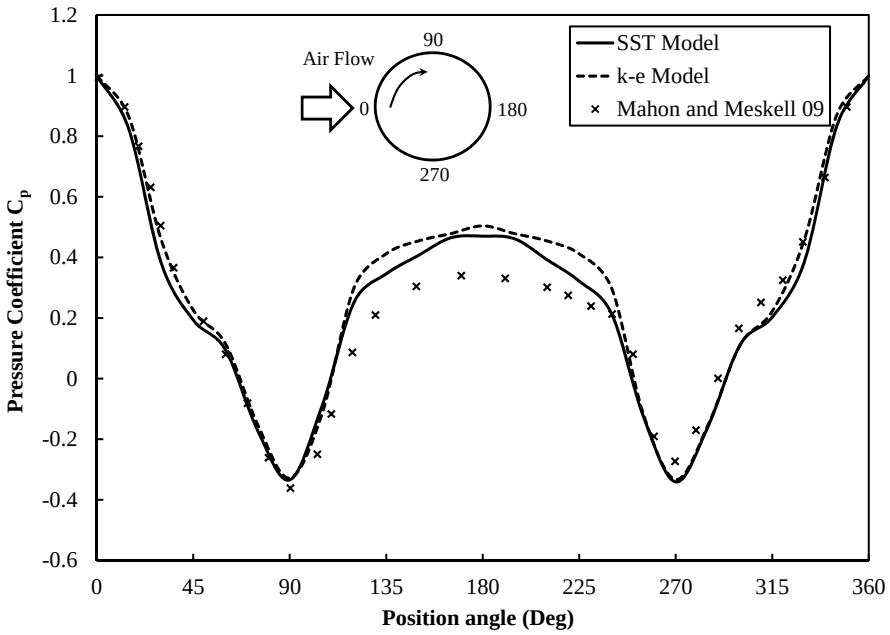

Figure E4: Tube surface pressure distribution using (SST) and $(k-\epsilon)$ turbulence models, NT array, $P_r = 1.32$, $R_e = 57000$.

The surface pressure distribution for a tube in a normal triangular array was calculated using $(k-\epsilon)$ and SST simulation as shown in Figure E4. It was found that the SST model had a better agreement with the experimental results, particularly in the wake region where the $(k-\epsilon)$ model over estimates the pressure coefficients. Therefore, the shear stress transport SST turbulence model was adopted in the consequent simulations.

E.6 Surface Pressure Distribution for a Parallel Triangular Array

The surface pressure distribution for a single flexible tube in a rigid parallel triangular array is shown in Figure E5. It is observed that there is a lack of symmetry in both the experimental and the numerical results. Mahon and Meskell [2010b] attributed this lack of symmetry to the jet switching of the flow in the array, which means that cross flow between the stream channels takes place leading to more mass flux on on side of the tube.

The numerical surface pressure distribution for the same tube array and Reynolds number showed also a lack of symmetry. Examining the flow field images show that, due to the finite number of rows in the array, the flow exiting the tube array tends to form an unstable downstream wake which may snap to either sides of the array as

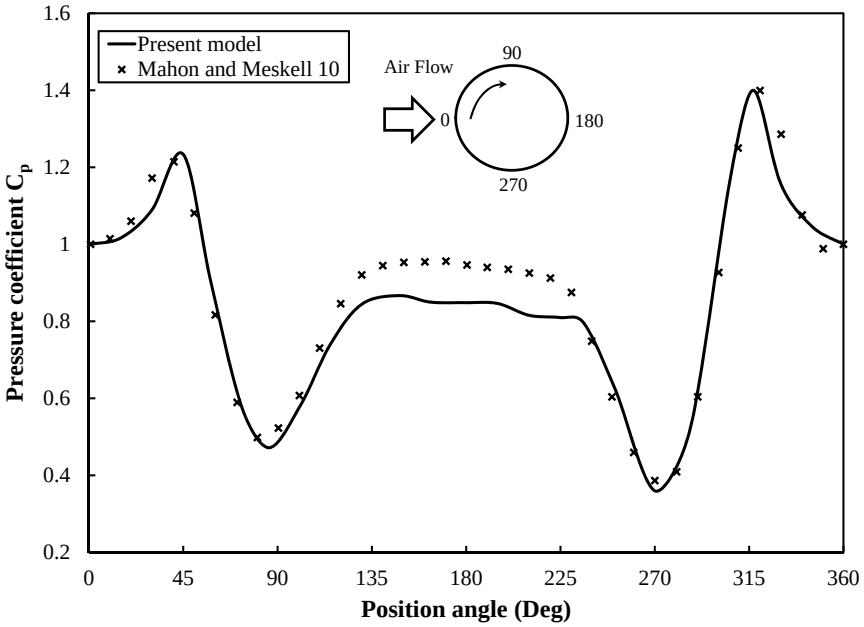

Figure E5: Surface pressure distribution on a tube located in the third row of a parallel triangular array, $P_r = 1.54$ and $R_e = 39000$.

shown in Figure E.6(a). Comparison of the flow field images for a parallel triangular array, Figure E.6(a), and a normal triangular array, Figure E.6(b), shows that the downstream wake was stable in the normal triangular array, and thus the pressure distribution was symmetric.

Similar behavior was reported by Hassan et al. [2010] where they observed that the downstream wake instability affects the pressure distribution around the tube. In order to overcome this effect in the simulations, the authors set an outlet boundary condition at the minimum gap between the tubes in the last row. They reported that this modeling technique eliminated the effect of the downstream wake instability and reduced the domain size significantly. The technique of setting an outlet boundary condition at the minimum gap of the last tube row in the array was adopted by other researchers as well [Longatte et al., 2003; Ridluan and Tokuhiro, 2008].

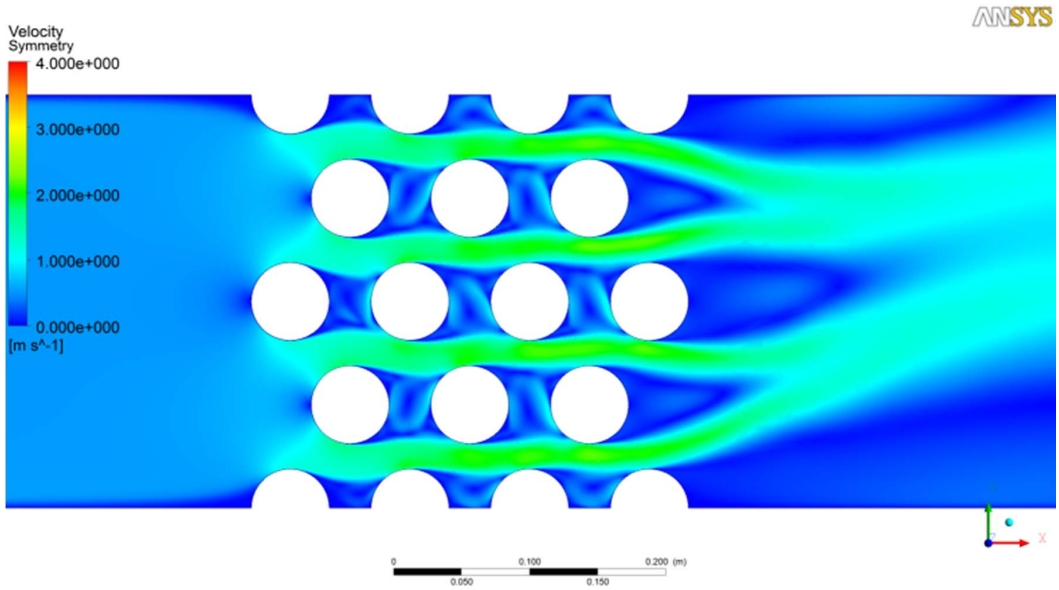

(a) Parallel triangular array, $P_r = 1.54$, $R_e = 39000$.

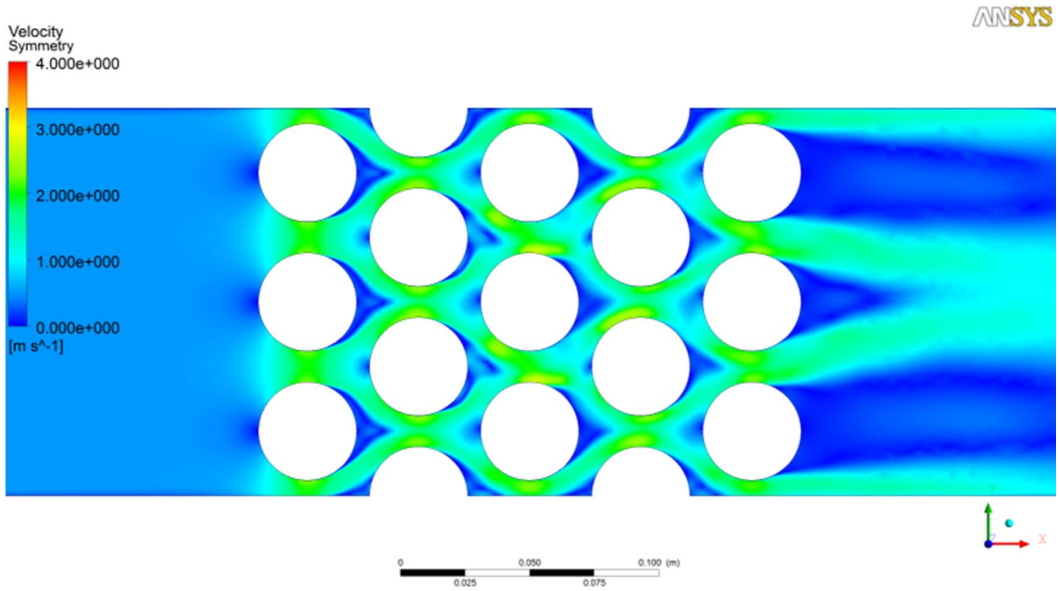

(b) Normal triangular array, $P_r = 1.32$, $R_e = 57000$.

Figure E6: Flow field images showing the downstream wake instability.